Fluid physiology in the spinal cord and subarachnoid space with relevance to syringomyelia pathogenesis

Shinuo Liu

BSc (Med)Hons, MBBS, Master of Surgery

A thesis submitted to fulfil the requirements of Doctor of Philosophy at the Faculty of Medicine and Health Sciences, Macquarie University

MACQUARIE University

TABLE OF CONTENTS

Figures

Videos

Tables

Abstract

There is mounting evidence that disruption of cerebrospinal fluid (CSF) circulation and CSF/interstitial fluid exchange is likely to contribute to a number of central nervous system disorders including syringomyelia. However, there is an incomplete understanding of the pathways of spinal fluid flux, in particular, fluid outflow. Moreover, the physiological factors that govern CSF flow in the spinal subarachnoid space (SAS) and fluid transport in the spinal cord have not been well studied. The aims in this thesis were to determine 1) the fluid outflow pathways in the normal spinal cord and 2) the effects of heart rate, blood pressure and respiration, specifically intrathoracic pressure, on fluid flow in the SAS, as well as into and out of the spinal interstitium.

Fluorescent tracers were injected into the cisterna magna and the cervicothoracic spinal cord parenchyma of Sprague Dawley rats. Various fluorescence imaging techniques were performed either *in vivo* in real-time, or *ex vivo* in perfusion-fixed extracted brain and spinal cord specimens. The macroscopic and microscopic redistribution of tracer within and around the spinal cord, particularly in relationship to vascular structures, was characterised. To investigate the effects of respiration, heart rate and blood pressure on fluid dynamics, each physiological parameter was carefully controlled and separately manipulated.

Free breathing animals (in which cycles of negative and positive intrathoracic pressure are generated) had significantly greater flow of CSF in the SAS as well as inflow of tracer into the spinal cord compared with mechanically ventilated control rats (positive intrathoracic pressure only). Hypertension and tachycardia had no significant effect on CSF flow in the SAS. Hypertension produced conflicting results but likely had a modest effect on inflow. Increased tracer influx was not observed with tachycardia. Both tachycardia and hypertension stimulated tracer efflux, but respiration was not found to

affect spinal interstitial clearance. Spinal intramedullary movement of tracer was slow, and its redistribution was limited by isotropic and anisotropic properties of white and grey matter. Perivascular spaces of all vessel types provided preferential pathways for both tracer influx and efflux to pial and ependymal surfaces. Tracer deposited within the internal basement membrane of the tunica media of arteries and arterioles.

Intrathoracic pressure has a significant effect on spinal CSF flow and parenchymal fluid ingress. Arterial pulsations play a smaller role in SAS hydrodynamics but have profound effects on spinal interstitial fluid homeostasis, particularly outflow.

Statement of originality

I hereby declare that the work presented in this thesis has not been submitted for a higher degree to any other university or institution. To the best of my knowledge this submission contains no material previously published or written by another person and is my own work unless stated otherwise. Any contribution made to the research by others is explicitly acknowledged.

The work was carried out with ethical approval from the Macquarie University Animal Ethics Committee (ARA 2016/032), and the University of Sydney Animal Ethics Committee (ARA 2018/1402).

Shinuo Liu

Department of Clinical Medicine

Faculty of Medicine and Health Sciences

Macquarie University

24th October 2019

Publications

Journal Article

1. **Liu S**, Lam MA, Sial A, Hemley SJ, Bilston LE, Stoodley MA *Fluid outflow in the rat spinal cord: the role of perivascular and paravascular pathways* Fluids Barriers CNS. 2018; 15: 13. doi: 10.1186/s12987-018-0098-1 Received: 11 February 2018 Accepted: 16 April 2018 Published: 29 April 2018
2. Shinuo Liu, Neftali Flores Rodriguez, Courtney Wright, Marcus A. Stoodley, Lynne E. Bilston, Rob Lloyd, Simon McMullan, Sarah J. Hemley

   Intrathoracic pressure and arterial pulsations exert different driving forces on spinal cerebrospinal and interstitial fluid flow

   Prepared for submission to Nature Communications.

Conference Presentations

1. "Fluid outflow in the rat spinal cord: the importance of perivascular and paravascular pathways". Poster presentation at the 2018 GRC Barriers of the CNS conference, New London, New Hampshire.
2. "Fluid outflow in the rat spinal cord: the role of perivascular and paravascular pathways". Podium presentation at the 2018 Neurosurgical Society of Australasia (NSA) Annual Scientific Meeting, Gold Coast. Peter Leech Prize finalist
3. "What drives fluid in and around the spinal cord?" Podium presentation at the 2019 CSF Flow at Niagara Falls: Chiari, Syringomyelia and EDS conference, Buffalo, New York

Acknowledgements

This thesis could not have materialised without my better half, the Marie to my Pierre, Dr Susannah Lyes. She has been my pillar of unwavering support and an inexhaustible source of encouragement. I am blessed with a unicorn, a partner in crime who always has my back! I am sincerely grateful to my family for nourishment of the mind and body, and for their staunch belief in me and all my pursuits.

Professor Marcus Stoodley has been my intellectual lighthouse since medical school. I am continually guided by his erudite beacon. Time and again he has shown me the possible, where others only see the impossible. Dr Sarah Hemley has been the voice of reason, a wonderful mentor and an invaluable friend. Her patience with me should be celebrated as a national treasure.

Special thanks to collaborator Dr Magda Lam for providing critical support during the larval stages of my PhD. I am grateful for help from Drs Jeff Rogers, Anita Turner, Mark Butlin, Isabella Tan and the animal housing staff at Macquarie University and University of Sydney. Many thanks to my pressure relief valve, Macquarie Sports and Aquatic Centre, without which my sanity would have evaporated long ago.

This work was not possible without the support of the Brain Foundation, Column of Hope Research Foundation, the National Health and Medical Research Council, and Macquarie Neurosurgery.

Declaration of contributions

	Fluid outflow in the rat spinal cord: the role of perivascular and paravascular pathways	Intrathoracic pressure and arterial pulsations exert different driving forces on spinal cerebrospinal and interstitial fluid flow
Conception of original idea	M.A.S. L.E.B.	M.A.S. L.E.B. S.J.H
Experimental design	S.L. M.A.S. L.E.B. M.A.L.	S.L. M.A.S. L.E.B. S.J.H S.M
Conduction of experiments at Macquarie University	M.A.L. S.L. S.J.H. A.S.	S.L. S.J.H.
Conduction of experiments at the University of Sydney		S.L. S.J.H. C.W. N.F.R.
Processing of results	S.L.	S.L. S.J.H R.L.
Data analysis	S.L.	S.L. S.J.H
Manuscript drafting	S.L.	S.L
Manuscript review	S.L. A.S. M.A.L S.J.H L.E.B. M.A.S.	S.L. C.W. N.F.R L.E.B. M.A.S. S.M R.L. S.J.H

S.L.	Shinuo Liu
M.A.S	Marcus A. Stoodley
S.J.H	Sarah J. Hemley
L.E.B	Lynne E. Bilston
M.A.L	Magdalena A. Lam
A.S.	Alisha Sial
N.F.R	Neftali F. Rodriguez
C.W	Courtney Wright
R.L.	Rob Lloyd
S.M.	Simon McMullan

Abbreviations

AFO-647	Ovalbumin conjugated to Alexa-Fluor®-647
AOM	Atlanto-occipital membrane
ASA	Anterior spinal artery
APQ4	Aquaporin-4
BBB	Blood brain barrier
BP	Blood pressure
BPM	Beats per minute
CED	Convection enhanced delivery
CFD	Computational fluid dynamics
CSF	Cerebrospinal fluid
CNS	Central nervous system
CT	Computer tomography
ECS	Extracellular space
EPI	Echo planar imaging
FB	Free breathing
GM	Grey matter
GMi	Grey matter injection
HR	Heart rate
HRP	Horse radish peroxidase
ICG	Indocyanine green
ICP	Intracranial pressure
IOI	Integrative Optical Imaging
ISF	Interstitial fluid
MAP	Mean arterial pressure
MRI	Magnetic Resonance Imaging
MV	Mechanically ventilated
NDS	Normal Donkey Serum
NIFR	Near infrared
PBI	Pencil beam imaging
PBS	Phosphate buffered solution
PC-MRI	Phase contrast magnetic resonance imaging
PFA	Paraformaldehyde
PSA	Posterior spinal artery
PTS	Post-traumatic syringomyelia
RECA-1	Rat Endothelial Cell Antigen-1
ROI	Region of interest
SAS	Subarachnoid space
SD	Standard deviation
SEM	Standard error of mean
SMA	Smooth Muscle Antibody
Time-SLIP	Time-Spatial Inversion Pulse
WM	White matter
WMi	White matter injection

1 Introduction

1.1 Syringomyelia

1.1.1 Background

Derived from the Greek words: συρινξ ("syrinx") meaning pipe, and μυελος ("myelos") meaning marrow [1-3], syringomyelia is an enigmatic condition where fluid-filled cavities form and enlarge within the spinal cord. The precise nature of syrinx fluid is unclear but is thought to be similar to cerebrospinal fluid (CSF) [4-6]. These cavities, or syrinxes, are manifestations of numerous acquired and congenital pathologies. There may be a common pathophysiology, but the precise details remain elusive. Syrinxes can encroach upon and damage normal spinal neural tissue, resulting in pain, paralysis and even death [4, 7, 8]. However, in many cases, treatment options remain limited and long-term failure rates are high [9, 10]. Improved understanding of the pathogenesis of this condition is imperative in developing more effective therapies.

Until the late 20th century, the terms syringohydromyelia and hydrosyringomyelia have often been used interchangeably with syringomyelia [11, 12]. Hydromyelia has also been employed to describe dilation of the central canal. In this thesis, "syringomyelia" will refer to all abnormal fluid-filled cavities within the spinal cord. The exceptions are small non-enlarging cavities caused by trauma.

1.1.2 Epidemiology, classification and pathology

The history of syringomyelia, while of interest, is beyond the scope of this literature review. The topic has been reviewed by others and the reader is highly encouraged to peruse these sources [13-18].

Table 1 A classification system of syringomyelia (from Milhorat et al, 2000 [19])

Classification of syringomyelia

I Communicating canalicular syringomyelia
    Central canal dilations
        • communicating hydrocephalus (posthemorrhagic, postmeningitic)
        • complex hindbrain malformations (Chiari II, encephalocele)
        • Dandy-Walker cyst
II Non-communicating canalicular syringomyelia
    Central canal/paracentral syrinxes
        • Chiari malformations
        • basilar invagination
        • spinal arachnoiditis (post-traumatic, postmeningitic)
        • extramedullary compressions (spondylosis, tumors, cysts)
        • tethered cord
        • acquired tonsillar herniation (hydrocephalus, intracranial mass lesions, craniosynostosis)
    Primary parenchymal cavitations
        • spinal cord trauma
        • ischemia/infarction
        • intramedullary hemorrhage
III Atrophic cavitations (ex-vacuo syringomyelia)
IV Neoplastic cavitations

1.1.2.1 Classification

The most common conditions associated with syringomyelia are Chiari malformation (51%) [20] spinal cord injury (11%) [21], tumours (10%) [22] and arachnoiditis which refers to scarring in the subarachnoid space (6%) [6, 10, 22-24]. There are many ways to classify syringomyelia, but Milhorat's system [19] is the most widely recognised (**Table 1**).

Communicating syringomyelia is secondary to obstruction of CSF pathways distal to the fourth ventricle outlets (Fig. 1). On histological sections it is characterised by simple dilatation of the central canal, lined by ependyma [19, 22].

If the dilated central canal does not communicate with the fourth ventricle (such as in Chiari malformation) then the syrinx is a non-communicating canalicular type (Fig. 1) [5]. Unlike communicating types, non-communicating syrinxes have a predilection for dissecting into the spinal cord (particularly the dorsolateral area). Histological findings demonstrate central canal stenosis as well as isolated cavities [19, 22].

Extracanalicular syrinxes do not communicate with the central canal and originate in the spinal cord parenchyma (Fig. 1). Trauma, ischemia, or spontaneous intramedullary haemorrhage may precipitate these cavities. The cysts normally arise in the dorsolateral watershed area of the spinal cord [19]. Histological appearance includes necrosis, neuronophagia, and Wallerian degeneration [22, 25].
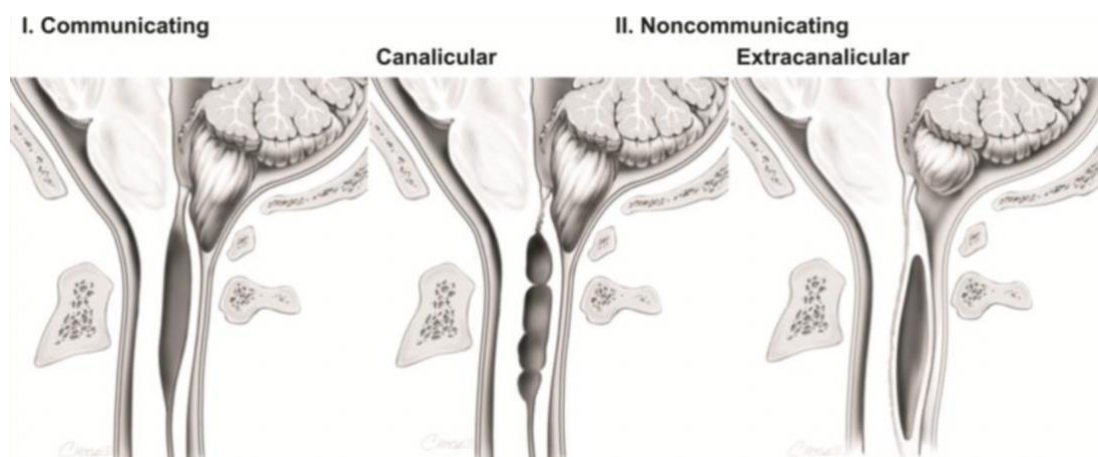
Fig. 1 Popular classification system of syringomyelia. Most syrinxes are either communicating or noncommunicating. The most common type is the noncommunicating canalicular syrinx which is characteristic of Chiari Malformations. Reproduced from Brodbelt & Stoodley, 2003 [1].

Intramedullary tumours, such as astrocytomas and ependymomas, can form syrinx-like cavitations. Necrosis begins centrally and extends rostrally and caudally from the tumor boundaries. The membrane of the necrotic cysts is usually lined by tumour or glial tissue [19]. The fluid within these syrinxes is markedly different from CSF and is highly proteinaceous [19].

Ex-vacuo cavitations result from degenerative changes and atrophy in the spinal cord [22]. They do not expand so are generally not considered to be true syrinxes.

Although Chiari malformation and spinal cord injuries are most common, there is a plethora of other associated diseases at the craniocervical junction or affecting the spinal subarachnoid space (SAS). These are summarized in **Table 2** [26]. Note that some dysraphic disorders affect neither the SAS nor the foramen magnum.

Table 2 Conditions associated with syringomyelia (from Brodbelt, Stoodley & Jones, 2005 [26])

Craniocervical junction

Congenital	*Acquired*
• Chiari malformation Type I	Tonsillar herniation secondari to:
• Chiari malformation Type II	• Posterior fossa tumor
• Dandy-Walker malformation	• Supratentorial tumors
• Posterior fossa arachnoid cysts	• Lumboperitoneal shunts
• Apert's syndrome with tonsillar herniation	• Chronic Subdural haematoma
• Crouzon's syndrome	• Lhermitte-Duclos disease
• Noonan's syndrome	• Nocardia brain absecess
• Achondroplasia	• Basilar impression
	• Arachnoiditis
	• Idiopathic

Spine

Congenital	*Acquired*	
	Intramedullary:	*Extramedullary:*
• Myelomeningocoele	• Neoplastic	• Neoplastic
• Tethered spinal cord	• Primary ependymoma	• Meningioma
• Diastematomyelia	• Haemangioblastoma	• Schwannoma
• Lipomyelomeningocoele	• Astrocytoma	• Lymphoma
• Spinal Dermoid	• Lymphoma	• Myeloma
• Neurenteric cysts	• Metastases	• Lipomatosis
• Sacral agenesis	• Non-Neoplastic	• Non-Neoplastic
• Anorectal anomalies	• Spinal Trauma	• Intervertebral disc protrusion
• Familial spinal arachnoiditis	• Demyelination	• Cervical spine stenosis
	• Multiple sclerosis	• Arachnoiditis
	• Spinal Sarcoidosis	• Arachnoid telangiectasia
	• Tuberculosis	• Intraventricular haemorrhage
		• subarachnoid Haemorrhage
		• sarcoidosis
		• Idiopathic

1.1.2.2 Epidemiology

Syringomyelia is mainly an affliction of the young. The average presenting age is less than 29 years [1, 21, 27, 28]. As magnetic resonance imaging (MRI) use has become ubiquitous, the reported world incidence of syringomyelia is approximately 8.5 cases per 100,000 per year [29-31]. The prevalence of syringomyelia is particularly high in some parts of Russia, reaching 130 cases per 100,000 [32].

Based on autopsy data up to 30 years after injury, up to 28% of all patients suffering a spinal cord injury will have a syrinx, and up to 50% will have spinal cord cystic changes [33-38]. However, less than 10% of those with a spinal cord injury will have a symptomatic syrinx [39-44]. Others, however, have reported an incidence as high as

64% in spinal cord injured patients [45]. Males have a higher prevalence of post-traumatic syringomyelia (PTS), likely due to higher spinal cord trauma rates [27].

1.1.3 Clinical features and diagnosis

The natural history is uncertain with significant variability. Some patients have a static course, while others present with rapid deterioration. PTS may occur anytime between 1 month to 37 years after the initial injury [1, 46-48]. Rarely, syrinxes may spontaneously resolve [49].

The clinical presentation of syringomyelia is diverse and probably reflects the location of the syrinxes within the spinal interstitium, as well as the underlying associated pathology. The cervical and thoracic spine are the most common locations for syringomyelia [27, 50]. In Chiari-related syringomyelia, two-thirds become symptomatic in teenage years or early adulthood [51, 52]. Symptoms may be related to the Chiari malformation or directly to a cervical syrinx, such as upper extremity sensorimotor disturbance. In patients with PTS, the mean age of presentation is 43 years [42, 51]. The primary symptoms are limb weakness, sensory changes, radicular pain and axial spinal pain [47, 48]. Due to increasing availability of MRI scans, the detection of incidental syrinxes is increasing [29].

The classic presentation is dissociated sensory loss. Patients complain of loss of pain and temperature sensation but preservation of light touch and proprioception [43, 53]. This was previously believed to be secondary to central syrinxes that compromise decussating spinothalamic fibres in the anterior commissure [54]. New research has shown that the various pain syndromes associated with syringomyelia is likely due to dissection of syrinxes into the dorsal horn with concomitant release of neurotransmitters such as Substance P [56]. The three most common presenting symptoms are pain, numbness, and weakness, occurring in 50–90% of adult patients

[55, 56]. The classic dissociated pattern occurs in only 40–70% of cases [42, 51]. Motor weakness usually occurs with sensory disturbance and can be asymmetrical with delayed onset [1, 42]. A wide range of descriptions of pain has been reported. Pain may be instigated by Valsalva manoeuvres such as coughing or sneezing [1, 42, 50].

Other symptoms include Horner's syndrome, anhidrosis and oculomotor dysfunction (if syrinxes extend rostrally to involve the lower brainstem—a very rare occurrence), gait disturbance, autonomic sphincter dysfunction (if syrinxes involve the conus medullaris [50]), hyperhidrosis and muscle spasms [57, 58]. In longstanding cases, muscle atrophy, trophic changes and Charcot joints are evident [59-64]. In children, scoliosis may be caused or exacerbated by syringomyelia; successful treatment of the syrinxes can stabilize or improve the curvature [65, 66].

1.1.4   Diagnosis

The diagnostic imaging of choice is MRI. It is noninvasive and multi-planar. It provides superior definition of neurological structures compared with Computed Tomography (CT) scans [1]. MRIs play an integral role in the initial diagnosis of syringomyelia, identification of associated pathologies and subsequent monitoring of syrinx progression [50, 67, 68].

In T1-weighted sequences, hypointense fluid is identified within the syrinx cavity. In T2 weighted sequences, areas of gliosis, demyelination and oedema are characteristic [67, 69]. Interstitial oedema in the spinal cord may herald the development of a syrinx [59, 69, 70]. MRI does however have its limitations and it may still be challenging to differentiate spinal cord myelomalacia and oedema from syringomyelia [50, 71].

The introduction of phase-contrast cine-MRIs and cardiac-gated balanced fast-field echo sequences has allowed direct visualisation of CSF flow around areas of obstruction, such

as the foramen magnum in Chiari-related syringomyelia and arachnoiditis in PTS [71-73].

Myelography and CT scans have largely been superseded by MR imaging. CT myelograms are occasionally used to delineate the spinal cord and to detect subarachnoid adhesions [1].

1.1.5 Treatment

Treatment outcomes for syringomyelia remain largely unsatisfactory. Like other disorders of central nervous system (CNS) fluids, surgical techniques are the mainstay of treatment. Although various operations have been described, most clinical series appear to have reasonably good short-term efficacy rates but significant recurrence or failure rates after 5 years [1]. The primary aim in treating these diverse lesions is to either drain the syrinx cavity or to normalise fluid flow pathways in the SAS. Where possible, the associated or underlying pathology should be addressed [74].

Early treatment attempts included percutaneous aspiration or myelotomy to decompress the syrinx [51]. This failed to maintain ongoing decompression of the syrinx. Terminal ventriculostomy has also had some success in cases of communicating syringomyelia [8, 75-77]. Complete cord transections are still effectively used today in those with complete spinal cord injuries [1].

When associated with craniocervical junction disorders, such as Chiari malformation, the most commonly performed surgical procedure is a posterior fossa decompression, as first proposed by Gardner and Fahy [78]. It involves reconstitution of the normal SAS overlying the cerebellum at the foramen magnum and has been reported to be relatively effective in stabilising or collapsing the syrinx. Short-term efficacy is as high as 82%, although a relapse rate of 50% has been reported [52]. Other case series have indicated that syrinxes reduce over a median time period of 4–5 months after surgery. This was

maintained at follow-up of up to 8 years [78, 79]. However, some authors [64] have reported a large percentage of patients with incomplete symptom resolution [64, 78]. Posterior fossa decompression can be combined with syringosubarachnoid shunting as a secondary therapy [80]. Some authors propose that the size of the syrinx (larger than 70% of the cord width), and the presence of symptoms attributable purely to the syrinx (as opposed to the tonsillar descent) should determine whether shunting is required [81, 82]. Up to 93% of patients treated with a syringosubarachnoid shunt have improvement in pain according to Iwasaki and colleagues [81], while others have reported some success in neurological improvement [83]. Even the precise technique of posterior fossa decompression is subject to wide variation amongst surgeons. Operative nuances relate to reconstruction of the posterior fossa dura (duraplasty), exploration of the fourth ventricle outlets and whether to debulk the cerebellar tonsils [1]. It has been reported that posterior fossa decompression with duraplasty is more effective than decompression alone at reducing syrinx size in Chiari-associated syringomyelia [84, 85]. In paediatric populations, some advocate craniectomy without dural opening [86]. Plugging of the central canal at the level of the obex has largely been relegated to a historical procedure due to the high complication rates [80] and the realisation that most syrinx cavities do not communicate with the fourth ventricle

Spinal cord detethering or adhesiolysis with or without duraplasty have been performed for arachnoiditis with less clear outcomes [87]. To restore physiological CSF flow, following bony decompression scar tissue is resected and the dura expanded to reconstruct the SAS [88]. When the arachnoiditis is not focal, or there is unacceptable surgical risk to neurological structures, shunting is considered. Syrinx fluid is diverted to various compartments. They include: the spinal SAS (syringostomy, syringosubarachnoid shunt), the pleural cavity (syringopleural shunt), or peritoneal

cavity (syringoperitoneal shunt). The procedure of choice is based not on evidence, but rather dependent on surgeon preference. Sgouros et al, Batzdorf et al and diLorenzo et al [30, 89, 90] for example are proponents of the syringopleural shunts. Syringosubarachnoid shunts have good short-term results. It has been reported they improved pain scores in up to 89% of patients, weakness in 63% and ascending sensory level in 30% [42]. Similarly, after syringopleural shunting 69% of patients reported favourable outcomes [41]. However, they are prone to blockage and syrinx recurrence [50, 91-93] in up to 50% of cases [89, 90]. Other authors of shunt case series have reported complication rates of 10–100 %. Challenges faced by investigators include spinal cord tethering, low CSF-pressure states, infections, shunt dislocation, epidural fibrosis and spinal instability [1, 94]. In a series of 18 patients who underwent adhesiolysis and duraplasty, Schlesinger et al cited an efficacy rate of 38%, but failure rate of 44% [51]. Finally, Klekamp et al reported a recurrence rate of 97% in patients undergoing direct shunting procedures for spinal arachnoiditis. Symptoms recurred on average within 2 years [24].

In those with extradural compression, such as from a prolapsed intervertebral disc, epidural tumour or spinal deformity, removal of the offending pathology or reduction of the spinal fracture may lead to syrinx resolution [34, 106, 107]. Similarly, in communicating syrinxes associated with hydrocephalus, ventriculoperitoneal shunting is indicated initially [30].

Other novel treatment therapies have been trialed with limited or no success. These include radiotherapy [51, 95] and transplantation of human foetal or embryonic spinal cord grafts into a syrinx [96-98].

The optimal time to offer surgical treatment is also unclear. On the one hand, there is evidence that early treatment will lead to improvement in pain, sensory changes, and

weakness, although headache, spasticity, and autonomic dysfunction are less affected [99, 100]. On the other hand, however, conservative therapy involving rehabilitation has been demonstrated to be superior to surgery in improving neurological outcomes in a small cohort of PTS patients [101]. Most clinicians agree that treatment is indicated for worsening symptoms and neurological function as well as progressive myelopathy [91, 102]. It is unclear whether asymptomatic syrinx enlargement on serial imaging is a sufficient indication for surgery [103].

Overall, there is a lack of consensus on the indications and general strategy in dealing with this challenging collection of disorders. There appears to be reasonably positive short-term clinical outcomes for some therapies, but long-term results are poor, especially for shunts. The rationale behind surgical treatments do not reflect a complete understanding of the pathophysiology of syrinxes. It is unclear why re-establishing normal CSF flow in the SAS often leads to syrinx reduction. No data exist to consistently promote one technique over another. Thus, the fundamental problem is that the pathophysiology of syringomyelia is far from understood.

1.1.6 Theories about aetiology

Early attempts at explaining syringomyelia were inspired by post-mortem examinations of Chiari II malformations, resulting in the belief that spinal dysraphism or developmental anomalies were involved [17, 104, 105]. Subsequently, various authors suggested diverse hypotheses, largely centred on the development of canalicular syrinxes. These theories generally lacked supporting clinical or experimental evidence. Propositions have included familial factors [106-109], birth trauma [33, 107, 110, 111], inflammatory [107, 112-114] and immunological factors [115] and a secretory hypothesis [116, 117].

24

From the mid to late 20th century, a succession of "hydrodynamic theories" have been posited. These attempted to explain the formation and expansion of canalicular and extracanalicular syrinxes by offering various mechanisms by which changes in pressure and pulsations within the SAS promote CSF flow into the spinal cord or the central canal. Brief descriptions of the central tenets, the primary collaborators and the major shortcomings of each theory are summarised in **Table** *3*.

It has been argued that the major common flaw with hydrodynamic theories is that the intrasyrinx pressure must be higher than the spinal SAS pressure in order for the syrinx to expand [118, 119]. Other authors have suggested that fluid from other sources might be responsible for the continued enlargement of syrinxes [120]. Such sources and theories have included:

- Extracellular fluid: Interstitial fluid (ISF) accumulation can result from obstruction of fluid outflow pathways (presumably to the spinal SAS). Extracellular fluid may exceed the interstitial space volume in the parenchyma due to obstruction of perivascular spaces, cord tethering, changes in arterial circulation [6] or impaired venous drainage. The latter may occur via leakage of fluid from the microcirculation secondary to compression of venous circulation, or through reduced ISF flow in to the venous system [104, 121]. Others have used computational models to show that in the presence of arachnoiditis there is a pressure gradient directed towards the SAS, forcing fluid from the central canal into the interstitium [122].

- Intramedullary pulse theory: obstruction by the cerebellar tonsils leads to lower SAS pressures distal to the block, but the pulse wave propagates in the spinal cord, expanding it and causing accumulation of extracellular fluid [123, 124]. However, intraoperative observations of extremely high intrasyrinx pressures

make passive filling of the cavity unlikely. Additionally, the spinal cord can remain oedematous after elimination of the Venturi effect upon durotomy and CSF efflux from the SAS [120].

- ▪ Disruption to the blood-spinal cord barrier: SAS obstruction leads to pressure mediated dysfunction of the microcirculation and fluid accumulation through mechanisms that are unclear [125]. Hemley et al demonstrated in a rodent model of extra-canalicular syringomyelia that the blood-spinal cord barrier was dysfunctional even after the acute period during which the syrinx cavity is formed [126].

Neoplastic lesions, most commonly haemangioblastomas, astrocytomas and ependymomas [127], produce extra-canalicular syrinxes. Previously, it has been suggested that the cystic cavity is part of the tumour, or the tumour and syrinx result from developmental defects. It is likely, however, that neoplastic factors such as neo-angiogenesis, blockage of fluid outflow pathways, dissemination of oedema and tumour breakdown products, or haemorrhage play more important roles [127-130]. A point of contention is whether the composition of the cyst is more like CSF or is proteinaceous, which results from breakdown of the blood-spinal cord barrier [128].

Intramedullary haemorrhage and infarction, both arterial and venous, have been implicated in syrinx induction in animal models and human autopsy results [22, 131-133]. However, there is no evidence to support, or plausible theories to explain how this contributes to syrinx progression and expansion [104, 134]. Various groups have used mathematical and animal models to investigate the link between arachnoiditis in the SAS and syrinx development. Bertram et al [7, 135, 136] postulated that tethering of the cord initiated syrinx cavity formation secondary to tensile radial stress. A low pressure state in the cord was thought to facilitate inflow of extracellular fluid into the cavity.

Others have proposed that changes in the pulsatile pressure waves in the SAS encourage fluid influx into the spinal parenchyma [122, 137]. Animal models have demonstrated that arachnoiditis may exacerbate underlying oedema or cysts but did not precipitate the formation of the syrinx cavity [138, 139].

Thus, a multitude of pathogenesis theories have been proffered. Some hypotheses have been based on clinical observations, mere thought experiments or limited laboratory data. Recently, there has been a more systematic experimental approach to understanding the fundamental mechanisms of syrinx formation and expansion. This has been supplemented by powerful new computational techniques to model fluid flow and tissue properties of the spinal cord. However, a universal model to explain how fluid accumulates to produce a syrinx within the spinal interstitium is lacking. There are still many unanswered questions surrounding the composition and source of syrinx fluid, the relationship between the SAS and the syrinx, as well as the role of cellular and molecular changes in syrinx pathogenesis. A fruitful direction of research is likely towards a better comprehension of altered fluid inflow and outflow from the syrinx. Unfortunately, this endeavor currently lacks context, as the fundamental understanding of how fluids physiologically enter and exit the spinal parenchyma is woefully incomplete.

1.1.7   Current research and animal models

No animal model perfectly replicates human syringomyelia, and many have methodological characteristics that make translation of experimental findings problematic. Most animal models have been designed to examine only limited aspects of syringomyelia. The difficulties encountered in animal studies pertain to the size of the animals, efficacy of syrinx formation, ability to perform *in vivo* measurements on fluid pressures and flow within and around the spinal cord, and the fidelity with which the associated pathological condition is modeled. Hydrocephalus, spinal cord injury and

Chiari malformations, for example, are not simple entities to recreate in a laboratory setting. ***Table 4*** summarises the major canalicular and extracanalicular animal models created and used by various authors, their experimental methodologies, main findings related to syrinx pathology or pathogenesis, relevance to pathophysiology theories (if applicable) and their shortcomings.

1.1.8   Summary—the problem

Syringomyelia is a serious, but poorly understood condition. Those afflicted may be condemned with tremendous long-term suffering. Treatment is directed towards the underlying pathology (if known, and where possible), consists primarily of surgical options, but is overwhelmingly unsatisfactory in a large portion of cases. The crux of the problem in treatment is that the pathophysiology of fluid accumulation within the spinal cord — the final common pathway of a heterogeneous collection of pathologies associated with syringomyelia — is unclear. Thus far, laboratory and computational efforts at clarifying the pathogenesis have been valiant. However, they are hampered by an incomplete understanding of the pathways and factors that govern fluid inflow and outflow from the spinal cord. The remainder of the introduction will review the relevant dynamics of CSF and ISF of the CNS.

Table 3 Summary of various theories of the pathogenesis of syringomyelia and their shortcomings

Theory name/ Author(s)	Description	Shortcomings
Water hammer/ Gardner [140, 141]	A hindbrain abnormality leads to obstruction of the normal CSF outflow pathways from the fourth ventricle. This results in CSF being driven directly into the central canal, causing enlargement of the canal within the spinal cord [120].	
Respiratory transmedullary/ Ball and Dayan [143]	Raised intrathoracic and intraabdominal pressures during coughing and straining translates to increases in epidural venous pressure and thus spinal CSF pressure. Normally, a rostral displacement of spinal CSF occurs. However, for those with foramen magnum obstruction, CSF is directed into the spinal cord parenchyma via enlarged perivascular spaces. This fluid accumulates in the extracellular space to form a syrinx [143]. The central canal is involved only if the syrinx dissects into it.	In most patients the central canal is occluded between the fourth ventricle and the syrinx so fluid cannot be driven directly from the fourth ventricle into the central canal [114].
Obstructed CSF drainage / Aboulker [144]	Obstruction at the foramen magnum prevents CSF return from the central canal to the fourth ventricle. Impairment of CSF absorption in the SAS, the dorsal root entry zone or by the CNS vasculature predisposes ISF accumulation. Ellertson and Greitz [119] later measured the pressure in the spinal SAS and in a syrinx, demonstrating that changes in pressure in the SAS was reflected in the syrinx cavity, albeit with a time delay. This was evidence of communication between syrinx and the SAS. The time delay allows fluid to flow against the pressure gradient into the syrinx, and when fluid inflow exceeds outflow (due to obstruction), the syrinx enlarges.	Syrinxes without craniocervical junction pathology cannot be accounted for. Craniospinal dissociation theory resulted from "thought experiments". Experimental evidence from animals or imaging studies do not support central tenets (especially "slosh and suck") [142].
Pressure dissociation/ Williams [33]	The craniospinal pressure dissociation theory described high intracranial pressure and low spinal pressure. In Valsalva manoeuvres, there is raised epidural venous pressure and CSF is driven rostrally. In patients with a craniocervical obstruction, CSF is unable to flow normally in a caudal direction in the SAS [30, 120]. Instead CSF is "sucked" into the central canal, enlarging it to form syrinx. In the "slosh" part of the theory, increases in arterial and respiratory pulse pressures are transmitted to the syrinx fluid, dissecting the cord [2, 197] in a rostral direction (similar to above). Caudal dissection by the syrinx cavity can be explained by the Venturi effect due to low SAS pressures below constrictions [142].	
Arterial transmedullary/ Oldfield and Heiss [29, 145]	Physiological compensatory flow of CSF between the cranium and spine in response to cardiac pulsations is disrupted by obstruction in the foramen magnum. In this environment of CSF flow stasis, the cerebellar tonsils are displaced downwards during systole, like a "piston", producing high-pressure waves that compress the spinal cord and force syrinx fluid rostrally and CSF into the spinal cord via perivascular and interstitial spaces [30].	The pressure generated by the tonsils is unlikely to be great enough to overcome a pressure gradient exerted by the syrinx cavity [119]. Cerebellar tonsillar movement is limited in many cases of syringomyelia [118].
Arterial pulsation perivascular space flow / Stoodley and colleagues [146-149]	Stoodley et al established that normally there is an arterial pulsation driven flow of CSF from the SAS to the central canal via perivascular spaces. In an animal model of canalicular syringomyelia, CSF tracers were detected around perivascular spaces and in the syrinx cavity within the central canal [147]. In computational models Bilston et al analysed the wave properties of fluid flow in the perivascular spaces and the SAS. They showed that a mismatch in timing between the arterial and CSF pressure wave pulsations at the junction of the perivascular space and the SAS may lead to increased flow during systole [150, 151]. A partial one-way valve may arise, driving fluid along the perivascular space to	Does not explain syringomyelia without SAS block, for example in tethered cord.

overcome the mean positive pressure gradient between the syrinx and SAS. This timing mismatch was later confirmed by Clarke et al [152] in patients with Chiari malformation, but not in normal subjects based on measurements from cine-MRI CSF flow studies.

Other authors have applied this theory to excitotoxic extracanalicular animal models [153] demonstrating increased perivascular tracer deposition and increased fluid flow at the level of the obstruction. Bilston et al suggested a similar mismatch mechanism in arachnoiditis associated syrinxes. This was supported by a theory, later championed by Elliot et al, that used a lumped-parameter model [154].

Elastic-jump hypothesis/ Carpenter et al [155]	A mathematical model employed fluid-filled coaxial elastic tubes to simulate a pressure wave generated by coughing or straining. It was hypothesised that where there is a SAS obstruction, a focal rise in pressure in the spinal cord interstitium occurs. Fluid can accumulate either in the central canal or outside of it [120].	Later analysis from a mechanical perspective demonstrated that the magnitude of the effect was too small to be significant [154].

Table 4 Summary of previous animal models of syringomyelia

Author(s)	Experimental Details	Pathophysiology theory/ findings	Shortcomings
Communicating canalicular syringoymelia			
McLaurin et al [156]	Injection of fatty acids, sodium nucleinate and kaolin into the cisterna magna of dogs to produce hydrocephalus and syrinxes.	Constriction of vessels caused by dense arachnoid reaction. Promoted ischemia hypothesis [157].	Cavities were microscopic in size.
Hall et al [158]	Injection of kaolin into the cisterna magna of dogs.	Cavity thought to be secondary to distention and rupture of the central canal.	Central canals were normal in size and intact.
Bekers et al [159]	Cisterna magna injection of kaolin with or without central canal occlusion in the obex in a cat model [225].	The cavities produced were believed to support William's craniospinal dissociation theory.	
Willliams et al [142]	Similar to Bekers, but demonstrated that concurrent pressures in the ventricles, syrinx cavity and cervical spine SAS were different.	Intra-syrinx pressure was higher than ventricular or SAS pressure.	In humans, intracranial pressure is similar to spinal SAS pressure at rest. Pressure in the ventricles and syrinxes were different in animal models compared with those reported in humans.
Yamazaki et al [160]	Mammary cancer cells implanted into the rat supraoccipital bone. Over 2-3 months, the neoplastic cells caused an extradural compression of the cerebellum and tonsillar herniation. In 60% a thoracic syrinx developed, with central canal dilatation.	Ependymal cells were stretched and thinned, astrocytic processes were swollen and extracellular oedema was produced [161].	
Non-communicating canalicular syringoymelia			

Williams and Weller [162]	Repeated injection of saline or CSF via a catheter inserted into the spinal cord in beagle dogs [163]. The syrinxes were found between the dorsal horns.	Sponge-like interstitium and adhesive arachnoiditis at catheter insertion site reported.	Unclear mechanism
Milhorat [164]	Between 1.2 - 1.6 μL of kaolin injected into the dorsal columns and grey matter of the rat cervical spinal cord. Kaolin and leukocytes entered the central canal within 24 hours and drained rostrally. Ependymal cells proliferated, causing obstruction in the central canal at the level of kaolin injection. The central canal caudal to the obstruction became dilated within 6 weeks.	Central canal thought to act as a "sink". Thought to be a suitable model due to histological resemblances to human syrinxes and good neurological status of animals.	No abnormality at the craniocervical junction detected so model does not imitate the human clinical condition completely.
Stoodley et al [149]	Similar model to above. Volumes of 1.5 μL of kaolin injected into the dorsal columns and grey matter of the rat cervical spinal cord [147].	CSF tracer, injected into the cisterna magna, demonstrated flow toward the central canal through perivascular spaces even in the presence of a large syrinx cavity [148]. Support for the perivascular pulsatile flow theory.	
Lee et al [165]	Extradural injection of concentrated kaolin through dorsal laminectomies performed at L1 and L5 in rats. High mortality and neurological morbidity, but 85% developed syrinx rostral to injection.	First group to model syrinx secondary to tethering pathology (albeit experimentally mediated by epidural compression).	Tethering not strictly modeled. Injection site not anatomically similar to most dysraphic lesions. Syrinx development does not correlate with clinical findings.
Extracanalicular syringomyelia			
Allen et al [166, 167]	An early spinal cord contusion model achieved by weight-drop method [168]. Arachnoiditis was not induced.		Inconsistent syrinx cavity induction.
Cho et al [139]	Combination of a weight drop spinal cord injury with a subarachnoid kaolin injection in Japanese rabbits.	Arachnoiditis believed to be important in syrinx formation.	Mechanism of syrinx induction unknown.
Radojicic et al [169]	Thoracic cord injury caused by spinal cord impactor (250 KDyn force) in rodents. No additional arachnoiditis. Ascending central canal enlargement, ependymal cell loss, and glial scarring with evidence of syrinx formation observed.	Central canal dilation accompanied by disruption in the ependymal cells may contribute to chronic spinal cord injury.	
Wong et al [170]	Spinal cord impactor used, with additional subarachnoid kaolin injection in rats. A force of 75 KDyn produced initial cysts in 92% of animals after 3 months without neurological deficits in animals.	Multiloculated interstitial cavities formed separate to the central canal.	

Mizuno et al and Seki et al [171, 172]	Mizuno et al combined epidural clip compression injury with subarachnoid kaolin in rats. Kaolin not found to make a difference. Seki et al, used a modified clip compression injury with subarachnoid injection of kaolin rostral to the site of injury. Kaolin had a significantly greater rate of syrinx formation.	In Mizuno's study, 83% of animals developed a syrinx.	Rats developed severe neurological deficits post-injury.
Josephson et al [173]	Silk suture ligature used to obstruct the spinal SAS of rats. Dorsal vein of the spinal cord was occluded. Syrinx cavities were detected on MRI and histology.	Slow accumulation of gadolinium in the cyst suggested that passive filling mechanism characterises syrinx formation.	All animals developed severe neurological deficits post-surgery. Difficult to differentiate whether the syrinx cavities were produced from ischaemia, spinal cord injury, or hydrodynamic disturbances. High rates of neurological deficits in animals.
Tauber and Langworthy [132]; Fried et al [131]	Ischaemic cystic cavity developed mainly in the posterior columns of the upper thoracic cord following ligation of the anterior spinal artery. Later Fried et al also demonstrated ischaemic cystic cavities in rhesus monkeys after anterior spinal artery ligated above the artery of Adamkiewicz.		
Brodbelt et al [174] Yang et al [179]	Produced an excitotoxic model of post-traumatic syringomyelia by combining intraparenchymal quisqualic acid and subarachnoid kaolin injections. After the initial injections, all animals developed a syrinx within 6 weeks. Cavities were large. Syrinx expansion was contingent on multiple doses of quisqualic acid combined with kaolin. This model has been used in subsequent investigations due to the reliability of syrinx production, absence of severe neurological deficits, and histological similarities to human post-mortem specimens [175]. Others have investigated CSF flow into the syrinx cavity, the effect of altered SAS compliance, the role of the blood-spinal cord barrier and the fate of neural progenitor cells [150, 176].	A rise in the level of excitatory amino acids was found after spinal cord injury, promoting excitotoxic cellular death. This process potentiates syrinx formation [177]. Others have demonstrated that excitatory amino acids are involved in spinal cord injury [178, 179].	Does not completely replicate the compression or contusion injury that characterises human spinal cord injuries.

1.2   Spinal cord anatomy

A detailed treatise on the embryology, general gross and microscopic anatomy of the vertebral column and spinal cord is beyond the scope of this thesis. Instead, the structures that are central to understanding the physiology of CNS fluids will be reviewed.

1.2.1 Microscopic anatomy

1.2.1.1 *Histological overview*

Viewed in axial section, the spinal cord grey matter is located centrally and is surrounded by white matter. Anteriorly, there is a deep ventral median fissure, while posteriorly the posterior median septum marks the midline. The grey matter is butterfly shaped, consisting of bilateral ventral and dorsal horns, and an intermediate zone where the central canal runs longitudinally [180]. The cell bodies of white matter tracts are found in the dorsal horns, while alpha and gamma motor neurons are located in the ventral horns [180, 181].

The grey matter is densely packed with cells. These include neurons, interneurons and neuroglial cells. Neuroglial cells encompass oligodendrocytes, astrocytes, microglia and ependymal cells [182]. Astrocytes provide not only mechanical support, but also facilitate metabolite exchange between neurons and the vascular system, participate in tissue repair, and contribute to the formation of the blood-brain barrier (BBB) [182]. Oligodendrocytes are analogous to the Schwann cells of the peripheral nervous system; they form the myelin sheath within the CNS. Finally, microglial cells are cells of the immune system, falling under the monocyte-macrophage classification system [183-185]. The cells of the grey matter are organized into ten laminae that are topographically preserved across spinal levels (although the relative size varies according to cervical or lumbar enlargements). These were originally described by Rexed in 1952 in cats [186] but have been confirmed in other species including rats and humans. Each lamina serve different functions, the details of which are described elsewhere [186].

The dorsal and ventral rootlets separate the white matter into the dorsal columns, lateral columns and ventral columns. The dorsal rootlets enter the spinal cord

immediately as the dorsolateral tract of Lissauer [187]. Further details about the numerous white matter tracts will not be reviewed here.

1.2.1.2 Central canal

Present in all vertebrates, the central canal is initially continuous with the brain ventricular system [188]. By the second decade of adulthood, however, stenosis or occlusion of the lumen at most spinal levels has been documented in human autopsy series [114, 188]. The central canal remains patent in rats, and has been postulated to facilitate CSF flow in a caudal to cranial direction [185]. The central canal is formed by an uninterrupted layer of ependymal cells and tanycytes.

Derived from the germinal matrix, the ependyma is a monolayer of cuboidal to columnar ciliated epithelium [189, 190]. Ependymal cells participate in the regulation of water movement through specialised aquaporin channels (1.5.2.1). They also contribute to the brain- and spinal cord-CSF barrier. This is achieved by the presence of gap junctions and zonula adherens between ependymal cells [190, 191]. Tanycytes are specialised ependymal cells, found occasionally along the ependymal lining of the central canal. They are characterised by basal processes that radiate outwards into the neuropil, encasing blood vessels [189, 190, 192]. It is thought that these cells mediate neuronal guidance and some neuroendocrine functions. There is also experimental evidence suggesting a role in axonal regeneration [189, 190, 192, 193].

Made of glycoprotein and glycolipids, the basement membranes of the ependymal layer form complex labyrinths that connect with the basement membrane of subependymal capillaries and venules. Leonhardt and Desaga [193] demonstrated differences among species, but these membranes can be distended by absorbing fluid and form lacunae. These basement membrane labyrinths may be considered interstitial spaces near the

ventricles that provide pathways between the ependyma and the subependymal vessels [193].

Reissner's fibre is an amalgamation of glycoproteins secreted by the diencephalic subcommissural organ [194, 195]. It runs from the third ventricle along the central canal. In rats, it is thought to participate in regulation of CSF production, maintenance of central canal patency, ependymal cilia functions, and mediating fluid flow along the central canal [194-196].

1.2.2 Meninges

The spinal meninges are not merely protective coverings—they are central to the development, homeostasis, and the regeneration of the CNS and CSF [197, 198]. Three concentric sleeves envelope the spinal cord: the outer dura mater, the middle arachnoid mater, and the inner pia mater. The spinal dura mater is a thick, highly vascularised, single layer of connective tissue [198, 199]. Beginning at the foramen magnum, it ends as a contraction into the filum of the spinal dura at S1/2, encases the filum terminale and attaching to the periosteum of the first coccygeal segment [200, 201]. At each level, the dura encloses the ventral and dorsal spinal roots, merging into the epineurium around the dorsal root ganglion [201].

On the inner aspect of the dura, the arachnoid mater is attached by thin strands of collagen. The subdural space is therefore just a potential space. It is filled with amorphous substances and mesothelial cells, and therefore has a low resistance [200-202]. The arachnoid mater ensheathes the spinal cord, nerve roots, spinal blood vessels, and the intradural portion of radicular vessels. A fine network of connective, flexible trabeculae bridge the pia and the arachnoid membrane. The SAS *is* a physical space (occupying a third of the spinal canal) where nerves, denticulate ligaments, blood vessels and nerve roots traverse. CSF also flows in this compartment. The denticulate

ligaments project laterally from the sides of the spinal cord to the inner dura, stabilising the cord and dividing the SAS into ventral and dorsal compartments [203]. The spinal SAS is continuous with that of the cranium and enlarges into a terminal sinus to encapsulate the cauda equina [201, 202, 204]. Arachnoid proliferations are formed from the arachnoid mater. Most commonly, they traverse the dura and extend into the extradural space, however they may exist entirely within the nerve root dura or penetrate an extradural vein [205, 206]. They are analogous to the cranial arachnoid granulations and are likely important for CSF resorption (up to a quarter of CSF outflow in animal studies [207]). In rat experiments, obliteration of cranial CSF absorption led to increased flow along the lumbosacral nerve roots [208, 209].

The pia mater is a thin layer of areolar tissue that is affixed to the spinal cord, the ventral median sulcus, the conus medullaris, the filum, and the nerve roots. The pia merges with the arachnoid mater halfway between the lateral aspect of the thecal sac and the dorsal root ganglion to form the perineurium [200, 202]. Where the two layers combine, a SAS lateral recess is formed and is delimited before the nerve exits the intervertebral foramen. This recess allows the nerve roots and nerves to be bathed by CSF [200]. The spinal pia mater is thicker, more compact, and less vascular than its cranial counterpart [200]. Vessels of the SAS are enveloped in a leptomeningeal layer that is continuous with the pia mater. The spinal subpial space is filled with collagen and separates the pia mater from the glia limitans [199]. This is formed by astrocyte end feet and is the boundary between the CNS and the pia mater. The pia mater contributes to the microscopic anatomy of the perivascular space [210]. This will be covered in more detail later (1.5.2).

1.2.3 Vascular supply

In humans the spinal cord vasculature is highly collateralised and complex with wide anatomical variations [211]. Branches from the aorta and the vertebral arteries supply

the spinal cord. The anterior spinal artery (ASA) runs continuously along the ventromedian sulcus and is responsible for supplying most of the ventral two-thirds of the cord parenchyma (Fig. 2). The ASA can be segmental [212] and has a diameter between 1.2 mm (at the artery of Adamkiewicz) and 350 μm (at the conus). The two posterior spinal arteries (PSAs) supply the rest of the spinal cord and can be segmental and narrow [213].

The vasocorona, or rami perforantes, join the anterior and posterior spinal arteries [213]. It is an intricate pial arterial network that encompasses the spinal cord, sending numerous penetrating branches that terminate either in the grey matter or the white matter tracts [213] (Fig. 3). These irregular vessels inconsistently provide collateral blood flow. Up to 210 central arteries (with an internal diameter up to 260 μm) run into the ventromedian sulcus. They then turn laterally to supply the grey matter on either side, as well as the ventrolateral white matter [214]. In the cervical spine there are 7–12 central arteries/ cm, but few are found in the thoracic cord [214].
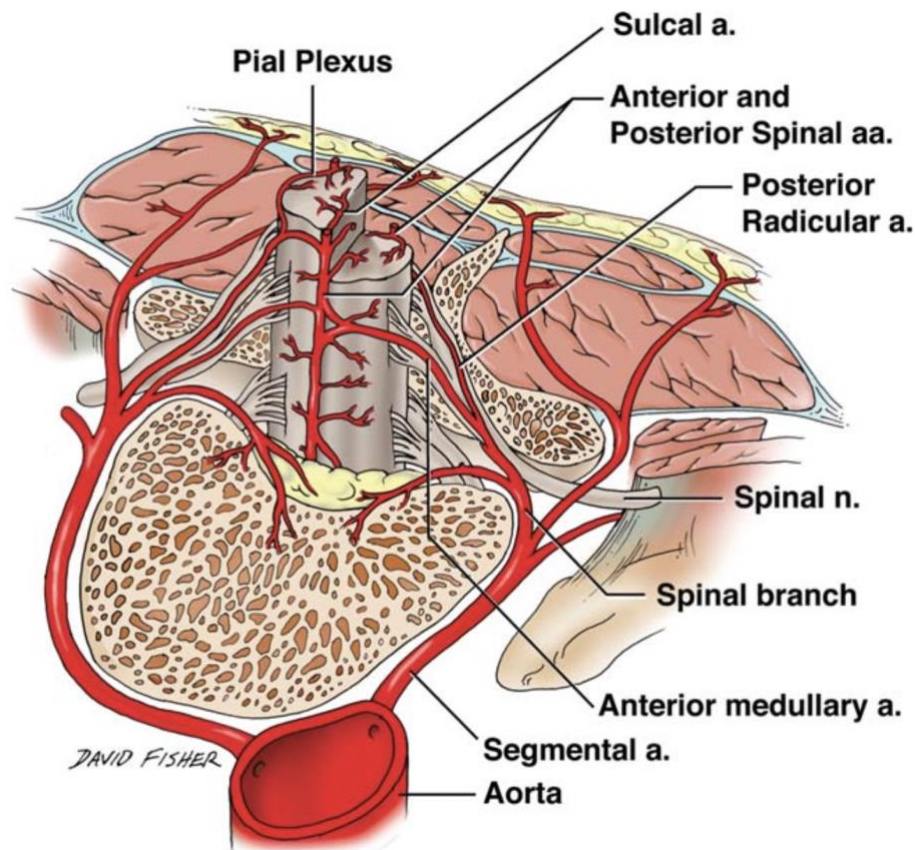
Fig. 2 Branches from the aorta and the vertebral arteries supply the spinal cord. The ASA runs continuously along the ventromedian sulcus and is responsible for supplying most of the anterior 2/3 of the spinal parenchyma. Reproduced from Bosmia et al, 2013 [215]

The ASA and PSA are supplied by the anterior and posterior radicular arteries that follow the spinal nerve roots through the intervertebral foramina [216]. The radicular arteries at C2–C4 are usually supplied by the posterior inferior cerebellar arteries. In the thoracic and lumbar spine, the posterior branches of the intercostal arteries supply the radicular arteries [216]. The ASAs and PSAs between C8 and T9 are supplied by only two radicular arteries. The largest radicular artery is the artery of Adamkiewicz [217]. This usually originates from the left side of the aorta at the level between T9 and T12 and is responsible for blood supply for the inferior two-thirds of the spinal cord [218]. The radicular arteries that reach the spinal cord directly are called anterior and posterior radiculomedullary arteries [213, 218].
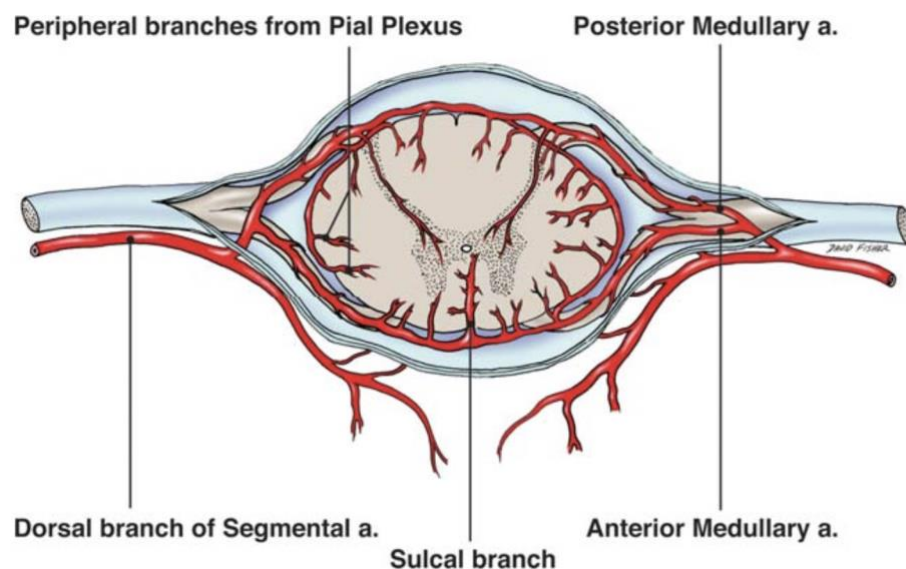
Fig. 3 Note the origins of the circumferential pial arterial vasocorona which joins the anterior and posterior spinal arteries. There are numerous penetrating branches that terminate in the grey or white matter [213]. Reproduced from Bosmia et al, 2013 [215]

The spinal venous network mirrors that of the arterial supply [219]. Ventrally, an anterior spinal vein runs in parallel to the ASA [187]. There is a prominent dorsal median vein spanning the length of the spinal cord. In the thoracic level the diameter of the vein is diminished [219]. Like the vasocorona, a rich, circumscribing venous network connects the ventral and dorsal median veins. In the cervical and thoracic enlargements, the calibre of these veins is increased. In the parenchyma, penetrating radial veins drain blood towards the pial surface [220]. In the cervicothoracic regions, radial veins are particularly important in draining the ventrolateral white matter tracts and adjacent grey matter [214, 221]. Sulcal veins generally drain the ventral horns and grey commissure [214]. Both radial and sulcal veins empty into the superficial, longitudinally running ventral and dorsal veins that ultimately end up in the caval venous system via the extradural venous plexus [220].

In the normal adult, the total spinal cord blood flow/ cm of the cervical, thoracic and lumbosacral segments is thought to be 0.45, 0.04, and 0.11 ml/min/cm, respectively. These values were extrapolated from Rhesus monkey data [222]. Like the brain, the

spinal cord is exquisitely sensitive to ischaemia [211, 223], with particularly vulnerable segments in the cervical and lumbar enlargements.

Similar vascular anatomy has been found in rats and other mammals [224]. The ASA, PSA and a dominant radicular artery corresponding to the Adamkiewicz artery have all been identified in murine models [225]. Interestingly, in the cervical spinal cord of the rat, the median dorsal artery and bilateral dorsal spinal arteries have been documented [225]. Some authors have suggested that in rodents a larger portion of the white matter is supplied by the central branches of the ASA instead of the ventral vasocorona [221].

1.3   Cerebrospinal fluid

The term, "cerebrospinal fluid" was probably coined by the French physiologist, Francois Magendie in the 19th century [226, 227]. A comprehensive review of the history of CSF experimentation has been compiled by Matsumae et al [226].

Most authors generally regard CSF as the clear, colourless fluid produced by the choroid plexus that circulates in the ventricular system and SAS of the brain and spinal cord [228, 229]. There is still ongoing contention, however, regarding the exact function and physiology of CSF. Historically, criticism has been levelled at the extrapolation of data from flawed animal experiments to humans [229, 230]. In the 21st century increasingly sophisticated non-invasive imaging modalities are providing important insights into hydrodynamics of CNS fluids. It would be incomplete to examine CSF in isolation; there is incontrovertible evidence that CSF interacts intimately with the ISF that bathes the cells in the extracellular space (ECS). This section will discuss the current concepts of CSF and ISF that are relevant to syringomyelia.

1.3.1   Function of CSF

The functions of CSF are manifold [198, 231-233]. They include, but are probably not limited to:

1. A sink for clearing metabolites, particularly waste products with high molecular weight. In haemorrhage and injury, proteins and debris can be removed via this pathway.

2. A compensatory mechanism to maintain constant intracranial pressure (ICP) within the rigid skull despite volume changes that occur normally with the cardiac cycle, and abnormally with space occupying lesions. This is at the core of the Monro-Kellie hypothesis [229].

3. A means to reduce the operational "weight" of the brain from 1200 g to about 45 g by providing buoyancy [230]. This can be extended to the idea of CSF providing a "cushion" against trauma.

4. Paracrine roles whereby nutrients, hormones and other macromolecules are dispersed throughout the CNS. There is increasing recognition that CSF may be a "nourishing liquor" [229] and may play an important part in neurogenesis [234]. Hormones released by circumventricular organs into CSF may be homogenised in the third ventricle and are able to mediate slow global brain functions, such as sleep, wakefulness, circadian rhythms, and sexual behaviour [235].

1.3.2 Biochemistry of CSF

The electrolytic constituents of CSF have been determined by selective ion microelectrodes. The principal ions are Na_+, Cl_- and HCO_{3-} with smaller quantities of K_+, Mg_{2+} and Ca_{2+} [232]. Other molecules include proteins such as [236-238]:

- vitamins (for example, folate, AA, thiamine and pyridoxal monophosphates);

- peptides actively transferred into CSF from blood (leptin) or synthesised in the choroid plexus (insulin-like growth factor)

- Proteins that diffuse from plasma through barriers, mainly albumin.

Plasma has almost 300 times the concentration of protein as CSF due to barriers of CNS (addressed in 1.3.3) preventing hydrophilic substances crossing from plasma to CSF. Proteins are generally anionic, so in their relative absence in CSF, Cl⁻ is elevated to maintain electrical neutrality [239]. Thus, although the pH is similar, the overall composition of plasma and CSF are different for the most part.

1.3.3 Anatomical Barriers

Water is able to exchange freely and rapidly between blood, CSF and neural tissue [229]. The water content of the CNS under normal circumstances remains constant [229]. There is, however, a multitude of barriers to movement of large molecules in the CNS. This section will provide context to the rest of this introductory chapter and will examine the effects of various barriers on solutes and macromolecules.

1.3.3.1 Blood-CNS barrier

Within the neural parenchyma, endothelial cells lining the lumen of microvessels (capillaries and venules) are linked by tight junctions that prevent free movement of molecules and ions via a paracellular route. Tight junctions are formed by plasma membrane-bound molecules (including claudin, occludin, and adherens) and cytoplasmic proteins (such as zonula occludens). Molecules up to 0.8 nm are able to pass through these junctions [240]. For larger molecules, there are only two pathways to cross this barrier. The first is to traverse the bilipid membrane layer. The second, which applies to hydrophilic substances, is via specific membrane transporters found in both the luminal and basal aspects of the cell. Molecular charge also determines ability to penetrate this barrier. Directly surrounding the basement membrane of the endothelium, in which pericytes reside, are the end-feet processes of astrocytes. The basement membrane and the glial end-feet regulate passage of large molecules [230]. The basement membrane, pericytes and astrocytic end-feet, rather than contribute physically to the BBB, promote mutual cellular integrity, maintenance of tight junction

integrity and proliferation by unclarified mechanisms that result in the non-fenestrated phenotype [241].

There is emerging evidence that ultrastructural differences exist between the BBB and the blood-spinal cord barrier. These include the presence of glycogen deposits in spinal microvessels, increased permeability to tracers and cytokines in the spine and reduced expression of transporter molecules, tight junction proteins and endothelial adherence junction proteins. These data were obtained from isolated animal studies and cultured murine cells [242]. Whether these differences have pathophysiological significance in spinal cord disorders is unknown.

1.3.3.2 Blood-CSF barrier

The arachnoid layer is a thin layer of cells held together by tight junctions, most abundant in the external layer. It is impermeable to water and therefore, CSF. The choroid plexus epithelium is a layer of cuboidal cells also linked by tight junctions overlying networks of capillaries that are fenestrated. Tight junctions of the apical end (facing the ventricles) of the choroid plexus epithelium, and of the arachnoid layer form the blood-CSF barrier. This limits paracellular passage of molecules between CSF and the choroid vasculature and from the SAS vessels [230, 243]. Choroid plexus epithelium, however, is capable of transporting large quantities of iso-osmotic fluid due to numerous transporters found in the microvilli of the basolateral folds [230].

1.3.3.3 CNS–CSF barrier

Ependymal cells lining the ventricles and central canal do not possess tight junctions. Instead, the intercellular connections are by gap junctions that permit the free exchange of small solutes between CSF and ISF [230]. In fact, even large molecules such as albumin are able to penetrate this porous barrier, although this process is very slow [229, 244]. The ependyma overlying parts of the third and fourth ventricles

(infundibular recess, median eminence, area postrema and choroid plexus) are exceptions — the cell contacts of these specialised ependymal cells, tanycytes, are by tight junctions [245-247]. This is in distinct contrast to the fenestrated vascular endothelial cells characterising this group of circumventricular organs. The glia limitans are similarly permeable to macromolecules and water due to the absence of tight junctions.

1.3.4 CSF formation and absorption

1.3.4.1 Choroidal Formation

Most investigators assume CSF is produced mainly by the choroid plexus of the ventricles. A widely quoted figure is that approximately 400 mL/day of CSF is produced in humans, of which 90% originates from the choroid plexus [228, 241, 248]. Walter Dandy, demonstrated in dogs with bilaterally occluded foramina of Monro and unilateral choroid plexectomy, that the side with the preserved choroid plexus had unilateral ventricular entrapment. Unfortunately, attempts to reproduce these results by others have failed [249]. Welch compared the haematocrit of blood entering and exiting the rabbit choroid plexus and calculated the rate of CSF production [250], which was found to be similar to the rate of CSF absorption. It is also recognised that CSF overproduction is associated with choroid plexus neoplasia. Therefore, the choroid plexus is likely an important source of CSF.

There is increasing knowledge about the precise mechanism of CSF secretion by choroid plexus. Multiple transporters that transfer Na_+, Cl_-, and HCO_{3-} from blood into CSF across the choroid plexus are found in the epithelium and are central to CSF formation. These ions are transported from plasma to epithelial cells (a transcellular process across the basolateral and apical membranes) and thence into the ventricles [229]. Water is then osmotically translocated in response to inorganic ion movement. The exact mechanism is unclear, but aquaporin-1 may play a small role. Kao et al demonstrated

that in sla4a5 knock-out mice (sla4a5 transports $NaHCO_3$), the ventricular volume and CSF pressure were 25% of normal and there was reduced CSF HCO_3- concentration [251].

1.3.4.2   Extrachoroidal formation of CSF

There is mounting evidence that CSF is also produced in sites other than the choroid plexus. Milhorat demonstrated in animals that had undergone choroid plexectomy that CSF production continued [252, 253]. Although in humans there is evidence, albeit conflicting, that choroid plexectomy can be an effective treatment for hydrocephalus [254-256], it can be concluded that at least some CSF must be extrachoroidal in origin. Perfusion experiments on isolated rabbit ventricular ependyma suggest that about 30% of CSF is produced by the ependymal surface [257]. An even higher value of ependymal fluid secretion rate was derived from a study of the central canal in cats [258]. Another study in dogs involving infusion of inulin into the lumbar spine concluded that the source of CSF was the spinal SAS [259]. Criticisms of these experiments relate to the use of heavily instrumented anaesthetised animals, methodological shortcomings and flawed interpretation of results. The Klarica/Oreskovic group have long asserted that CSF production is widespread in the CNS capillaries, with the choroid plexus having a water filtration role [260]. Their interpretations of ventricular perfusion experiments in cats have been heavily criticised and this model remains eschewed by most. Finally, others have posited the brain itself as being a source of extrachoroidal CSF [261].

1.3.4.3   Absorption at arachnoid villi

Anatomical differences between animals and humans fuel controversies around CSF absorption. It has been established that arachnoid villi are well developed in humans but not in rats.

The classic model of CSF removal in humans is via the arachnoid granulations located along the dura of the superior sagittal sinus. This was based on Weed's 1914 landmark study where non-toxic dyes were injected under low pressure into the SAS in cadavers [262]. Later, it was established that a pressure gradient of at least 3 mmHg is required for drainage of CSF into the venous sinuses. Intracellular vacuoles and intercellular clefts may facilitate the movement of CSF by endothelial pinocytosis and vacuolisation [208]. However, there are contending theories that promote instead passive transport via extracellular routes involving intercellular cisterns. In these theories, arachnoid villi act as one-way valves and are covered by endothelium that prevent free passage of fluid [226, 249]. These endothelial cells, however, are not universally present in humans. Arachnoid cap cells that abut the lumen of the superior sagittal sinus are thought to be essential for active CSF transport [263]. Finally, recent imaging techniques employing Time-Spatial Inversion Pulse (Time-SLIP) MRI have revealed surprisingly no net flow of tagged CSF towards the superior sagittal sinus, suggesting that the arachnoid villi may not be the major site of CSF absorption [235].

1.3.4.4   Absorption at other sites

Spinal clearance of CSF has been clearly documented in animals including sheep and rats [264]. Spinal arachnoid granulations are most often seen around the dorsal nerve root and are structurally similar to their cranial counterparts [265]. The most common subtype is likely one that protrudes through the dura dorsally to penetrate either the epidural space or vein. Previously it was believed that spinal arachnoid granulations concentrated around thoracic spinal nerves, but a recent report found greater abundance in the human cadaver lumbar spine [266]. It is also unclear whether these spinal arachnoid granulations involve drainage into veins or lymphatics [265]. Analysis of monkeys suggested a greater importance of lymphatic absorption than venous outflow, but in human cadaveric specimens spinal arachnoid granulations were closely

associated with epidural veins, with a close correlation between the size of the vein and number of granulations [267]. Several animal experiments have attempted to establish the importance of spinal arachnoid granulation outflow in the context of dysfunctional cranial absorptive mechanisms by inducing craniocervical arachnoiditis with kaolin injection. Delayed normalisation of ICP despite high outflow resistance indicated recruitment of spinal outflow pathways [268]. This was further corroborated by the findings of markers exiting the spinal SAS via the thoracolumbar rootlets. Another similar study demonstrated the passage of ferritin tracer through the central canal, via the ensuing syrinx that ruptured into the dorsal column, and into extradural lymphatic vessels [269]. As humans are upright (at least for a significant part of the day) and there is greater hydrostatic pressure in the lumbar cisterns, spinal CSF outflow was postulated to be even greater.

The lymphatic outflow of CSF is predominantly perineural via the olfactory nerve space that crosses the cribiform plate. Other cranial nerves (such as the optic, trigeminal and vestibulocochlear in sheep [270]) have been implicated but there is little evidence to support their significance in humans. Johnston et al [271] injected coloured microfil into the CSF of pigs, rabbits, rats, mice, monkeys and fresh human cadavers. The microfil filled the SAS and entered the network of lymphatic vessels in the nasal submucosa of all species. The precise microscopic anatomy of the interface between the perineural space and lymphatic vessels is unknown, although there is suggestion that in humans the olfactory nerve sheath end is a blind sac and lymphatic CSF absorption is mediated by pinocytosis. Recently, dural lymphatic vessels have been characterised around the cerebral venous sinuses of mice and humans [272, 273]. In mice, they also extensively cover and penetrate the skull base around cranial nerves. These "meningeal lymphatics" connect with the cervical lymphatics and in mice may directly drain fluid from the brain

parenchyma based on injected tracer studies. The exact pathways have not been described. So far, there is no evidence parenchymal lymphatics exist in the CNS in humans. Intriguingly, there is at least one case report of a parotid gland glioblastoma metastasis that was first diagnosed by lymph node biopsy [274]. In this patient, there were no prior cranial operations, which excluded the possibility of dissemination by scalp lymphatics. While it does not prove the concept of brain lymphatics, this long held dogma should be re-examined. Finally, the lymphatic system has been demonstrated to develop before the arachnoid villi across a variety of species and could be the dominant CSF outflow pathway in the neonatal period [275-277]. There is also convincing evidence that the arachnoid villi system loses efficiency with age, leading to possible neurodegenerative sequaelae [208].

It has not been possible to determine precisely in primates the relative proportion of total CSF transport that drains to each outflow system. In animal experiments involving injected radioactive tracers, 15% to 50% of CSF has been found to drain into the cervical lymphatics [270, 278-281]. In humans there is probably both a high- and low-pressure outflow system and, based on sheep studies, the olfactory perineural lymphatic system may be the lower pressure system [208]. Edsbagge et al [282] calculated CSF formation and drainage using lumbar radionuclide cisternograpy in young human adults. The rate of tracer activity decline was about 20% in the first hour and enhanced by physical activity. Based on nuclide activity reduction, the spinal absorption was found to be 0.11 to 0.23 ml/min [43]. These values were somewhat higher than previously reported.

Current evidence, therefore, supports the importance of both the cranial arachnoid villi and lymphatic systems in the drainage of CSF from the SAS. The spinal arachnoid villi play a lesser but nevertheless vital compensatory function particularly when cranial arachnoid villi and lymphatics fail [265].

1.3.5 Fluid secretion and absorption in the CNS

A mere tenth of 1% of total cerebral blood flow contributes to fluid secretion into the brain [283]. The CSF secreting choroid plexus (see 1.3.4) accounts for the majority of this secretion. Up to 99% of cerebral blood flow is separated from the brain by the BBB. There is likely a net fluid transport across the BBB (contributing to the formation of ISF), but its rate is still unknown (see 1.4.1). Given the relatively high permeability to water, fluid transfer across the BBB may be dependent on transport of solutes, particularly Na_+ and Cl_- [283]. Water would then follow osmotically. Small ions such as Na_+ and Cl_- cannot diffuse across the BBB and blood-CSF barrier. However, much is still unknown about the precise events and arrangement of ion transporters on the endothelial cell and the rate of net Na_+ and Cl_- transport across the barrier [283]. There is a relative balance between the efflux and influx of Na_+ and Cl_- at the BBB (suggested by the stability of these ionic concentrations). At the blood-CSF barrier, however, more Na_+ and Cl_- are transferred into the CSF from the blood than in opposite direction. Therefore, CSF accounts for more of the total fluid influx into the CNS than ISF.

Despite the high permeability of both barriers to water [283], neither the BBB nor the blood-CSF barrier are the sites of major net fluid drainage for the CNS. Instead, CSF and ISF outflow is likely mediated by pressure driven mechanisms involving the arachnoid villi, dural lymphatics, skull base and spinal cord perineural routes and perivascular pathways. Imbued with a bird's eye view of the current understanding of net fluid inflow and outflow from the CNS, the intricacies of these systems can now be further examined.

1.3.6 Circulation of CSF

Neurosurgeon Harvey Cushing in 1926 proposed a "third circulation" of CSF that is still widely held by most authorities today. This classical view is one where CSF is secreted by the choroid plexus into the ventricular system and escapes into the SAS over the cerebral convexity and spine down to the lumbar cisterns. The fluid is reabsorbed by the

arachnoid granulations and thus "circulates" by pressure dependent bulk flow. Aspects

of this model have stood the test of time, but there are likely oversimplifications. Recent

insights into CSF dynamics indicate that rather than unidirectional displacement, there

are bidirectional ebbs and flows that create complex mixing patterns in the ventricles

[229, 284, 285]. Overall, there is a net flow of CSF from the ventricles to the basal

cisterns at a rate of about 0.4 mL/min in humans, with a higher rate at night (up to 1.0

mL/min) [229, 286]. In the following sections, the flow of CSF in the ventricular-SAS

axis, and the factors that influence this, will be reviewed.

1.3.6.1 *Subarachnoid space flow*

Modern concepts of fluid flow in the spinal canal were derived mainly from radiological

investigations, where *in vivo* flow patterns and velocity measurements were acquired

with cine phase-contrast (PC-MRI) and other dynamic MRI techniques.

The pulsatile nature of CSF, initially thought to be wholly imparted by the cardiac cycle,

has been well characterised since the last decade of the 20th century [287]. In the

cranium, there is marked oscillatory movement of CSF without net flux. Additionally,

there is a much smaller volumetric bulk component derived from secretion of CSF from

the choroid plexus [230]. Time-SLIP MRI provides evidence of bi-directional exchange of

CSF between the third and lateral ventricles via the foraminal of Monro. This process is

attenuated or absent in hydrocephalus, contrary to what is observed in CT

cisternography and radioisotope studies. Time-SLIP has also revealed chaotic CSF

turbulence within the third and fourth ventricles [235]. This finding has supported the

emerging theory (see 1.3.1) that CSF facilitates a paracrine hormonal function. There is

marked fluid pulsatility in the cerebral aqueduct, with craniocaudal movement during

cardiac systole and reverse displacement during diastole [288]. Peak flow rates in each

direction through the aqueduct are normally up to 10 times larger than the average flow

over the entire period [230]. Recently, there has been evidence from Time-SLIP MRI studies that respiration has several fold more influence on pulsatile flow than cardiac factors [235]. This will be addressed in later sections (see 1.5.5.2). There is at least one report that is in apparent support of the Klarica/Oreskovic model of CSF dynamics (see 1.3.4.2). Analysis of data from Time-SLIP MRI by a CSF tracer program suggested there may be no displacement of CSF despite its pulsatile nature [235].

There is emerging data about the flow of CSF in the spinal SAS. During a normal cardiac cycle, up to 2 mL of CSF is displaced from the intracranial compartment into the cervical SAS in systole. In diastole, there is reverse flow into the cranial SAS [289]. Regions of elevated CSF flow rates include the prepontine area (in a craniocaudal direction) and the cervical ventral SAS [290] as demonstrated by 4D MRI (time-resolved PC-MRI with velocity encoding along 3D flow directions and anatomic coverage). Caudal displacement of the brain and spinal cord by up to 0.5 mm during systole has been described in normal adult individuals from analysis of PC-MRI studies [291].

After a series of experiments involving exogenous CSF tracers, Di Chiro in 1964 proposed that when CSF moves craniocaudally it does so dorsal to the spinal cord. Conversely, caudocranial flow is ventral to the spinal cord. There is new evidence from Time-SLIP MRI that the CSF pulsatile movement in the SAS is contingent on posture and thus, resistance to flow. When supine, CSF preferentially flows ventral to the cord throughout the spine, and when prone, the reverse is true [235].

When CSF flows into the spinal SAS, there is expansion of the fluid-filled cisterns with consequent accommodation by the dura, which in turn results in compression of the venous system and epidural fat, especially in the lumbar spine [289]. The concept of the spinal thecal sac as a CSF reservoir was first proposed by Martin et al. After analysing the dural sac diameter and cord dimensions of spinal myelograms, they concluded that

the capacity of the dural sac can change according to prevailing pressure gradients across its walls in response to changes in cerebral blood flow [292]. PC-MRI has characterised a gradual reduction of stroke volume as CSF moves craniocaudally in the lumbar spine. There is also an accompanying reduction in the volume of venous blood displacement and incremental increase in the phase lag of the maximum velocity [289, 293]. In a computational model aimed at predicting the CSF dynamics in the entire CNS, Tangen et al found that the caudal flow phase spanned 20–30% of the cardiac cycle [294]. The cisterna magna had a stroke volume of 0.76 mL with reduction in amplitude craniocaudally from cisterna magnum to sacrum. The amplitude of both pressure and volumetric flow rate in the SAS gradually decreased in this direction. Others have reported peak CSF velocities increasing from C1 to C4 (from 5 to 10 cm/s) secondary to the tapering of the spinal canal [295]. The craniocaudal pressure wave is sharp and short in systole, followed by a reversal in the slower diastolic phase. There were substantial phase lags between pressure and velocity waves, increasing craniocaudally along the spinal column. In adults, velocity and pressure fluctuations are normally approximately 90_o out of phase [296], but in obstruction the phase difference narrows [297]. Modeling studies suggest that as flow oscillates between cranial and caudad directions, flow direction reverses at slightly different times such that there is simultaneous or synchronous transient bidirectional CSF flow [296]. This is not reflected in *in vivo* imaging due to spatial and temporal limitations of MRI. Future improvements in measuring velocity waves and their timing are likely to increase the sophistication with which spinal dura deformations can be localised and spatially quantified.

In the spinal SAS, microflow patterns are encountered. These are secondary to microstructures such as ligaments, nerve roots, trabeculae, meningeal layers, as well as the white matter and grey matter [289, 294, 298-300]. Pulsatile CSF flow is disrupted by

nerve roots, breaking the laminar fluid layers and generating geometry-induced flow profiles. Microcirculatory eddies may form adjacent to nerve roots. Trabeculations increase pressure drops (by up to 2.5-fold according to Tangen et al [294]) and local vorticity. These microcirculatory patterns contribute to flow resistance which result in complex mixing patterns that could be responsible for rapid dispersion of macromolecular moieties when administered to the spinal SAS. Patterns such as eddy currents and vortices are a result of "flow separation" which is caused by inertial properties of fluid in some geometries according to modeling studies [301].

Furthermore, PC-MRI and flow simulations demonstrate that within a spinal axial cross section there are heterogeneous flow velocities and characteristics. Flow jets are found anterolateral to the spinal cord with lower velocities elsewhere. In parts of the cord with a persisting central canal, transient pressure waves from pressure fluxes in the SAS may result in centrifugal and centripetal pressure gradients according to mathematical models [302]. This theoretically generates radially directed fluid flow in the cord. The effects of stenosis on lumbosacral CSF dynamics were recently studied by Kim et al. Using PC-MRI they compared L2 and S1 CSF velocities in healthy individuals and in those with lumbar canal stenosis. They found that in both populations flow was markedly attenuated in the sacral cisterns compared to that of the lumbar cisterns, but in patients with stenosis increased CSF flow was not observed in response to walking. The severity of stenosis did not correlate with the degree of attenuation [303].

There are differences in paediatric CSF flow dynamics. In children, the cervical spinal canal tapers more steeply. As there is also greater systolic expansion of arterial beds, the CSF velocities are greater than in adults. Circadian rhythm is a modulating factor. In paediatric hydrocephalus patients, ICP measurements have been recorded to be up to double that of adult controls, and given that CSF production in normal adults has been

reported to be more than three times higher in sleep compared with awake states, there may be increased CSF production in paediatric populations [286, 304].

1.3.6.2 Central canal fluid flow

Fluid flow in the central canal has been studied in a variety of animals since the 1960s. CSF tracers such as Evans blue, ^{131}I-albumin, colloidal graphite and India Ink have been injected either into the lateral ventricles or the cisterna magna. Staining of the central canal was observed in most early experiments. Cifuentes and colleagues infused horseradish peroxidase (HRP) into the lateral ventricles of rats and documented rapid tracer spread (13 minutes after injection) not only throughout the central canal, but also in the basement membrane of subependymal capillaries and within endothelial pinocytotic vesicles. Based on tracer labelling of the central branches of the ASA, they proposed a fluid pathway linking the spinal SAS and the central canal via the ventral median sulcus. The perivascular basement membrane, the ECS and the labyrinthine extensions were thought to mediate this fluid influx [305]. The same group concluded that the Reissner's fibre potentiated a craniocaudal direction of CSF flow along the central canal [306]. Milhorat injected a smaller volume of tracer, Evan's blue, into the cisterna magna and found no appreciable central canal accumulation. However, tracer was detected after interstitial delivery of tracer. They proposed that spinal arterial and venous pulsations generated a cephalad fluid flow in the central canal that acted as a sink for metabolites [307].

Stoodley et al [148] performed similar injections of HRP into the SAS. They observed rapid distribution of tracer in the perivascular spaces around the central canal. They argued that the possibility of flow of tracer from the fourth ventricle down the central canal was unlikely. This further supported the concept of fluid flow from the SAS across the interstitium and into the central canal which functions as a sink for debris. Later

work by this group [146] demonstrated flow of tracer into the central canal in sheep when the SAS pressure was lowered. In subsequent models of syringomyelia in rats and sheep (induced by intraparenchymal and SAS injections of excitotoxic materials as well as by direct trauma), central canal deposition of HRP was reported. The authors have consistently proposed a model of arterial pulsation-dependent perivascular fluid flow [146, 147, 149, 150, 153, 308]. A very recent study involving cisternal infusion of cadaverine in mice reported central canal labelling by tracer in only a few specimens. The authors speculated that tracer was preferentially taken up by cells in the parenchyma before reaching the central canal [146-149, 153, 170, 264, 309]. Thus, there is strong support from a series of experiments for rapid fluid inflow into the central canal at least from the parenchyma. There are likely pathways from the spinal SAS via the perivascular space. Whether there is a predominance of cephalad or caudad flow is unclear. Tracer molecular size, volume, route of administration and species likely account for conflicting results.

In one of the most comprehensive autopsy studies of the human central canal, Milhorat et al [310] found increasing incidence and length of stenosis (particularly between T2 and T8) of the central canal with age. Interestingly, there was evidence that central canal obliteration may be a pathologically acquired process as opposed to involution. Others have questioned this [311, 312], but Milhorat et al's study remains the largest to date. Thus, it appears unlikely that the central canal is a major pathway of fluid out flow in humans.

1.3.7   Studying CSF and fluids of the CNS
1.3.7.1   Animal studies
Animal experimentation made up the bulk of research into CSF and CNS fluids last century [249]. In extrapolating data to humans, other than the fact that most non-primate species are not upright, there are several technical caveats. Different

anaesthetics, each with varying dose, timing and route of administration, have complex effects on cerebral blood flow, CSF production, cerebral function and widespread cardiorespiratory parameters. In the anaesthetised animal, certain drugs have potent effects on the choroid plexus. Acetazolamide, for example, can uncouple choroid plexus blood flow and CSF production in the chloralose–anaesthetised rabbit. A lower body temperature was found to reduce the choroid plexus epithelial metabolic rate, thus decreasing CSF production [313]. As anaesthesia generally depresses respiration, depth of anaesthesia can affect CSF hydrodynamics (see 1.5.5.2). Instrumentation in the CNS and parenchymal injections can result in a florid inflammatory response which may alter normal physiology and the creation of hydrostatic pressure gradient abnormalities [249]. There are variations in spinal cord anatomy across species. The ovine conus medullaris, for examine, ends at S2, and the rodent filum terminale is surrounded by grey matter [314, 315]. Reissner's fibre, which may have a role in binding macromolecules such as serotonin and monoamines from CSF, is notably absent in humans [316]. Furthermore, CSF outflow anatomy is different across animals (see 1.3.4.3). However, the choroid plexus of rodents and humans is remarkably similar in function, histology, CSF production rates and relative mass [229]. Cell cultures can sometimes be misleading. Although brain capillaries *in vivo* do not express SVCT-2 or Aquaporin-1, after several passages endothelial cells dedifferentiate to express these molecules [237]. Past methods have not universally reported the state of the CNS at the end of the experiment as this can affect the choroid plexus and BBB functions. Finally, if the myodural mechanism (see 1.5.5.3) were to exist in small animals, then a laminectomy or exposure of the atlantooccipital membrane for cisterna magna injections could in theory disrupt the myodural bridges and the CSF pump [317].

Recent investigations have attempted to elucidate the changes that occur in perfusion-fixation of tissue for *ex vivo* analysis. Documented in real-time with two-photon intravital microscopy, the Nedergaard group has raised concerns that intravascular perfusion of rodent brain with 4% paraformaldehyde not only attenuates the perivascular space by up to ten-fold, but the process directly causes transmural migration of tracer into the basal lamina of the leptomeninges [318]. This would account for the presence of tracer in the "vascular basement membrane" that the Carare/Weller group (see 1.5.3) has described over the course of many investigations [319]. Unfortunately, this study by Nedergaard and colleagues did not support their observations with detailed confocal microscopic analysis of axial sections. Proulx et al [320] observed with near infrared (NIFR) fluorescence microscopy that shortly after death, there was greater accumulation of tracer around penetrating arterioles in the mouse brain. Again, it was not clear whether histological confirmation was performed, but the authors warned that there is likely an overestimation of tracer influx within the parenchyma in *ex vivo* studies. Future investigations into CSF and ISF of the CNS need to take heed of these findings, and results from *ex vivo* studies should be corroborated by evidence from the living organism.

Although difficult to attain, the ideal experiment would involve normal, uninstrumented and conscious subjects, as anatomically close to humans as possible. Close histological follow up at the conclusion of the study would be mandatory.

1.3.7.2 Tracers

CSF and ISF have long been studied by injection of water soluble substances under the assumption that they follow the fluid being investigated. Tracers have also been employed to investigate transport processes across the choroid plexus and the BBB.

Bulk flow, diffusion and rate of elimination determine the distribution of tracers [321, 322].

Besides being easily quantifiable, for a marker to measure effectively the flow of CNS fluids it must move only *because* there is net flow and must move at the same rate as the fluid. For example, if the tracer is too small (for example, Evan's blue dye which has a molecular weight of only 789 Da) it will not follow the flow of CSF, instead rapidly diffusing non-specifically [230]. In most animal studies, another important factor to consider is the ease of fixing the tracer to tissue. Rapid fixation, as a principle, is ideal to prevent artifactual distortion of CSF flow by post-perfusion diffusion. Charge and molecular size also affect penetration of the tracer across barriers. Blue dextran 2000 has a molecular weight of 1000 kDa and a low diffusion coefficient (approximately 1×10^{-7} cm^2 sec^{-1}) which renders it almost immobile by diffusion alone, and too large to pass through gap junctions. India ink (particle diameter of 1.5 μm) and HRP (molecular size 43 kDa), due to their sizes, have been useful for delineating routes of bulk flow, but not for quantifying rates of flow [170, 323, 324].

On the one hand, some tracers such as HRP and cadaverine are not inert and are phagocytosed or endocytosed by cells of the CNS such as neurones and pial cells [243, 325]. On the other hand toxic tracers should be avoided. These include lanthanum (as a colloid), Prussian blue and trypan blue. Ferritin [240, 269], ^{99}Tc-DTPA [326] and ^{131}I-albmin [278] have been used previously in small animals and humans.

Super-heavy water (tritium oxide, ^3H_2O) is unsuitable for determining rates of bulk flow as it diffuses out of the fluid being measured down its concentration gradient, and water diffuses bidirectionally across a barrier [230]. In other words, there could be large tracer fluxes with zero net flow due to an equal but opposite flux of water and solutes. Measurement of heavy water fluxes into or out of tissues can be thousands of times

greater than the net rate of filtration of water [230]. In the CNS, it is important to bear in mind the distinction between tracer flux and net flux of water.

Use of fluorescent tracers in the brain has become popular. Iliff et al, used Alexa-Fluor®-594 hydrazide, Fluorescein-d2000, Texas Red-dextran 3, and Alexa-Fluor®-647 ovalbumin to investigate fluid transport in the brain of mice [327]. Ovalbumin has certain advantages that make it suitable for characterising fluid movement in the CNS. It has a molecular size similar to HRP (45 kDa), is non-toxic and can be conjugated to a fluorescent particle, allowing visualisation and quantification of fluorescence intensity. Larger dextrans and albumin are appropriate for studying perivascular fluid dynamics as they efflux almost exclusively via these routes [328].

Recently, in two studies [318, 329] large tracers—1 μm fluorescent polystyrene microspheres—were injected into the SAS to investigate CSF flow. Using particle tracking velocimetry and high temporal and spatial resolution imaging (such as multiphoton intravital microscopy), flow measurements were quantified and computed. This technique cannot be used with traditional fluorescent tracers due to the lack of contrast in the flow.

Tracers attempting to access the CNS interstitium from the perivascular space (see 1.5.3) may be obstructed due to the size of the gaps between neighbouring astrocyte endfeet. This effect is termed "sieving", and some have attributed the distribution of differently sized dextran tracers to this phenomenon [327]. Although such gaps have been reported to be around 20 nm in conventionally prepared, aldehyde-fixed tissue, new transmission electron microscopy techniques using cryofixation have revealed a less extensive coverage of the endothelium by endfeet. The exact size of the gap is difficult to confidently estimate, but it has raised the possibility that astrocytic sieving may not exist [330]. Instead, the basement membrane might be the more efficacious

filter. Recent experiments have shown that small single-domain antibodies (17 kDa; 4.5 nm diameter) can better deposit in perivascular basement membranes than large IgG antibodies (150 kDa; 10 nm) [331].

1.3.7.3   MRI techniques

In recent decades, many insights into CNS fluids have come from humans lying supine and motionless in MRI scanners. New dynamic MRI techniques, relevant to subsequent discussions of CNS fluids, will be briefly discussed here.

In PC-MRI, blood flow velocity can be determined. The cine phase contrast technique allows derivation of quantitative CSF flow data by synchronising the acquisition of the images with the cardiac cycle. CSF flow is temporally represented as an averaged back and forth movement in a region of interest (ROI). A single acquisition is derived from a cardiac cycle, but lines of data from multiple cardiac cycles are necessary to construct one image. This shortcoming prevents phase contrast cine from being employed to investigate rapid temporal changes in CSF flow, such as with respiration [332]. There needs to be favourable conditions for detection of CSF due to slower movements. Hladky and Barrand discussed the difficulties associated with measuring slow flow, as signal subtraction of a stationary point is required [230]. The CNS moves in synchrony with the cardiac cycle so this motionless point may not exist. Past studies of CSF flow may not all be calibrated in "phantom models", artificially controlled environments that detect time-dependent arterial blood flow with accuracy. There is also concern that CSF velocity data have been derived under the premise that the anatomical area examined lies within enough voxels to calculate the average. The cross section of structures such as the cerebral aqueduct has been assumed to be constant. Finally, technical characteristics of the MRI scanner, such as the gradient strength, can affect the flow measurement [230].

The Time-SLIP single shot fast spin echo technique has a higher signal-to-noise ratio than the cine PC-MRI technique. This permits fast single-shot acquisitions to improve temporal resolution without the multi-averaging required in the PC-MRI technique. Furthermore, compared with the Echo Planar Imaging (EPI) method, much higher spatial resolution can be achieved. A superior temporal resolution (about 720 ms per image) employing single shot fast spin echo, as opposed to the cine PC-MRI technique (temporal resolution of around 4 seconds per image) allows visualisation of CSF flow [332]. Although Time-SLIP MRI techniques are thought to better discriminate between respiratory and cardiac effects on CSF, some cardiac pulsation effect is incorporated during deep inspiration and expiration. The six second acquisition window (which reflects the temporal resolution) captures deep inhalation or exhalation, but not breathing at rest which only requires two to three seconds. This difference reflects the short delay between respiration and CSF movement. Therefore, this method is limited to the deep respirations [332].

EPI enables acquisition of data with high temporal resolution but limited spatial resolution [332]. Visualisation of CSF flow is therefore reduced. In the aqueduct and spinal canal cardiac generated pulsatile flow varies during the different phases of respiration as it is not possible to separate the effect of these two forces driving CSF flow [332]. Moreover, EPI uses intensity variations of MR images which are qualitative. Neither CSF flow direction nor velocity or CSF can be measured [333].

In Pencil Beam Imaging (PBI), the MR phase signal is not entirely determined by flow within the spinal cord. The nominal boundaries of the pencil beam may encompass structures outside of the cord, allowing contributions from other flow sources such as the epidural veins. Selection of the shape and size of the pencil beam is therefore required [334].

Finally, techniques such as diffusion weighted imaging may be employed to study parenchymal water movement in the CNS [335]. Thus, although increasingly sophisticated MRI modalities are being applied to CNS fluid research, all have shortcomings in applicability and spatio-temporal resolutions.

1.3.7.4 Computational fluid dynamics

Computational fluid dynamics (CFD) employ mathematical modeling for the study of intracranial fluid flow in health and pathology. Although they are becoming more widely established [289], there have been far fewer studies on spinal fluid dynamics. Computational domains are reconstructed with image segmentation software and have become invaluable in resolving flow and pressure fields in space and time, beyond the capabilities of imaging modalities [289].

Loth et al studied CSF flow in short segments of the spine with idealised geometries and the impact of annular geometric variation [336]. They adjusted the boundary conditions for each segment and yielded CSF motion data in 1 cm segments. Subsequent groups have calculated predicted peak diastolic and systolic velocities, stroke volume and flow rate of CSF at various locations of the cervical spine. These values are summarised in **Fig. 4**. Model fidelity can be improved by using medical image reconstruction to represent subject-specific anatomical spaces [289].
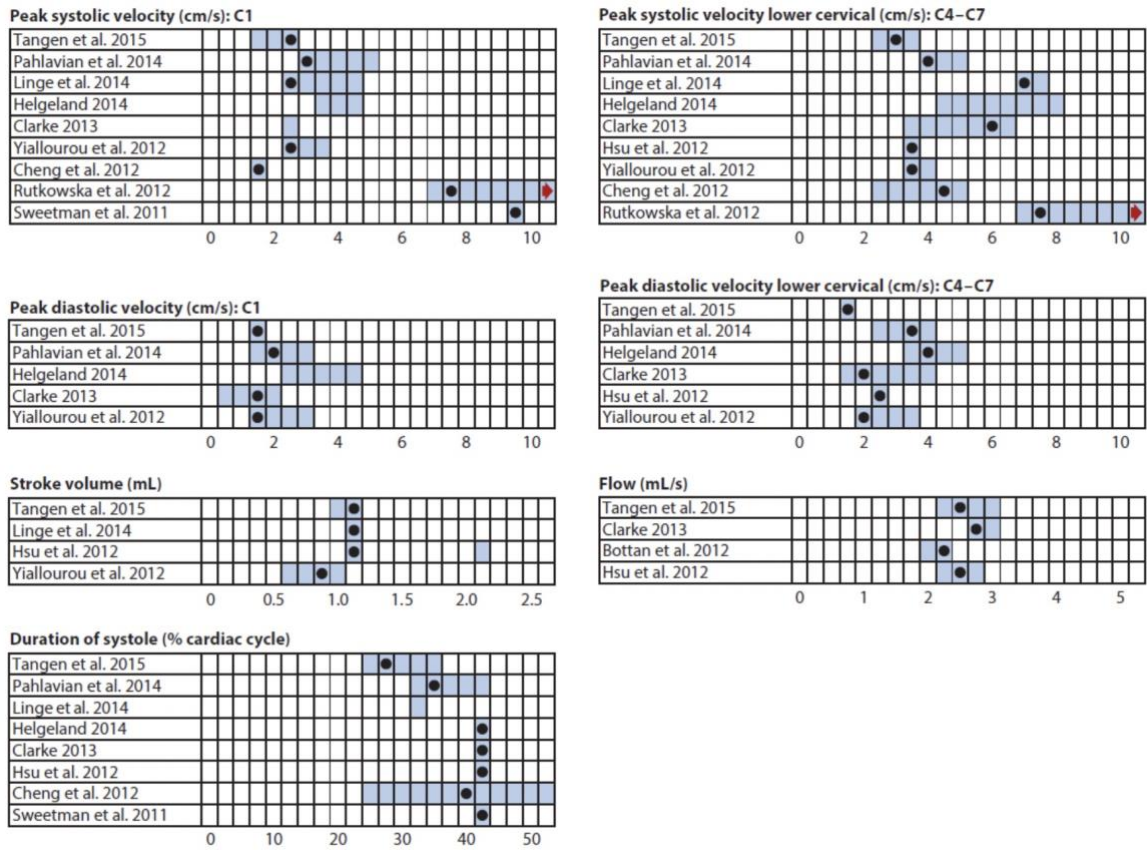
Fig. 4 Linninger and colleagues compiled from the literature the values of human spinal CSF flow parameters as predicted by CFD models. Boxes shaded blue indicate the data range, and black points represent the average value. Red arrows refer to values that extend beyond range. Reproduced from Linninger et al, 2106 [289].

Computational meshes that incorporate patient-specific geometry allow the direct comparison of simulations with *in vivo* data for an individual. The scarce anatomical features, boundary assignment uncertainties, and omission of fluid surface interactions (the movement of neural tissue in CSF) are still some shortcomings that explain inaccuracies of CFD predictions [289]. An open, patient-specific reconstruction of the cervical and thoracic SAS was modeled by Cheng et al to investigate whether fluid surface interactions affected CSF pressure. The group concluded that the pial deformations had minimal impact on the CSF velocity and pressure characteristics [337].

As far back as 1971, spinal microanatomy was proposed to induce complex mixing eddies [338]. However, nerve roots, ligaments, and trabeculae are beyond medical imaging resolution. Computational analysis can help quantify their effects on microfluid

patterns and flow resistance. Pahlavian and colleagues added nerve root pairs to a section of the cervical spine modeled as an open, rigid annular space [298]. Their calculations indicated that nerve roots increased both peak velocities and the duration of bidirectional CSF flow in the SAS. Other computational models by earlier groups include lattice Boltzmann simulations [300, 339] and the simulated porous model of the cerebellomedullary cistern and the spinal SAS [340].

The abovementioned CFD models employ rigid walls and open cross sections delineating only a specific subdomain of the CSF-filled spaces. Such models are not reflective of *in vivo* dynamics as CSF is permitted to exit the computational domain, and boundary conditions are adjusted to achieve the desired or measured velocities. There is less work on closed models of the CSF flow encompassing the entire CNS. Closed models do not have open adjustable boundary conditions. They enforce assumptions about the mass and momentum exchange in the entire CNS. CSF displacement is accounted for by force coupling with the distensible vasculature or compliant boundaries. Linninger's group [341-344] has developed a whole CNS model of CSF flow with deformable walls. This model predicted cerebrovascular pulsations driving CSF velocities throughout the CNS. Additionally, it described realistic phase lags between the arterial and venous blood vessels, CSF motion in the ventricles with oscillatory CSF movement between cranial and spinal SAS, and the deformation of the spinal SAS. In an extension of Linninger's model, Tangen et al [294] employed a computational meshing approach with reconstruction of the entire CNS from patient specific imaging data. They added microscopic trabeculae that could not be visualised by MRI (see 1.3.6.1).

The viscous and inertial properties of CSF and their effects on flow patterns have also been modeled. Viscosity generates a laminar flow pattern.[1] The mass and velocity of CSF result in inertial forces, which in turn involves application of pressure gradients to laminar flow [296]. The resulting velocities depend on initial velocity of the fluid, and different regions of the laminar flow in the SAS are affected differently by pressure gradients (centre vs the boundaries or meninges) [296]. The transient synchronous bidirectional flow of CSF [345] has been conceived as CSF flow direction reversing at slightly different times as fluid flow oscillates rostrally and caudally. Eddies and vortices in the SAS may also be predicted based on the inertial properties of fluid in some geometries [301]. It has been predicted that CSF pressure fluctuations, which are coupled with velocity fluxes, result in transient pressure waves and gradients in the spinal cord parenchyma. In spinal cord models with an anatomically accurate central canal, ventral median sulcus as well as grey/white isotropic differences (see 1.4.2.1), pressure waves at the pial surface was found to induce interstitial radial pressure gradients and complex patterns of fluid movement [113, 119].

The relative effects of inertia and viscosity on fluid can be deduced from the Reynolds[2] and Womersley[3] numbers [296]. The CSF and blood in large arteries have similar numbers (CSF has a slightly lower Womersley number) and so are thought to share some flow patterns according to CFD models.

Advances in imaging (for example, 4D MRI) will provide volumetric flow data in real-time, which will be superior to the point velocity measurements using multiple

[1]Layers of uninterrupted flowing fluid result in fluid moving faster in the centre of a channel and slower near a boundary due to friction.
[2] The ratio of inertial to viscous forces.
[3] Measures the transient inertial forces in proportion to viscous effects.

heartbeat averages. Better image quality and measurements will improve CFD model predictions [289].

Computational modeling is an increasingly powerful tool to generate and test hypotheses on fluid dynamics at macroscopic and microscopic levels. Its sophistication is still contingent, however, on data derived from careful designed laboratory and imaging experiments. Having obtained a panoramic view of CSF, attention should now be turned to ISF.

1.4   Interstitial Fluid

The cells of the CNS are densely packed together, resulting in tortuous narrow gaps that make up the ECS in continuity with the basal lamina of capillaries [346, 347]. The fluid in the ECS is the ISF. In the brain, the volume of ISF is approximately 280 mL [348].

1.4.1   Function, composition, production and absorption

There is consensus that CSF is able to penetrate neural tissue and mix with fluid and solutes in the ECS microenvironment, which are by-products of cellular metabolism and secreted across brain capillary endothelium [349-352]. Compared with the rest of the body, filtration of solutes and water in the brain is markedly reduced due to the BBB [348]. A variety of compounds, metabolic substrates, ions, and O_2 cross the BBB (the larger, hydrophilic molecules requiring transporters) from blood towards the brain tissue. The molecules then diffuse over small distances of up to 25 μm through the interstitium [353, 354]. Specific endothelial membrane transporters also exist for the metabolites that require clearance across the BBB into the blood (for example, Aβ, lipid soluble toxins) [348]. Although the composition of ISF may be similar to CSF near the pial or ependymal surfaces, diffusion reduces CSF/ISF exchange the further the distance from such interfaces. Moreover, cell-bound macromolecules, such as polysaccharides (including negatively charged, hydrophilic glycosaminoglycans), are not exposed to the

comparatively acellular CSF, further limiting fluid exchange, and contributing to the composition of ISF [353].

Although there is increasing agreement that an important source of extra-choroidal CSF is ISF, the corollary is not true. There is significant evidence for ISF production across the BBB [355]. In *in vivo* experiments, plasma concentration changes do not lead to fluctuations in regulation of brain ions [356, 357]. To achieve this, various ion channels and transporters have been described at the brain side of the BBB, capable of net secretion of a sodium chloride rich fluid powered by ionic gradients generated by the $Na_+/K_+/ATPase$ pump [356]. Water then passively follows this secreted fluid. This, and other ion transporters, have been documented in primary cultured brain endothelial cells. Thus, most ISF is "fresh", conducive to the stringent ionic microenvironment of the CNS and free from waste products of recycled CSF. A component of ISF likely comes from water that results from oxidation of glucose to CO_2 [356].

1.4.2   Fluid movement in the parenchyma

Whether fluid movement in the ECS of the CNS occurs via diffusion or convection is a subject of intense debate. Neuroscientists as far back as Cushing in 1914 [358] postulated that ISF might drain out of the brain via privileged, low resistance pathways into the CSF. In the 1970s, this idea was further developed by Cserr et al [359-361] and others who studied various radiolabeled tracers injected into subcortical brain structures. Eventually, two camps emerged: 1) one group proposed fluid flow was convective in nature and that these specialised pathways were along blood vessels and along white matter tracts [362-364], while 2) the opposing group rejected the idea of interstitial bulk flow, promoting diffusion as the mechanism for CSF/ISF exchange instead [365].

Evidence is gathering to support diffusion as the mode of solute transport in the ECS of the CNS, at least in the grey matter [331]. In the 20th century, *in vitro* and *in vivo* investigations included ventriculo-cisternal and subarachnoid-cisternal injection of radiolabeled tracers (such as inulin and sucrose) [366-368], as well as real-time iontophoresis studies of small tetramethylammonium ions [369] that demonstrated random movements of solutes through the ECS due to its tortuous microarchitecture (see below). An important point in the argument for diffusive transport has centred around the width of the CNS ECS. Early electron microscopy ultrastructural studies of conventionally perfusion-fixed neuropil yielded results in the range of 10–20 nm [370-372]. Recently, Thorne and colleagues demonstrated that the ECS width in the living rodent somatosensory cortex is greater than these previous estimates [373, 374]. Using an *in vivo* diffusion measurement technique, integrative optical imaging (IOI), dextrans and 3-35 nm quantum dots were injected into the grey matter. They concluded that diffusion theory could account for solute transport in the neuropil,[4] without any predilection for drainage to arterial or venous structures. They additionally derived an ECS width of 40-60 nm after applying their experimental results to a model of brain ECS as cylindrical pores [373]. These results were corroborated by further computational modeling of hippocampal neuropil, where actual tissue geometry from serial electron microscopy had been corrected to reflect the *in vivo* ECS volume [375, 376]. They concluded that under most circumstances, the ECS geometry is convoluted and narrow where the hydraulic resistance is likely to be so high that a pressure mediated convective flow is implausible [377, 378]. In recent years, mathematical models have further argued against bulk flow in the interstitium. Jin et al [376] constructed a 2D model of the ECS, assuming ISF had the viscosity of water. They concluded that with

---

[4] It should be noted that a durotomy was performed in these experiments, which affects hydraulic integrity.

physiological paravascular pressure gradients of <5 mmHg, no advective flow of solutes was possible. Aquaporin-4 (AQP4) permeability to water had little effect on overall parenchymal resistance. A subsequent computational simulation, using more realistic 3D electron microscope reconstruction of a rat hippocampus including smaller more numerous objects that resist flow in the ECS, demonstrated that even for large molecules, clearance from the brain interstitium via diffusion was easier than bulk flow [375].

1.4.2.1 Grey matter vs white matter

Important work by Rosenberg et al [379] on ventriculo-cisternal perfusion of ECS molecules in cats has demonstrated that although ISF flow in grey matter is consistent with diffusion, bulk flow occurs in white matter tracts (as described originally by Cserr et al [360] and Abbott [355]). Grey matter is unmyelinated and is also the site of penetrating arteries from the ventral median fissure. Its ECS is packed with somas and neurites that have no preferential orientation. The tortuosity5 (λ) for diffusing molecules is high [348]. Diffusion here is isotropic (confirmed in rat spinal cords [23]). Tortuosity is modulated by the viscosity of the ISF, as well as the molecule size. The smaller the diffusing molecule, the less hindered its path through the ECS. Efficacy of diffusion also diminishes as the square of distance. Tortuosity has regional variations in the CNS grey matter; the neocortex has a higher value than the hippocampus, for example [374]. Fluid is constrained by and diffuses along parallel white fibre tracts that are relatively free of interconnections. Tortuosity is therefore lower. Here, diffusion in the ECS is facilitated by anisotropy, which has also been confirmed in the developing rat spinal cord in *ex vivo* experiments [23].

---

5 Tortuosity (λ) = diffusion coefficient in water (D)/ apparent diffusion coefficient (D*)$_{1/2}$

The difference in diffusion isotropy between grey and white matter has been further demonstrated in human MRI studies [15]. This was confirmed in computational simulation of the rat spinal cord by Sarntinoranont et al using diffusion weighted MRI [335]. They found a lower hydraulic conductivity in the grey matter and thus increased tissue resistance. Diffusion along ECS of white matter tracts, however, was unaffected by these factors.

Spinal cord white matter tracts differ from that in the brain; myelinated tract fibres run parallel to its long axis. Convection-enhanced delivery (CED) experiments on animal spinal cords give insight into ISF movement. Endo et al [380] employed Evan's blue tracer, a smaller molecule that is more effective in studying diffusion, to characterise the delivery of macromolecules into the grey matter of rat cords. Evan's blue spread in a radial pattern after delivery into the grey matter but was confined to the white matter after white matter injections. The tracer travelled slightly further rostrocaudally in the white matter compared with grey matter. A durotomy was performed prior to cannulation of the cord parenchyma, resulting in CSF leak and altered hydraulic integrity of the SAS and perivascular spaces. This may in turn affect fluid inflow dynamics. Much of the earlier work on ISF movement in spinal cord was performed *ex vivo*, and in models where there was a breach in the dura [381-385]. These results should be interpreted with caution. Other CED studies in animal spinal cord have yielded similar findings of anisotropic movement of ligands through the white matter tracts [386, 387]. In these experiments, infusate was homogeneously distributed over a long segment of the cord. However, these studies were plagued by large durotomies and significant CSF leak.

It is increasingly clear that diffusion largely governs fluid movement in the CNS parenchyma, especially in the grey matter. Fluid flow is likely different in the white

matter, and it is unclear whether bulk flow is more prominent here. Indeed, Abbott's 2004 seminal investigation found a bulk flow rate of 0.1–0.3 μL/min/g in the rat white matter tracts [356]. Recently, a study examined clearance of injected tracer from the rat basal ganglia towards ventricles. The authors noted regional variations in fluid drainage patterns that were dependent on white or grey matter was involved [388]. Whether these findings apply in the spinal cord is largely unknown.

1.5   Interaction between fluids

In the contemporary literature, most of the efforts to elucidate the precise mechanisms governing CSF and ISF exchange have been directed towards intrathecal pharmacological delivery systems [331], or the pathophysiology of neurodegenerative diseases where there is putative dysfunction of interstitial waste clearance. Fluid exchange also subserves physiological functions. Examples include the paracrine-like redistribution of CNS proteins by CSF (such as melatonin), or proteins that are secreted across the blood-CSF barrier at the choroid plexus, or even by the choroid plexus for dissemination (such as vitamin C [389, 390], folate and IGF-II [391]). A more complete understanding of inflow and outflow systems is relevant to CNS fluid disorders such as syringomyelia.

Current evidence strongly suggests that the CSF moves into the CNS parenchyma, where it interacts with the ISF [328]. If there is net movement of fluid into the spinal cord, there must be endogenous fluid drainage (and ipso facto, solute elimination) to maintain homeostasis. Ultimately, there are only two modalities through which substances can be eliminated from the CNS parenchyma: 1) transport across the BBB or 2) efflux to the CSF or lymphatics [328]. Even products of metabolic breakdown still require eventual removal by either or both of these routes.

The gross inflow and efflux of water across the BBB is large. However, the net flux of water is so small its overall direction is not known. There is evidence in humans suggesting a net movement of water from blood to brain of ~10 mol/ day [283]. This is approximately a third of CSF output by the choroid plexus. Similarly, the net movement of Na_+ and Cl_- across the BBB is likely small. The net displacement of these ions is likely a result of active transport, a significant part of which occurs in perivascular compartments. Near ependymal surfaces, ISF and CSF exchange can be mediated by diffusion so perivascular ionic transport can be supplemented by this process [230, 283, 328].

Given the paramount importance of these ions to fluid flow, the exchange of substances via perivascular, transependymal and transpial routes will be discussed.

1.5.1 Transpial and transependymal exchange

The reader is reminded that water freely passes between blood, CNS parenchyma, and CSF, and that large gap junctions exist in the pia and ependyma to facilitate CSF/ISF diffusion and exchange [328](see 1.3.3.3).

Experimental evidence supports the notion of bidirectional exchange between CSF and ISF via transpial and transependymal routes [392, 393]. In rabbits, rats and humans [394-399], intraventricularly administered tracers (ascorbic acid, inulin, mannitol sucrose) have been shown to diffuse readily from the CSF through the ependymal lining, and then gradually towards the para-ependymal parts of the brain. Eventually, as the tracers reach the SAS, transpial migration of these molecules into the surrounding CNS parenchyma has been observed. The time taken was found to be a function of molecular size. Labelled Na_+ and Cl_- have also been reported to exhibit similar transependymal movements [400], and such fluxes actually represent ionic exchanges between ISF and ventricular CSF [229]. Conversely, there is clear diffusion of homovanillic acid (from

dopamine metabolism) and 5-hydroxyindoleacetic acid (serotonin metabolism), products of neuropil metabolism, from the ISF to CSF [238].

The kinetics of CSF/ISF exchange of soluble molecules are complex. They are dependent on the principles of diffusion, as well as microarchitecture of the cell–interstitium relationships (such as tortuosity and viscosity of the extracellular matrix) [229]. Other driving forces in the ECS such as cardiovascular pulsations, respiration, conscious state and posture may affect solute movement (discussed later, 1.5.4). As a general rule, however, exchange between CSF and ISF is passive and is therefore a slow process, taking hours or days for CSF tracers to equilibrate with the brain parenchyma at depth [229]. Due to the porous nature of the ependyma, it is possible to conceive the CSF–ECS as one continuous large compartment. Substances such as $Na+$ (that penetrate BBB poorly, are not metabolised and are transported into the CSF continuously) equilibrate slowly via diffusion throughout the entire CSF–ECS compartment. At steady state there is no net flux between ISF and CSF despite the ongoing mixing between the compartments [229]. For tracer molecules that have poor permeability through the BBB or blood-CSF barrier, observations after short experimental times (such as 30 mins) may be misleading. Indeed, investigators such as Iliff et al [327] have cast doubt on transependymal movement of solutes because they noted intraventricularly infused dextrans and ovalbumin do not penetrate the brain parenchyma. On the other end of the spectrum, molecules such as penicillin rapidly disappear after intraventricular administration because of bulk flow and clearance by the choroid plexus by OAT-3 transport found in capillaries and the choroid plexus [401]. Interpretation of passively infused tracer studies, therefore, should be circumspect and take into account time, solute characteristics and pharmacokinetics.

1.5.2 Definition and anatomy of the perivascular space

The "perivascular spaces" of the CNS have recently become the focus of CNS fluid research [353]. A consensus on the precise definitions and constituents of the "perivascular" and "paravascular" space is conspicuously absent. These terms have been interchangeably used (and misused), but appear to be supplanting the older nomenclature, "Virchow-Robin space". This confusion arises partly from the increasing recognition that the microanatomy is complex, technically difficult to study, and likely altered in *ex vivo* preparations [318]. In this chapter, the term "perivascular space" shall be used for the small spaces around blood vessels.
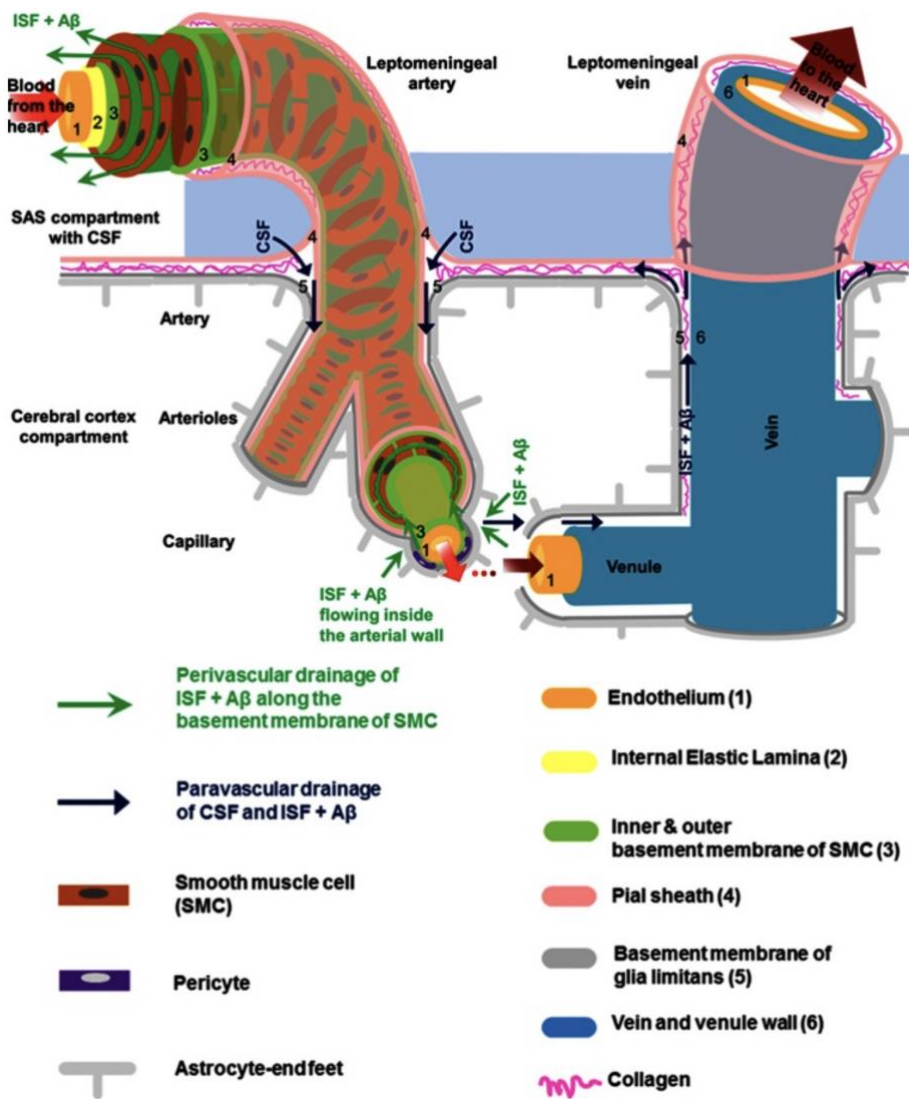
Fig. 5 Anatomy of the perivascular spaces around an arteriole and a venule, as proposed by the Weller/Carare group. Reproduced from Bakker et al, 2016 [348]

Perivascular spaces are found in both large leptomeningeal vessels and in the vasculature of the CNS interstitium [353]. The latest ultrastructural studies employing electron microscopy have revealed increasingly intricate anatomy (**Fig. *5***) [348, 402]. Firstly, the "space" around penetrating vessels may in fact be filled with fluid and compact layers of cell processes and basement membrane [249, 403]. This "space" occupies the connective tissue of the adventitia as well as, according to some authors, the basement membrane within the tunica media (vascular basement membrane) [331, 404-407] and the capillary basal lamina [353]*.

The arterioles in the SAS are ensheathed in fenestrated leptomeninges derived from the pia which continues with the vessel deep into the parenchyma, fusing with the glia limitans of the astrocytes at the level of the capillaries [347, 408] (**Fig. *5***). The pial sheath is thought to continue with the cerebral leptomeningeal vessel as it traverses the skull [348] (and presumably also the bony spinal column). Collagen is found between this pial sheath and the outer basement membrane of the smooth muscle cell, constituting the adventitia [348]. This is the expandable component of the perivascular space. As veins cross the SAS into the parenchyma they lose their pial sheath, thus the subpial space is in contact with the adventitia of the vein. It would be logical to distinguish the compartment formed by the glia limitans and venular adventitia as a "perivenular space". The discrete compartment between the glia limitans and the pial sheath (that delimits the "peri-arterial space") might warrant separate labelling. Some have referred to this as the "paravascular" space, but perhaps it may be more reasonable to call this the "para-arterial" space, a subdivision of the perivascular space. As the arteriole divides into capillaries, the tunica media and the layer of pia mater are lost (**Fig. *5***). At the level of the capillary, the glia limitans is in direct contact with the wall of the capillary. The perivascular space may continue within the basal lamina of the capillary [327, 331, 362,

409]. Fenestrations have been described in the adventitia of leptomeningeal arterioles (in the rat), as well as in the pia and pial sheaths. These openings offer little resistance to molecules as large as 2000 kDa [410], and intrathecally injected IgG antibodies are able to reach even microvessels [331]. The porous nature of these barriers means that CSF can potentially access the entire cerebrovascular tree. The above descriptions are derived from brain studies [230, 249, 403, 411]. Ultrastructural studies of the perivascular space and SAS in the rat spinal cord by the Stoodley group suggest similar anatomy [402], although a pial sheath was not observed accompanying penetrating vessels in the SAS.

The perivascular space is likely a site of significant exchange between ISF and CSF [353] . The mechanisms surrounding this exchange, the role that astrocytes play and the fundamental fluid dynamics at this microscopic level are topics of ongoing enquiry and debate.

1.5.2.1 Aquaporins

As one of the centrepieces of the glymphatic model [327], aquaporins and their role in health and disease have garnered considerable interest. Aquaporins are a family of cell membrane water-selective channels. These 0.5 nm pores regulate osmotically driven water (and sometimes other small molecules) through the lipid bilayer [412]. Aquaporin-1 is present on the epithelial cells of the choroid plexus. AQP4 is enriched particularly on the astrocyte foot processes and ependymal cells—that is, at CSF interfaces. They have polarised expression at the pial surface-facing glia limitans, and within perivascular endfeet that form the boundary between the CNS blood vessels and the neuropil [413, 414]. Aquaporin-9 is localised to tanycytes and astrocyte end-feet [415]. Together with a medley of neuronal and glial ion cotransporters and neurotransmitters, aquaporins play a central role in regulating water homoeostasis in

the ECS. The impact of AQP4 deletion is not completely understood. Observations include:

1. Reduced ependymal production of CSF [416].

2. Increased diffusion in mice, suggesting that solutes move quicker in ECS with less water content [417].

3. Reduced CSF/ISF exchange with diminished paravascular water and solute entry and ISF flow (see 1.5.3) [327] .

4. Increased brain ECS volume fraction, basal water content and greater ICP spikes in response to vasogenic oedema. This suggests AQP4 has a role in induction and resolution of oedema via fluid shifts between brain compartments [418-420].

5. Loss of AQP4 polarisation in the ageing rodent brain is associated with reduced CSF circulation and paravascular inflow of intracisternal delivered tracers, as well as decreased clearance of Aβ [421].

1.5.3 Fluid flux theories

The precise interaction between the CSF, ISF and perivascular fluid remains controversial. It was hypothesised over a century ago that ISF and CSF might mix. Beginning with Weed [262] in the 1910s, experiments by various groups demonstrated that tracers can enter the CNS (the vast majority of studies focused on the brain) via an inward perivascular route, or a diffusive transpial pathway [353]. Ichimura et al [422] demonstrated communication between the ECS, the perivascular space, the subpial space and the SAS. They observed, however, a slow, variable, back and forth longitudinal movement of large tracer molecules in the perivascular spaces that did not support rapid fluid flow into brain via these channels. This was in contrast to the findings by Rennels [362] who laid the foundation for a model of ISF clearance via rapid "para-

arterial inflow" (with HRP tracer) and "para-venular" outflow of CSF. A model of fluid circulation within the CNS was thus established. At the close of the 20th century, Stoodley et al [148] later found evidence for rapid fluid flow via perivascular spaces into the spinal cord interstitium and central canal in the normal rat using HRP.

The "glymphatic" system, described in 2012, revived interest in perivascular flow and the concept of fluid circulation [327]. This theory was borne out of well-designed *in vivo* experiments using multiphoton microscopy on transgenic mice that exhibited fluorescent vascular smooth muscle cells. Intraventricular, intracerebral and intracisternal injections of fluorescent CSF tracers (dextran and ovalbumin) led to a theory of CSF convective inflow into brain via a "para-arterial" route (histological clarification of tracer deposition was not performed). Bulk interstitial flow through the ECS then washed the tracer towards para-venous spaces for efficient clearance out of the brain. "Paravascular" tracer and water entry (and exit from the interstitium) was hypothesised to be dependent on AQP4, found in abundance on astrocytic end-feet in spaces around penetrating vessels [327]. The basis of this claim was made after observing reduced inflow and outflow of tracer in AQP4-null animals. Smaller, lipophilic tracers were also injected and were observed to follow spatially restricted interstitial pathways. AQP4 modulation did not affect this phenomenon.

Although well publicised, the glymphatic theory has been levelled with major criticisms regarding the methodology and interpretation of results within the study [230, 249, 351, 376, 423]:

1. The precise mechanism(s) by which perivascular astrocytic AQP4 channels mediate directed arteriovenous transparenchymal ISF and macromolecular flow have not been elucidated. There is no explanation for continued rapid periarterial inflow of large tracers in AQP4-null mice. Other authors have consistently

questioned whether generation of the required hydrostatic pressure or osmotic gradient is possible to support interstitial convective flow [424]. The results of subsequent animal experiments and computational modeling [376, 423] by other groups have suggested high hydraulic resistance values in the ECS that would impede any significant bulk flow [375, 425].

2. AQP4 is not known to transport large proteins [353].

3. Convective flow of ISF, solutes, and waste through the parenchyma is at odds with the stringent homeostasis of the ECS microenvironment necessary for synaptic transmission [353].

4. Smith et al [426] repeated central aspects of the original glymphatic experiments including similar intracisternal delivery of tracers in both wild type and AQP4-null mice. They, and others [331], reported that there was transpial tracer influx and this mechanism was dependent on size and consistent with diffusion, with symmetrical spread of parenchymally injected dextrans *in vivo*. Whether the mice were AQP4-null did not result in any qualitative or quantitative differences in CSF tracer deposition.

The Carare/Weller group has long promulgated a vascular basement membrane model [427] centred on fluid influx and efflux via different layers within the perivascular space that is present as a continuum from capillary to artery (**Fig. 5**). In a recent publication [403], intrahippocampal injection of fluorescent Aβ resulted in its deposition in the superficial leptomeningeal arterial wall. Transmission electron microscopy verified the protein was found with high specificity in the basement membrane within the tunica media (as opposed to endothelial basement membrane). This was interpreted as "perivascular" ISF and solute clearance, along arterial conduits directly to lymphatic systems in the skull base [249, 428]. This route was fast, and limited penetration by

larger particles. Accumulation of 15 nm gold nanoparticles in the "pial glial" layer (corresponding to the para-arterial space—for definition refer to 1.5.2) after injection into the cisterna magna suggested fluid inflow via a paravascular route. In the capillaries, there was adjacent bidirectional flow of fluids with CSF inflow next to the glia limitans and ISF outflow next to the endothelium. Notably, there was no venular involvement in fluid transport. Earlier work by the group reached the same conclusions with dextran and ovalbumin tracers (3 and 40 kDa respectively) [427, 429]. After entering the basement membrane at the capillary level, ISF was observed to drain along the basement membranes of cerebral arteries by bulk flow. Further key evidence for this was acquired with intravital multiphoton microscopy of fluorescent tracers injected into mouse brains to study ISF clearance [430]. A rapid co-localisation of dextrans of different sizes to the arterial basement membrane was reported. The tracers deposited in the perivascular space within the smooth muscle cell layer. Again, no tracers were detected around venous structures. Biexponential reduction of tracer over 30 mins was demonstrated, which the authors interpreted as consistent with bulk flow in the perivascular space. This study was notable for its real-time *in vivo,* high temporal resolution tracking of small volumes of intraparenchymally delivered tracer in single vessels. The caveat was that a durotomy was performed presumably for the imaging and stereotactic injection, compromising hydraulic integrity. It should be noted that Iliff et al injected 125I-labelled Aβ into mouse brain and found that 60 mins after delivery, the iodinated tracer was detected along capillaries and veins [327].

Thus, the major points of contention between the dominant models of fluid flux are centred around: 1) the involvement of basement membranes in fluid influx/efflux and 2) the types of vascular structures involved. If, on the one hand, vascular basement membranes (within and binding the smooth muscle layer) mediate perivascular fluid

influx, then cardiovascular pulsations cannot be the driver of fluid flow due to their incompressibility and higher resistance to flow. It should be noted at this point that it is not established whether bulk flow exists in the perivascular space at all. In another critical analysis of the glymphatic theory, a recent modeling study concluded that bulk flow driven by steady state pressure (between the SAS and the parenchyma) in perivascular spaces around arteries is implausible [431]. The authors showed that the hydraulic resistance of vascular basement membrane is too high to facilitate ISF clearance, unless there was direct lymphatic drainage in the CNS parenchyma. There was also an inadequate driving force from local pressure differences to effect "paravascular" bulk flow in arteries and veins. However, in recent *in vivo* animal experiments, Mestre and colleagues derived a high Peclet number for fluid flow within leptomeningeal perivascular spaces of mice, consistent with advection [318] (which would align with the original glymphatic assertion of bulk flow, see 1.5.5.1.2).

On the other hand, if fluid and solutes flowed instead within fluid filled, compressible extramural compartment(s) of perivascular spaces then arterial pulsations, associated with modest changes in blood pressure, can drive fluid flow. Pizzo and colleagues suggested that both basement membrane routes and other, extramural routes exist with their relative importance depending on the size of vessel and the size of the solute [331, 409]. Others have suggested that extramural basement membrane mediate influx, while the intramural basement membrane route between smooth muscle cells facilitate efflux [319, 347].

The available evidence suggests that both influx and efflux occur along both arteries and veins [320] either via common pathways or separately along parallel pathways. Efflux along unspecified blood vessels has also been observed [426]. At the level of the capillaries, the hydraulic resistance of the basement membrane (as modeled by Asgari et

al [423]) may be irrelevant. The small distance between any two large blood vessels is small enough that diffusion can drive fluid movement without the need for a preferential fluid drainage pathway.

If a fluid filled, compressible perivascular space is likely, another possibility is to-and-fro convective mixing (also known as dispersion [423]) of fluids in the perivascular spaces of arterial and venous structures. This could, according to a recent mathematical model, facilitate relatively rapid movements of solutes both inwards and outwards [432]. Diffusion would then be adequate to explain movements within the interstitial spaces in the parenchyma due to the small distances involved (as explained earlier). The driver of the mixing is the full vessel length deformation of the perivascular space dimensions by changes in blood pressure. Some experimental support of this to-and-fro movement has recently emerged in intravital particle tracking of microspheres in the perivascular space of leptomeningeal vessels in the murine brain cortical surface [329]. Moreover, there is a computational model of the spinal cord demonstrating transport of macromolecules down their concentration gradients against the direction of net CSF flow, and at rates greater than diffusion allows [433].

In recent years only two groups have investigated the pathways of fluid flux in the spinal cord. Using a variety of intracisternally infused fluorescent fluid tracers, Wei and colleagues [325] and the Stoodley group [402] examined the distribution of these molecules in *ex vivo* preparations under fluorescence, confocal and transmission electron microscopy. Wei et al found that the small tracer, cadaverine, was able to penetrate the parenchyma via transpial and perivascular routes but made no distinction between arteries or veins. Interestingly, the authors injected an AQP4 inhibitor which reduced the amount of tracer detected in the cord. They concluded that the glymphatic theory governed fluid transport in the spinal cord as well as the brain. Lam et al

observed accumulation of tracer around arterioles and venules, but not capillaries. They concurred that the basement membrane around perivascular spaces facilitated solute transport (as opposed to the fluid-filled model of the perivascular space). The anatomical description of perivascular tracer deposition appeared to conform to the compartment between the glia limitans and the outer limits of the vessel adventitia. The authors also reported a novel finding of the apparent crossing of the blood-spinal cord-barrier by the tracer. This has not been described elsewhere in the literature [402].

1.5.3.1 Lymphatics

The nature of connections between the perivascular space around penetrating vessels, the CSF in the SAS and the perivascular spaces of leptomeningeal vessels is still unclear. Perivascular outflow of fluid and solutes from the interstitium appear to distribute partly to the SAS (water exchange occurring through the pial sheath), and partly to the dura [434]. A significant amount of perivascular efflux of large solutes may be directed straight to lymph, bypassing CSF altogether. Szentistvanyi and colleagues [435] found that injected radio-iodinated serum albumin redistributed from the brain ISF to the walls of the intracranial arteries, but could not be detected in the walls of the neck carotid artery. This was interpreted as ISF draining from the intramural vascular basement membrane to the cervical lymph nodes [436]. Papolla found that the rate of production of interstitial mutant Aβ correlated with the amount found in the cervical lymph nodes in transgenic mice that overexpressed amyloid precursor protein [437]. Aspelund [273] recently demonstrated that tracers delivered into the brain flowed into dural lymphatics and thence into the deep cervical lymph nodes. The original glymphatic theory also postulated drainage from perivenous spaces to the neck lymphatics [327]. Recently, Proulx and colleagues published findings from injection of NIFR fluorescent tracers into the lateral ventricles *in vivo*. Although not strictly a study of interstitial clearance, they provided indirect evidence of a brain fluid outflow mechanism into the

lymphatics and systemic circulation [260, 320]. The precise pathways were not elucidated in either of their papers. It should be noted there were methodological problems mainly pertaining to CSF leak secondary to removal of injecting needles.

1.5.4 Summary

There is mounting evidence against the model of the glymphatic circulation of fluids, as originally described in 2012. A perivascular fluid system, characterised by convective flow or dispersion along the perivascular spaces of large vessels, is more likely. These well-regulated channels are minimally disruptive to neural functions, bringing CSF inwards from the SAS and removing ISF towards the pial surface. It is not possible to rule out entirely the existence of a net flow between the perivascular spaces of arterioles and venules. It is increasingly clear, however, that bulk flow through the neuropil is improbable. Diffusion is at least partly capable of accounting for movement of solutes and CSF/ISF exchange at the at the level of the capillary, as neurons and other constituents of the neurovascular unit are within 20 μm from the pericapillary spaces. Convection in the basal lamina of the capillaries, as a means to connect arteriolar and venular perivascular spaces, is still possible. Finally, some ISF is also likely to cross the ependymal surfaces.

1.5.5 Drivers of fluid flow

Great strides are being made not only in elucidating the anatomical pathways of fluid flux in the CNS, but also in determining the driving forces behind fluid movements. There is widespread consensus that the production and absorption of CSF do not contribute significantly to the pulsatile bulk flow of fluid in the SAS [289]. Various authors have raised the possibility that fluid dynamics in the SAS may not be similar to those in perivascular spaces [353]. Therefore, we will consider the SAS and perivascular spaces separately.

1.5.5.1   Coupling pulsations to cardiovascular parameters
1.5.5.1.1   In the subarachnoid space

There is strong integration of the CSF system with the cerebrovascular, cardiovascular and respiratory systems [211]. Pulsatile CSF flow throughout the SAS of the spine and cranium is thought to be linked to the phase difference in the egress and ingress of cerebral blood flow. In the skull, pulsatile CSF results in ICP oscillations (around 0.5–3 mmHg peak-to-peak amplitude), which rise with increases in CBF, and decrease rostrocaudally along the spinal SAS [211]. The CSF stroke volume in the spinal SAS at C2 is thought to be approximately 0.3–1 mL/cardiac cycle with almost no net flow [336]. Here, pulsation is the sum of total inflow and outflow of cerebral blood flow, with intracranial compliance causing a small difference in magnitude and phase [438-443].

In the brain, the precise source and type of force coupling the expanding and contracting vasculature, CNS movement and induced CSF dynamics are uncertain. Early theories from Du Boulay et al [444] suggested that bilateral thalamic movement was responsible for pumping CSF. Enzmann in the 1990s modified this to include the theory that arterial pulsations of the whole brain propelled fluid flow [291].

During systole expansion of the cerebral vasculature triggers displacement of CSF from the fixed cranial vault (Monro-Kellie doctrine). The 1–2 mL of cerebral blood volume flux (and the equivalent exchange of CSF between cranium and spine) during the cardiac cycle has been corroborated by MRI [445]. Pulsations occur along every ramification from the major arteries to the capillary bed. The distension of the vessel is transmitted to the surrounding parenchyma, dilating the brain, a view supported by Greitz [446]. This produces motion as documented by Enzmann and Pelc [291]. Zhu et al employed PC-MRI to quantify ventricular wall motion [447]. They found that choroidal arterial expansion may impart energy to the ventricular walls, leading to pulsations against the ependymal and ventricular dilatation, thus generating oscillatory CSF flow [447, 448].

Others have questioned this proposal [449-451]. It is also possible that ventricular contraction could arise from vascular expansion at the cortical surface that is conveyed through the brain parenchyma. Du Boulay believed, additionally, that expansion of the cerebral hemisphere produced basal cistern pulsations [449]. Alternatively, compression of the brain by vascular pulsation could lead to displacement of ISF into the ventricles, a consequence of an accommodating reduction in the overall ECS [452]. In at least one canine experiment [453], venous pulsations have been shown to contribute to cisternal CSF pulsations, although arterial pulsations were shown to be the dominant driving force. The dural venous sinus system has also been hypothesised to be compressible or even collapsible by raised ICP. It has been suggested that deformation of the venous wall would trigger, through negative feedback, a reduction in vertebral artery flow with resultant alteration in CSF dynamics [454]. Harmer et al, however, concluded that intracranial CSF pulse amplitude in dogs increased with raised ICP [455].

The source of spinal CSF pulsations has been elusive. A number of investigators have posited that lumbar CSF pressure waves originate from a combination of brain and spinal arterial pulsations [456-458]. Urayama [458] claimed that at least three quarters of the lumbar pressure pulse wave can be attributed to spinal vasculature pulsations (in which arterial and venous pulsations contributed equally), and a quarter from transmitted cranial pulsations. This was further supported by Dunbar and colleagues' canine studies involving spinal blocks and aortic occlusions. They concluded that the arterial vasculature of the spinal cord supplied most of the lumbar CSF pulse wave, with minimal contribution from cranial vascular pulsations (including those from choroid pleuxs) [456].

Martin et al [211] modeled the relationship of spinal cord blood flow and CSF pulsations along the spinal SAS to investigate the spinal arterial to CSF pulse delay. Coupling of the

cardiovascular and CSF system was achieved by a transfer function based on *in vivo* measurements of CSF and cerebral blood flow. Craniospinal SAS compliance was varied. Then, the pressure and the flow of CSF and blood were calculated. A greater spinal SAS compliance resulted in increased CSF flow wave attenuation and reduced flow rate along the spinal canal from the cervical to lumbar spine. Compliance and vertebral level significantly affected the delay between the spinal cord blood flow and CSF pulsations. Arterial pulsations arrived earlier than CSF pulsations when there was greater compliance.

1.5.5.1.2 *Perivascular effects*
1.5.5.1.2.1 Animal studies

There is consensus that arterial pulsations impart the motive force for perivascular flow of solutes and fluid. This has come from observations in animal experiments where perivascular fluid movement is attenuated after ligation of major afferent arteries or cardiac arrest (and the corollary when sympathomimetics are administered) [146, 427, 459]. Reduction of parenchymal efflux as well as influx into the CNS have been reported [146]. Hadaczek et al [460] showed adrenaline-induced hypertension and tachycardia promoted apparent bulk flow of different sized macromolecules through the brain ECS, while hypovolaemia-induced bradycardia and hypotension had the opposite effect. The authors coined the term "perivascular pumping" to describe the undulating expansion and contraction of the arterial wall propelling solutes. They posited that pulse pressure provided the motive force, and that flow was also modulated by the elasticity of the vessel (greatest near the suface) and resistance (highest distally). Rennel's and Stoodley's experiments involved ligation of the brachiocephalic artery in dog and sheep respectively, resulting in reduced perivascular CSF tracer inflow into the brain and spinal cord [146, 362].

The Nedergaard group [461] also reported results from *in vivo* and *ex vivo* animal experiments in this area. Using two-photon intravital microscopy in mice, they demonstrated that carotid artery ligation reduced pulsations in penetrating cortical arteries and was associated with reduced CSF tracer accumulation around both leptomeningeal arteries and superficial penetrating arterioles. This was confirmed in extracted and fixed histological samples of brain. The methodology in these experiments was rigorous. Mice were subjected to both injected and isoflurane anaesthesia, thinned skull and open cranial window preparations, as well as sham operations. The authors then tested the effects of a single intraperitoneal injection of dobutamine and found uniformly increased tracer influx throughout the brain on fluorescence imaging of the extracted brain (no *in vivo* data were acquired here). Increased pulsatility of all blood vessel types was detected, but the blood pressure rise was not sustained and there was a reflexive tachycardia associated with the inotrope administration. This effect was not discussed further by the authors. In a follow up study, the same group attempted to quantify physiological changes at the level of the perivascular space. Mestre et al [318] employed two-photon intravital microscopy and particle tracking velocimetry on 1 μm fluorescent polystyrene microspheres, injected into the cisterna magna, to derive the CSF flow velocities in what the authors assumed were the perivascular spaces of mouse brains, and thence the Reynold and Peclet numbers (see 1.3.7.4). By synchronising the electrocardiogram and respiratory waves to the velocity of the tracked microspheres, they demonstrated that the particle motion was yoked to the cardiovascular pulsations, but not to respiratory patterns. They thus concluded that the displacement of the arterial walls was the source of the "perivascular pump" driving CSF in the same direction as arterial blood flow. The authors then acutely raised the mean arterial pressure of the mice with Angiotensin II and found that the particle velocity reduced. They posited that the increased arterial stiffness, induced by hypertension, diminished

the efficacy of the "pump". A major shortcoming in this study was that no microspheres were detected deep to the SAS so their observations and derived values reflect the leptomeningeal vessels, as opposed to subcortical vessels that may have different physiology. These vessels were identified in their previous work as the vessels that were most acutely modulated by vessel ligation and inotrope injection [461]. A reasonable assumption is that if there was slowing of tracer movement, then there would be reduced total tracer influx (this was not explored). No explanation was given as to why these results differed from their earlier study. Using similar methods, Bedussi et al [329] performed intravital confocal microscopy (albeit single photon) to track CSF infused microspheres on the surface of mouse brains. They found no microspheres below the SAS, but unlike Mestre et al's findings, particles were present around both arteries and veins in this study. This group's interpretation of the pulsatile nature of the bead movement was that arterial pulsations generated mixing in the penetrating vessel perivascular space (see 1.5.3). The authors concluded that fluid movement observed in the perivascular space was instead generated by the choroid plexus.

In an animal model of ischaemic stroke [430], arterial occlusion resulted in rapid, localised and marked reduction in perivascular efflux of solutes along that vessel. This finding has raised the question of whether blood flow through a patent vessel also contributes to perivascular transport. Accumulation of leptomeningeal mural Aβ was also observed after cerebral hypoperfusion in a mouse model of Alzheimer's Disease [462].

1.5.5.1.2.2 Computational models
The concept of a valve action from pulse waves was explored in a biophysical model [463]. Fluid and solutes may be driven by contrary or reflection waves generated by the pulse wave. The contrary wave travels against the direction of the pulse wave and blood

flow. This model stipulated the existence of a valve-like action to prevent reflux during the major pulse wave's passage along the vessel wall. Carare and colleagues adapted this contrary wave model and hypothesised that it may be plausible for deformation of the vascular basement membrane (and other biochemical interactions) to instigate an appropriate valve action. This would drive solutes and fluid centrifugally along arterial walls. With ageing, vessels stiffen, lose elasticity and with it, the ability to drain along perivascular routes [464]. In a follow up combined analytical and numerical model a decade later, the same collaborators confirmed that a general valve mechanism producing net reverse drainage along the vascular basement membrane was feasible, but the computed arterial pulsations were eight times too weak to generate outflow in the basement membrane (when correlated to experimental results) [465]. This was secondary to the long wavelength of the arterial pulsations relative to the artery section, which resulted in small pressure gradients along the length of the vessel. The authors supported this argument with injection of Aβ into mice hippocampi and demonstrated no difference in drainage between groups receiving a beta-blocker and saline [465].

Bilston et al [151] used computational modeling to show that arterial pulsations (modeled as travelling waves on the arterial wall) induce fluid movement in the perivascular space in the direction of the arterial wave. They found the greater the pulse wave velocity and arterial deformation, the greater the flow rate. It was suggested that these pulsations could lead to fluid flow in the perivascular space even against "adverse" pressure gradients (the implication here is the loss of fluid kinetic energy)[150]. In another study, the same group explored the consequence of a timing mismatch between arterial pulsations in the perivascular space and the SAS pressure wave (which may arise from SAS arachnoditis, for example, elevating the SAS pressure [466]). When the peak SAS pressure occurred at a time when the perivascular space was largest (this

occurred when the artery was the smallest), resistance to CSF flow would be lowest. Later in the cycle, as the artery was at its maximum width and the SAS pressure was at its nadir, the smallest amount of CSF backflow into the SAS could occur [151]. Thus, using an axisymmetric model, they showed that a mismatch in relative timing in arrival of a CSF pressure wave in the spinal SAS and an arterial pulse could theoretically drive perivascular fluid inflow along a small artery entering at right angle to the spinal cord.

Other mathematical studies have postulated peristaltic wave motion induced by pulsations [467]. A recent mathematical paper using two hydraulic network models investigated the effects of blood vessel pulsations on solute transport in the parenchyma and the perivascular space [432]. Increased pulsatility was shown to increase dispersion, not convection. A Peclet number in the perivascular space of $<10_3$ was calculated. Peak fluid velocity in the parenchyma and perivascular spaces increased with pulse amplitude and vessel size.

In Martin et al's (1.5.5.1.1) coupled spinal cardiovascular and CSF model, the authors assumed a high spinal SAS compliance, and mismatched arrival of arterial pulsations and CSF pulse waves [211]. They found perivascular flow of CSF into the spinal cord accounted for bulk fluid movement out of the parenchyma. Additionally, a reduction in SAS compliance was associated with greater perivascular flow into the spinal cord. The degree of perivascular flow fluctuations with compliance changes decreased from the cervical spinal cord to the lumbar region [211]. Other factors that modified the hydraulic resistance of the perivascular spaces included irregular spinal SAS or arterial geometry resulting from stenosis. Overall, the perivascular flow calculations represented predictions about egress and ingress of bulk fluid near the surface of cord but were based on many simplifications and assumptions [211].

1.5.5.2 Effect of respiration
1.5.5.2.1 In the subarachnoid space

Intrathoracic and CSF pressures are intimately linked [468-471]. This relationship can be modulated by postural changes, coughing, Valsalva, and abdominal pressure [284]. The epidural venous plexus and the dural venous sinuses transmit pressure changes from the abdomen to the SAS [211].

A respiratory influence on the CSF oscillations in the cerebral aqueduct has been established [284, 332, 334, 469, 472-474]. Yamada et al [332] studied normal adults employing a modified Time-SLIP MRI technique with single shot fast spin echo. Early deep inhalation was associated with cephalad movement of CSF in the ventricular system and in the prepontine cistern. During early exhalation, there was reverse flow. Breath holding was characterised by small rapid oscillatory movements of CSF [332]. Interestingly, the authors found that respiration had a much larger magnitude of effect on CSF movement than arterial pulsations. Similar findings were obtained recently by Chen et al [475] using simultaneous multi-slice EPI MRI. Reduced CSF velocity was recorded in the Sylvian fissure with little respiratory and cardiac motion present in smaller sulci in SAS [475]. Kao et al also showed using dynamic EPI that there were respiratory rhythms present near the ventricles, the SAS and the sagittal sinus [473].

New MR imaging techniques such as PBI, real-time simultaneous multi-slice EPI velocity phase contrast imaging, real-time gradient echo, and spin labelling have demonstrated that respiration has a major impact on CSF flow in the SAS [284, 332, 334, 476]. Recently, Dreha-Kulaczewski et al demonstrated in human subjects, using real-time PC-MRI, significant rostral movements of CSF at the beginning of forced inhalation. The inspiration-induced CSF wave was more prominent than that associated with cardiac pulsations, which were consistently low amplitude [284, 472]. This was observed both in the cervicothoracic spine and intracranially. Conversely, expiration demonstrated a

trend towards caudal movement of CSF, but this was variable. At the ROI examined they were able to quantify the net flow of CSF volumes rostrally. They also showed that there was concurrent caudal drainage of blood in the cervical epidural veins with rostral CSF flow, with greater venous flow corresponding to deep inspiration. Interestingly, spinal epidural veins and venous plexuses were found to be less affected by changing intrathoracic pressures than large neck veins that collapsed with inspiration. This phenomenon would maintain a constant intracranial volume as stipulated by the Monro Kellie doctrine. In a later high spatiotemporal resolution investigation of the entire vertebral column [477], this group again reported rostral movement of CSF with forced inspiration. However, forced expiration resulted in caudal flow from T6 (approximately the level of the heart) to the sacrum, and very low flows rostral to T1-4. The authors hypothesised that a "watershed" point at the level of the heart divided the spinal SAS into two compartments. They postulated that this binary pattern was a reflection of the intimacy of the intrathoracic and intraabdominal pressures, and the pressures within epidural venous plexus (transmitted via the large caval veins) that are thought to modulate CSF pressure. It has been long observed that above the heart, epidural venous pressure increased during expiration and decreased during inspiration. A criticism of the methodology in this study was that PC-MRI is a technique that employs cardiac cycle triggering to acquire and average images, potentially overlooking respiratory contribution of CSF flow [235]. However, Yildiz et al validated the accuracy of real-time PC-MRI in quantifying the contributions of cardiac and respiratory factors to CSF velocity at the foramen magnum. This group agreed that deep inhalation resulted in rostral movement of CSF, however, cardiac and respiratory components contributed equally to CSF velocity during deep breathing but not natural breathing. Cough was found to increase peak CSF velocity almost three-fold [333]. Takizawa et al [478] employed an asynchronous two dimensional PC-MRI technique under respiratory

guidance to separately analyse the respiratory and cardiac components of CSF flow in healthy adult brains. They observed larger CSF displacement secondary to respiratory events compared with cardiovascular impulses, although this gave rise to higher velocity flows. They provided quantitative evidence of small, rapid CSF pulsations due to cardiac drivers while respiration generated slow, large fluid waves. This was particularly evident in the cerebral aqueduct, but the effect was attenuated at the foramen magnum.

Bhadelia et al [334] studied eight patients using fast cine PC-MRI and two patients with PBI MRI to investigate the effects of Valsalva manoeuvres on CSF flow. CSF flow in the SAS between the foramen magnum and C2 decreased during Valsalva and exceeded the resting flow rate in the post-Valsalva period. These results were consistent with previous experiments in the 1980s performed by Williams who performed simultaneous invasive measurements of CSF pressure in the head and spine [468, 469]. Williams demonstrated that Valsalva retards the pressure wave from the head to the lumbar spine. PBI revealed a gradual reduction in pressure followed by a sharp rebound in pressure fluctuation amplitude at the end of the manoeuvre. Bhadelia and colleagues proposed that during Valsalva, high intrathoracic pressures are transmitted to the spinal SAS and consequently the epidural veins distend. There is a smaller concomitant rise in the ICP because the cardiac output is reduced. CSF flow across the foramen magnum is thus reduced due to the relative increase in spinal CSF pressure compared with ICP. Upon resumption of normal breathing intrathoracic pressure drops, collapsing the epidural veins which decreases the spinal SAS pressure. Cardiac output and ICP, however, rise, which promotes flow across the foramen magnum, resulting in the post-Valsalva rebound.

In a two dimensional PC-MRI study, Yiallourou and colleagues [479] found that application of a full-fitted continuous positive airway pressure mask (at 15 cmH_2O) in

young adult males resulted in reduced intracranial venous outflow (a decrease in pulse amplitude of jugular venous flow), as well as reduced stroke volume and pulse amplitude of CSF at C2/3. There were no changes to total cerebral blood flow characteristics. Expected reduction in cutaneously-measured changes in CO_2 levels did not correlate with CSF dynamics. An intriguing clinical study by Ju et al [480] reported diminished CSF Aβ (in addition to other neuronally derived proteins) in patients with obstructive sleep apnoea. The authors hypothesised that repeated intrathoracic pressure increases and elevated ICPs followed by sharp reversal attenuates CSF/ISF interactions, and therefore outflow of metabolites into the CSF.

1.5.5.2.2 *Perivascular effects*

There are very little data about the effects of respiration on fluid flow at a microscopic level. Recently, novel ultrafast MR encephalography [481] with synchronous electrophysiological monitoring was used to study pulsations propagating in the brain parenchyma. This technique enables three-dimensional imaging of the whole brain at 100 ms intervals and is free of cardiorespiratory aliasing and spin-history artefacts (that plague sequential 2D acquisitions due to bulk head motion across slices). Respiration evoked a MR encephalograhic pulse several times slower and lacked an inverted arterial initialisation of the cardiovascular impulse. It was found to begin from perivenular areas in the cortex and spread centripetally towards the centre. This was in contradistinction to the centrifugal pulse induced by arterial pulsations. A counter-pulsation mechanism was postulated to occur during the respiratory cycle [481]. The authors hypothesised that negative intrathoracic pressure associated with inspiration collapsed perivenular spaces, increasing fluid outflow from the CNS.

Smith and colleagues [424, 426], however, recently demonstrated that cardiac and respiratory pulsations contribute minimally to cerebral interstitial solute transport in

mice. Efflux of injected fluorescent dextran continued unimpeded for several minutes following cardiorespiratory arrest. Transport was only impaired after anoxic depolarisation and cell swelling.

1.5.5.3 Effect of other parameters

There is increasing interest in how different conscious states—that is awake, sleeping or anaesthetised—might affect fluid and solute transport into and out of the CNS. The Nedergaard group [482] proposed that the inflow of small tracers (3 kDa dextrans) into the brain is reduced in awake mice compared with those that are sleeping or have been anaesthetised with ketamine/xylazine. They hypothesised that the phenomenon could be explained by attenuated ECS volume and altered ISF ionic composition, which they measured using real-time iontophoresis. The authors attempted to consolidate this theory by demonstrating that mice in a lateral decubitus position, compared with those in prone or supine positions, exhibited elevated brain tracer efflux and influx (visualised with paramagnetic gadolinium contrast and fluorescent dextran). Gakuba et al [483], however, challenged these findings. The investigators injected gadolinium, Evan's blue and ICG intrathecally in awake mice and those anaesthetised with isoflurane, ketamine/xylazine, and ketamine. *In vivo* imaging with MRI and NIFR fluorescence demonstrated that there was reduced tracer influx in the anaesthetized group. This group hypothesised that the findings on tracer transport from the earlier study by Nedergaard and colleagues could be explained by other effects such as change in the configuration of the perivascular space or the glial endfeet. There has been some indirect experimental evidence suggesting that fluid and solute transport could be affected by other neurological events. Induction of cortical spreading depression (thought to be the instigator of migraine with aura) in mice has been shown to result in the rapid closure of the perivascular space around superficial arteries and veins using multiphoton intravital microscopy [484]. Moreover, there was reduced perivascular

efflux of intraparenchymally injected tracer. The authors hypothesised that the mechanisms underlying their observations could be AQP4 mediated astrocytic endfeet swelling as they did not detect any changes to the blood vessels *per se*. Ma et al [320] used NIFR fluorescence imaging to demonstrate that after an intraventricular infusion of a small tracer, mice that were allowed to wake had higher levels of the tracer in their systemic circulation than those anaesthetised with isoflurane and medetomidine. Tracer efflux was inversely correlated with perivascular deposition. This group posited that changes in respiratory and cardiovascular profile in awake animals (which were not measured in this study) as well as increased muscle activity resulted in greater clearance of the tracer, perhaps via a lymphatic route (which was also explored in *ex vivo* experiments in this paper). Clearly, more work is needed to resolve the conflicting results obtained from different imaging techniques and tracers.

Xu et al have recently proposed a novel theory in which occipitocervical musculature acts as CSF pumps via direct connections to the cervical dura (myodural bridges) [317]. In this study, human subjects were studied with PC-MRI and after one minute head rotations, there was increased CSF flow across the craniocervical junction. A predilection for direction of flow could not be established. Simultaneous Time-SLIP MRI measurements demonstrated CSF agitation in the lateral ventricles when subjects moved their heads.

Finally, ependymal cilia have been recently proposed as having a major influence on CSF flow adjacent to the ventricular wall in mice. Siyahhan and colleagues modeled CSF dynamics in the centre of ventricles and proposed that fluid was driven mainly by wall motion and choroid plexus pulsations [485].

1.6 Other fluid disorders of the central nervous system

A more complete understanding of normal fluid physiology in the CNS is critically relevant to a wide spectrum of clinical disorders. Syringomyelia is not the only disease characterised by abnormal fluid homeostasis. There are significant knowledge gaps in the pathophysiology of hydrocephalus, pseudotumour cerebri as well as brain and spinal cord oedema [486]. It is very likely that the interaction between ISF and CSF plays a large role in diverse conditions such as CNS tumour dissemination [487], trauma, stroke [488], multiple sclerosis, neurodegenerative diseases such as Alzheimer's disease [489], cerebral vasospasm and even sleep disorders [490]. Intrathecal drug delivery technologies are being developed based on this emerging field [491, 492].

1.6.1 Hydrocephalus

One of the most common, puzzling and debilitating Neurosurgical conditions, hydrocephalus has been recently defined as "an active distention of the ventricular system of the brain resulting from inadequate passage of CSF from its point of production within the ventricles to its point of resorption into systemic circulation" [493]. However, in light of recent mathematical modelling and laboratory experiments, hydrocephalus can no longer be considered merely an imbalance between production and absorption or an obstruction of CSF flow. The mechanics of the brain and fluid transport systems need to be considered. There is increasing recognition, for example, that CSF is able to flow across the ventricular ependymal layer into the brain interstitium when pressure in the ventricles increases [494-496]. This may manifest as periventricular oedema of the white matter, particularly in acute hydrocephalus in children and young animals [348]. Curiously, it has been observed that such oedema tends to spare grey matter [497]. Reduced production (through administration of acetazolamide) or diversion of CSF via shunting have been shown to reverse the degree of perivascular oedema [498]. It is not clear why compensatory mechanisms of fluid

drainage in the white matter are less robust than those in the grey matter. Like the spinal grey matter, cerebral grey matter is highly tortuous and vascularised, and could therefore have more numerous outflow pathways. How perivascular spaces contribute to these outflow pathways is still a subject of scrutiny, but there is evidence of transependymal flow into perivascular spaces [499].

The cause of ventriculomegaly is another contentious topic where old assumptions are being challenged by revived interest in brain and fluid mechanics. It was previously believed that if ventricular pulsatile ICP exceeded the ICP in the SAS over the cerebral convexity, ventricular expansion occurred. As the ventricles are in communication with the SAS, there is increasing doubt surrounding this concept of the "transmantle pressure gradient". Furthermore, this pressure gradient transgresses LaPlace's law. Ventriculomegaly might instead be contingent on factors such as resistance to fluid flow through the brain ECS and the inherent viscoelastic properties of brain tissue [500]. There is now significant interest in examining the dynamic relationship between blood flow, intracranial pulsatility and CSF flow as a mechanism of ventricular expansion, as a predictor for effectiveness of shunting and to explain why third ventriculostomies are inexplicably effective in conditions such as normal pressure hydrocephalus [488]. For a more detailed treatment of this nuanced condition, the reader is referred to numerous recent radiological, laboratory and computational studies that have challenged traditional paradigms [501-504].

1.6.2 Neurodegenerative disorders

The accumulation of Aβ plaques and neurofibrillary tangles of hyperphosphorylated tau protein is central to the pathogenesis of Alzheimer's disease [505]. Recent animal studies have focused much attention on the fluid pathways that might be involved in the clearance of Aβ. Two studies involving AQP4-knockout mice have demonstrated

reduction in the clearance of radiolabeled ^{125}I-Aβ and unlabeled Aβ from the brain parenchyma compared to wild type [327, 506]. Whether this effect was due to decreased outflow of ISF, impaired BBB transport, an intrinsic neuroprotective function provided by AQP4 has not been established. Although some human genetic studies on the role of APQ4 (and other proteins that potentiate fluid and solute transport) in Aβ metabolism have been conducted, genome-wide association studies are required. Further work on CSF/ISF dynamic imaging with corresponding *ex vivo* Aβ measurements may be necessary [505]. Ageing mice have been shown to exhibit reduced parenchymal clearance of tracers [507]. In similarly aged rodents with altered AQP4 expression and reduced arterial wall pulsatility, radiolabeled Aβ outflow was compromised [506]. These findings have not been reproduced in humans but are intriguing as they may partially explain accumulation of Aβ in the elderly population. Investigations into altered vascular compliance and fluid transport in animal models are urgently needed. Interest in AQP4 will yield more studies into ageing and neurodegeneration. AQP4 mislocalisation in the perivascular space has been observed to greater extent in elderly individuals with dementia compared with those who are cognitively intact in a post-mortem study [508]. A similar effect has been found in aged mice [488]. Finally, there is early evidence from murine studies that Aβ itself may be a cause of perivascular space fluid transport dysfunction. This would potentially instigate a feed-forward cycle where reduced clearance of Aβ results in increasingly attenuated ISF/CSF exchange and escalating levels of Aβ [509].

1.6.3 Traumatic brain injury

The Nedergaard [510] group demonstrated in mice that after traumatic brain injury with a controlled impactor, there was reduced tracer inflow and impaired clearance of intracortically injected radiotracers from the brain. This effect was observed for more than four weeks after injury. In AQP4-knockout mice, these effects were exacerbated,

resulting in accumulation of phosphorylated tau and axonal degeneration. These are mechanisms that are thought to contribute to cognitive decline after head injuries but have not been demonstrated in humans. Nevertheless, these changes have clear diagnostic as well as therapeutic implications. Transport of brain injury biomarkers to the circulation has been shown to be reduced in mice after head injuries, raising the possibility of a future diagnostic serum test [511].

1.7 Summary

There are still many questions surrounding the fundamental nature of CSF and ISF. Efforts to elucidate the fluid inflow and outflow pathways into the CNS, particularly via perivascular spaces, are escalating. Unresolved questions surrounding perivascular flow include its anatomical configuration (the role of vascular basement membranes), the direction of solute movement around arterioles and venules, the driving force of the perivascular flow (convection versus mixing), whether lymphatics play an important role in CSF outflow, and whether a net flow from arterioles to venules occurs (either through parenchyma or via capillaries, as proposed by the glymphatic model). The focus has, however, largely been on the brain. The literature on ISF dynamics is also comparatively sparse. Much of the recent research has come from computational modeling. Very few studies, laboratory or mathematical, have been conducted into the normal fluid pathways of the spinal cord, particularly concerning how fluid travels through and egresses from the cord.

In contrast to the ventricles, the spinal cord central canal is much smaller and encased in grey matter, while white matter forms the superficial layer [512]. Whether this reversed anatomical configuration affects transparenchymal flow [487] is unknown. It has been demonstrated that CSF flows from the SAS into perivascular spaces in the spinal cord central grey matter, and that there may be flow across the parenchyma to the central

canal [148]. With age, there is narrowing or occlusion of the central canal, so it is improbable all the fluid entering the spinal cord exits this small calibre channel [146].

There is growing recognition that the spinal thecal sac is a dynamic, pliable structure, and is highly responsive to intraabdominal and intrathoracic pressure fluctuations [292]. As recent MRI studies have intimated, the respiratory cycle exerts concomitant changes in the epidural venous network which may be responsible for significant fluid fluxes in the SAS. The effect of these transmitted thoracic pressures on perivascular flow remains unexplored. Arterial pulsations have been thought traditionally to be the driver of CSF flow, but there is still a lack of consensus from animal and mathematical models on its role in perivascular transport. The focus has almost entirely been directed towards the brain, while the spinal cord remains uncharted territory.

2 Aims and Hypotheses

There is an urgent need to elucidate the pathophysiology of syringomyelia and other fluid disorders in the CNS. Efforts to achieve this end have been hindered by an incomplete understanding of the fundamental details surrounding fluid physiology in and around the spinal cord. In an attempt to fill these gaps, the experimental work described here tested the following hypotheses:

1. Fluid outflow to the SAS is predominantly via a perivenular route in the grey and white matter of the spinal cord.

2. Increases in arterial pulse pressure and heart rate will increase perivascular flow into and out of the spinal cord.

3. Negative intrathoracic pressure will increase perivascular flow into and out of the spinal cord.

The aims are to:

1. Determine the fluid outflow pathways in the grey and white matter of the normal rat spinal cord.

2. Determine the effects of heart rate, blood pressure and respiration on fluid flow in and around the rat spinal cord.

3 Fluid outflow in the rat spinal cord: the role of perivascular and paravascular pathways

3.1 Abstract

3.1.1 Background

Cerebrospinal fluid (CSF) is thought to flow into the brain via perivascular spaces around arteries, where it mixes with interstitial fluid. The precise details concerning fluid outflow remain controversial. Although fluid dynamics have been studied in the brain, little is known about spinal cord fluid inflow and outflow. Understanding the normal fluid physiology of the spinal cord may give insight into the pathogenesis of spinal cord oedema and CSF disorders such as syringomyelia. We therefore aimed to determine the fluid outflow pathways in the rat spinal cord.

3.1.2 Methods

A fluorescent tracer, Alexa-Fluor®-647 Ovalbumin, was injected into the extracellular space of either the cervicothoracic lateral white matter or the grey matter in twenty-two Sprague Dawley rats over 250 s. The rats were sacrificed at 20 or 60 min post injection. Spinal cord segments were sectioned and labelled with vascular antibodies for immunohistochemistry.

3.1.3 Results

Fluorescent tracer was distributed over two to three spinal levels adjacent to the injection site. In grey matter injections, tracer spread radially into the white matter. In white matter injections, tracer was confined to and redistributed along the longitudinal axonal fibres. Tracer was conducted towards the pial and ependymal surfaces along vascular structures. There was accumulation of tracer around the adventitia of the intramedullary arteries, veins and capillaries, as well as the extramedullary vessels. A distinct layer of tracer was deposited in the internal basement membrane of the tunica media of arteries. In half the grey matter injections, tracer was detected in the central canal.

3.1.4 Conclusions

These results suggest that in the spinal cord interstitial fluid movement is modulated by tissue diffusivity of grey and white matter. The central canal, and the compartments around or within blood vessels appear to be dominant pathways for fluid drainage in these experiments. There may be regional variations in fluid outflow capacity due to vascular and other anatomical differences between the grey and white matter.

3.2 Keywords

Cerebrospinal fluid, outflow, spinal cord, syringomyelia, perivascular, interstitial fluid

3.3   Background

Details of the circulation of cerebrospinal fluid (CSF) and interstitial fluid (ISF) of the CNS remain controversial [249, 410]. In recent decades, the concept of CSF circulating through the brain parenchyma, as a mechanism for metabolite transport and clearance [230, 249, 351, 410], has gained momentum. ISF consists of water and solutes that are the by-products of cellular metabolism and synaptic transmission in the extracellular space. There may even be a component of ISF that passes across the brain capillary endothelium (although compelling in vivo evidence is contentious) [229, 349-352]. Perivascular spaces have received renewed interest as a crucial facilitator of fluid inflow in neural tissue [150, 327, 362, 427, 513]. If fluid can enter brain parenchyma, there must also be efflux pathways [230]. The assumption is that ISF must be cleared, probably into the SAS [381, 514], but the precise mechanism is unclear.

The "glymphatic" theory of fluid homeostasis posits that fluid flow into and out of the parenchyma is via arterial and venular pathways respectively [327, 459, 515]. Studies to date have largely focused on the brain, with few investigations of spinal cord. Although there is some evidence of similar mechanisms governing fluid ingress [146, 148, 309], how fluid egresses from the cord is almost unknown [380, 516]. Compared to the brain the spinal cord is not only much smaller, but the arrangement of the grey and white matter is reversed. Furthermore, spinal cord axonal tracts are oriented parallel to its long axis. These fundamental anatomical differences mean diffusion and transport of fluid in grey and white matter are likely to be different [230, 381, 517].

Syringomyelia is a puzzling condition where fluid filled cysts develop in the spinal cord, usually secondary to another pathology, such as trauma, that results in CSF obstruction in the SAS. There is emerging evidence that its pathogenesis is a dynamic process involving imbalances in fluid inflow and outflow. The important contribution of

perivascular spaces to mechanisms of fluid entry into syrinxes has been characterised in previous animal experiments [147, 148, 153]. Recent work [170] on fluid outflow pathways in an ovine model of post-traumatic syringomyelia indicated diffuse fluid movement away from the syrinx cavity and towards the central canal and perivascular spaces. However, the precise pathways of fluid drainage in the spinal cord under normal physiological conditions, and whether perivascular spaces play a crucial role in this context are unknown. A more complete understanding of the mechanisms governing spinal cord fluid homeostasis may lead to new insights into the pathogenesis of syringomyelia.

In this study, we aimed to determine the fluid outflow pathways in the rat spinal cord. We injected a CSF tracer, ovalbumin conjugated to the fluorophore Alexa-Fluor®-647 (AFO-647), into the spinal grey and white matter of Sprague-Dawley rats. Our hypotheses were: 1) fluid outflow from the spinal cord is via the perivenular spaces; and 2) the pattern of fluid flow in the white matter is different from that of grey matter.

3.4   Methods

Ethics approval was obtained from Macquarie University Animal Ethics Committee (ARA 2016/032–5). Outflow from the grey and white matter was separately investigated at two time points in 22 male Sprague Dawley rats, weighing from 155–345 g.

3.4.1   Surgical procedure

After induction of general anaesthesia with 4% isoflurane in oxygen, the animal was positioned prone in a stereotactic frame, and maintained under anaesthesia with 2.5% isoflurane (adjusted as necessary) in 0.2 L/min of oxygen. Heart rate, oxygen saturation, respiratory rate and rectal temperature were continuously recorded.

Under an operating microscope, a dorsal midline occipitocervical incision was made followed by subperiosteal muscle dissection. Segmental laminectomies at C7/T1 or

T1/T2 were performed with fine rongeurs. A window of thecal sac, eccentric to the right, was exposed. A 34G Nanofil needle, loaded onto a glass syringe (World Precision Instruments, Florida, USA), punctured the dura in a single pass. For grey matter studies, the entry point of the needle was 0.5 mm right of the midline at the C7/T1 interspace. For white matter studies the entry was at least 1 mm right of the midline at the T1/T2 interspace, where the grey matter is less prominent. The needle passed into the parenchyma to a depth of 1 mm targeting either the junction of the ventral and dorsal horns (for grey matter injections), or the lateral white matter funiculus. An Ultramicro pump (World Precision Instruments, Florida, USA) was used to deliver 500 nL of Ovalbumin Alexa-Fluor®-647 conjugate (Life Technologies, Victoria, Australia) with 10% fluorescent microspheres (v/v %) (Thermo Fisher Scientific, Massachusetts) at a rate of 2 nL/s. The needle was left in situ for either 20 or 60 mins. The animal then underwent transcardiac perfusion with heparinised 0.1 M phosphate buffered saline (PBS) followed by 4% paraformaldehyde (PFA) (Lancaster Synthesis, Pelham, New Hampshire).

3.4.2   Tissue processing

The spinal cord and brain were harvested en bloc for macroscopic fluorescent imaging. After post fixation in 4% PFA overnight, the specimen was stored in 30% sucrose for cryoprotection. The spinal cord was segmented from C2–T4. Each segment was snap frozen, and 40 μm axial sections were taken on a cryostat and mounted onto glass slides.

3.4.3   Immunohistochemistry

The glass slides were washed twice for 10 min in tris-phosphate buffered saline, and then in 50% ethanol for cellular permeabilization. After application of 15% normal donkey serum (NDS) blocking solution, the slides were incubated overnight with 1:100 Rat Endothelial Cell Antibody (RECA-1, Abcam, Cambridge, United Kingdom) in 4% NDS. The secondary antibody, 1:400 anti-mouse IgG Alexa-Fluor®-488 (Molecular Probes,

Life Technologies, New York, USA) was then applied. This was followed by anti-actin α-smooth muscle antibody at 1:400 dilution (SMA-Cy3, Sigma-Aldrich, St. Louis, Montana). Primary and secondary controls were established to exclude autofluorescence. The slides were cover-slipped with fluorescent mounting medium (DAKO, NSW, Australia).

3.4.4 Image acquisition

After post fixation, macroscopic white-light and single channel fluorescent images were captured with the In-Vivo MS FX PRO (Bruker, Billerica, MA). The fluorescence camera was set at excitation and emission wavelengths of 630 nm and 700 nm respectively, with an exposure time of 4 secs.

Spinal cord axial sections from C2–T4 were imaged with a Zeiss Axio Imager Z1 fluorescence microscope (Carl Zeiss Microimaging GmbH, Germany) for qualitative and quantitative analysis. The fluorescent microspheres were used to verify the location of the injection site. SMA- and RECA-1- positive vessels were identified as arterioles. SMA-negative, RECA-1-positive vessels were designated venules or capillaries. Those with largest diameter ≥ 6.5 μm were considered venules, and those < 6.5 μm capillaries. Further delineation of vascular and anatomical structures was undertaken with confocal microscopy (LSM 880, Carl Zeiss Microimaging GmbH, Germany).

3.4.5 Image analysis

Quantitative analysis of fluorescent signal intensity was performed using Image J, version 1.46r [518]. Subtraction of background fluorescence was performed in all measurements. In macroscopic fluorescent acquisitions, the spinal segment levels were identified by counting nerve roots on the white light images (Fig. 1a). These were then overlaid onto the fluorescence images. Mean pixel densities were measured in each spinal segment from C2–T4 to yield fluorescence intensities.

In fluorescent photomicrographs of axial sections, the integrated density of the CSF tracer (mean pixel density multiplied by area) was calculated. The mean pixel densities of the white and grey matter were measured separately. At least three sections were analysed per spinal level from C2–T4, and then averaged to give a mean integrated density.

3.4.6 Statistical analysis

Grey matter and white matter integrated densities were compared using two-way analysis of variance (ANOVA) and adjusted for multiple comparison using Bonferroni's post-hoc tests (GraphPad Prism v7.02, GraphPad Software Inc, California). A p value < 0.05 was considered statistically significant. All values were expressed as mean ± standard error of the mean (SEM).
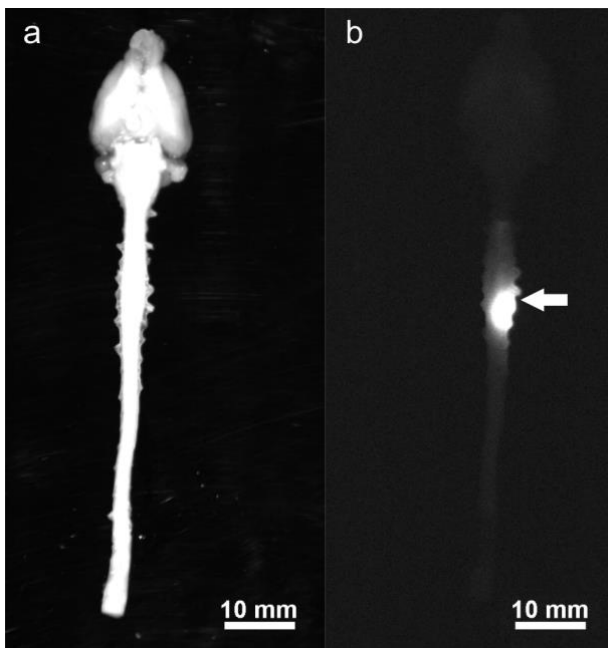
Fig. 6 White light and single fluorescence channel acquisition of harvested brain and spinal cord with the In-Vivo MS FX PRO Multispectral Imager System. Brightness and contrast have been uniformly adjusted for optimal visualisation. **a** White light enabled spinal level localisation. **b** Macroscopic appearance of tracer distribution. There is a sharp drop off in fluorescence intensity within 1-2 spinal levels rostral and caudal to injection site at C7/8 (arrow)

3.5　Results

3.5.1　Rostral-caudal tracer distribution

In macroscopic fluorescent imaging, CSF tracer was observed to be localised to the injection site in all experiments (**Fig. 6**b). The macroscopic mean fluorescence intensity was determined for each spinal cord level. A sharp drop-off in intensity within two levels rostral and caudal to the injection site was observed (**Fig. 7**). At the 60 min time point, but not at the 20 min time point, the cord had significantly higher mean fluorescence intensities after white matter injections (WMi) compared to grey matter injections (GMi) (p = 0.0026). On post hoc analysis, significance was reached one and two levels rostral to the injection point (p = 0.045 and 0.026 respectively) (**Fig. 7**b). Post hoc analysis also demonstrated a significant difference between white and grey matter injections at the 20 min time point one level caudal to the injection site (p = 0.034) (**Fig. 7**a).
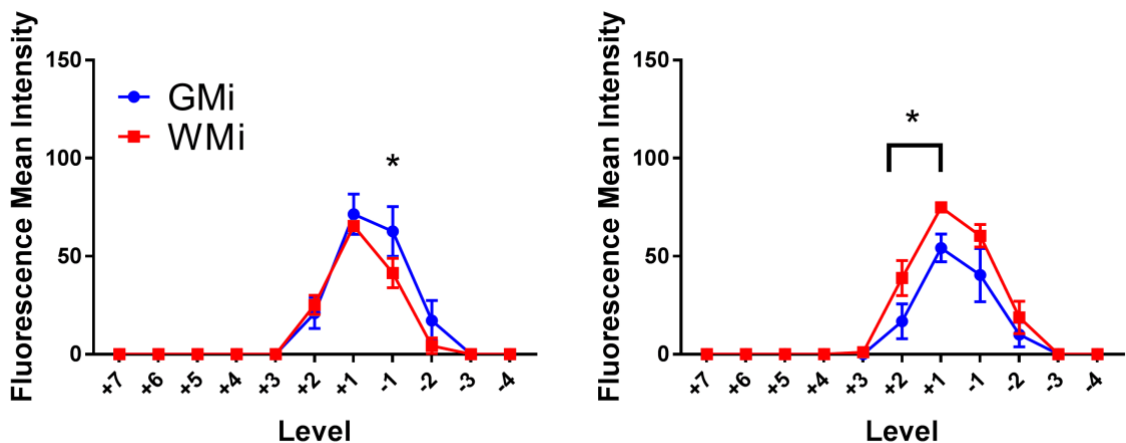
Fig. 7 Quantification of CSF tracer fluorescence per spinal level. Each spinal cord level ("Level") is expressed as the number of levels rostral (positive integers) or caudal (negative integers) to injection site. All error bars are expressed as ±SEM. Macroscopic analysis of of mean fluorescence intensity versus spinal cord level in grey (n=10) and white (n=10) matter injections at **a** 20 mins and at **b** 60 mins. In both white and grey matter injections at both time points, there was a sharp drop off of tracer fluorescence within 2 levels rostral and caudad to the injection. At the 20 min time point **a**, there was no difference in fluorescence intensity between white and grey matter injections, but on post hoc analysis a significant difference was reached at -1 level caudal to the injection site (* p = 0.0341). At the 60 min time point **b**, fluorescence intensity was significantly higher in the white matter injections compared to the grey matter injections (p = 0.0026). On post hoc analysis significant differences were observed at +1 and +2 levels rostral to the injection point (* p = 0.0448 and 0.0259 respectively)
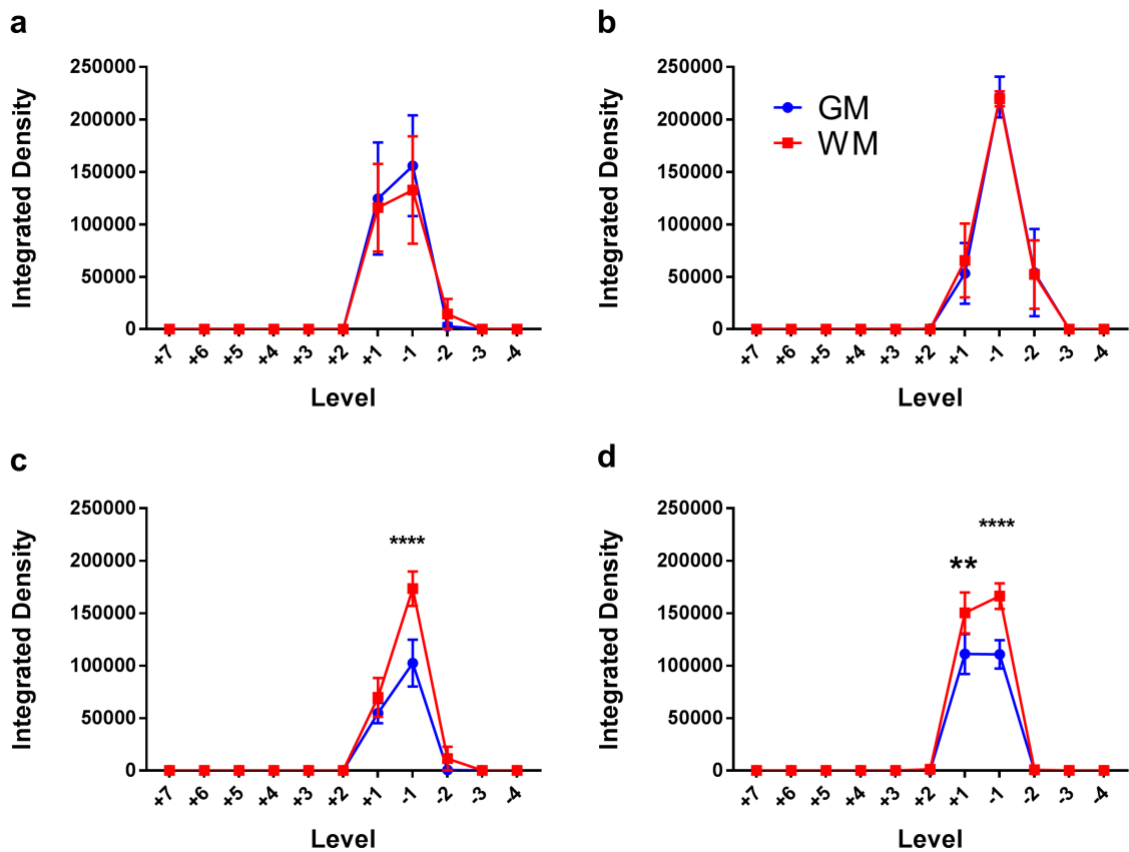
Fig. 8 Quantification of CSF tracer fluorescence (integrated density) per spinal level. Each spinal cord level ("Level") is expressed as the number of levels rostral (positive integers) or caudal (negative integers) to injection site. All error bars are expressed as ±SEM. Microscopic analysis of axial sections after grey and white matter injections. **a** After grey matter injections at 20 mins (n=5) there was no statistical difference between grey and white matter fluorescence. **b** This was also observed in grey matter injections after 60 mins (n=5). However, after white matter injections at **c** 20 mins (n=5) and at **d** 60 mins (n=5), there was significantly greater tracer fluorescence in the white matter compared to the grey matter (p = 0.0094 and 0.0041 for 20 mins and 60 mins respectively). On post hoc analysis, a statistically significant difference was observed at one level caudal to the injection site (*** p < 0.0001) at 20 mins **c**, and one level rostral and caudal at 60 mins **d** (** p = 0.0017, **** p < 0.0001)

3.5.2   Axial tracer distribution

Quantification of AFO-647 intensity from microscopic analysis of axial sections is summarised in **Fig. 8**a–d. The fluorescence intensity within the grey and white matter, expressed as integrated density, is represented in relation to spinal level at the 20 and 60 min time points separately. After white matter injections, at both 20 and 60 mins, fluorescence was significantly greater in the white matter compared to grey matter (p = 0.0094 and 0.0041 for 20 mins and 60 mins respectively) (**Fig. 8**c, d). On post-hoc analysis, at the 20 min time point, a significant difference was observed at one level caudal to the injection site (p < 0.0001). At 60 mins, white matter fluorescence was

112

found to be significantly greater one level rostrally (p = 0.0017) and caudally (p < 0.0001). Following grey matter injections, however, tracer fluorescence was not significantly different between grey and white matter, at either time point (**Fig.** *8*a, b).

3.5.2.1 Pattern of tracer distribution: grey matter injections

In six of 12 animals, tracer was delivered to the junction of the ventral and dorsal horns. There was a continuous radial decrease in fluorescence intensity in all directions away from the injection site. Tracer signal was detected in the white matter surrounding the grey matter at the injection level (**Fig.** *9*e). In rostral and caudal axial sections, CSF tracer was detected predominantly in the grey matter.

In the other six animals, tracer was delivered into either the middle of the ventral or dorsal horn, and although the highest fluorescence intensity was found within the grey matter, there was substantial tracer signal in the adjacent white matter. In rostral and caudal sections there was prominent tracer signal in the white matter (**Fig.** *9*f). In all but one animal, tracer was detected in the contralateral grey matter.

3.5.2.2 Pattern of tracer distribution: white matter injections

In eight of 10 animals the distribution of AFO-647 conformed to the shape of the lateral funiculus, staying primarily in the white matter (**Fig.** *9*g). A radial reduction in tracer fluorescence was also observed. A small amount of tracer entered the lateral horn of the grey matter. Rostrocaudally, ovalbumin was almost exclusively found in the white matter (**Fig.** *9*h). Within this subgroup of animals, no tracer was detected in the contralateral grey matter except in one animal.

In two of 10 animals, there was a similar pattern of tracer spread in the white matter but considerable ovalbumin also redistributed into the grey matter. Rostrocaudally, however, tracer was confined to the white matter.

3.5.2.3 Tracer in relation to vascular structures

In all animals CSF tracer accumulated around the walls of arterioles, venules and capillaries in both the grey and white matter (**Fig. 10**, **Fig. 11**g). Arterioles were more numerous in the grey matter than the white matter (**Fig. 9**d). Selective tracer labelling of vascular structures was particularly evident in areas of low background tracer concentration (**Fig. 10**a, d). In the white matter, tracer concentrated along arterioles and venules that extended from the grey matter to the pia (**Fig. 10**d).

CSF tracer co-localised with arterioles and venules of the ventral median fissure in all but one animal (a white matter injection, sacrificed at 20 mins) (**Fig. 10**d, f, h). Tracer was present in the wall of the anterior spinal artery (ASA) and its central branch in 10 animals (**Fig. 10**d), of which nine were grey matter injections. Fluorescence was further present in the walls of the arterial vasocorona in 13 animals (**Fig. 11**d–f), of which 10 were white matter injections. Confocal microscopy demonstrated tracer deposition external to the smooth muscle layer of the ASA. Additionally, there was a distinct layer of tracer between the endothelial and smooth muscle layers (**Fig. 10**e). This pattern of tracer distribution was also observed in parenchymal arterioles and other extramedullary arteries, such as the central branch of the ASA and the arterial vasocorona. AFO-647 was discretely deposited external to the endothelial layer of capillaries and venules of the cord parenchyma (**Fig. 10**h, i and **Fig. 11**g).

In at least six animals (two from white matter injections), tracer deposited prominently around "remote" arterioles (**Fig. 10**f, g). These labelled vessels were far removed from the bulk of the contiguous tracer at the injection site. Tracer labelling of the pia and subpial space was generally limited or absent as fluorescence intensity decreased from the site of injection towards the cord surface. Instead, ovalbumin concentrated around vessels that traversed the cord parenchyma towards the pial surface. Tracer appeared to be

transported from the injection site to the extramedullary vasculature (**Fig. *11*i**), along these conduit-like arterioles and venules.

3.5.2.4   Central canal

CSF tracer was detected in the central canal ependymal cell layer in six of 12 grey matter injections. In three animals, central canal tracer fluorescence was present in at least eight contiguous spinal levels, rostral to the injection site. Furthermore, tracer was observed within the lumen of the canal, confirmed by confocal microscopy. The bordering layer of ependymal cells was heterogeneously delineated by fluorescence. Nuclear labelling by tracer was absent. The apical ends displayed greater tracer intensity compared to the basal surface (**Fig. *11*a–c**). In two animals, central canal ependymal tracer was detected rostrally over only 2 spinal levels. In one animal, tracer extended caudally only from T1—T4. No tracer was found in the central canal in any of the white matter injection animals.
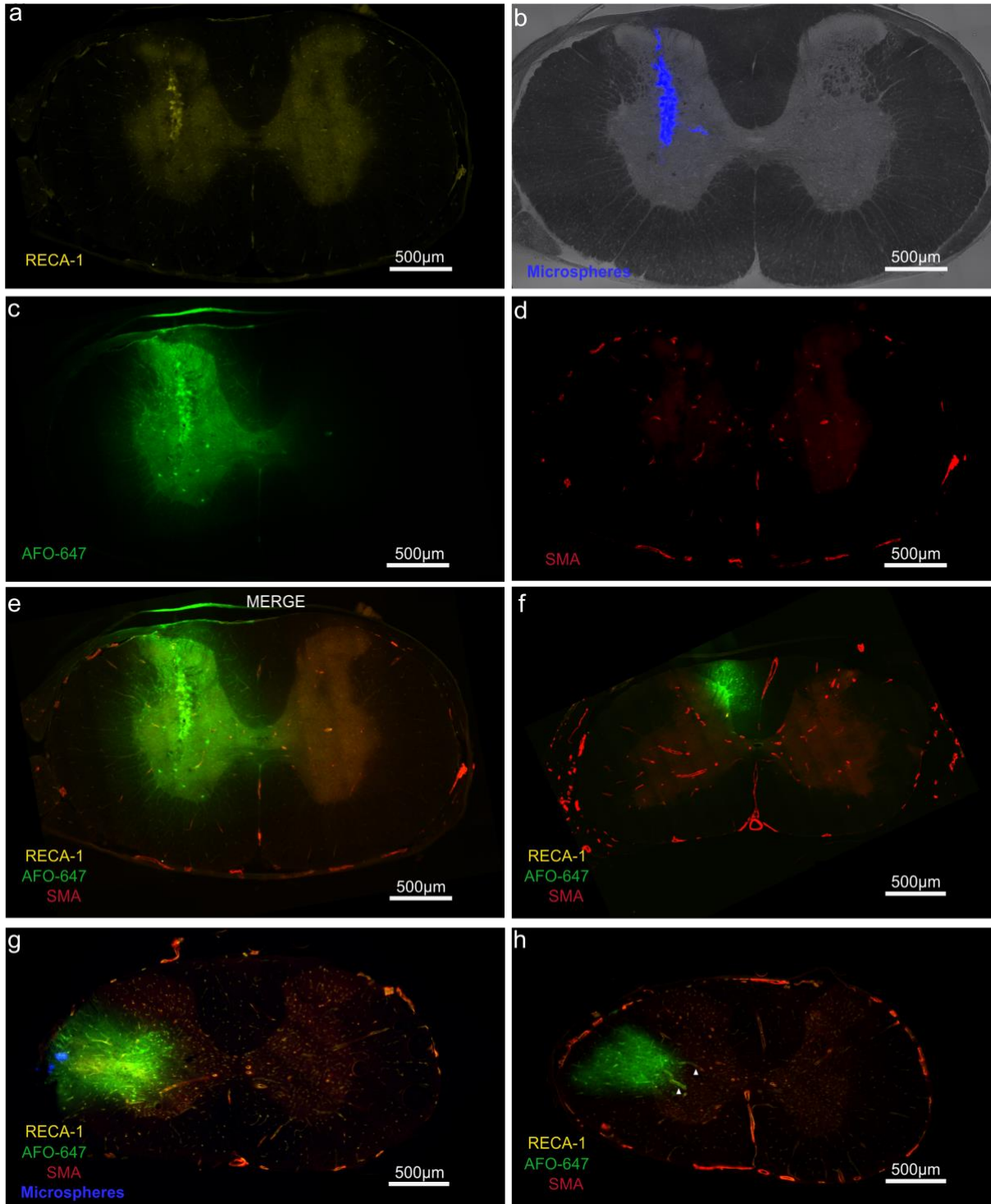
Fig. 9 Typical axial sections at the cervicothoracic junction after injection of fluorescent CSF tracer into the spinal grey and white matter. **a–e** Grey matter injection. **a** RECA-1 and **d** SMA immunofluorescent staining of arterioles, which were present in greater numbers in the grey matter compared to white matter. **b** Fluorescent microspheres confirmed the Nanofil needle had traversed the grey matter. **c, e** Radial redistribution of tracer from the middle of the grey matter in all directions. **f** Axial section rostral to a grey matter injection site where a significant amount of tracer had spread into dorsal column. Note tracer fluorescence was mainly confined to the dorsal white matter column at this level. **g** After delivery into the white matter, AFO-647 tracer conformed to the shape of the lateral funiculus with limited spread into the grey matter. **h** In rostral sections in the same animal, tracer was confined to the white matter. Arrow heads demonstrating selective tracer deposition around arterioles. All fluorescent photomicrographs were taken at x20 magnification
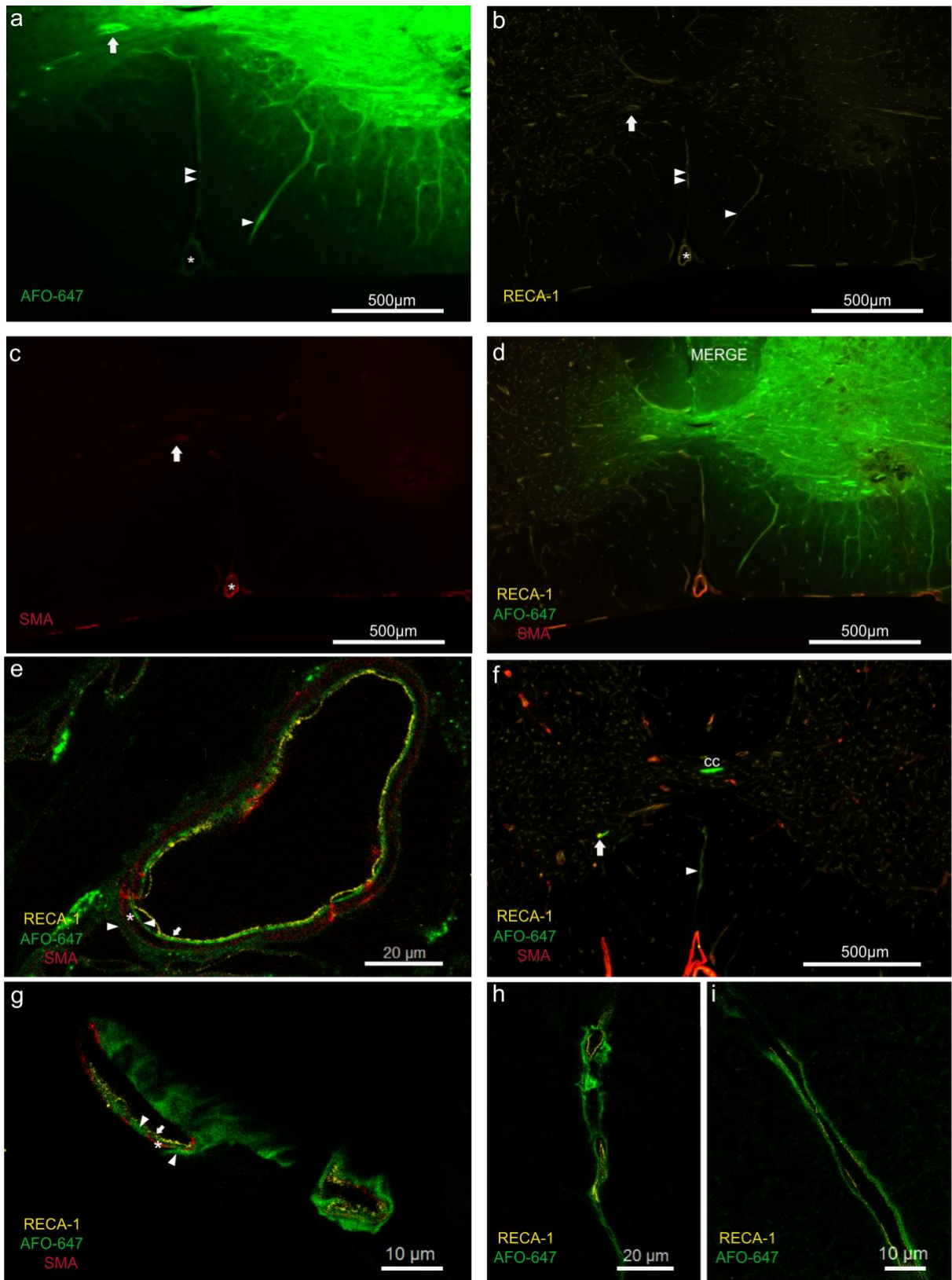
Fig. 10 Relationship of injected CSF tracer to vascular structures. **a–d** Fluorescent microscopy of grey matter injection. Tracer co-localised with the wall of the anterior spinal artery (ASA) (*). A radially directed venule (single arrow head) and veins (note RECA-1 positive and SMA negative) in the ventral median sulcus (double arrow heads) appeared to conduct ovalbumin away from the injection site towards the pial surface. Prominent accumulation of tracer around an arteriole (marked by arrow) against a relatively low background fluorescence suggests it is a pathway for fluid outflow. **e** Confocal photomicrograph of the ASA found in **d**. A layer of AFO-647 tracer (indicated by right pointing arrow head) was detected external to the tunica media (SMA positive,

indicated by *). Another distinct layer of CSF tracer was also found internal to the tunica media layer (left pointing arrow head), separate from the endothelial layer (RECA-1, marked by arrow). **f** Pronounced tracer deposition around a "remote" arteriole (arrow) and vein in the ventral median sulcus (arrow head). These vessels were one level rostral to the grey matter injection site, and therefore tracer accumulation around these structures could not be explained by contiguous tracer spread. It is likely ovalbumin was transported over a distance in the spaces around these vessels. Note tracer labelling of the central canal (indicated by "cc"). **g** "Peri- and para-arterial" pattern of tracer deposition in specific compartments external and internal to the tunica media of parenchymal arterioles (arrow heads, arrow and * denote the same anatomical layers as in **e**). **h** Tracer accumulation between the adventitia and the glia limitans of veins in the ventral median sulcus (found in **f**). **i** The same "para-venular" pattern demonstrated in a radially directed parenchymal venule, found in **d**. All fluorescent and confocal photomicrographs were taken at x20 and x63 magnification respectively

3.5.3 Effect of time

Fig. *12*a–d compares CSF tracer fluorescence intensity (derived from axial microscopic photomicrographs) in both the white and grey matter at the 20 min time point to that of the 60 min group. There was no statistically significant difference in the grey matter fluorescence intensities between the two time points after either grey or white matter injection (**Fig. *12*a, b**). However, on post-hoc analysis significantly greater grey matter fluorescence was observed at one spinal level rostral to the white matter injection site after 60 mins compared to 20 min (p < 0.0001). There was no overall significant difference in the white matter fluorescence intensities between the two time points after either grey or white matter injections. Post hoc analyses demonstrated significantly higher white matter fluorescence at 60 mins compared to 20 mins at one level caudal (p = 0.009) and one level rostral (p < 0.0001) to the injection site following grey matter and white matter injections respectively (**Fig. *12*c, d**). At the longer time point, it appeared that after white matter injections there was greater redistribution of tracer from the white matter into the grey matter, and also along white matter tracts rostrally. After grey matter injections, there also appeared to be greater tracer spread into the lateral white matter caudally with time.
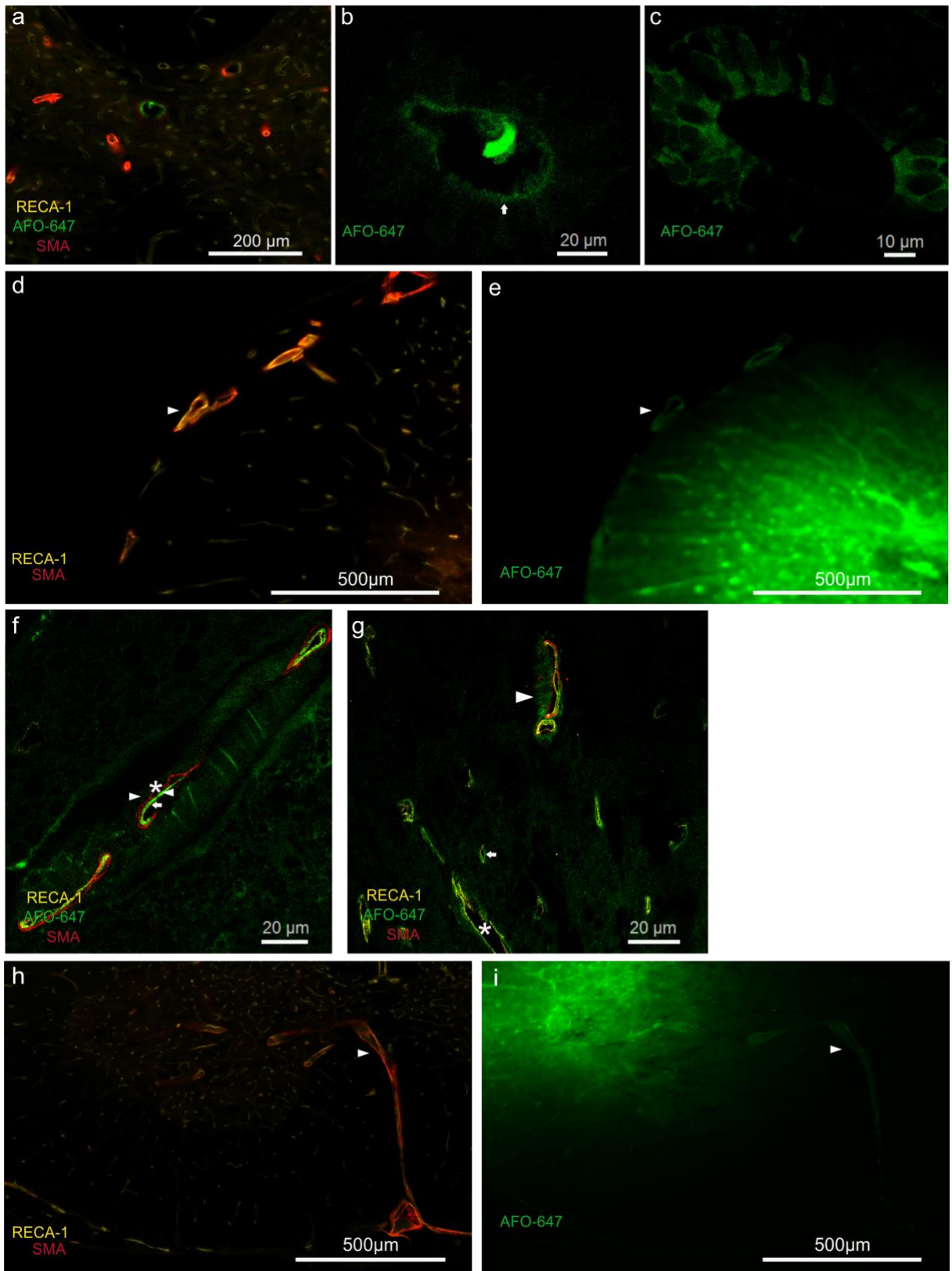
Fig. 11 CSF tracer delivered into the spinal cord parenchyma accumulated around ependymal and extramedullary structures. **a–c** Fluorescent (**a**) and confocal (**b**) micrographs demonstrating tracer accumulation in the central canal. Note the presence of tracer within the lumen in **b** (12 o'clock position). **c** Confocal microscopy of central canal in another experiment. The ependymal cells were heterogeneously delineated by fluorescence, with the noted absence of nuclear tracer signal. In both **b** and **c**, the apical ends displayed greater tracer intensity compared to the basal surface. **d, e** Tracer deposition around the arterial vasocorona (arrow heads, note RECA-1 and SMA positivity) of the dorsal spinal cord surface. **f** Confocal microscopy view of the same arterial vasocorona

demonstrating the characteristic "peri-arterial" and "para-arterial" distribution of the tracer (arrow heads) with respect to the tunica media (*) and endothelium (arrow). The absence of subpial tracer signal excludes the possibility of contiguous tracer spread from injection site to artery. The arterial vasocorona could be the dominant pathway for fluid outflow from the white matter. **g** Fluid outflow appeared to involve all vascular structures. Confocal microscopy of grey matter showing arteriolar (arrow head), venular (*) and capillary (arrow) labelling by tracer. Note the "paravascular" location of tracer in venules and capillaries. **h-i** Fluorescent microscopy of grey matter injection demonstrating conduction of tracer along the central branch of the anterior spinal artery towards the ventral median fissure. This suggests drainage of interstitial fluid towards the pial surface via vascular structures. All fluorescent and confocal photomicrographs were taken at x20 and x63 magnification respectively
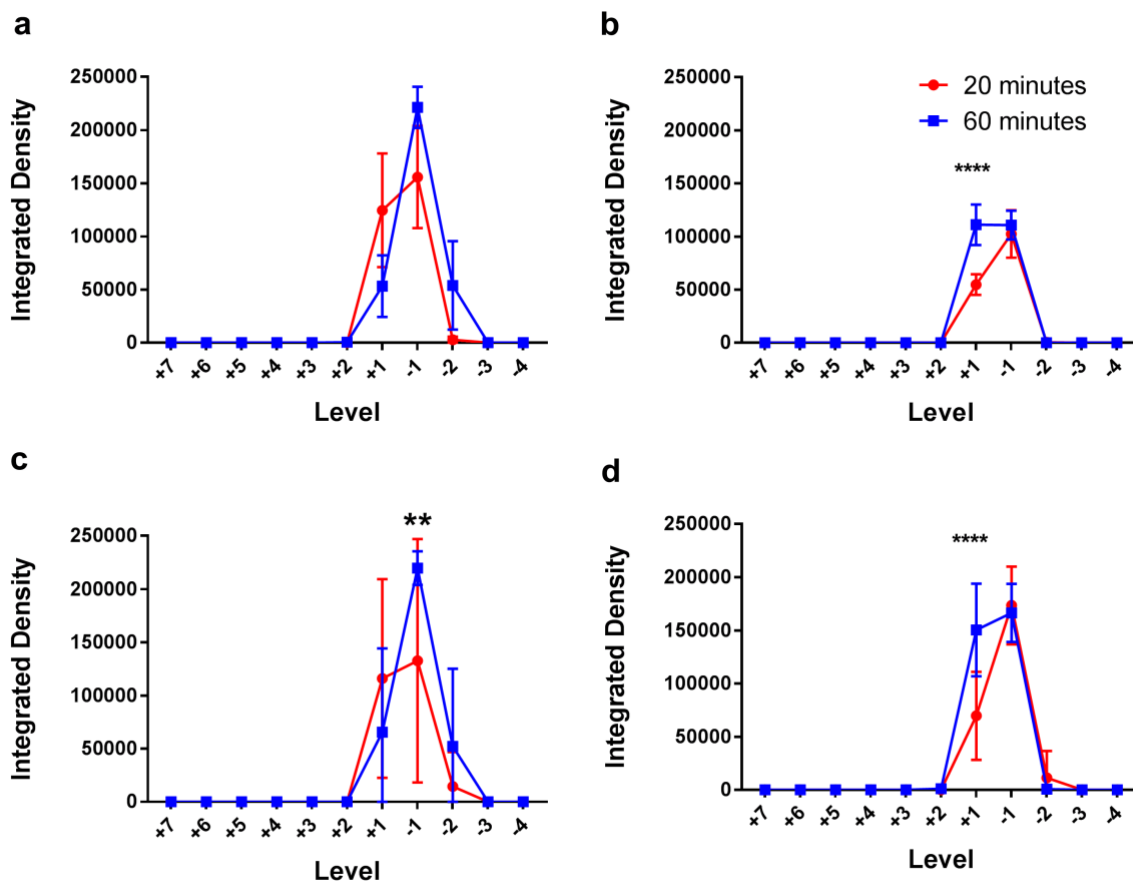
Fig. 12 Comparison of CSF tracer fluorescence (integrated density) in axial sections at the 20 and 60 min time points per spinal level to assess the effect of time on tracer distribution. Each spinal cord level ("Level") is expressed as the number of levels rostral (positive integers) or caudal (negative integers) to injection site. All error bars are expressed as SEM. **a** After grey matter injections, no statistical significant difference between the time points was observed in the fluorescence intensity in the grey matter. **b** Following injection of tracer in the white matter, no statistically significant difference was observed between the 20 min and 60 min groups in the grey matter. However, on post hoc analysis there was significantly greater fluorescence at +1 level rostral to the injection site after 60 mins (**** $p < 0.0001$). Similarly, after both **c** grey matter injections and **d** white matter injections, there was no overall statistical significant difference between the 20 min and 60 min groups in the white matter. However, post hoc analysis demonstrated greater integrated densities at 60 mins (compared to 20 mins) - 1 level caudal (** $p = 0.009$) and +1 level rostral (**** $p < 0.0001$) to the injection site in **c** grey matter and **d** white matter injections respectively

3.6   Discussion

In this study, the distribution of CSF tracer up to 60 mins after injection into the spinal

cord interstitium was limited to the adjacent two to three spinal cord levels. Tracer was

distributed in a radial pattern after delivery into the grey matter, with dissemination

into white matter. The absence of statistically significant differences between tracer fluorescence intensities of the grey and white matter after grey matter injections **Fig. *8***a, b) is consistent with this observation. However, there was limited redistribution of tracer from white into grey matter after white matter injections. The statistically significant differences between grey and white matter tracer fluorescence intensities after white matter injections support this observation. There was some evidence these patterns were amplified over time. Greater spread of tracer along white matter tracts longitudinally was also observed. There was prominent labelling of all vascular structures by AFO-647. Tracer appeared to be conducted away from the injection site towards the pial surface by depositing around radially projecting arterioles and venules. Support for this inference was provided by the detection of tracer fluorescence around extramedullary vessels. This finding was unlikely to have been secondary to diffusion (or other means of contiguous solute transport such as bulk flow) of tracer because of the general absence of subpial fluorescence (**Fig. *11***e, i), particularly after grey matter injections. Further microscopic analysis revealed accumulation of ovalbumin both in the perivascular and paravascular spaces of arterial vessels, which will be discussed below.

Although it was not possible in this study to conclude whether diffusion or bulk flow governed interstitial tracer movement, our findings are in concordance with theoretical and animal models of spinal ISF movement. Confinement of tracer to white matter tracts is characteristic of anisotropic diffusion, well described in the literature on CNS diffusion tensor imaging [517], and has been confirmed in the developing rat spinal cord in ex vivo experiments [382, 519]. Here, fluid diffuses along, and is constrained by, myelinated white matter fibres that run parallel to its long axis. The unmyelinated grey matter, however, is the site of penetrating arteries and its extracellular space (ECS) is rich with somas and neurites that have no preferential orientation. Diffusion here is

isotropic which may explain why in our experiments tracer in the grey matter was able to redistribute in all directions. Convection enhanced delivery (CED) studies in animal spinal cord have yielded similar findings of anisotropic movement of ligands through the white matter tracts [386, 387]. Endo et al [380], employing Evan's blue tracer, observed comparable results to ours but described almost no tracer penetration into grey matter after white matter injections. Moreover, Evan's blue tracer was redistributed further rostrocaudally from the injection site in the white matter compared to the grey matter. These differences could be secondary to the larger delivered volume of tracer (2 μL) in their experiments, and the smaller molecular size of Evan's blue compared to ovalbumin. Like other CED models and earlier ex vivo work on spinal cord ISF movement [381-387], in Endo's study a large durotomy was performed, resulting in substantial CSF leak and altered hydraulic integrity of the SAS and perivascular spaces, which may in turn alter fluid inflow dynamics. Computational simulation of the rat spinal cord by Sarntinoranont et al [520] yielded a lower hydraulic conductivity in the grey matter and thus increased tissue resistance. They showed that diffusion of macromolecules *through* ECS is limited by tortuosity (higher in grey matter) and efficacy of diffusion diminishes as the square of distance. Diffusion *along* ECS is unaffected by these factors [410, 521]. This would account for the greater penetration of CSF tracer from grey to white matter (compared to white to grey matter) in this study, and the higher fluorescence signal rostral to the injection site observed at 60 mins in white matter injections (**Fig. 7**b). It may also explain the apparent increase in white matter fluorescence after white matter injections at 60 mins compared to 20 mins, and the absence of this in the grey matter after delivery of tracer into the grey matter (**Fig. 12**a, d).

3.6.1 Perivascular clearance

Various authors have used the terms "Virchow-Robin space", "perivascular space" and "paravascular space" interchangeably, but also at times to refer to discrete anatomical

compartments. A comprehensive review of the ultrastructure of the "perivascular" space is beyond the scope of this article, but readers are referred to excellent treatises by Bakker et al [411] and others [230, 403, 522]. For our purposes, we distinguish the "peri-arterial space", which consists of multiple compartments within the pial sheath that accompanies the arteriole/artery as it enters the CNS parenchyma, from the "para-arterial space". The latter is the space formed by the glia limitans and the pial sheath of the penetrating artery. The "para-venular space" is formed by the venular adventitia and the glia limitans. Collectively the "para-arterial" and paravenular" spaces form the paravascular compartment. Henceforth, "perivascular space" loosely refers to all the compartments between vessel and glia limitans. These descriptions have been derived from brain studies [230, 249, 403, 411]. Ultrastructural studies of the rat spinal perivascular space suggest similar anatomy [523].

There is compelling evidence from our study supporting the importance of the vascular basement membrane in fluid outflow in the spinal cord. Controversy still surrounds the relationship of CSF, ISF and perivascular flow in the brain. There are two prominent contemporary theories of brain perivascular flow — the "glymphatic" system [327] and a vascular basement membrane model [427]. The former was borne out of experiments on transgenic mice where intraventricular, intracerebral, and intracisternal injections of CSF tracers established CSF inflow into brain via a "para-arterial" route, bulk interstitial flow, and "para-venous" outflow. Other groups later raised concerns regarding the methodology and interpretation of observations [229, 230, 249, 351, 376, 423]. The Carare-Weller group has long promulgated that fluid influx is via the para-arterial space and clearance of solutes and ISF occurs via the "peri-arterial" vascular basement membrane found within the tunica media. Their model has been backed by experiments from their own laboratory [403, 427-429] and from other groups employing intravital

multiphoton microscopy [430]. They also assert that at the level of the capillaries, there is adjacent bidirectional flow of fluid, with inflow occurring adjacent to the glia limitans, and outflow of ISF occurring next to the endothelium. Notably, there is no venular involvement in fluid transport. The major points of dissent are: 1) the types of vascular structure(s) that are involved in ISF and solute egress; and 2) the precise relationship of the outflowing fluid to the various compartments surrounding these vessels. In this study, confocal microscopy demonstrated the presence of tracer not only in the "para-arterial" and "paravenular" spaces, but also in the "peri-arterial" compartment. It appeared that arterioles, venules and even capillaries are implicated in fluid outflow, and hence elements of both dominant theories (that are based on brain studies) have relevance in the spinal cord. Moreover, the vascular basement membrane (as proposed by Carare-Weller) has been shown here to play an important role in solute clearance in the spinal cord, which in turn suggests ISF outflow occurs both within *and* outside the wall of the arteriole. While injection pump pressure could confound our interpretation of interstitial perivascular tracer deposition, it is unlikely to explain tracer accumulation around only some extramedullary vessels and "remote" arterioles that are far removed from the bulk of the tracer. Moreover, our infusion rate of 0.12 µL/min is lower than that employed by other groups [230, 524], and thus is unlikely to alter the physiological drainage pathways. Uniform perivascular distribution of tracer around the spinal pial surface, which has been previously observed following cisterna magna injections [309, 523], was not detected in our experiments. Therefore, accidental delivery of tracer into the subarachnoid space is highly improbable.

Our findings raise the possibility of a model of spinal perivascular fluid dynamics characterised by rapid bidirectional movement. Some authors have suggested that there is little or no directed net fluid displacement in the perivascular space, a concept that

aligns with earlier experimental data [249, 422]. A recent mathematical modelling study proposed that although there might be fast water movement to-and-fro in the perivascular space, solute transfer is facilitated by advection or dispersion [423]. Dispersion is in turn driven by arterial pulsations, which authors of disparate theories can all agree underlie the mechanism of perivascular flow [146, 427, 459, 463]. Additionally, solutes may freely communicate between the "para-arterial space" and the "peri-arterial" space through porous barriers that have been confirmed in ultrastructural studies of the spinal cord [249, 522, 523]. If this "convection" [230] theory of bidirectional fluid displacement also applies to the "para-venous" space, then tracer molecules injected into the cord parenchyma would disperse along both arteriolar and venular pathways by way of the capillaries [427]. Initially, there is "peri-arterial" drainage of solutes via the vascular basement membrane, but tracer is then able to infiltrate the "para-arterial" space. As pulsations are much stronger in arteries, tracer is propelled further along arterioles (towards the extramedullary arteries) compared to venules. This is reflected in the preponderance of tracer around extramedullary arteries and "remote" arterioles. However, we would also expect greater "paravenular" tracer deposition at 60 mins compared to 20 mins. This was, however, not observed, challenging this conjecture on perivascular fluid outflow. Future studies would mandate longer time points to investigate paravenular tracer distribution.

3.6.2   Central Canal

Central canal labelling by tracer was detected in 50% of grey matter injection experiments, with a predilection for rostral migration. This corresponds to the earlier observation by Milhorat [516] of cephalad flow within the central canal, which gave rise to the theory that it acts as a "sink" for excess solutes and fluid from the cord interstitium. Previous work by the Stoodley group and others has indicated that the central canal is a route of clearance in normal and injured rat and ovine cords [146-148,

153, 170, 264, 309, 525]. Bedussi et al have suggested that in the brain, ISF drains preferentially towards the ependymal surface. However, this was only true in close proximity to the ependymal lining and the effect decreased away from the ventricles [514]. In the spinal cord the distance between the ependymal and pial surfaces is much smaller, so the relevance of this hypothesis is unclear. A more likely explanation for the disparate central canal labelling between grey and white matter injected animals is that diffusivity differences (which in turn are dependent on factors such as tortuosity and distance) at the grey/white matter junction result in the central canal playing a critical role in fluid outflow from the grey matter. It was not possible to clarify, based on confocal micrographs, whether tracer migration into the central canal was transcellular, paracellular or both. Further ultrastructural studies may address this.

3.6.3 Clinical Relevance

Although outflow pathways involve all vascular structures, there may be regional variations. In the spinal grey matter, there is prominent drainage of solutes and ISF via the ramifying arteries from the ventral median sulcus, as well as into the central canal. In the white matter, outflow efficiency may differ as there are fewer arterioles, and greater reliance on the smaller arterial vasocorona. Extra-canalicular syringomyelia (a consequence of spinal cord injuries) may be partly precipitated by pathological processes disproportionately compromising ISF drainage via white matter perivascular spaces. Outflow is unable to keep up with fluid influx, ultimately leading to fluid accumulation. Similarly, this may partially explain why spinal cord oedema preferentially follows white matter tracts, as in the grey matter there may be more robust drainage pathways.

3.6.4 Limitations

As some authors have emphasized [327] that for maintenance of perivascular bulk flow the hydraulic parameters of the subarachnoid and perivascular spaces cannot be

compromised. Although CSF losses were not observed during injections in this study, small leaks cannot be ruled out and may account for the relatively limited longitudinal displacement of ovalbumin, and the absence of statistical significance in tracer redistribution between 20 and 60 mins. Other groups have noted that in CED studies, spinal cord injury results in migration of tracer across the grey-white border [387]. We used the smallest calibre needle possible, but there was still some evidence of local parenchymal trauma due to the cyclical movements of respiration. Unlike in Endo's study where Evan's blue did not cross the grey/white junction after white matter injections, tracer in this study was not completely contained within white matter at the level of injection. As with other tracer studies, labelling of the "pial glial" layer and the smooth muscle basement membrane may be explained by selective binding of tracer or by a sieving effect [229]. Fluid passage within the dorsal white columns was not directly investigated. As this area is isolated from the rest of the white matter the pattern of fluid outflow could theoretically be different. In future investigations of spinal cord fluid outflow, longer experimental time points are recommended. This would validate some of the observed differences between grey and white matter tracer distribution patterns. It may also provide insight into the role arterial pulsations might play in driving tracer outflow – paravenular tracer deposition may increase with time (see above). Finally, these results were obtained in anaesthetised prone small animals and extrapolation of these findings to upright large mammals should proceed cautiously as volatile anaesthetics are known to alter cardiovascular parameters and CSF production, which in turn affects CSF hydrodynamics [229].

3.7   Conclusions

This study investigated the pattern and pathways of fluid outflow in the rat spinal cord. Our results suggest interstitial fluid is transported radially in the grey matter, and along the parallel axonal fibres in the white matter. Fluid outflow appears to be limited

predominantly to a few spinal segments after 60 mins. Paravascular and perivascular pathways, including both arterial and venous routes, likely play important roles in fluid efflux. The precise mechanisms by which the vascular basement membrane of arteries act as a conduit for fluid and solute drainage from the spinal cord warrants further investigation. There may be regional variations in fluid outflow pattern within the spinal cord due to the presence of the central canal and differences between grey and white matter in vascular anatomy. These results suggest interstitial fluid dynamics are more complicated than that described by the glymphatic model.

4 Intrathoracic pressure and arterial pulsations exert different driving forces on spinal cerebrospinal and interstitial fluid flow

4.1 Abstract

4.1.1 Background

There is mounting evidence that disruption of CSF circulation and CSF/interstitial fluid exchange is likely to contribute to a number of CNS diseases including syringomyelia. However, the physiological factors that govern CSF flow in the SAS and fluid transport in the spinal cord are poorly understood. The aims of this study were to determine the effects of heart rate, blood pressure and respiration on the flow of fluid in the SAS, as well as into and out of the spinal cord interstitium.

4.1.2 Methods

In Sprague Dawley rats, physiological parameters were manipulated such that the effects of free breathing (generating alternating positive and negative intrathoracic pressures), mechanical ventilation (positive intrathoracic pressure only), tachy/bradycardia, as well as hyper/hypotension were separately studied. To investigate spinal CSF hydrodynamics, *in vivo* near infrared imaging of intracisternally infused indocyanine green was performed. Spinal fluid inflow at a microscopic level was quantitatively characterised by *ex vivo* epifluorescence imaging of fluorescent ovalbumin, AFO-647, injected into the SAS. Fluid and solute transport at the level of the perivascular space was further characterised with *in vivo* two-photon intravital imaging of intracisternally delivered fluorescent ovalbumin and microspheres. To assess fluid outflow, AFO-647 was injected into the cervicothoracic spinal grey or white matter for epifluorescence analysis.

4.1.3 Results

Compared to controls, free breathing animals had significantly higher flow of CSF in the SAS. There was also greater inflow of AFO-647 into the spinal cord interstitium. This correlated with higher microsphere tracer velocity and displacement. Hypertension and

tachycardia had no significant effect on SAS CSF flow. In hypertensive animals, there was reduced AFO-647 influx compared to some of the control cohorts, although higher microsphere velocities and displacement were noted. Tachycardia did not result in greater AFO-647 inflow compared to some of the control animals. There was no difference in microsphere velocity or displacement compared to control groups. Tachycardia and hypertension stimulated AFO-647 tracer efflux, while respiration did not affect spinal interstitial clearance.

4.1.4   Conclusions

Intrathoracic pressure has a significant effect on spinal CSF flow and cord parenchymal fluid influx. Arterial pulsations play a smaller role in SAS hydrodynamics but have profound effects on spinal cord interstitial fluid homeostasis, particularly in outflow.

4.2   Keywords

Cerebrospinal fluid, spinal cord, syringomyelia, perivascular, interstitial fluid, respiration, intrathoracic pressure, pulsations, hypertension

4.3 Background

There is mounting evidence that the exchange between CSF and ISF is vital for many homeostatic functions in the CNS [198, 231, 353]. Many investigators have proposed that the interface between the two fluids occurs at spaces around penetrating blood vessels—the perivascular spaces—with additional interactions via transpial and transependymal routes [230, 328, 353]. The precise anatomical configuration of the perivascular space, as well as the mechanisms that mediate fluid and solute exchange, have not been fully elucidated [348]. There are compelling data, largely derived from MRI studies and computational modelling, that physiological forces such as arterial pulsations and respiration drive fluid flow in the SAS [211, 289, 468, 469]. Inspiration has been identified as one of the major drivers of CSF flow [284, 472, 477]. MRI studies suggest that respiratory forces may displace more CSF than cardiac pulsations [478]. The cardiorespiratory effects on fluid transport into and out of the CNS have been the subject of far fewer studies. Stoodley et al demonstrated that perivascular inflow of a fluid tracer into the sheep spinal cord was dependent on pulse pressure [146]. However, there are conflicting findings on the role of induced hypertension in perivascular flow. In mice studies employing multiphoton intravital microscopy, both increased periarterial inflow of tracers, as well as attenuated perivascular flow after administration of inotropes, were reported [318, 461]. An ultrafast magnetic resonance encephalographic study suggested a role for respiration driving fluid centripetally (counter to arterial pulsations) through the brain parenchyma with inspiration promoting fluid efflux from perivenular spaces [481]. However, this nascent technology lacks temporal and spatial resolution for quantification of hydrodynamics [318]. Most investigators have explored the effects of either the cardiac or the respiratory cycle on fluid transport. There have been no previous attempts at examining discretely the effects of blood pressure, heart

rate and ventilation on CNS fluid dynamics. In such experiments, all other cardiorespiratory variables must be carefully controlled.

The focus of most studies, thus far, has been on the fluid dynamics of the brain. There is a conspicuous paucity of similar research into spinal cord fluid transport. Not only is the spinal cord parenchyma anatomically different compared to the brain (the grey and white matter are reversed), but the extradural venous anatomy is configured such that there is direct exposure of the epidural venous plexus to intrathoracic pressures [211]. The transmission of pressure waves to the spinal SAS cannot simply be extrapolated from intracranial studies. Moreover, the segmental arterial supply of the spinal cord is distinct from the highly collateralised circulation of the brain [213]. Elucidating the physiological effects of arterial pulsations and respiratory pressures on spinal fluid mechanics may further understanding of the pathophysiology of CNS fluid disorders such as syringomyelia and spinal cord oedema. There is also the potential for therapeutic advancements in other CNS disorders such as multiple sclerosis and subarachnoid haemorrhage [348].

To comprehensively assess the impact of cardiorespiratory drivers on spinal CSF flow and CSF/ISF exchange, the effects of *hypertension* (pharmacologically induced), *tachycardia* (induced by sinoatrial node pacing) and *spontaneous respiration* (in which cyclical positive and negative intrathoracic pressures were generated) were compared to mechanically ventilated *controls* in animal experiments. In control groups, animals were subjected to positive intrathoracic pressures only, as well as relative hypotension and bradycardia. Fluid inflow and outflow were investigated separately after manipulation of each of the three physiological variables. It was hypothesised that elevated pulse pressure, tachycardia, and negative intrathoracic pressures (in

spontaneous respiration) would result in greater CSF flow and fluid transport compared to mechanically ventilated controls.

Here, it is demonstrated with complementary *ex vivo* epifluorescence imaging and novel *in vivo* techniques—near infrared (NIFR) and two-photon intravital microscopy—that negative intrathoracic pressure is a crucial driver of CSF flow and subsequent fluid influx into the cervicothoracic spinal cord. Tachycardia and hypertension have comparatively smaller effects. Finally, both tachycardia and hypertension, but not respiration, stimulate outflow from the spinal cord interstitium into the SAS.

4.4   Methods

Male Sprague Dawley rats (aged between 8–12 weeks and weighing 280–430 g) were used in all experiments. Ethics approval was obtained from the Animal Ethics Committees of Macquarie University (ARA 2016/032) and the University of Sydney (ARA 2018/1402). **Table 5** summarises the number of animals in each experimental group (refer to 7.1 for elaboration).

Table 5 Number of Sprague Dawley rats included for analysis in each experimental arm. Note complementary *in vivo* and *ex vivo* studies were performed to investigate fluid inflow. Note that two control groups, MV and MV_{normal}, were established for fluid inflow only (refer to 4.4.2). A total of 111 rats were used

	Flow in SAS	**Fluid Inflow**		**Fluid Outflow**
		In vivo	*Ex vivo*	
Free Breathing	6	3	7	10
Blood Pressure	6	2	7	10
Heart Rate	6	3	7	10
Mechanical Ventilation (MV) – *control*	6	4	7	10
MV_{normal} – *control*			7	
Total	24	12	35	40

4.4.1   Instrumentation and preparation

After induction of general anaesthesia with 5% isoflurane in oxygen, each animal was positioned supine on a heating pad and maintained under anaesthesia with isoflurane in

0.2 L/min of oxygen. Heart rate, oxygen saturation, respiratory rate, and temperature were continuously monitored by pulse oximetry and rectal thermometer. Rats undergoing intravital microscopy were pre-medicated with subcutaneous midazolam (1 mg/kg) and buprenorphine (0.05 mg/kg).

A right transverse inguinal incision was made, and the femoral neurovascular bundle was exposed for cannulation by arterial and central venous polyethylene catheters. This was followed by a midline suprasternal incision. The trachea was exposed for insertion of an endotracheal tube. This was connected to a respiratory circuit, delivering isoflurane in oxygen. The egress tubing was connected in series to a capnometer (Capstar-100, CWE Inc., Ardmore, PA, USA), for continuous end-tidal carbon dioxide (CO_2) monitoring, as well as to a custom-made respiratory circuit pressure manometer. At this point, for the subset of rats where heart rate was modulated, a three centimetre length of the right external jugular vein was dissected out. A custom manufactured atrial pacing wire was inserted into this vein to rest just above the sinoatrial node. The pacing wire was connected to an isolated pulse stimulator (A-M Systems Inc, model 2100) [526].

The animal was then repositioned prone and the respiratory circuit manometer and arterial line were connected to pressure transducers, enabling the continuous measurement of blood pressure and circuit pressure. All vital statistics were recorded continuously for the remainder of the experiment on a data acquisition interface, Power1401 (Cambridge Electronic Device, Cambridge, UK). Arterial blood gas was analysed for pH, partial pressure of oxygen, and partial pressure of CO_2. Each physiological variable – respiration, blood pressure and heart rate – was then manipulated in isolation to investigate its effect on spinal SAS flow, parenchymal inflow, or outflow.

4.4.2 Modulation of physiological parameters

To examine the effects of negative intrathoracic pressure generated by free respiration, rats were either allowed to breathe spontaneously on the respiratory circuit, or a neuromuscular blockade was administered (pancuronium bromide 0.8 mg induction, 0.4 mg/h maintenance) followed by mechanical ventilation using a small animal ventilator (Harvard 7025 Rodent Ventilator, set at a tidal volume of approximately 1.2 mL). Any prolonged vagolytic effects of pancuronium resulting in hypertension and tachycardia were reversed with small boluses of metoprolol. The end tidal CO_2 was adjusted to a physiological range of 3.5–4.5%. In anaesthetised spontaneously breathing rats, bradypnoea of 50–55 breaths/ min was observed, with resultant CO_2 retention and respiratory acidosis. Therefore, mechanically ventilated control rats were ventilated to either a respiratory rate of 66 breaths/ min, which normalised the partial pressure of CO_2 and pH, or their respiratory rate matched that of their free breathing counterparts. This was done to detect the effects, if any, of blood pH, partial pressure of CO_2 and rate of ventilation on ISF/CSF fluid dynamics. Thus, in initial *ex vivo* studies of effects of respiration on fluid inflow there were three cohorts: free breathing (FB), mechanical ventilation to a normalised blood gas profile (hereafter designated as "MV_{normal}"), and mechanical ventilation where the blood gas profile matched that of FB (designated as "MV"). The latter two cohorts, MV_{normal} and MV, were control groups for the FB animals, but also served as control for later experiments investigating the effects of heart rate and blood pressure modulation on fluid inflow (Table 5). In all other experiments, there was only one control group. These rats were mechanically ventilated at a respiratory rate and to a blood gas profile similar to that of the MV cohort. Other variables including mass, heart rate and mean arterial pressure (MAP) were kept constant between FB and control groups.

To examine the effects of blood pressure, hypertensive rats were compared to the mechanically ventilated group(s), which had an approximate MAP of 70 mmHg. In hypertensive rats, the MAP was raised to a target of 140 mmHg (a ~40% increase from the normal physiological value, or approximately double that of controls) by an escalating infusion of phenylephrine, a selective α_1-adrenergic receptor agonist. In order to maintain a constant heart rate and prevent baroreflex compensation, the nicotinic receptor antagonist hexamethonium was administered. All hypertensive animals were mechanically ventilated to relative hypercapnic levels (matching the MV control group). Mass, heart rate and ventilation were kept constant between hypertensive and control groups.

To examine the effect of heart rate, tachycardic rats were compared to the mechanically ventilated group(s), which had an approximate heart rate of 330 beats/min (bpm). A pacing wire (described above) was connected to an isolated pulse generator (A-M Systems Inc, model 2100). A square pulse duration of 2 ms and an amplitude aiming for 1.0 V was used to generate a heart rate of at least 500 bpm. There was no appreciable change in blood pressure on pacing, even over prolonged periods. All tachycardic animals were mechanically ventilated to a relative hypercapnic level (matching the MV group). Mass, MAP and ventilation were kept constant between tachycardic and control groups

After the desired physiological parameter target was reached and maintained, one of four surgical procedures was performed to investigate fluid transport in the spinal SAS, into and out of the spinal cord.

4.4.3 Surgical procedures for investigation of fluid dynamics
4.4.3.1 Spinal subarachnoid space
To characterise the flow of CSF in the cervicothoracic SAS *in vivo*, NIFR imaging of an intracisternally injected fluorescent CSF tracer, indocyanine green (ICG), was performed.

Under an OPMI Pentero 800 microscope (Carl Zeiss, Oberkochen, Germany) a midline dorsal incision was made, followed by muscle dissection to expose the atlanto-occipital membrane (AOM) and the dorsal bony elements from C1–T2 (these were kept intact). The cisterna magna was accessed via a single pass through the AOM of a 30G Hamilton needle loaded onto a glass syringe (Hamilton Company, Nevada, USA) mounted on a stereotactic frame. Approximately 1 mm of the needle tip was left *in situ*, and cyanoacrylate glue was applied around the cannulation site to prevent CSF leakage. After the physiological targets were achieved, the Pentero NIFR camera function, IR800, was then activated (set at a zoom of ×4.0 and a focal length of 300 mm) to encompass the surgical field from the craniocervical junction to T2. A carefully agitated 10 μL aliquot of 5 mg/mL ICG (Verdye, Aschheim-Dornach, Germany) was delivered into the cisterna magna at 33 nL/s via an Ultramicro pump (World Precision Instruments, Florida, USA). The intraoperative *in vivo* fluorescence of redistributed tracer and the corresponding operative field under white light were continuously and simultaneously recorded from the start of injection for 20 min. The animal then underwent transcardiac perfusion with heparinised 0.1M phosphate buffered saline (PBS) followed by 4% paraformaldehyde (PFA) (Lancaster Synthesis, Pelham, New Hampshire).

4.4.3.2   Spinal fluid inflow
4.4.3.2.1   Ex vivo experiments

The flow of fluid from the SAS into the spinal cord was qualitatively and quantitatively assessed by analysing the redistribution of fluorescent tracer from the cisterna magna to the cervicothoracic spinal cord interstitium. A limited midline dorsal incision was made to expose the AOM. As described above, a 30G needle was used to inject a 10 μL volume of fluorescent ovalbumin tracer, Ovalbumin Alexa-Fluor®-647 conjugate (Life Technologies, Victoria, Australia) (AFO-647) into the cisterna magna at a rate of 33 nL/s.

The needle was left *in situ* ensuring CSF leakage did not occur. After 10 mins the animal underwent transcardiac perfusion.

4.4.3.2.2 *In vivo two-photon intravital experiments*

To study the dynamic interaction between CSF and the spinal cord at the level of the perivascular space, multiphoton intravital microscopy was employed to evaluate the real-time flux of fluorescent microspheres and fluid tracer. After extensive muscle dissection of the upper thoracic levels, T3 and T4 laminectomies were performed. A polyethylene sheath attached to a rubber ring was used to create a custom-made tubular spinal imaging window. A rapid-setting silicon glue (Twinsil®, Picodent, Wipperfürth, Germany) was used to adhere the window to the surrounding soft tissue, creating a watertight seal for the immersion fluid. The AOM was then exposed and a cannula inserted into the cisterna magna. The cannulation site was reinforced with cyanoacrylate glue. The cisterna magna catheter was fashioned from the 3 mm tip of a 29G needle fitted into a polyvinyl chloride catheter. The cisterna magna catheter was prefilled with CSF tracer mixture and loaded onto a 10 μL Hamilton needle and syringe. The instrumented animal was moved *en masse* to the stage of the SP8 DIVE Deep *In Vivo* two-photon intravital microscope (Leica Microsystems, Wetzlar, Germany), equipped with the InSight™X3 Ti-Sapphire (Spectra-Physics) laser system (maintained at constant power at a range of 10-20%). There was continuous physiological recording throughout the experiment. A target leptomeningeal vessel measuring 150–200 μm in width was acquired, and a 100–200 μL bolus of 2 mg/mL fluorescein dextran or tetramethylrhodamine dextran vascular tracer (ThermoFisher Scientific, Massachusetts, USA) was administered intravenously to delineate the vasculature.

Following manipulation of the target physiological parameter, a 10 μL volume of a CSF tracer mixture of AFO-647 and 1 μm fluorescent microspheres (13% v/v), FluoSpheres™

(ThermoFisher Scientific, Massachusetts, USA) was delivered at 33 nL/s through the cisterna magna catheter. Vascular tracers fluorescein and tetramethylrhodamine, AFO-647 and FluoSpheres were excited with excitation wavelengths of 500–550 nm, 570–620 nm, 660–710 nm and 420–470 nm respectively (gains between 10.0 and 100.0). Images were acquired with a ×25 water immersion objective (IRAPO L 25x/1.0 W motCORR with an NA of 1.0, Leica Microsystems). Images and videos were obtained in the *x, y* and *z* axes. At the completion of imaging, the rats were euthanised by administration of pentobarbital.

4.4.3.3 Spinal fluid outflow

The outflow of spinal ISF was assessed by analysing the egress and craniocaudal redistribution of a fluorescent tracer injected into the spinal parenchyma. The spinal grey and white matter were separately investigated. Following a limited dorsal incision and muscle dissection, a right sided hemilaminectomy at T1 was performed. A 34G needle loaded onto a glass syringe (Hamilton Company, Reno, USA) punctured the dura perpendicularly and cannulated the parenchyma in a single pass. The dural entry points for the grey and white matter injections were 0.5 mm and 1 mm lateral to the dorsal midline vein, respectively. A comprehensive description of spinal cord injection has been previously described [527] (3.4.1). A 500 nL volume of AFO-647 was delivered at 2 nL/s. The point of injection was confirmed by the location of endogenously inert fluorescent microspheres (**Fig.** *23* a). Cyanoacrylate glue was applied around the dural puncture site to prevent CSF leakage. The needle was left *in situ* for 180 mins, after which the animal underwent transcardiac perfusion.

4.4.4 Tissue processing and immunohistochemistry

The brain and spinal cord of all animals, except those that had undergone intravital microscopy, were harvested *en bloc* for macroscopic fluorescent imaging (4.4.5) [527]. The spinal cord was then segmented from C2–T4 after post-fixation and cryoprotection.

Each segment was snap frozen, and 40 μm axial sections were acquired and mounted onto glass slides for immunohistochemistry. To label the endothelium, slides were incubated with the primary Rat Endothelial Cell Antibody (RECA-1, Abcam, Cambridge, United Kingdom) in 4% NDS, followed by the secondary antibody, anti-mouse IgG Alexa-Fluor®-488 (Molecular Probes, Life Technologies, New York, USA). Smooth muscle cells were then labelled by anti-actin α-smooth muscle antibody (SMA, Sigma-Aldrich, St. Louis, Montana). Immunohistochemistry was not performed on specimens exposed to ICG as the processing degraded the tracer. Instead, in these animals, the glass slides were washed in tris-phosphate buffered saline for 10 min and were then cover-slipped with fluorescent mounting medium (DAKO, NSW, Australia).

4.4.5 Image acquisition

The craniocaudal macroscopic distribution of ICG and AFO-647 over the neuraxis was captured with white-light and single fluorescent channel using the small animal optical imaging system MS FX PRO (Bruker, Billerica, MA). For AFO-647, the fluorescence camera was set at excitation and emission wavelengths of 630 nm and 700 nm, respectively, with an exposure time of 4 s. For ICG, excitation and emission wavelengths were 760 and 830 nm, respectively.

All spinal cord axial sections from C2–T4 were imaged with a Zeiss Axio Imager fluorescence microscope (Carl Zeiss Microimaging GmbH, Germany). In axial sections that had undergone immunohistochemistry, arterioles were positive for RECA-1 and SMA, whereas venules and capillaries were labelled by RECA-1 only (vessels that had a luminal diameter < 6.5 μm were classified as capillaries). Further delineation of vascular structures and the central canal was undertaken with confocal microscopy (LSM 880, Carl Zeiss Microimaging GmbH, Germany).

4.4.6 Image processing and analysis

4.4.6.1 Fluid flow in the subarachnoid space

In the NIFR study, videos of the intraoperative fluorescence as well as the corresponding

white light channel were converted to image stacks using Image J, version 1.46r. The

background signal was subtracted in each frame to give the mean pixel intensity (a

measure of fluorescence intensity) at each spinal level from C2–T2. Fluorescence

intensity was measured every second for 20 min. Pulse-like wavefronts of tracer

fluorescence were observed to propagate rostrocaudally from the point of injection and

were particularly prominent between C1 and C2. Surface plots of fluorescence intensity

versus displacement were constructed in ImageJ to reconstruct this phenomenon. The

peak amplitude of these tracer wavefronts was tracked (via the surface plots) between

C1 and C2 to compute its velocity in pixels/s (***Fig. 13*** d–g).
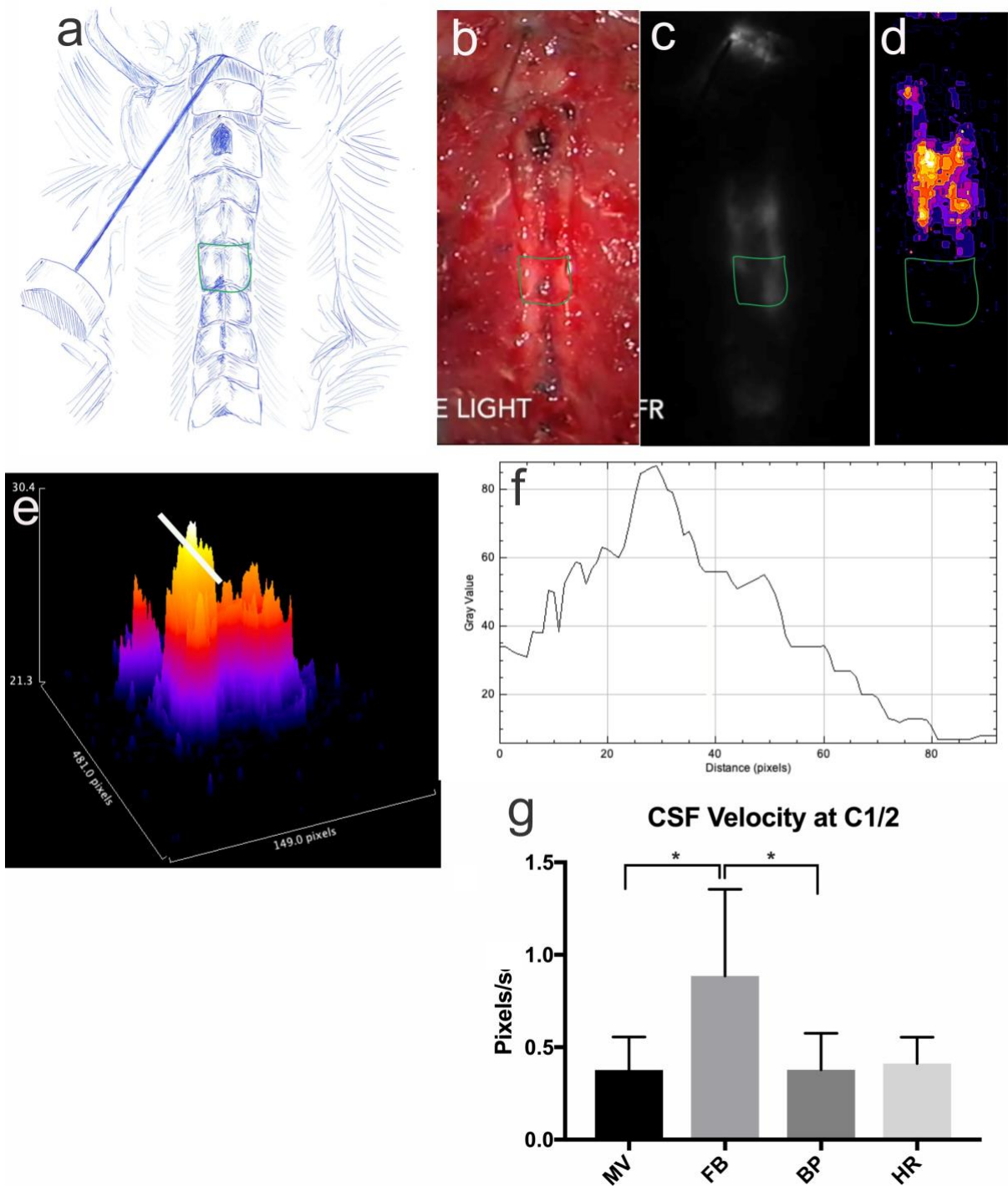
Fig. 13 Intracisternal injection of ICG to characterise CSF flow in the spinal SAS. **b** Extensive muscle dissection to expose the bony anatomy from occiput to T2, allowing infusion of ICG into the cisterna magna. **a** Artist's depiction of exposed dorsal elements, as well as the corresponding intraoperative view under white light, **b**, and NIFR filter using the IR800 function, **c**. Heat maps in 2D, **d**, and 3D, **e**, were generated from tracer fluorescence **c**. The green box denotes the spinal level C5 in each of the views. In the heat maps, high tracer signal lies towards the yellow, while low signal lies towards the violet end of the spectrum. The white bar marks the interval between C1 and C2. In **f**, a surface plot of tracer signal intensity demonstrates a pulse like wavefront of CSF tracer. Tracer waves propagated in a craniocaudal direction and their velocities were computed between C1 and C2, summarised in **g**. In this study, velocity was significantly higher in free breathing rats compared to control (FB vs MV * p = 0.036) as well as hypertensive rats (FB vs BP * p = 0.039). All error bars are expressed as ±SEM

4.4.6.2 Ex vivo experiments on spinal fluid inflow and outflow

In all macroscopic fluorescence images, the tracer signal was measured at each spinal level from C2–T4 on the dorsal and ventral surfaces. In fluorescence microscopic axial sections, the integrated density of the CSF tracer (mean pixel density multiplied by area) was calculated. The integrated density of the whole spinal cord, the white matter, and grey matter were separately calculated in each axial section. The dura and nerve roots were meticulously excluded. At least three sections were analysed per level from C2–T4, and averaged.

In *ex vivo* spinal fluid inflow experiments, the number of fluorescent "grey matter vascular events" larger than 50 pixels in the grey matter was calculated. The number of discrete "events" was assumed to reflect accumulation of tracer around the perivascular space of grey matter central arteriolar branches. The aggregate area of these "events" was also expressed as a percentage of the total grey matter area. These two calculations were adjunctive measures of central inflow into the spinal cord.

Although intracisternally infused ICG was primarily used to characterise fluid flow in the SAS, there was also endogenous penetration by this tracer. Therefore, ICG fluorescence within the whole spinal cord axial section was also quantified.

4.4.6.3 In vivo experiments on spinal fluid inflow

The time-series videos obtained from the two-photon microscopy were 16-bit, each with spatial dimensions of 256 x 256 pixels. The blue channel captured the fluorescent microspheres. The red and green channels captured the tetramethylrhodamine-dextran and fluorescein-dextran, respectively, in the vasculature. The dextrans were injected at different times, so in each video, the brightest dextran was kept and the other channel, either the red or green channel, was deleted. Images were processed using a Gaussian

Filter, Median Filter and background subtraction in Imaris x 64 v9.0.2

(Bitplane, http://www.bitplane.com/).

The videos were then analysed using the TrackMate plugin in FIJI

(NIH, https://imagej.nih.gov/ij/). Each of the microsphere tracks identified in the

software were manually checked and adjusted as needed. Only microspheres that could

be tracked over multiple frames with confidence were included. Microspheres that

appeared to be adhered directly to the blood vessel wall (as opposed to static

microspheres in the space immediately adjacent to the vessel wall) were excluded. Net

velocity and displacement values were generated for each tracked microsphere.

4.4.7   Statistical analysis

Physiological vital statistics were compared with two tailed Student's t-test. Where there

were three groups, one-way analysis of variance (ANOVA) was employed and adjusted

for multiple comparisons with Tukey post-hoc tests. Fluorescence intensities (integrated

densities and mean pixel densities) were compared using two-way ANOVA and adjusted

for multiple comparison using Bonferroni's post-hoc tests. A p value < 0.05 was

considered statistically significant in all analyses. All fluorescence values were

expressed as mean ± standard error of the mean (SEM). All physiological parameter

values were expressed as mean). GraphPad Prism (v7.02, GraphPad Software Inc,

California) was used to perform all statistical analysis.

In the intravital study, the mean velocity and displacement were computed for each of

the cohorts. The mean values were compared with one-way ANOVA and adjusted for

multiple comparisons with Bonferroni's post-hoc tests. Velocity and displacement were

expressed as mean ± SD.

4.5 Results

4.5.1 Respiration is a major driver of fluid flow in the subarachnoid space

Following intracisternal injection of ICG, the distribution of tracer was qualitatively and quantitatively assessed in real-time *in vivo* with a NIFR camera (***Vid. 1*** and ***Vid. 2***). In all rats, ICG tracer migrated in a rostrocaudal fashion down the lateral aspects of the vertebral canal. Over time, increasing fluorescence was detected at the more caudal spinal levels, and the area of highest intensity shifted caudally. Tracer signal, initially greatest in the lateral aspects of the spinal canal, slowly spread medially. Eventually, fluorescence was detected over most of the exposed C2–T2 region. There were, however, areas of relative signal attenuation. They included C1, the central portion of C2, as well as a continuous central thin strip in the middle of the spinal canal corresponding to the spinous processes. Fluorescence spread rostrally towards the brain from the injection point, but this was not evaluated.

FREE BREATHING
FLOW IN THE SPINAL SUBARACHNOID SPACE
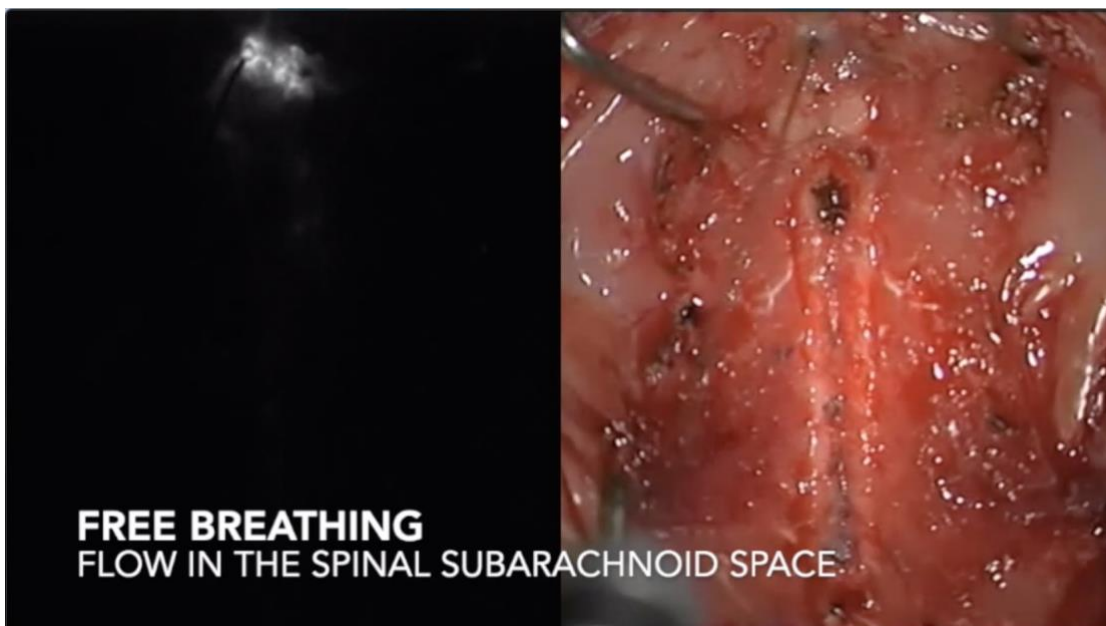
Vid. 1 Intracisternal injection of ICG to assess cervicothoracic CSF flow in the free breathing rat. Extensive muscle dissection permitted real-time *in vivo* recording (x32 speed) of ICG tracer redistribution. The panel on the right is the intraoperative view under white light, demonstrating intact dorsal elements from occiput to T2. On the left, is ICG fluorescence captured by a built-in NIFR camera. The video starts shortly after injection of ICG into cisterna magna. Both channels have been recorded simultaneously. Right panel: note the needle entering the AOM with the Hamilton syringe at the bottom left corner. The exposed laminae run vertically through the centre of the panel. The spinous processes have been marked by a black pen. Bleeding was controlled by swabs. Left panel: the needle entry point was outlined against tracer contamination of the AOM. ICG fluorescence migrated on the lateral aspects of the vertebral canal in a rostrocaudal direction, before spreading in a lateral to medial fashion to involve the

whole spinal canal. Centrally there was a thin strip of relative low fluorescence, likely secondary to poor penetration of light through the spinous process. Note the attenuated fluorescence signal at the higher cervical levels. Video access via Supplementary files
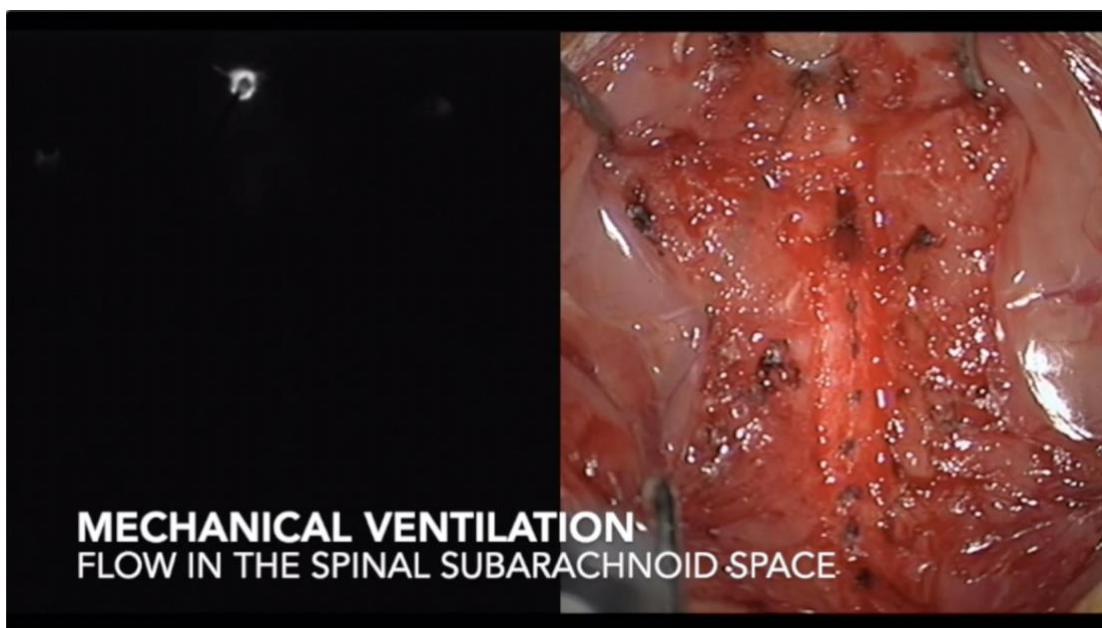
Vid. 2 Intracisternal ICG injection in the mechanically ventilated rat. Compared to the free breathing rat, respiratory movements were attenuated. Extensive muscle dissection permitted real-time *in vivo* recording (x32 speed) of ICG tracer redistribution. The panel on the right is the intraoperative view under white light, demonstrating intact dorsal elements from occiput to T2. On the left, is ICG fluorescence captured by a built-in NIFR camera. The video starts shortly after injection of ICG into cisterna magna. Both channels have been recorded simultaneously. Right panel: note the needle entering the AOM with the Hamilton syringe at the bottom left corner. The exposed lamina run vertically through the centre of the panel. The spinous processes have been marked by a black pen. Bleeding was controlled by swabs. Left panel: the needle entry point was outlined against tracer contamination of the AOM. ICG spread in a rostrocaudal, then lateral to medial fashion. The magnitude of fluorescence intensity was lower on visual comparison to the free breathing rat, and tracer signal was markedly reduced at the cervicothoracic junction. Video access via Supplementary files

Fluorescence intensities at each spinal level were quantitatively sampled at 150 s intervals after injection (Fig. *14*). At every time point analysed after injection of tracer, significantly higher fluorescence intensities were measured in free breathing rats compared with the mechanically ventilated controls (Fig. *14* "Respiration", refer to figure for p values). On post hoc analysis, significant difference at C4 was detected 2.5 mins after tracer injection (p = 0.0026). At 10 min time point, a fluorescence intensity peak was observed at the mid cervical levels. The difference in signal intensity between the free breathing and mechanically ventilated groups tapered rostrocaudally thereafter. As noted earlier, tracer signal in the upper cervical levels was relatively low throughout all time points. The velocity of the CSF tracer wavefront travelling between C1 and C2

was significantly higher in free breathing rats compared with controls (*Fig. 13* g). In free breathing and mechanically ventilated rats, the mean values were 0.89 and 0.38 pixels/s (95% CI 0.042 – 0.98, p = 0.036 two-tailed t-test), respectively.

When hypertensive rats were compared with controls, no statistically significant difference in fluorescence intensity was detected during the 20 min period (*Fig. 14* "Blood Pressure"). On post hoc analysis, the fluorescence at C2 was transiently higher in the control than the hypertensive group at 2.5 min after injection (p = 0.004). From 12.5 min, there appeared to be a slight relative increase in tracer intensity in the hypertensive group from C4–T1 but this failed to reach significance. Similarly, there was no overall difference in fluorescence signal intensities between control and tachycardic rats at any time point (*Fig. 14* "Heart Rate"). The rats with a high heart rate had slightly elevated fluorescence levels mostly at C4–5 from 10 mins, but this was not statistically significant. There were no significant differences in CSF wave velocity at C1/2 between the control, hypertensive and tachycardic groups (*Fig. 13* g).

Therefore, negative intrathoracic pressures of spontaneous respiration were associated with greater cervicothoracic CSF flow than that observed in continuous positive intrathoracic pressures of mechanical ventilation. Increasing the MAP or heart rate resulted in little effect on SAS fluid flow.
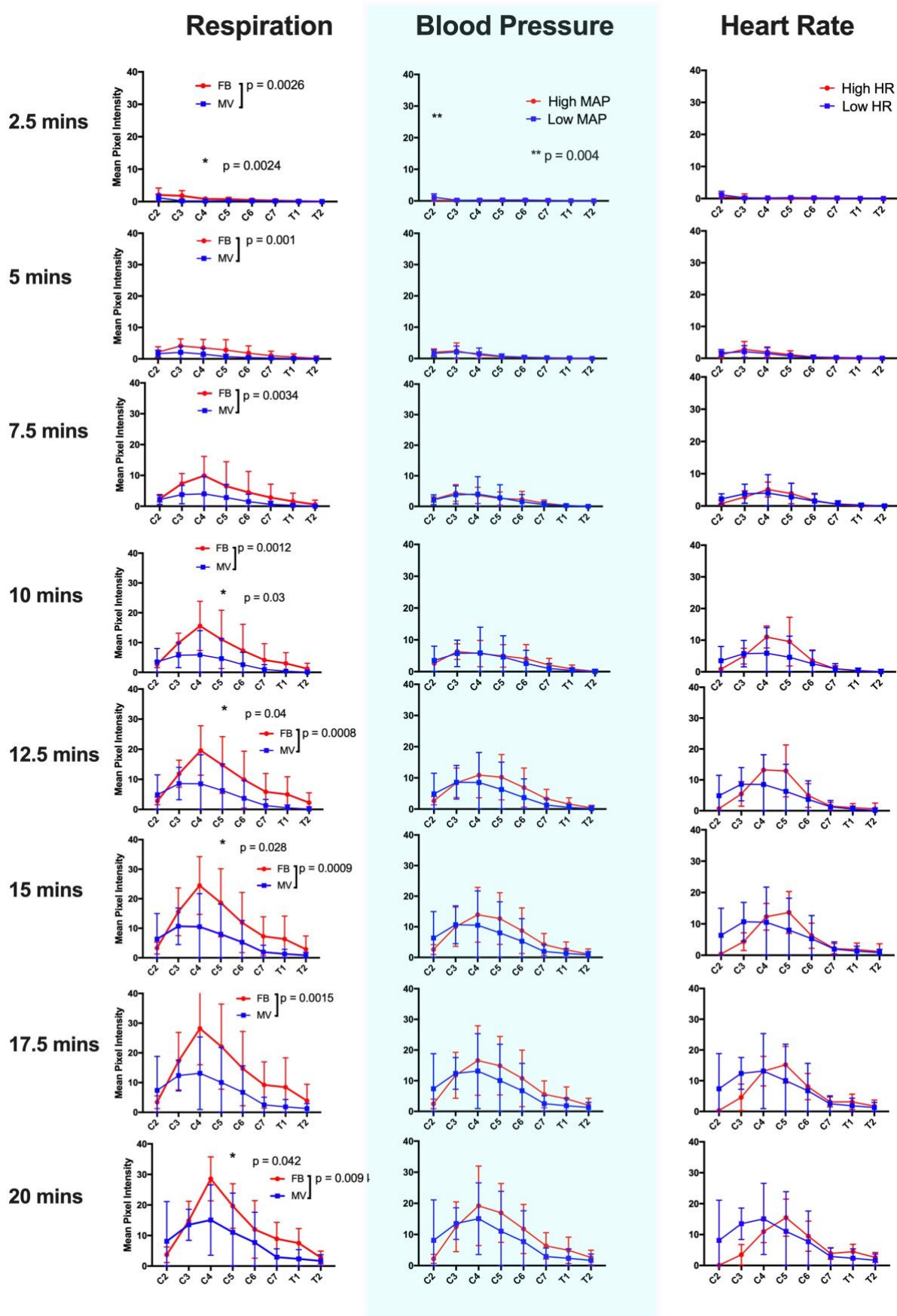
Fig. 14 Flow of CSF in the cervical SAS. Following cisterna magna injection of ICG, the redistribution of this tracer from C2–T2 was evaluated with a NIFR filter on a commercial operating microscope. Fluorescence signal intensity was deemed to reflect amount of CSF in the dorsal ± ventral SAS. Continuous fluorescence data were

collected in real-time over 20 mins. Collated here are snapshots of fluorescence intensities from C2–T2 at 150 s intervals. The column labelled "Respiration" compares the effect of mechanical ventilation (MV) to free breathing (FB). At every time point, significantly higher fluorescence intensities were measured in FB rats compared with the MV controls. On post hoc analyses, an early significant difference at C4 was detected. From the 10 min mark a consistently higher fluorescence was maintained at C5. By 20 mins, most fluorescence emanated from the mid-cervical levels. When hypertensive rats (column labelled "Blood Pressure") were compared with controls, no statistically significant differences were detected at any time up to 20 mins. The fluorescence at C2 was transiently higher in the control than the hypertensive group at 2.5 mins after injection (** p = 0.004). Tracer signal intensities between control and tachycardic rats (column heading "Heart Rate") were similar at all time points. All error bars are expressed as ±SEM

4.5.2 Negative intrathoracic pressure promotes fluid flow into the spinal cord

4.5.2.1 Macroscopic quantification of AFO-647 and ICG tracers
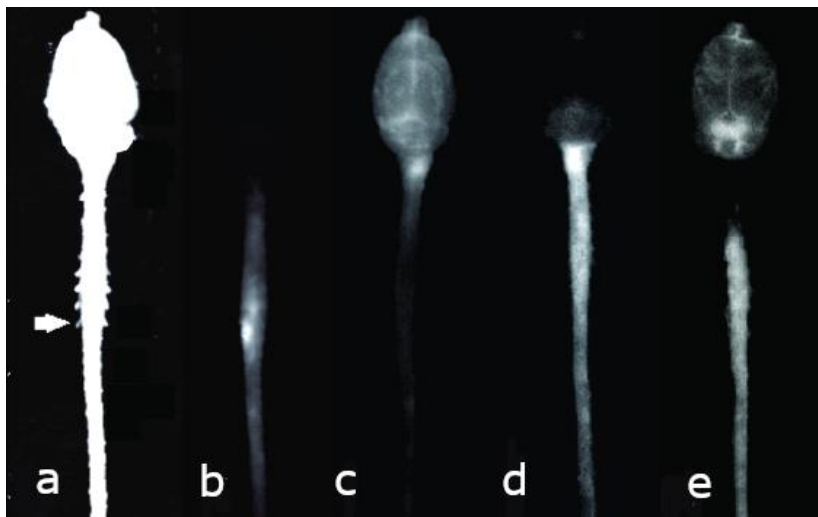
Fig. 15 Macroscopic assessment of tracers in *ex vivo* inflow and outflow experiments. In all *ex vivo* experiments, AFO-647 or ICG tracer was injected either into the cisterna magna or into the spinal parenchyma. The redistribution of tracers was then assessed under white light (for anatomical correlation) and single channel fluorescence imaging after harvesting the brain and spinal cord en bloc. **a** To assess spinal outflow, AFO-647 was injected into the spinal interstitium at C8 (specimen under white light). White arrow denotes level of injection. **b** The corresponding fluorescence view, demonstrating intense tracer signal at the point of injection and rostrocaudal redistribution. **c, d** Examples of fluorescence patterns after cisterna magna infusion of AFO-647 in a mechanically ventilated and free breathing animal respectively. Note that higher fluorescence in the free breathing rat. **e** An example of ICG fluorescence after cisterna magna injection. Although ICG was primarily used to characterise CSF flow *in vivo*, the neuraxis was extracted to determine the spinal inflow of this tracer. Note the consistent loss of ICG signal at the craniocervical junction

After infusion of ICG and AFO-647 into the CSF circulation, the tracers were fixed *in situ* and the spinal cord harvested for macroscopic fluorescence imaging to determine the rostrocaudal spread over the ventral and dorsal surfaces of the spinal cord and dura from C2 to T4. On visual inspection (***Fig. 15*** c, d), AFO-647 intensity was highest around the site of injection and progressively decreased in a craniocaudal direction. The overall tracer fluorescence was significantly greater in free breathing rats, compared with their mechanically ventilated controls, MVnormal and MV, over both ventral and dorsal surfaces

(p < 0.0001 for all groups). The markedly higher fluorescence intensities in free breathing animals reached significance at C7 and C8 on post hoc analysis (p = 0.025 and 0.04 respectively) (*Fig. 16*a). On visual inspection of the macroscopic fluorescence of intracisternally injected ICG, a conspicuous region of low signal at the craniocervical junction was universally present (*Fig. 15* e). Tracer intensity generally peaked around C6/7. There was higher overall tracer signal in free breathing rats compared with controls on the ventral (p = 0.0022), but not the dorsal surface (*Fig. 16* d).

In tachycardic and hypertensive rats, there was a lack of concordance between macroscopic ICG and AFO-647 tracer intensity patterns. The overall AFO-647 fluorescence was higher in hypertensive and tachycardic rats compared with mechanically ventilated controls (MV_{normal} and MV), over both the dorsal and ventral surfaces (both p < 0.0001) (*Fig. 16* b-f). On the dorsal surface, hypertension was associated with significantly higher signal intensity than controls at every spinal level, except C2 and T3/4, on post hoc analysis (see *Fig. 16* b for p values). On the ventral surface of hypertensive animals, a similar trend was found, except the higher signal intensities were significant in the cervical levels only. Similarly, higher fluorescence intensities were found on the dorsal surface of paced, tachycardic rats compared with controls from C4 to T4. On the ventral surface, fluorescence was significantly higher at all spinal levels in tachycardic rats compared with controls (*Fig. 16* c). Higher macroscopic ICG signal intensities were found in hypertensive rats over the ventral surface (p = 0.0007), but not the dorsal surface. ICG fluorescence was higher in control rats compared with paced tachycardic rats on the dorsal surface (p = 0.023), whereas no difference was observed on the ventral surface (*Fig. 16* e, f).
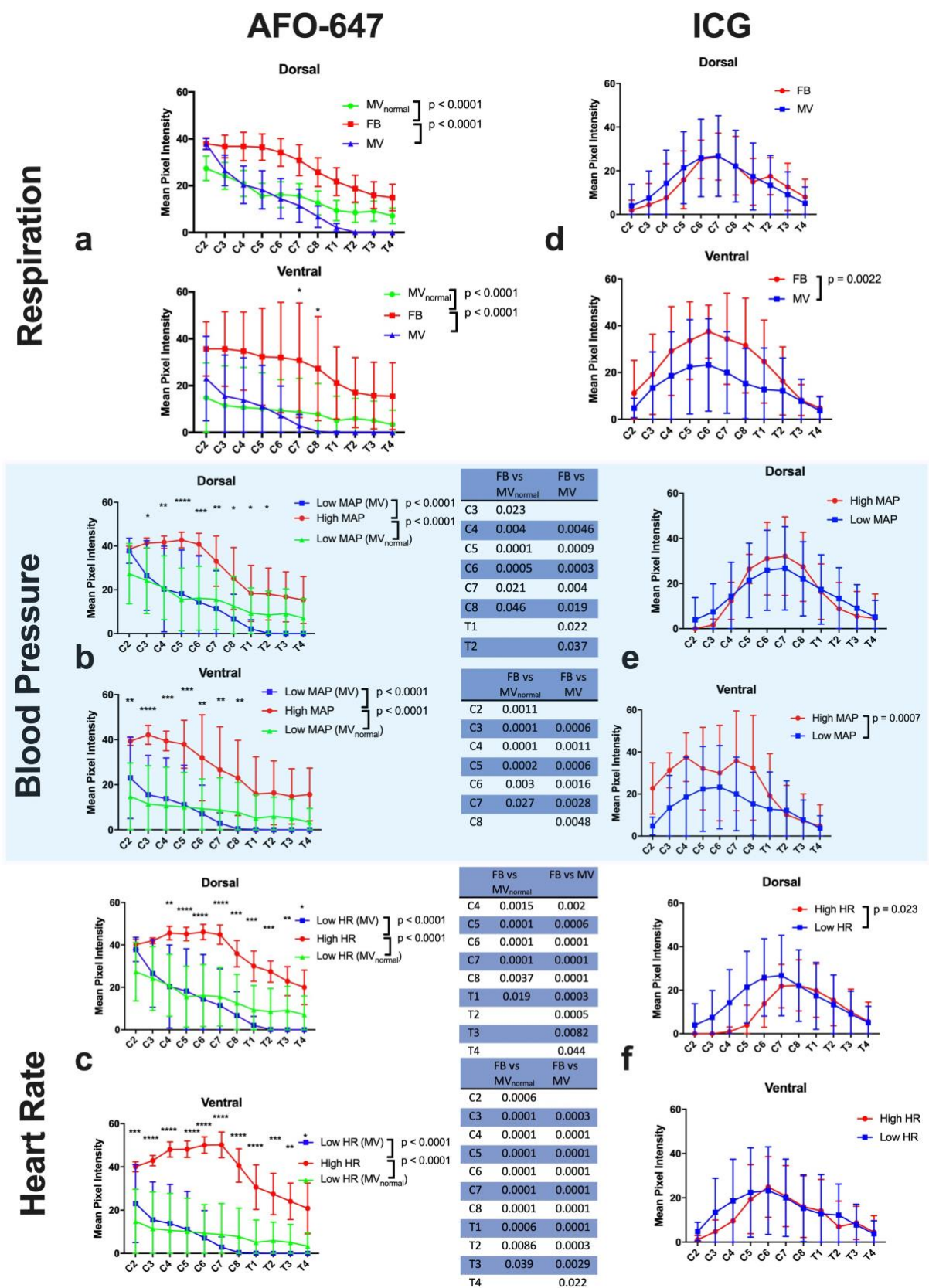
Fig. 16 Macroscopic distribution of intracisternally infused AFO-647 and ICG tracers. The fluorescence signal of each tracer was quantified at each spinal level. **a** There was significantly higher AFO-647 signal in free breathing animals (FB) compared with both control groups, on both dorsal and ventral surfaces. On the ventral surface, post hoc analysis showed that the higher intensity in FB rats (compared with controls) reached significance at C7 and C8 (p = 0.0251 and 0.0394 respectively). Similarly, after ICG injection, **d**, there was significantly higher signal intensity on the dorsal surface in FB animals, but not on the ventral surface. **b, c** AFO-647 fluorescence was

significantly higher in hypertensive and tachycardic rats compared with both control groups over both surfaces. Post hoc analysis demonstrated markedly greater tracer accumulation at multiple levels in FB, hypertensive and tachycardic groups compared with controls. The p values at these levels have been summarised in tables adjacent to the corresponding graphs. **e, f** Interestingly, these findings with AFO-647 were generally not replicated after injection of ICG into the cisterna magna. With the exception of the ventral surface **e** in hypertensive rats, macroscopic fluorescence in the hypertensive and tachycardic cohorts was not higher than that of the control groups; in fact, in tachycardic animals **f**, significantly higher intensities were recorded over the dorsal surface compared with control. All error bars are expressed as ±SEM

4.5.2.2 Microscopic quantification of AFO-647 and ICG tracers

After macroscopic evaluation of intracisternally infused tracers over the spinal cord, axial sections from C2 – T4 were acquired at each level to qualitatively and quantitatively assess the microscopic influx of tracer into the parenchyma. There was significantly higher AFO-647 signal within the whole axial section of the spinal cord, as well as the constituent grey and white matter, in free breathing rats compared with their ventilated controls, MV_{normal} and MV (**Fig. *17*** a-c, refer to figure for p values). On post hoc analysis, there was a striking difference in tracer signal between free breathing and control groups at C2 in both the grey and white matter. Higher fluorescence intensities were also found in the whole axial section and white matter of free breathing rats compared with controls at C3 and C4. There was a significantly greater number of discrete fluorescent entities (assumed to be perivascular tracer deposition) in the grey matter of free breathing rats compared with controls (p = 0.0001) (**Fig. *18*** g). Moreover, the proportion of the grey matter area occupied by fluorescence was higher in free breathing rats (p = 0.048) (**Fig. *18*** d). On post hoc analysis, more "perivascular events" were found at C2 and C3 in the free breathing group compared with controls. Thus, differences in AFO-647 inflow were the most pronounced at the upper cervical levels. The difference in fluorescence intensity between free breathing and control cohorts tapered in a craniocaudal direction. The results from analysing signal intensity of ICG influx mirrored that of AFO-647 (**Fig. *18*** a). Although the overall ICG fluorescence in free breathing rats was higher than that of the MV control group (p = 0.0006), none of the levels reached significance on post hoc analysis.

Two control groups, MV and MV$_{normal}$, were established to investigate whether the rate

of ventilation, hypercarbia and blood pH affected fluid exchange. Within the whole axial

section of the spinal cord, there was an overall higher fluorescence intensity in the

MV$_{normal}$ cohort compared with the MV group (p = 0.0008) (**Fig. 17**). There was also

higher AFO-647 signal intensity within just the white matter (p = 0.0006). On post hoc

analysis, these differences were significant only at C2 and C3 for whole spinal axial

section and white matter. No differences were detected between the two groups for grey

matter fluorescence or "perivascular events".

The overall AFO-647 fluorescence was significantly lower in hypertensive rats

compared with the MV$_{normal}$ control group, but higher compared with MV controls. This

was observed within the whole cord and the white matter (***Fig. 17*** d, e). On post hoc

analysis, this difference reached significance at C3 for the whole cord (p = 0.0083) and

the white matter (p = 0.0006). Curiously, within the grey matter there was significantly

higher AFO-647 signal in the hypertensive group compared with the MV$_{normal}$ and MV

controls. This trend reached significance at C2 on post hoc analysis (**Fig. 17** f). These

findings were not borne out in adjunctive analyses. Compared with hypertensive rats,

there were significantly more "perivascular events" (p = 0.039) and greater percentage

of grey matter occupied by tracer (p = 0.0001) in the MV cohort (**Fig. 18** e, h).

Furthermore, the amount of ICG measured in the whole axial spinal cord section in

hypertensive rats was greater than that of the control group (p = 0.017), although no

level reached significance on post hoc analysis (**Fig. 18** b).

When the overall fluorescence of AFO-647 within the whole cord and white matter of

tachycardic rats was compared with that of MV$_{normal}$, no difference was found. Compared

with the MV cohort, however, there was higher tracer signal in tachycardic rats (p <

0.0001) (**Fig. 17** g-i). Within the grey matter, the overall AFO-647 intensity was

significantly higher in tachycardic rats than either control groups (p < 0.0001) (**Fig. *17* i**).

Adjunctive analysis of "perivascular events", and the percentage of grey matter occupied

by tracer did not reveal any differences between tachycardic and control groups (**Fig. *18***

f, i). Higher overall ICG fluorescence intensity was found in tachycardic rats compared

with the ventilated control group (p < 0.0001), with post-hoc analysis demonstrating

significant differences at C3–C5 (p = 0.0032, 0.0049, 0.0031 respectively) (**Fig. *18* c**).

Multiple tracer experiments have, thus far, consistently demonstrated that free

breathing stimulates CSF flow in the spinal SAS as well as transport into the interstitium.

The findings from tachycardic and hypertensive rats have been less certain with

conflicting results obtained with different tracers. Intravital studies that permit real-

time tracking of fluid tracer fluxes were therefore performed to help clarify and explain
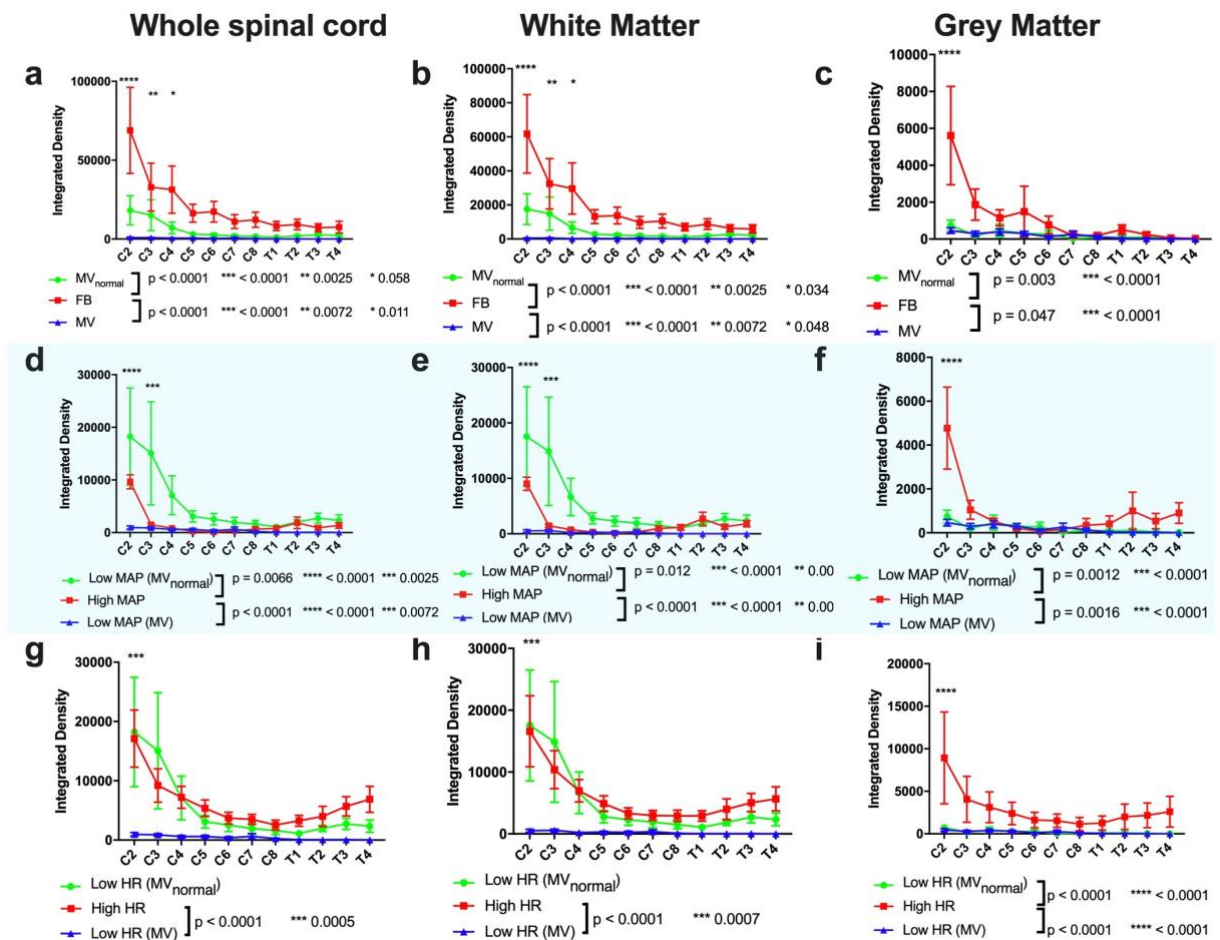
these observations.

Fig. 17 Quantitative analysis of AFO-647 inflow into the spinal interstitium after intracisternal infusion. The microscopic fluorescence intensities within the spinal cord from whole axial sections, grey matter and white matter were measured at every level from C2–T4. Experiments investigating the effects of respiration, blood pressure and heart rate correspond to the top, middle and bottom row respectively. **a-c** There was significantly higher fluorescence within the whole axial section **a**, grey matter **c**, and white matter **b** in free breathing (FB) rats compared with the control groups. On post hoc analysis, the difference between FB and controls reached significance at C2 in all compartments of the spinal cord, from C2–C4 in the white matter, and at C2 only in the grey matter. In the white matter and whole axial section **d-f**, the intensity of AFO-647 signal was significantly lower in hypertensive rats compared with controls with normalised ventilation (MV$_{normal}$). However, compared with their direct controls (MV), tracer fluorescence was higher in hypertensive rats. In the grey matter **f**, tracer signal intensity was higher in hypertensive rats than either of the control groups. **g, h** Within the whole axial section and white matter, there was no difference in AFO-647 intensity between tachycardic rats and MV$_{normal}$ control, but the tachycardic cohort had significantly higher fluorescence than MV. Tracer signal was significantly higher in the grey matter in tachycardic animals compared with controls, **i**. Refer to the figure for p values at each level marked by asterisks. All error bars are expressed as ±SEM
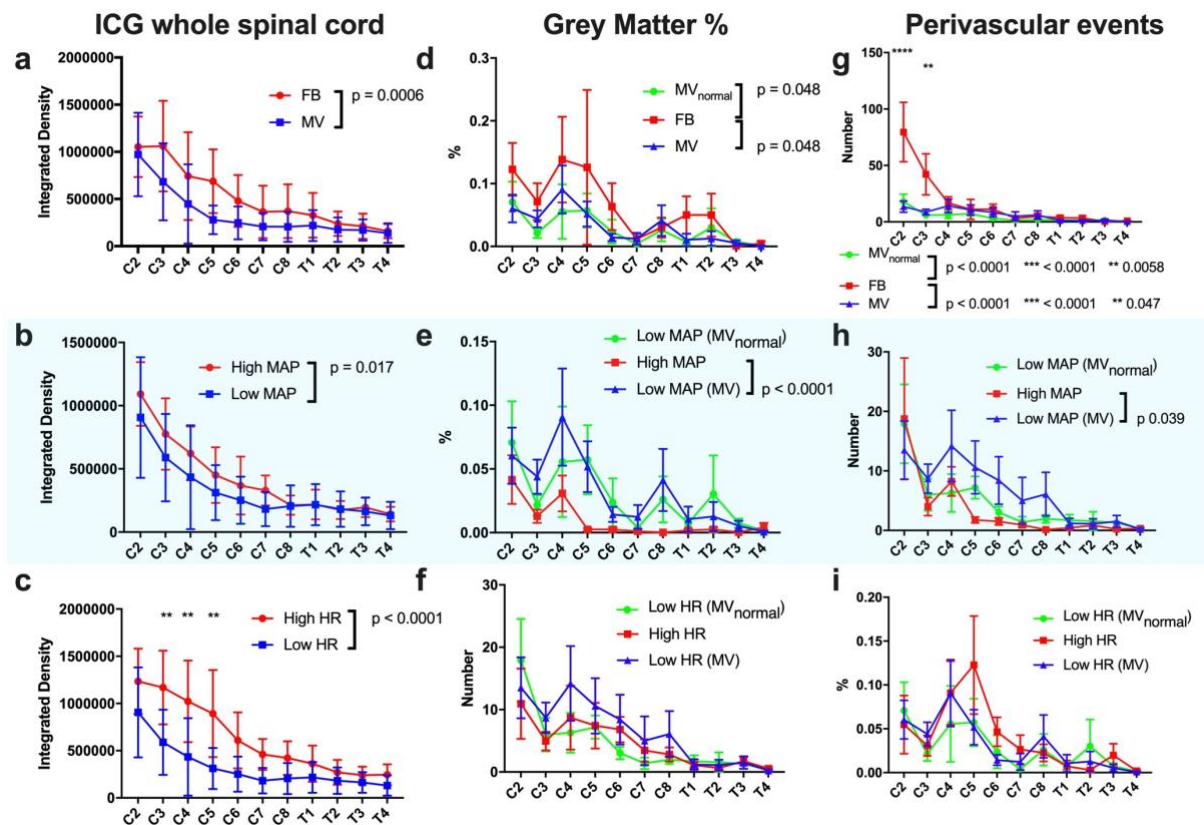
Fig. 18 Adjunctive characterisation of spinal interstitial inflow. Although intracisternally infused ICG was used to characterise fluid flow in the SAS, there was also endogenous penetration by this tracer. Therefore, ICG fluorescence within the whole axial section was also quantified. Experiments investigating the effects of respiration, blood pressure and heart rate correspond to the top, middle and bottom row respectively. **a** Free breathing (FB), **b** hypertension and **c** tachycardia all resulted in significantly increased tracer signal within the whole spinal cord compared with control. In tachycardic rats, the higher fluorescence intensity reached significance at C3, C4 and C5 (p = 0.0032, 0.0049, 0.0031 respectively). The number of fluorescent "perivascular events" within the grey matter was assumed to represent discrete accumulation of AFO-647 around perivascular spaces of central arteriolar branches, a measure of central cord inflow. In FB rats **g**, there were greater number of "events" compared with control groups, with C2 and C3 reaching significance on post hoc analysis. More "events" were found in the MV$_{normal}$ control group than in hypertensive rats **h**. There was no difference between the tachycardic and both control groups **i**. Another adjunctive measure of central spinal cord inflow was "grey matter %" (the aggregate area of "perivascular events" as a percentage of the total grey matter area). FB was the only variable that resulted in significantly greater "grey matter %" compared with controls **d**. There was a reduction in "grey matter %" in hypertensive animals **e**, while tachycardia resulted in no difference compared with controls. All error bars are expressed as ±SEM

4.5.2.3 In vivo imaging confirms respiration and arterial pulsations have different effects on fluid kinetics

In mechanically ventilated control rats, influx of AFO-647 and microspheres progressively increased with time. Some microspheres coalesced around and flowed along the long axis of blood vessels. Static microspheres were also present in these compartments. Other microspheres did not demonstrate a predilection for these spaces and appeared to flow in pathways unrelated to the vasculature (***Vid. 3***). Delineation of the vascular microanatomy was not possible as there were no intravital fluorescent markers for the tunica media or adventitia. Intramural blood flow velocity and vascular wall displacement were not quantified. In the control cohort, the velocity of 69 discrete microspheres were computed, yielding a mean particle velocity of 264.6 ± 233.01 μm/s. Many microspheres could only be tracked very limited frames before disappearing from view. Additionally, some displayed to-and-fro movements which resulted in the majority of particles displaying little net displacement. Despite the different lengths of time microspheres were tracked in each cohort, the mean displacement was calculated (within a constant ROI) as a reflection of the to-and-fro nature of particles. In mechanically ventilated controls, microspheres had a mean displacement of 9.1 ± 15.64 μm (**Fig. *19***).
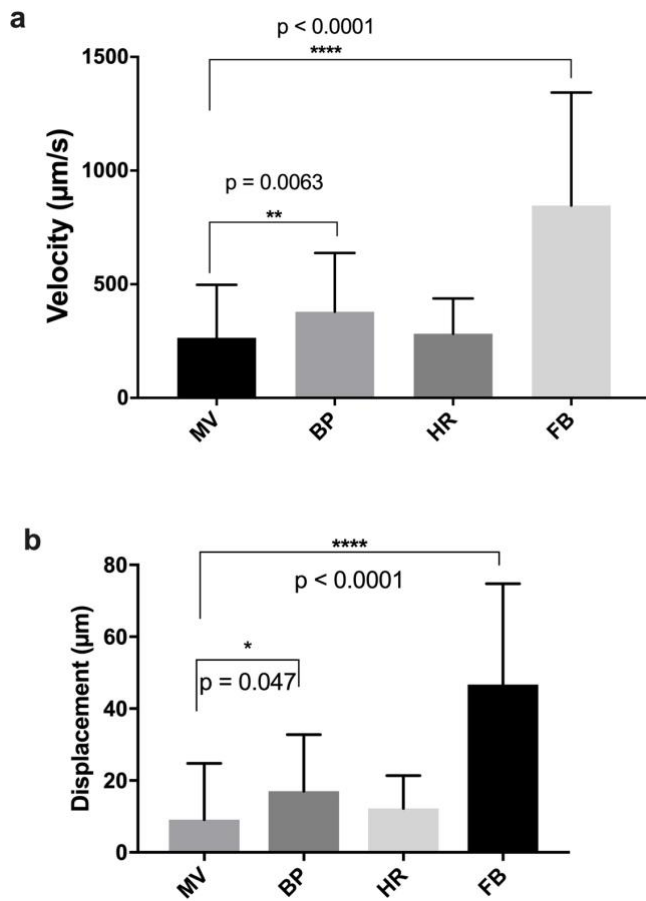
Fig. 19 Velocity and displacement of Fluosphere tracer in *in vivo* spinal inflow experiment. Fluorescent microspheres infused intracisternally were characterised real-time *in vivo* using two-photon intravital microscopy. **a** Microspheres were tracked to yield mean velocities. In free breathing (FB) and hypertensive rats, particles were significantly faster than those in the control group, MV. The difference in velocity was marked in FB animals compared with control. **b** The displacement of these microspheres (see text for explanation) was also computed. Unsurprisingly, similar relationships to **a** were observed in FB, hypertensive and tachycardic rats compared with control, MV. All error bars are expressed as ±SD
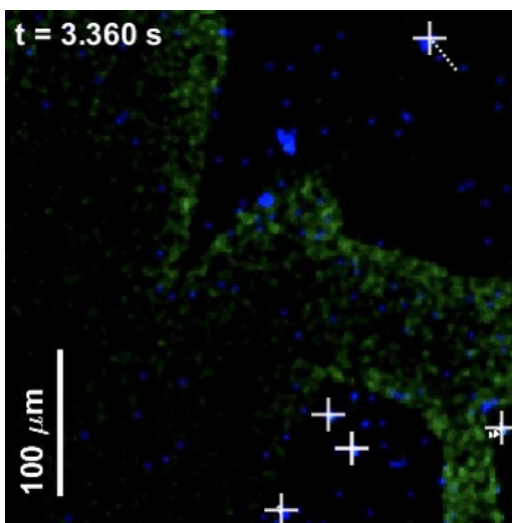
Vid. 3 Investigation of spinal inflow employing two-photon intravital microscopy. Intracisternally infused fluorescent microspheres were tracked and characterised *in vivo*. This is an example of a leptomeningeal blood vessel branch point, approximately 150 μm wide, in a mechanically ventilated control rat. Intravascular dextran tracer has been labelled green, microspheres in blue and AFO-647 has been selectively filtered out. Tracked

microspheres are labelled with white + and their tracks marked with dotted lines. Some microspheres flowed parallel to the long axis of the vasculature in pathways close to the vessel wall. Other microspheres exhibited to-and-fro movement that resulted in small overall displacement. This cohort of mechanically ventilated rats served as control for comparison with free breathing, hypertensive and tachycardic animals. The mean velocity and displacement of tracked particles were 264.6 ± 233.01 μm/s and 9.1 ± 15.64 μm respectively. Video access via Supplementary files

In free breathing rats, there was extensive movement of the spinal cord in the *z* plane (*Vid. 4*). Although the amount of tracer (per timepoint or in *z*-stacks) was not quantified, there appeared to be greater numbers of microspheres and AFO-647 compared with controls at all timepoints. Due to movement artefact, only 23 particles could be reliably tracked in one animal. The mean velocity and displacement of these microspheres were 846.4 ± 497.2 μm/s and 46.7 ± 28.56 μm respectively, which were significantly higher than the control group ($p < 0.0001$ for velocity and displacement) (**Fig. *19***).
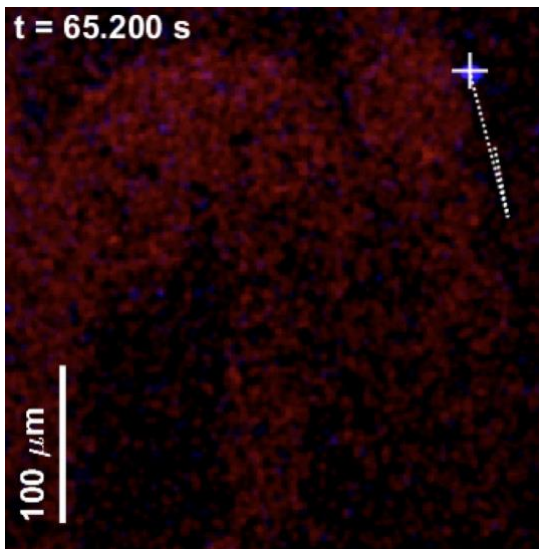
Vid. 4 Intravital experiment in a free breathing rat. This is an example of a leptomeningeal blood vessel branch point, approximately 120 μm wide. Intravascular dextran tracer has been labelled red, microspheres in blue and AFO-647 has been selectively filtered out. Tracked microspheres are labelled with white + and their tracks marked with dotted lines. Movement in the *z* axis was a consequence of spontaneous respiration, generating greater movement artefact compared with control animals. Note the chaotic movement of the particles with grossly higher velocities. The velocity and displacement were 846.4 ± 497.2 μm/s and 46.7 ± 28.56 μm respectively which were significantly higher compared with the control group ($p < 0.0001$). Video access via Supplementary files

In tachycardic and hypertensive rats, it was difficult to discern whether qualitatively more AFO-647 and microspheres were present compared with control. Fluorescent tracers were distributed in similar patterns to that observed in controls. In hypertensive animals, there was prominent oscillation of microspheres (as distinct to the overall to-

and-fro movements described earlier) in their net displacement in one direction (**Vid. 5**). This phenomenon was not present in tachycardic rats (**Vid. 6**). In the hypertensive rat that was suitable for particle tracking, 105 microspheres were tracked, yielding a mean velocity of 379.0 ± 258.6 μm/s. This was significantly higher than controls (p = 0.0063). The corresponding mean displacement of these microspheres, despite their to-and-fro movements, was 17.02 ± 15.73 μm and also greater than controls (p = 0.05). In tachycardic animals, 157 particles were analysed, yielding a mean velocity and displacement of 282.1 ± 155.8 μm/s and 12.2 ± 9.14 μm respectively. These quantities were not significantly different compared with controls (**Fig. _19_**).
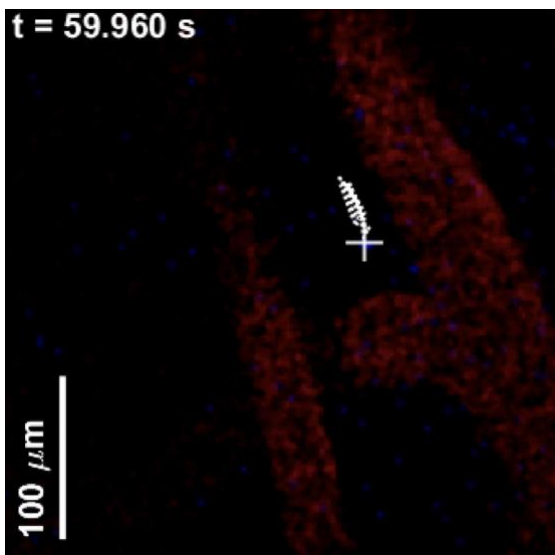
Vid. 5 Intravital experiment in a hypertensive rat. This is an example of a leptomeningeal blood vessel branch point where the parent vessel was just less than 100 μm wide. Intravascular dextran tracer has been labelled red, microspheres in blue and AFO-647 has been selectively filtered out. Tracked microspheres are labelled with white + and their tracks marked with dotted lines. Note the oscillatory pattern of particle flow near blood vessels. Despite this, the velocity and displacement were slightly greater than control at 379.0 ± 258.6 μm/s, reaching statistical significance (p = 0.0063). The corresponding mean displacement of these microspheres, despite their to-and-fro movements, was 17.02 ± 15.73 which was also significantly greater than control (p = 0.05). Video access via Supplementary files
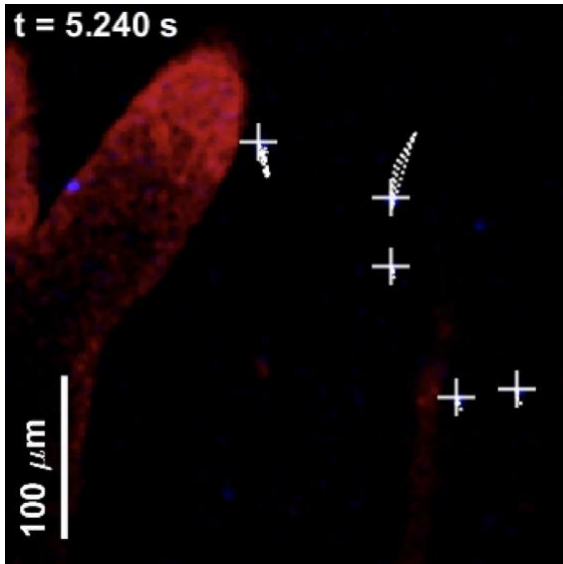
Vid. 6 Intravital experiment in a tachycardic rat. This is an example of a leptomeningeal blood vessel branch point where the parent vessel was just over 100 μm wide. Intravascular dextran tracer has been labelled red, microspheres in blue and AFO-647 has been selectively filtered out. Tracked microspheres are labelled with white + and their tracks marked with dotted lines. Again, some microspheres were found in spaces next to the vessel, moving in to-and-fro manner that resulted in little displacement. There did not appear to be gross difference in microsphere movement in tachycardic rats compared with control. This was confirmed by the mean velocity and displacement of 282.1 ± 155.8 μm/s and 12.2 ± 9.14 μm respectively. Neither values reached significant difference compared with control. Video access via Supplementary files

4.5.3   Fluid influx occurs via transpial and perivascular pathways

Further insights into spinal fluid transport may be gained from qualitative assessment of AFO-647 influx into the interstitium.

In all animals, AFO-647 deposited on the pial surface and around intramedullary and extramedullary blood vessels. A transpial, "parenchymal", diffusive pattern of tracer transport was also observed (***Fig. 20*** b), but this was largely observed in free breathing rats. In this cohort, the transpial pattern was observed in 33% of spinal levels, compared with just 10% in the MV_{normal} cohort, and none in the MV arm. In hypertensive and tachycardic rats, this transpial deposition of AFO-647 was found in 14% and 19% (respectively) of spinal levels, similar to that detected in MV_{normal} group. Note that further statistical analyses were not performed in these qualitative descriptions as tracer colocalisation to anatomical structures was either present or absent (after ensuring uniform adjustment of brightness and contrast in every photomicrograph).

Labelling of large extramedullary vessels such as the ASA was ubiquitous. In both the white and grey matter, tracer selectively accumulated around arterioles and venules, especially around radially projecting blood vessels (**Fig.** *20* b-e). Pericapillary tracer was detected but was not as abundant as periarterial or perivenular deposition. In ventilated control groups MV_{normal} and MV, tracer was identified around white matter arterioles in 76% and 39% of spinal levels. In free breathing, hypertensive and tachycardic rats this was observed in 86%, 62% and 76% of spinal levels. In the grey matter, periarteriolar tracer fluorescence was detected in 61% and 62% of spinal levels in MV_{normal} and MV cohorts, respectively. In free breathing animals, this phenomenon was observed more frequently (71%), while in both paced and hypertensive rats, this was observed less commonly (33% each).

In both extramedullary and intramedullary arteries and arterioles, confocal microscopy confirmed perivascular deposition of AFO-647 (**Fig.** *20* g, j-m). Distinct layers of tracer were detected immediately external, within as well as immediately internal to the smooth muscle cells of the tunica media of the ASA. This was also observed in the arterioles of the vasocorona and within the grey matter (**Fig.** *20* j-m). Tracer deposited immediately around the RECA-1 labelled endothelium of intramedullary venules and capillaries, as well as the extramedullary veins of the ventral median sulcus and the superficial pial network (**Fig.** *20* n, o). Furthermore, at higher magnifications, deposition of AFO-647 in the spinal cord ECS highlighted the tortuous nature of the interstitial microarchitecture (***Fig. 20*** o).

Tracer deposited around the central canal, but the spinal levels over which this was found were often non-contiguous. AFO-647 deposition around the central canal occurred in 47%, 17% and 8% of total spinal levels in free breathing, MV_{normal} and MV cohorts, respectively. Hypertensive rats exhibited a similar incidence (19%), while

tachycardic rats had increased tracer deposition around the central canal (75%) compared with the control groups. On confocal microscopy, tracer distributed heterogeneously within the ependymal layer of the central canal. There was preferential accumulation along the luminal border of ependymal cells, with less fluorescence along the abluminal aspect (**Fig.** *20* i). On higher magnification, there was speckled clumping of tracer on the luminal aspect (**Fig.** *20* i). It was not possible to confirm whether there was tracer uptake by ependymal cells. Occasionally, intraluminal tracer was detected. Serpiginous trails of tracer were also observed between the abluminal aspect of the ependymal layer and nearby subependymal microvessels (**Fig.** *20* h). This suggested a pathway linking subependymal perivascular spaces and the central canal.

Although ICG tracer was primarily employed to assess CSF flow in the SAS, its influx into the spinal cord was characterised. The tracer intensity was highest at the pial margins circumferentially, and rapidly attenuated radially towards the cord centre (**Fig.** *20* a). ICG labelling of intramedullary vasculature structures and the central canal was limited to some prominent blood vessels and only at upper cervical levels. Immunohistochemical labelling of blood vessels was not compatible with ICG so it was not possible to confirm perivascular deposition.
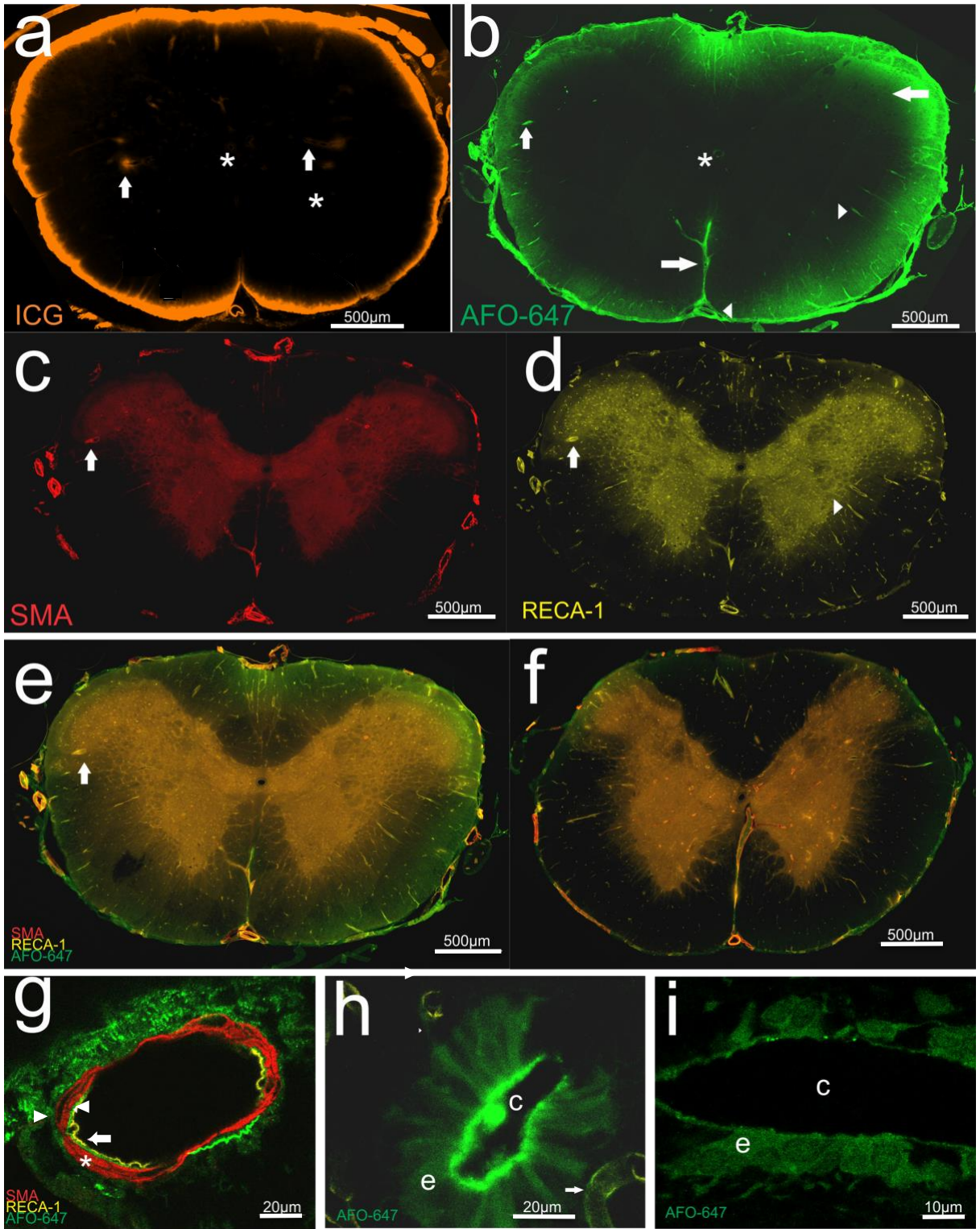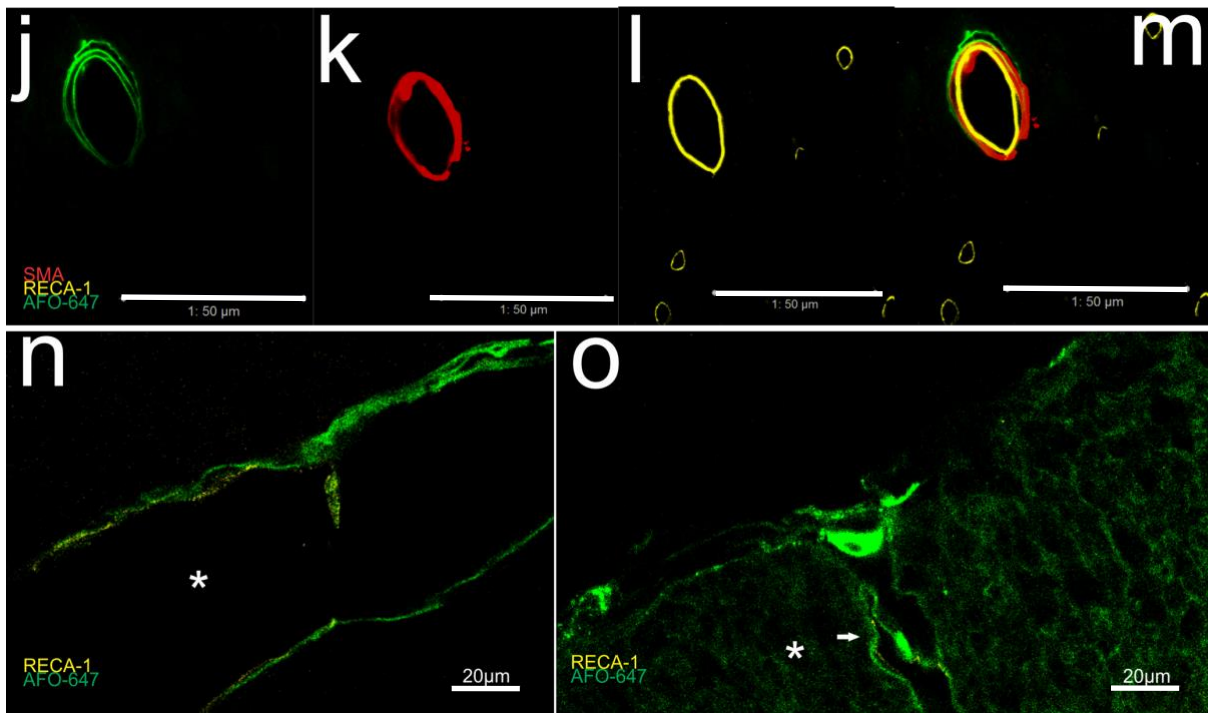
Fig. 20 Tracer inflow into the spinal cord is via perivascular and transpial routes. **a** After injection into the cisterna magna in a free breathing rat, ICG appeared to diffuse across the pia into the interstitium. In the upper cervical levels (**a** is at C2), there was some deposition of ICG around perivascular spaces in the grey matter and white matter (arrows), as well as around the the central canal (*). However, outside of the craniocervical junction, ICG tracer was limited to the subpial space. **b** AFO-647 displayed some ability to cross the pia circumferentially, appearing to diffuse into the spinal interstitium (left pointing arrow), but perivascular labelling was prominent (right pointing arrow head) with prominent intramedullary penetration, towards the central canal (*). Note the deposition of AFO-647 tracer around the ASA and the central branches distal to the ventral median sulcus (left arrow head and right arrow respectively). **b-d** Tracer colocalised with both arterioles (up arrow) and venules (right arrowhead), confirmed with immunofluorescent stains for smooth muscle actin **c**, and RECA-1 **d**. The merged fluorescent channel is shown in **e**. In a mechanically ventilated control rat at C2, **f**, there was reduced tracer signal in the whole axial section. Transpial fluorescence was conspicuously reduced, although perivascular deposition was still present. **g** An example of an ASA under confocal microscopy (x63 magnification). In all animals where extramedullary arterial AFO-647 deposition was evident, tracer was detected not only external to (right arrow head) the smooth muscle layer (*) but also within, and internal to the tunica media (left arrow). Left pointing arrow head denotes the endothelium. A similar example of an ASA in axial section has been rendered in a 3D video. Please refer to *Vid. 7*. **j-m** Depicts multiple distinct layers of AFO-647 tracer within and external to the smooth muscle layer of an intramedullary grey matter arteriole (AFO-647, SMA, RECA-1 and merged channels captured in **j**, **k**, **l** and **m** respectively, all x100 magnification). **n** AFO-647 accumulated around the outside of the endothelium of a large intramedullary venule (* marks the lumen) (x63 magnification). **o** A venule at the pial surface had similar deposition of AFO-647 around the endothelium (right arrow). In **o**, * marks transpial migration of tracer, depositing in a convoluted, lattice pattern which reflects the spinal ECS architecture (x63 magnification). **h, i** AFO-647 was detected within the ependymal layer of the central canal. There was an uninterrupted serpiginous trail of tracer (right arrow head) between subependymal microvessels and the central canal (right arrow marking venule, while *c* denotes the lumen of the central canal in **h** and **i**) (x100 magnification). This suggests privileged pathways may exist between the central canal and the subependymal perivascular spaces. AFO-647 tended to concentrate on the luminal aspect of the ependymal cells. Tracer was occasionally observed within the lumen of the central canal. **i** Tracer unevenly deposited on the luminal side of the ependymal layer (note speckled appearance). The nuclei of ependymal cells were demarcated by tracer (marked by *e*), suggesting uptake by these cells (x100 magnification)

4.5.4 Tachycardia and hypertension stimulate outflow from the spinal cord

The impact of respiration and arterial pulsations on spinal outflow mechanisms was assessed. AFO-647 was injected into the spinal grey or white matter without CSF leakage and allowed to circulate over three hours.

4.5.4.1 *Macroscopic quantification of AFO-647*

The harvested spinal cord (with intact dura) was imaged to determine the macroscopic extent of tracer redistribution 180 min after intramedullary injection. On inspection, fluorescence was generally highest within one level of the injection point at C8 (***Fig. 15*** a, b). Tracer signal tapered rapidly beyond that. In free breathing rats, the overall tracer intensity was significantly greater than that of ventilated controls over both dorsal and ventral surfaces, after injection into both grey and white matter (**Fig.** *21* a). On post hoc analysis, this difference reached significance at C5 dorsally as well as C6 ventrally after injection into grey matter (p = 0.012 and 0.0029 respectively), and at C5 on the ventral surface after injection into the white matter (p = 0.023 respectively).

There was also overall greater tracer signal in hypertensive (**Fig.** *21* b) and tachycardic (**Fig.** *21* c) animals compared with ventilated controls over both surfaces, after injection into the white and the grey matter. On post hoc analysis, there was a significant difference at C4 after white matter injections (p = 0.016) in hypertensive rats.
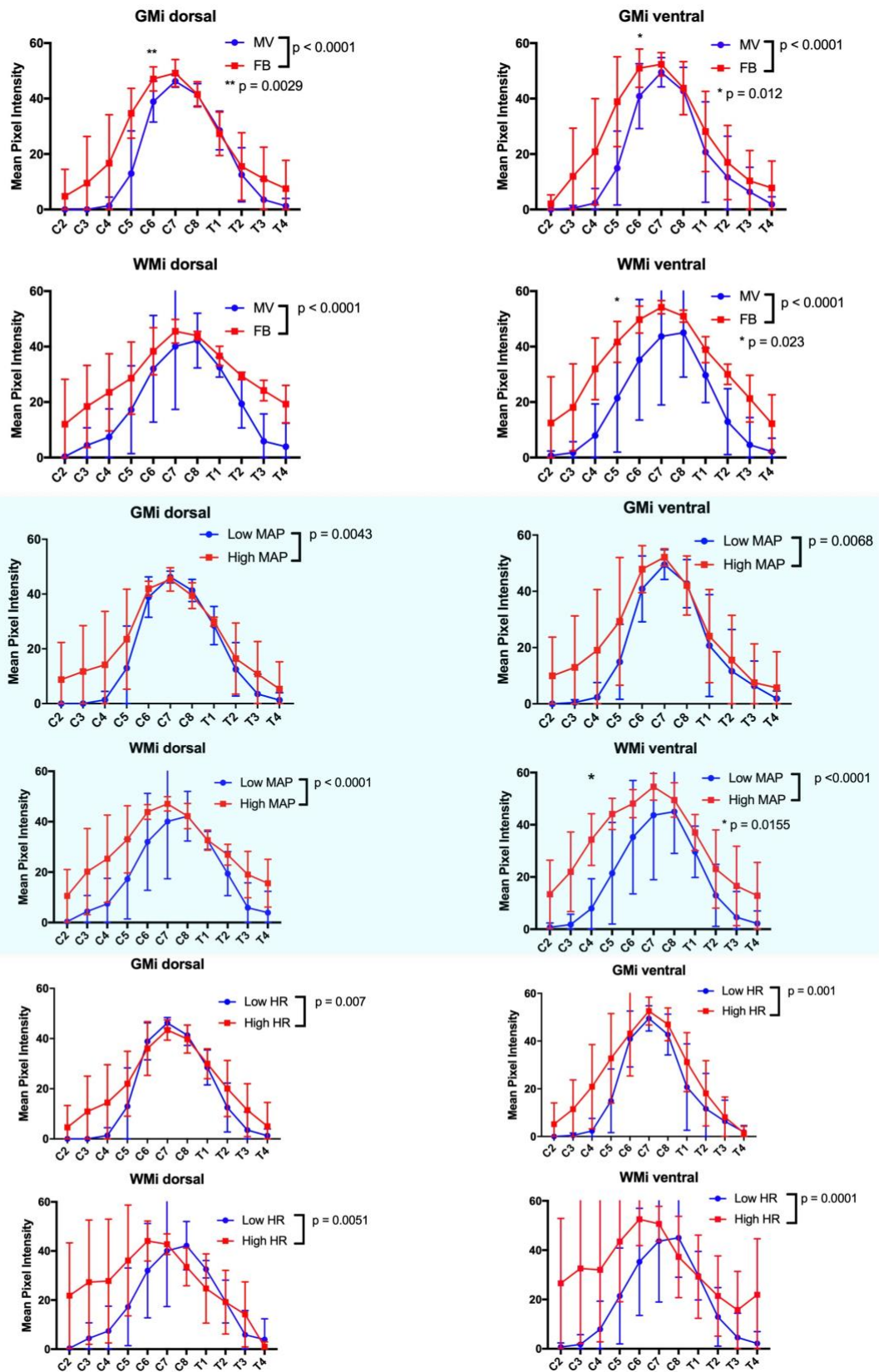
Fig. 21 Macroscopic distribution of AFO-647 after injection into the spinal grey or white matter. In all outflow studies, macroscopic fluorescence was highest around the point of injection at C8, tapering rostrally and caudally. Experiments investigating the effects of respiration, blood pressure and heart rate correspond to the top, middle and bottom row respectively. Compared with the controls (MV), free breathing (FB), hypertensive and tachycardic rats all displayed significantly higher tracer intensity over both the ventral and dorsal surfaces. This was true after

both grey and white matter injections (GMi and WMi respectively). On post hoc analysis, the difference in tracer intensities reached significance at C6 after grey matter injections, and at C5 after white matter injections in the respiration experiments. There was also significantly higher tracer intensity at C4 ventrally after white matter injections in hypertensive rats. All error bars are expressed as ±SEM

4.5.4.2 Microscopic quantification of AFO-647

After injection of AFO-647 into both the spinal grey and white matter, extremely high interstitial fluorescence intensities were observed locally. Endogenous spread of tracer was largely limited to within one level rostral and caudal to the injection point (approximately C8). After intramedullary injection, interstitial tracer effluxed slowly from the parenchyma into the spinal SAS where it could be redistributed, and thence back into the spinal cord interstitium at remote levels. Spinal outflow was indirectly, but more meaningfully, assessed by measuring tracer that had recirculated back into the parenchyma from the SAS. Comparing the amount of *redistributed* tracer, instead of *total* AFO-647 fluorescence, eliminated large fluorescence intensity values around the injection site which would have obscured differences between cohorts. Therefore, the amount of tracer bound by (and including) the pial surface from C2 to C6, and from T2 to T4 was quantified. Tracer signal from C7–T1 was selectively excluded. Fluorescence in the dura, nerve roots and within the SAS was also meticulously excluded.

There was no difference in overall fluorescence within the whole spinal cord (and its constituents) between free breathing rats and ventilated controls, after injection of tracer into the grey matter (**Fig.** *22* a-c). Similar results were obtained after injection of tracer into the white matter, although higher fluorescence was observed in the grey matter of free breathing rats compared with controls (p = 0.0082) (**Fig.** *22* d-f).

After injection into the white matter in hypertensive rats, however, the overall fluorescence level was significantly higher than that of control within the whole cord (p < 0.0001), the grey matter (p = 0.0066) as well as the white matter (p < 0.0001) (**Fig.** *22* j-l). On post hoc analysis, these differences reached statistical significance at T3

within the whole cord (p = 0.039) and in the white matter (p = 0.047), and at T2 in the grey matter (p = 0.017). There were similar findings after tracer injection into the grey matter (**Fig.** *22* g-i). In hypertensive rats, fluorescence was significantly higher than controls within the whole spinal cord (p = 0.05) and white matter (p = 0.028), but no difference was detected in the grey matter.

After injection into the white matter in tachycardic rats (**Fig.** *22* p-r), the fluorescence intensity was higher compared with controls within the whole cord, the grey matter and the white matter (p = 0.0021, 0.0032 and 0.0028 respectively). On post hoc analysis, a significant difference was reached at T2 in the grey matter and whole spinal cord (p = 0.043 and 0.029 respectively). After injection into the grey matter of tachycardic rats (**Fig.** *22* m-o), there was increased tracer signal within the whole cord and the white matter (both p < 0.0001) compared with controls. No difference, however, was observed in the grey matter. On post hoc analysis, significance difference was reached at T2 within the whole cord after injection (p = 0.027).
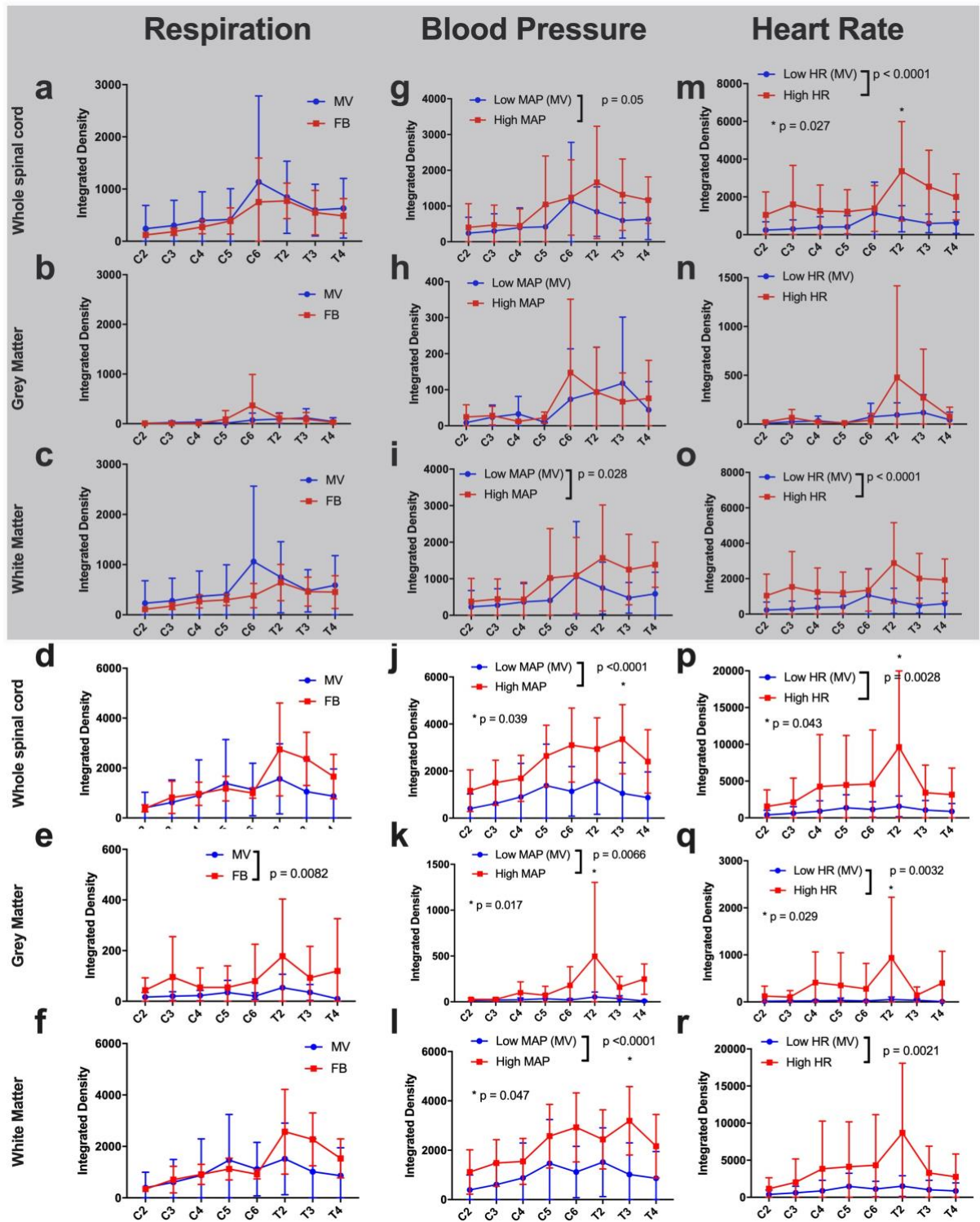
Fig. 22 Quantification of AFO-647 tracer fluorescence within microscopic whole axial sections, grey matter and white matter. After injection of AFO-647 into either the spinal grey or white matter, the fluorescence intensity of redistributed tracer was measured within the grey and white matter of levels remote from the injection site (C2–6 and T2–T4). The top half of the figure has been shaded grey, representing grey matter injection experiments. The bottom unshaded half of the figure therefore represents white matter injections. **a-c** After injection of tracer into the grey matter, there was no significant difference in whole axial section, grey and white matter fluorescence intensities between free breathing (FB) and control (MV) rats. **d-f** After injection into the white matter, there was similarly no difference in tracer intensity within whole axial section **d** and the white matter **f**, although significantly higher signal was detected in the grey matter in free breathing rats compared with controls, **e**. There was significantly higher fluorescence in hypertensive rats (compared with controls) after injection of tracer into both

the grey matter, **g-i**, and the white matter, **j-l**. This was observed within both the grey and white matter. However, after grey matter injections, **h**, no difference was found between hypertensive and control animals within the grey matter. On post hoc analysis of white matter injections, significant difference was reached at T2 in the grey matter, as well at T3 in the white matter and within the whole axial section. There were similar findings in tachycardic rats compared with controls. With the exception of the grey matter after grey matter injections **n**, there was higher tracer intensity in tachycardic rats after grey matter injections, **m-o**, and white matter injections, **p-r** in all parts of the spinal cord. On post hoc analysis, the difference in fluorescence intensities reached significance at T2 except in the white matter. All error bars are expressed as ±SEM

4.5.5 Fluid efflux occurs via perivascular pathways

Here, a qualitative study of interstitially delivered AFO-647 relative to spinal

microanatomical structures was undertaken. After grey matter injections, there was

radial redistribution of tracer from the point of injection towards the pial surface and

into the contralateral hemicord (**Fig. 23** b). The fluorescence intensity attenuated as an

inverse function to distance from injection point, such that subpial fluorescence was

absent. Rostral and caudal to the injection site, tracer was largely found within the grey

matter, although it readily transgressed the white/grey junction. After white matter

injections, tracer crossed from the white matter into the grey matter and even into the

contralateral hemicord around the site of injection (**Fig. 23** c, d). However, tracer was

largely confined to the lateral white column rostrocaudally (**Fig. 23** e).

Around the injection site of all rats, tracer selectively deposited around radially

projecting arterioles and venules (**Fig. 23** b, d, e). These appeared to be privileged

pathways for solute efflux towards the pia. The ASA and other extramedullary vessels

were invariably labelled even though subpial tracer was not present (**Fig. 23** b, i).

Remote from the point of injection, AFO-647 was detected circumferentially on the pial

surface and around extramedullary vessels (**Fig. 23** f, g). Pial tracer intensity decreased as

a function of craniocaudal distance from the injection site. At remote levels, interstitial

fluorescence was limited to the perivascular spaces of radially projecting arterioles and

venules (**Fig. 23** f), instead of depositing in the ECS. This was highly suggestive of tracer

effluxing from the injection site to the SAS, and then redistributing back into the spinal

parenchyma at remote levels, via perivascular routes.

Confocal microscopy confirmed that pathways of perivascular efflux are similar to inflow. In both extramedullary and intramedullary arteries and arterioles, distinct layers of AFO-647 interdigitated with the layers of the tunica media (**Fig. *23*** h-j). Tracer was found external to, as well as within, the smooth muscle wall. AFO-647 was found intimately around the RECA-1 labelled endothelial layer of intramedullary venules, capillaries as well as the venules within the ventral median sulcus. Whether tracer was injected into the SAS or into the ECS, there were no obvious differences in its pattern of perivascular deposition.

The colocalization of tracer around the central canal was analysed at each spinal level in all outflow experiments. After grey matter injections, ependymal deposition of tracer was detected in 45% of all spinal levels in control animals. This did not vary greatly after modulation of physiological parameters. In free breathing, hypertensive and tachycardic rats, 55%, 51% and 45%, respectively, of all spinal levels had AFO-647 labelled central canals. Similarly, after white matter injections, tracer was found around the central canal of 45% of all spinal levels in control animals. In free breathing rats, this was observed in 47% of spinal levels. Slightly higher rates were documented in tachycardic and hypertensive rats at 56% and 62% respectively. Unlike in spinal inflow experiments, AFO-647 was invariably detected over contiguous spinal levels in all rats. Confocal microscopy yielded further evidence of possible specialised pathways between subependymal perivascular spaces and the abluminal aspect of the ependymal layer (**Fig. *23*** l). Continuous bands of tracer appeared to bridge microvessels and the heterogeneously labelled central canal (**Fig. *23*** k, l).
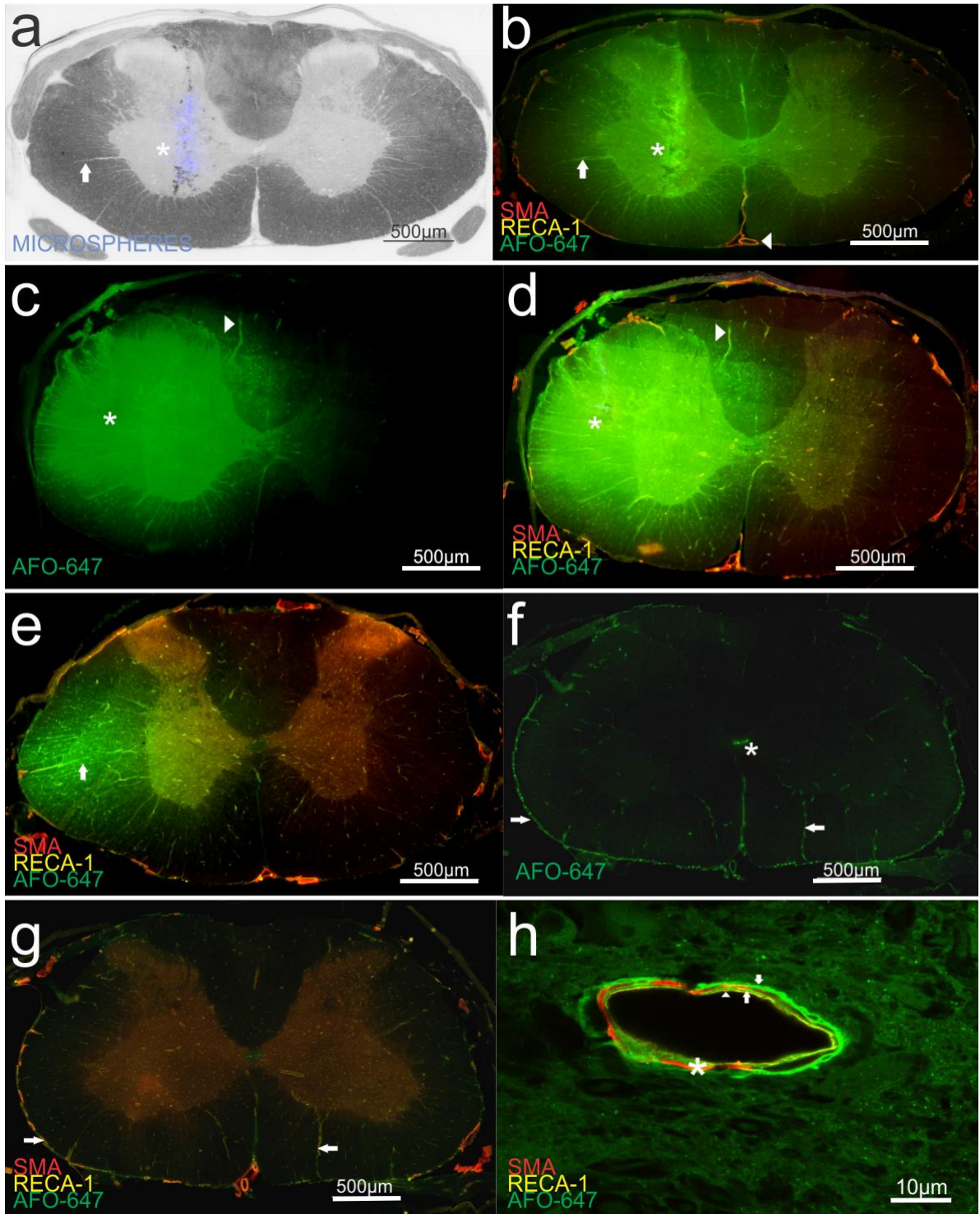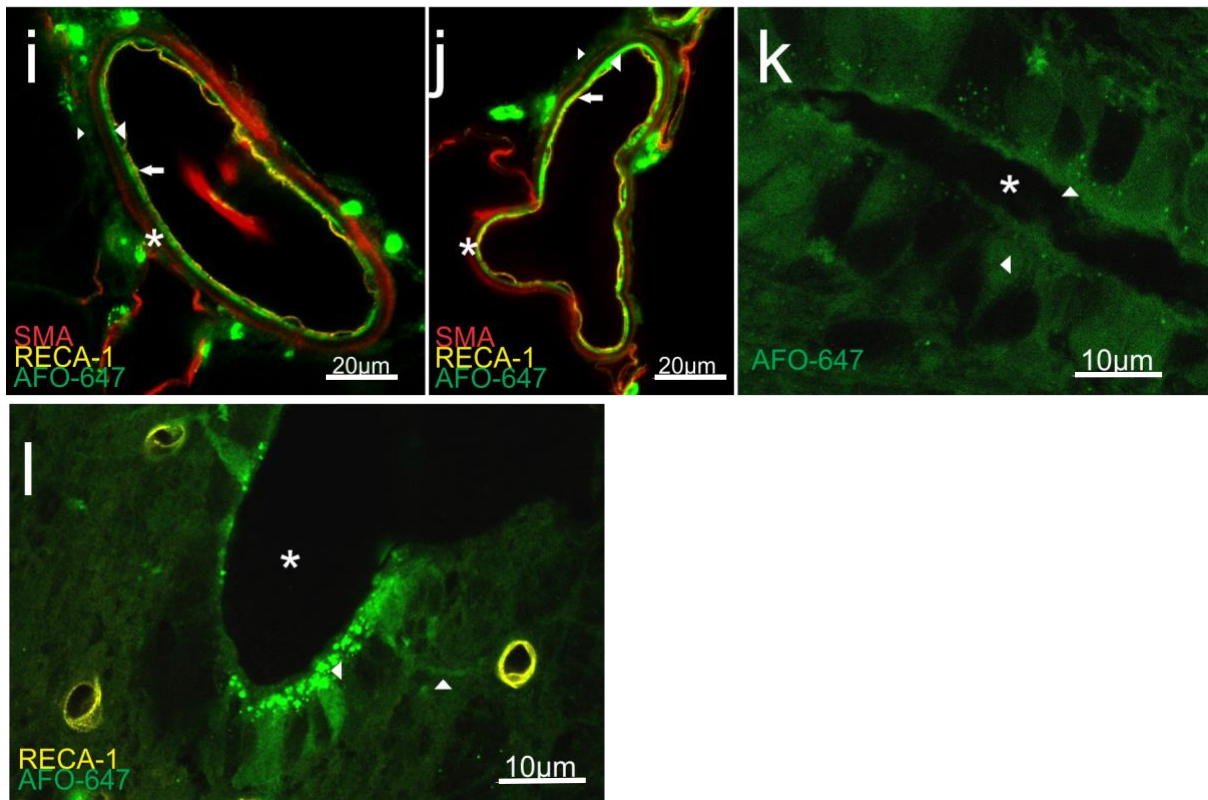
Fig. 23 Qualitative analysis of redistributed AFO-647 after injection into the spinal interstitium. The spinal grey matter **a**, and the lateral white matter tracts **c**, **d** were cannulated by a fine needle (at approximately C8). Inert fluorescent microspheres (marked by * in **a**) mixed into the AFO-647 tracer confirmed the injection point. **b** After grey matter injections (* marked injection point), there was radial redistribution of tracer locally into the surrounding white matter and into the contralateral hemicord. There was selective concentration of tracer around radially projecting blood vessels that end ultimately on the pial surface (up arrow). Extramedullary vessels, such as the anterior spinal artery (ASA, left arrow head) were also labelled by tracer. Note that subpial tracer was absent. **c, d** After white matter injections, there was local radial spread of tracer into the grey matter and nearby subpial white matter. Less of the contralateral hemicord was involved. There was accumulation of tracer around radially projecting blood vessels (right arrowhead). **b, d** Merged AFO-647, RECA-1 and SMA channels. **e** Just caudal to the white matter injection site (approximately T1), intramedullary tracer signal was delimited by the lateral white matter tracts (up arrow). **f** Three spinal levels rostral to the injection site (approximately C5), tracer was found circumferentially on the pial surface (left arrow head) and around penetrating radial blood vessels (right arrow head).**e,f** Note AFO-647 tracer deposition around the central canal (*) rostral and caudal to the injection site. This pattern of tracer distribution is highly suggestive of interstitially injected AFO-647 effluxing into the SAS, redistributing rostrocaudally and re-entering the cord parenchyma via perivascular spaces. **g** Merged AFO-647 and vascular antibody channels of a remote spinal level. **h-j** In both extramedullary and intramedullary arteries and arterioles, tracer deposited distinctly in multiple layers (confocal microscopy, x100 magnification). AFO-647 was found external to, and within the tunica media (marked by *) of the ASA, **i**, grey matter arteriole, **h**, and arterial vasocorona, **j**. Arrows mark the yellow endothelium, while the layers of green AFO-647 are marked by oppositely pointing sets of arrow heads and arrows. **h** Note the delineation of neuronal nuclei and the tortuous spinal ECS by AFO-647. **k,l** The central canal at x100 magnification on confocal microscopy. The left arrow head in **l** and the up arrow head in **k** emphasise the heterogeneous, speckled deposition of tracer favouring the luminal aspect of the ependymal lining (* is the lumen of the central canal). Tracer also deposited around ependymal nuclei (marked by left arrowhead in **k**). The up arrow head in **l** points to a serpiginous trail of tracer, suggestive of privileged pathways between the subependymal vasculature and the central canal

4.6   Discussion

We have undertaken a comprehensive study of CSF flow dynamics in the spinal SAS, as well as fluid and solute influx into, and efflux from the spinal cord. Complementary *in*

vivo and *ex vivo* imaging modalities characterised the effects of intrathoracic pressure and arterial pulsations on fluorescent tracers injected into the CSF and spinal cord interstitium. These studies have yielded largely concordant findings. In the cervicothoracic SAS, alternating negative and positive intrathoracic pressures of spontaneous respiration were associated with greater CSF flow compared with continuous positive pressures in mechanical ventilation. The same mechanisms likely exerted a dominant effect at a microscopic level, promoting fluid flow into the spinal interstitium via perivascular spaces and through the pial surface. Compared with respiration, arterial pulsations did not appear to play prominent roles in driving CSF through the SAS or into the spinal interstitium. Tachycardia did not affect spinal inflow. Although elevated mean arterial and pulse pressures did increase spinal inflow, its effect was eclipsed by a modest increase in respiratory rate. Elimination of solute from the spinal grey and white matter interstitium was stimulated by hypertension and tachycardia, but not by transmitted epidural pressure fluxes from the respiratory cycle. Finally, privileged tracer entry into and drainage from the spinal parenchyma via perivascular spaces were mediated by similar anatomical pathways.

The literature is replete with animal studies in which a tracer is injected into either the SAS or the brain parenchyma. This study has confirmed the paramount importance of respiration and cardiovascular pulsations as drivers of fluid flow in and around the spinal cord. The conflicting results obtained by different groups from previous tracer studies may, in part, be explained by uncontrolled variations in physiological parameters. Recently, intracisternally infused microspheres were used to study perivascular hydrodynamics of CSF in mouse brains by two groups. One group used free breathing animals [318] while the second group used mechanically ventilated mice [329]. The microspheres in both studies were observed to move in an oscillatory pattern

and their mean velocities were found to be similar (17±2 [329] vs 18.7 [318] μm/s). However, close scrutiny of the real-time videos revealed distinctly greater displacement of microspheres in the free breathing mice compared with ventilated animals. Moreover, the nature of the force driving microspheres along the vessel was a critical point of contention between the groups. One group contended it was CSF secretion by the choroid plexus, while the other group proposed it was arterial pulsations [318]. It is possible that the effects of mechanical ventilation may be responsible for divergent conclusions in otherwise similar experimental set ups. To ensure comparable results, meticulous attention should be paid to haemodynamic and respiratory factors in future experimental designs investigating fluid and solute transport in the CNS.

4.6.1 Fluid flow in the subarachnoid space

Here, we described the first novel deployment of ICG and the IR800 NIFR function on a commercial operating microscope to assess spinal CSF flow in real-time. Tracer injected into the cisterna magna of dead animals was not observed to redistribute caudally (results not shown). Similar results occurred when CSF leaks were detected. These negative controls indicate that cardiorespiratory pulsations are critical forces in driving CSF. In this study, tracer signal from the dorsolateral aspects of the SAS was acquired. It is not known whether ICG signal from the ventral SAS was detected.

Other groups have previously injected ICG into the SAS to assess CSF flow and lymphatic outflow [528-531]. However, in these studies real-time flow data were not acquired. Moreover, fluorescence was diminished by overlying soft tissue, impairing spatial resolution. In our experiments, muscle was extensively dissected to maximise tracer signal transmission, while preserving the dorsal bony elements to minimise disturbance of SAS hydrodynamics. The relationship between ICG concentration and photon excitation/emission (fluorescence quantum yield) is non-linear [532]. This raises the

possibility that fluorescence intensity in this study may not correspond directly to ICG concentration. The higher ICG signal detected in free breathing animals may be partially a consequence of greater mixing and turbulence in the SAS.

There was a conspicuous loss of ICG signal around the upper cervical spinal cord (observed in *ex vivo* macroscopic imaging and real-time *in vivo* flow). Intense subdural staining by ICG tracer was found at the craniocervical junction, raising the possibility that ICG precipitates had deposited in this area, either due to local reaction with ionic compounds (a known property of ICG [532]) or perhaps secondary to low or absent CSF flow. Advanced MRI studies in humans have demonstrated that at C2 there may be no net flow due to opposing CSF flow vectors [336]. In addition, fluorescence quenching (reduction in intensity) may occur above an ICG concentration of 50 μM [533], a consequence of stagnant flow in this area.

It has long been held that cardiac pulsations drive CSF flow in the cranial SAS [211, 291, 444, 446, 447], but whether this also holds true in the spinal SAS is unclear. A number of investigators posited that lumbar CSF pressure waves originate from spinal arterial pulsations with some contribution from the cranial vasculature (such as the choroid plexus) [454-456]. This is supported by at least one canine study involving spinal blocks and aortic occlusions [454]. Physiological drivers of CSF flow have only recently piqued the interest of CNS fluid researchers. Most of the data have been derived from human MRI brain studies, and the role of respiration in spinal CSF dynamics is not clear. In these studies, the dural venous sinuses transmit pressure changes from the thorax and abdomen to the cranial SAS [211]. Recently, the Dreha-Kulaczewski group demonstrated prominent rostral movements of CSF throughout the spinal canal at the beginning of forced inhalation in human subjects using real-time PC-MRI. Inspiration-induced CSF waves were more pronounced than those associated with cardiac pulsations, which

were low amplitude [282, 470, 475]. However, forced expiration resulted in caudal flow from T6 and very low flows rostral to T1–4. The authors hypothesised that a "watershed" point at the level of the heart divided the spinal SAS into two compartments. This in turn reflects the intimacy between intrathoracic and intraabdominal pressures, and the pressures within epidural venous plexus that are thought to modulate CSF dynamics. Yildiz et al [333] also employed real-time PC-MRI and found that deep inhalation resulted in the rostral movement of CSF, however, cardiac and respiratory components contributed equally to CSF velocity during deep breathing, but not natural breathing. A criticism of the methodology in this study was that PC-MRI is a technique that employs cardiac cycle triggering to acquire and average images, potentially overlooking the respiratory contribution of CSF flow [235]. Takizawa et al [478] employed an asynchronous two dimensional PC-MRI technique under respiratory guidance to analyse the respiratory and cardiac components of CSF flow separately in healthy adult brains. They observed larger CSF displacement secondary to respiratory events compared with cardiovascular impulses, although this gave rise to higher velocity flows. They provided quantitative evidence of small, rapid CSF pulsations due to cardiac drivers while respiration generated slow, large fluid waves.

To summarise, previous investigators have focused on brain physiology, and some authors contend that cardiac pulsations drivers impart a greater driving force on CSF flow than respiration. Recent studies investigating respiration have applied advanced MRI techniques to human subjects undergoing forced respiratory manoeuvres. We have demonstrated in an animal model for the first time, that intrathoracic pressure has a greater impact on the of modulation of spinal CSF hydrodynamics than arterial pulsations. The binary effects of free breathing versus mechanical ventilation may not be directly comparable to incremental changes in heart rate and pressure. However,

neither inducing tachycardia nor doubling the MAP resulted in as much spinal CSF flow as the introduction of negative intrathoracic pressures. It is possible these tracer studies may not have enough spatial resolution to discern contributions from arterial pulsations to fluid flow in the SAS.

In these studies, CSF tracer wavefront velocities were computed at the atlantoaxial interval. However, it is crucial to note that a mixing phenomenon was likely responsible for the tracer bolus redistributing craniocaudally. Spinal CSF flow is thought to have an oscillatory nature [235], modified by complex geometries of nerve roots and trabeculations resulting in eddies and vortices [287, 292, 296-298]. These hypotheses have largely crystallised from computational modelling studies. MRI and animal studies have traditionally lacked spatio-temporal resolution to confirm this phenomenon. Thus, it is important to be cognisant that the "velocity" of the tracer does not indicate a state of unidirectional flow of fluid but may reflect, instead, the rate of solute transport and redistribution in the spinal SAS.

There are conflicting results from the macroscopic analysis of SAS redistribution of ICG and AFO-647 in the *ex vivo* studies. There is no reliable way to distinguish whether fluorescence signal emanated from the extradural (secondary to leakage of tracer during perfusion/fixation), intradural, intramedullary or any combination of these compartments. The relatively low intramedullary AFO-647 fluorescence (but elevated tracer intensity macroscopically) observed in the tachycardic and hypertensive cohorts suggests there may have been prominent retention of tracer within the dura or even the leptomeninges. Analysis of the macroscopic distribution of AFO-647 should proceed with caution due to its possible poor specificity. Furthermore, all *ex vivo* studies involving ICG may be unreliable due to possible undefined chemical reactions with itself, or with surrounding structures.

4.6.2 Fluid flow into the spinal cord

Other groups have previously employed two-photon intravital microscopy to study murine brains. Here, we report the first ever application of this advanced technique to investigate fluid and solute transport mechanisms in the spinal cord. Spinal cord intravital imaging is challenging because of the greater distances the lasers are required to penetrate compared with cranial windows. Movement artefacts also hamper image acquisition and processing.

Two-photon intravital and epifluorescence microscopy were complementary techniques. Intravital microscopy provided multiple, small acquisition volumes of living tissue, centred at the pial interface. We acquired both real-time series and snapshots (not shown) of the dynamic rate and nature of fluid exchange, presumably from the SAS to a variable distance deep to the pia. The *ex vivo* epifluorescence experiments, however, allowed quantification of the total cervicothoracic solute and fluid inflow over a predetermined interval. The intravital finding of rapid microsphere velocities and displacement in free breathing rats provided the physiological explanation for the significantly greater tracer inflow in their *ex vivo* counterpart studies. It also suggests that the increased interstitial inflow of tracer is not merely a consequence of greater volumes of CSF in the overlying SAS. Transmitted cyclical intrathoracic pressures (via the epidural venous network) result in deformation of dura and fluid movement not only in the SAS, but also microscopically at the level of the pia. If negative intrathoracic pressures are eliminated, movement of fluid even at the perivascular level is also dampened. To our knowledge, the effect of intrathoracic pressure on fluid and solute transport into the spinal interstitium has not been previously characterised. Although the physiological effects of respiration on spinal CSF dynamics were the greatest at the mid cervical levels (suggested by NIFR experiments), T3 was chosen for these intravital studies as the superficial location minimised movement artefact.

In *ex vivo* spinal inflow studies employing AFO-647 tracer, two mechanically ventilated control groups were established. We have demonstrated that higher overall tracer intensity was found in the MV_{normal} cohort (ventilated at 66 breaths per minute), compared with the MV group (ventilated at 50 breaths per minute). It is plausible that the rate of ventilation could account for the difference in tracer inflow between the two groups. *In vivo* studies were, however, not performed to investigate whether CSF tracer wavefront and/or microsphere velocities were increased in the MV_{normal} cohort, that is, those with a higher respiratory rate. This should be a subject of future enquiry.

In hypertensive rats, inflow of tracer was reduced compared with control rats that had a higher ventilation rate (MV_{normal}). However, compared with the control group with similar respiration rate (MV), there was increased intramedullary inflow. In corresponding intravital experiments where the control cohort had matched respiratory rates, slightly higher particle velocities and displacements were observed in hypertensive rats. It was noted above that *in vivo* characterisation of perivascular flow in control rats with higher ventilation rates (MV_{normal}) has not been performed. However tempting it is to make the inference, it is still unknown whether a higher frequency of the respiratory cycle exerts a greater effect on fluid inflow than higher pulse pressures. It is possible that hypertension does induce elevated perivascular inflow, while impeding solute and fluid transport via other routes (for example, transpial). This would account for the elevated tracer signal within the grey matter (observed in **Fig. *17*** f and **Fig. *18*** d,g), where most of the intramedullary arterioles are located, but a paucity of fluorescence elsewhere. Other confounding factors in the intravital study include the small number of animals studied, and the limited sampling of perivascular spaces at only one spinal level.

Nevertheless, at least some of these findings from these *ex vivo* and intravital experiments support the long-held hypothesis that arterial pulsations generate the motive force for perivascular transport of fluid and solutes. These have largely been derived from animal models where brain perivascular fluid movement is attenuated after ligation of major afferent arteries or cardiac arrest (and the corollary when sympathomimetics are administered) [146, 360, 425, 457]. Hadaczek et al [460] coined the term "perivascular pump" to describe the undulating expansion and contraction of the arterial wall thought to propel solutes. The pump has, however, remained elusive as no anatomical structure(s) that could subserve this function has ever been described. The Nedergaard group initially demonstrated that carotid artery ligation reduced vessel pulsations in penetrating cortical arteries in mice and was associated with decreased CSF tracer accumulation around both leptomeningeal arteries and superficial penetrating arterioles. The authors then found that induced hypertension via intraperitoneal dobutamine uniformly increased tracer influx throughout the brain on fluorescence imaging of the extracted brain [461]. Recently, in the same laboratory Mestre and colleagues [318] employed two-photon intravital microscopy and particle tracking velocimetry on fluorescent microspheres, injected into the cisterna magna of mice, to derive brain perivascular CSF flow velocities. By synchronising the electrocardiogram and respiratory waves to the velocity of the tracked microspheres, they demonstrated that the microsphere motion was yoked to the cardiovascular pulsations, but not to respiratory patterns. They thus concluded that the displacement of the arterial walls was the source of the "perivascular pump" driving CSF in the same direction as arterial blood flow. The authors then acutely raised the MAP of the mice with Angiotensin II and found that the particle velocity reduced, concluding that the increased arterial stiffness, induced by hypertension, diminished the efficacy of the "pump" [318]. The authors did not address the earlier findings from their laboratory

that appear to give conflicting results after induction of hypertension. In a mathematical model, Bilston et al [151] used computational modelling to demonstrate that arterial pulsations could induce fluid movement in the perivascular space in the direction of the arterial wave. They found the greater the pulse wave velocity and arterial deformation, the greater the flow rate. It was suggested that these pulsations could lead to fluid flow in the perivascular space even against "adverse" pressure gradients. In a follow up axisymmetric model, they then showed that a mismatch in relative timing in arrival of a CSF pressure wave in the spinal SAS and an arterial pulse could theoretically drive perivascular fluid inflow along a small artery entering at right angle to the spinal cord [151]. Although blood pressure appears to be a crucial facilitator of fluid transport, there is inconsistent evidence from the literature and our experiments on the precise effects of hypertension on CNS fluid influx.

Raising the heart rate in isolation resulted in increased interstitial tracer inflow compared with control rats with similar ventilation rates (MV). Compared with animals that had higher respiratory rates (MV_{normal}), however, this difference disappeared. These findings, unlike in hypertensive rats, were not supported by intravital experiments. No difference in microsphere velocities were detected between the tachycardic rats and the control group (which had matched respiratory rates). Given these observations, it may be reasonable to conject that pulse rate may not have as much of an effect on spinal SAS hydrodynamics or interstitial inflow as pulse pressure. The number of fluid propelling "events" is not directly proportional to degree of endogenous penetration of the tracer. There was, however, isolated higher tracer influx into the grey matter in tachycardic rats compared with control. This raises the possibility that increased arterial pulsations may facilitate perivascular transport from the pial surface to the dense central arterial network. Other pathways such as transpial influx are not affected. This may be similar to

the proposed mechanism in which AFO-647 selectively accumulated in the grey matter of hypertensive animals. No other authors have previously investigated the effects of pulse rate on intraparenchymal CNS fluid inflow.

One of the major caveats in interpreting the results of the intravital studies is the co-localisation of the microspheres in relation to the perivascular space. It was evident that microspheres were often not present at the depths of z-stacks around small, presumably subcortical blood vessels. As the neuropil was not fluorescently labelled there was uncertainty as to whether the microspheres: 1) were in the SAS, at the level of the pial or subcortical and 2) accumulated in compartments that could be considered perivascular. If the microspheres were subarachnoid, it is possible they travelled in putative pial sheaths that according to some authors technically constitute the perivascular space [345, 346, 406]. Induced hypertension and tachycardia may exert different effects in these different compartments and potentially yield different microsphere velocities. Bedussi et al [329] recognised in their own intravital work the possibility of microspheres, either in isolation or in aggregates, being too large to traverse the tapering perivascular space. In future intravital experiments, it will be necessary to confirm histologically in harvested specimens whether microspheres are able to deposit in subpial perivascular spaces. Alternatively, the glia may be immunofluorescently labelled to visualise the relationship between tracer and the perivascular space.

Influx of tracer into the spinal interstitium involves both transpial as well as perivascular routes. Free breathing, but not hypertension and tachycardia, was strongly associated with a propensity for transpial migration of tracer from the SAS into the spinal cord. It accounted for the significantly higher fluorescence signal in both the white matter and the whole cord. This suggests that the entry of fluid and solutes via transpial pathways might be directly related to SAS hydrodynamics. After crossing the

pial boundary, AFO-647 fluorescence radially attenuated towards the central canal. This may suggest a diffusive process in the ECS (4.6.3).

In *ex vivo* samples, AFO-647 selectively coalesced around blood vessels of all types. This confirmed the perivascular space as a privileged pathway for fluid and solute transport. Lam et al [402] observed deposition of intracisternally injected AFO-647 tracer around spinal intramedullary arterioles, venules and capillaries. Wei et al [325] also observed preferential accumulation of cadaverine tracer around numerous blood vessels but did not clarify whether venules were present. Our findings are a distinct departure from the popular glymphatic theory, wherein fluid and solute gain peri-arterial access to the CNS, flow through the ECS to collect around major draining veins and exit the interstitium via peri-venular pathways [327, 461, 510, 515]. Others contend that venules have no role in fluid transport altogether and that different compartments within the perivascular space mediate efflux and influx [347]. We have detected discrete layers of AFO-647 tracer in both the tunica media and adventitia of intramedullary and extramedullary arterioles and arteries, as well as around the vessel adventitial walls of venules and capillaries. Firstly, this suggests that there is a continuous fluid conduit around blood vessels from the arteries to veins [230]. As veins and arteries are both exposed to the SAS, it is reasonable to deduce that both types of vessels may be involved in fluid exchange. Additionally, the finding of tracer within the smooth muscle layer lends credence to the model of the "vascular basement membrane" [427] as a channel for fluid and solute transport.

4.6.3 Fluid outflow from the spinal cord

In the previous study of fluid outflow from the rat spinal cord, tracer redistribution was assessed at 20 and 60 min after delivery into the parenchyma [527] (3.4.1). Interstitial spread was limited to within one level caudal and rostral to the injection point. Here, we

have demonstrated that even 180 min after delivery (the upper limit of length of time rats could be kept haemodynamically stable under altered physiology), endogenous tracer movement was similarly limited to adjacent spinal levels. AFO-647 exhibited similar isotropic and anisotropic patterns of spread within the grey and white matter, respectively. Tracer injected into the grey matter demonstrated radial redistribution outwards from the injection point. Delivered into the white matter, AFO-647 was largely confined within the parallel myelinated tracts. These results suggest that diffusion governs endogenous spinal solute and fluid transport, although advanced techniques such as integrated optical imaging (IOI) and real-time iontophoresis [331] will be required to confirm this. There is mounting *in silico* evidence that convective flow, as suggested by the glymphatic theory, is implausible in the ECS of the CNS [423]. Concerns about the interpretation of *ex vivo* preparations in outflow studies should be addressed by real-time *in vivo* imaging of injected ECS tracers. Arbel-Ornath et al [534] employed two-photon intravital microscopy to track fluorescent dextrans injected into murine brain. A rapid co-localisation to the arterial basement membrane of the perivascular space was reported. No tracers were detected around venous structures. Biexponential reduction of tracer over 30 min was interpreted by the investigators evidence of bulk flow in the perivascular space. However, in these experiments the dura was opened, compromising the hydraulic integrity of the system. No equivalent investigation has been undertaken in the spine.

Whether CNS solutes are cleared primarily into lymphatics of the dura and large blood vessels, or into the SAS is still unclear [260, 320]. There are likely differences among animal species and may vary with age and pathological conditions. Substantial accumulation of tracer around the pia, with subsequent perivascular inflow into the parenchyma at remote spinal levels was not observed in our previous study, up to

60 min after injection [527]. Given we have observed this phenomenon after three hours, spinal outflow of tracer is at least partially to the SAS.

Intrathoracic pressure did not appear to affect the redistribution of injected tracer into the spinal cord away from the injection site (**Fig. *22***). However, there was greater tracer signal macroscopically in the craniocaudal axis in free breathing rats compared with control. This incongruence between macroscopic and microscopic results could be explained by the fact that the spinal cord itself (as opposed to the thecal sac and spinal SAS) is not directly exposed to epidural venous plexus pressure changes. The amount of solute egress from the cord is therefore minimally affected by respiration. However, any tracer that is drained into the SAS from the cord parenchyma is mixed more efficaciously and redistributed further away, possibly resulting in higher fluorescence intensities in the SAS. Moreoever, the amount of effluxed tracer in the SAS may be too small for a difference in tracer signal (between the free breathing and control groups) to be detected when it is subsequently redistributed back into cord parenchyma at remote spinal levels.

Hypertension and tachycardia, however, appear to encourage solute efflux from the cord into the SAS. There was concordance between the fluorescence intensities measured macroscopically over the rostrocaudal axis, and the axial microscopic signal intensities. As all groups were mechanically ventilated, and therefore under the influence of the same redistributive mechanism in the SAS, the amount of tracer at remote levels was a reflection of the amount cleared locally from the injection site.

Previously, Hadaczek et al [460] showed adrenaline induced hypertension and tachycardia promoted apparent bulk flow of different sized macromolecules through the brain ECS of rats. In a murine model of Alzheimer's Disease exposed to cerebral hypoperfusion, mural Aβ was observed to accumulate in leptomeningeal vessels,

reflecting reduced solute drainage [462]. Despite the paucity of similar laboratory data, there may be some insight from computational modelling on the mechanisms that explain our experimental findings. ISF and solutes of the CNS may be driven by counterflowing contrary waves generated by arterial pulse waves [463]. These contrary waves generate a valve-like action that prevents reflux during the pulse wave's passage along the vessel wall. Carare and colleagues hypothesised that deformation of the vascular basement membrane (and other biochemical interactions) could provide this valve action, driving solutes and fluid centrifugally along arterial walls [464]. However, in a later combined analytical and numerical model, these collaborators found that the computed arterial pulsations were eight times too weak to generate outflow in the basement membrane [465]. The wavelength of the arterial pulsations was too long relative to the artery section, resulting in only small pressure gradients along the vessel length. This group then injected Aβ into mice hippocampi and demonstrated no difference in drainage between groups receiving a beta-blocker and saline [465]. Other mathematical studies have postulated peristaltic wave motion induced by pulsations [467]. Recently, Sarntinoranont and Rey investigated the effects of blood vessel pulsations on solute transport in the parenchyma and the perivascular space using two hydraulic network models [432]. Increased pulsatility was shown to increase dispersion, but not convection. Peak fluid velocity in the parenchyma and perivascular spaces increased with pulse amplitude and vessel size. Thus, deformation of the vascular wall from arterial pulsations likely has a central role in promoting fluid and solute efflux from the spinal interstitium. The precise mechanisms require further laboratory and mathematical investigations, but is likely more complicated than valve like actions that participate in unidirectional "pumping".

In all outflow experiments, tracer accumulated in distinct layers intermingling with the tunica media of intramedullary and extramedullary arterioles and arteries (**Fig.** *23* h-j). There was also deposition of tracer external to the smooth muscle layer. Around veins, venules and capillaries AFO-647 circumscribed the endothelium. Thus, all blood vessel types have been implicated in spinal outflow, similar to findings from the spinal inflow studies. These findings recapitulate results from earlier work on fluid outflow pathways in the normal spinal cord [527] (3.5.2.3). Dedicated ultrastructural studies will be required to clarify the precise anatomical relationships of the tracer and the various compartments of the perivascular space. However, these results are supportive of the role of vascular basement membrane(s), as well as the compartments between the glia limitans and pial sheath, or the adventitia, in mediating solute clearance. These findings do not definitively address whether the perivascular space is fluid filled or is actually formed by the basement membrane. Findings from *ex vivo* preparations should be cautiously interpreted. Recent groups have reported transmural inward spread of tracer upon fixation with aldehydes [318]. Others have demonstrated increased macroscopic deposition of tracer around relatively superficial vessels of the brain upon animal sacrifice [320]. Nevertheless, it is intriguing that pathways of inflow and outflow appear shared. This raises the possibility that there is bidirectional, to-and-fro mixing of fluid in the perivascular space that is able to rapidly distribute solutes. The direction of tracer redistribution depends, therefore, on whether it is injected into the SAS (inwards, towards the central canal) or into the parenchyma (outwards, towards the pial surface) [230].

The central canal may be a reliable efflux pathway for the spinal interstitium. Milhorat and colleagues had previously ascribed the central canal with a "sink" function for solute and metabolites [516]. Free breathing, tachycardia and hypertension did not appear to

have major effects on drainage into this compartment from the ECS. However, the labelling of the central canal was related to the degree of overall tracer influx. Therefore, tracer signal was increased in free breathing rats and relatively attenuated in hypertensive cohorts. The mechanisms governing flow towards central canal may be similar to those responsible for perivascular spinal inflow of fluids. In both inflow and outflow studies, contiguous bands of tracer were detected between the subependymal microvasculature and the central canal ependymal cells. To confirm and further examine this putative pathway, the next step is to fluorescently label ependymal cells (such as with F-actin [535]) in future intravital studies of inflow and outflow. Tanycytes and complex ependymal basement membranes (labyrinths) are thought to subserve this putative connection between CSF, ISF and the central canal [193]. Moreover, Cifuentes et al had proposed more than two decades earlier the possibility of bidirectional fluid transport between the central canal and the SAS via perivascular spaces, particularly via peri-arterial pathways of the central branches of the ASA [305]. The role of the central canal in fluid exchange may not be important in humans as there is progressive atresia of this structure with age [310].

A comprehensive model of fluid transport that consolidates the findings from these experiments, as well as data from previous laboratory and computational studies, may still be just out of reach. There is, however, evidence that the same anatomical pathways subserve inflow and outflow, so it is reasonable to deduce that the two processes occur simultaneously and may be subject to the same physiological drivers. This study provides new insight into the dramatic effects of cyclical intrathoracic pressures on fluid flow from the SAS to the perivascular space (at least at the leptomeningeal level). Arterial pulsations likely result in complex deformation of the vascular wall that propel perivascular fluid and solute transport. We have provided evidence that tachycardia and

hypertension are associated with motive forces for tracers injected either into the SAS or the ECS. However, this has not necessarily resulted in increased overall solute influx or drainage. An interplay of factors—such as the width of the perivascular space as dictated by the phase difference of the arterial wave with CSF pulse wave [151], the stiffness of the arterial wall, the possible predominance of egressive or ingressive flow at the microscopic level as the extremes of physiology are approached—may ultimately determine the net direction and magnitude of fluid and solute exchange. Moreover, the possible effects of bidirectional fluid flow at the level of the perivascular space [230], the role of the central canal in mediating intramedullary drainage, and local microanatomical geometries in the SAS at different spinal levels add further layers of complexity. Simple tracer experiments in animal models, while invaluable in our attempts to elucidate the basic mechanisms of fluid transport, capture only a few colours of the kaleidoscope of driving forces governing a dynamic process.

4.6.4   Limitations

In the intravital studies a mixture of AFO-647 and fluorescent microspheres were intracisternally injected. The intention was to characterise the perivascular accumulation of AFO-647 *in vivo*. Although this tracer was successfully detected and visualised, it has proven difficult to quantitatively characterise AFO-647 inflow in both the *xy* and particularly, the *xyz* planes. There are, however, ongoing efforts to extract this data so that *in vivo* observations and measurements can be compared with the completed *ex vivo* experiments. This would mitigate some of the concerns about the effect of death on tracer redistribution; some authors have noted that upon perfusion of the animal there is a rapid surge in interstitial deposition of tracer [320]. The haemodynamic profile and vessel wall kinetics of the target blood vessels in intravital experiments have also yet to be characterised. It may be possible to delineate arterioles from venules based on erythrocyte velocity, and to track vessel wall displacement with

every arterial pulse wave. These properties can then be compared in control and test groups, which may clarify the relationship between deformation and stiffness of the arterial wall, and perivascular fluid transport.

4.6.5 Clinical applications and future directions

Syringomyelia is a disabling condition where fluid-filled cysts develop within the spinal cord and can lead to pain and neurological dysfunction [4, 7, 8]. It is secondary to a variety of pathologies but ultimately, is thought to result from an imbalance of spinal cord fluid inflow and outflow. Treatment in many cases is difficult as the underlying pathophysiology is incompletely understood. Fluid-filled cysts commonly develop when there is an obstruction in the SAS such as in Chiari malformation [20] or after spinal trauma in the form of arachnoiditis. The spinal SAS is clearly essential in transmitting forces that drive inflow. Moreover, alterations to the ECS and intramedullary vasculature that may be associated with spinal cord trauma can disturb ISF drainage mechanisms. The pathogenesis of syrinx initiation and growth is clearly much more complicated. However, a complete picture of the *normal* physiology of spinal fluid transport is required before *patho*physiology can be addressed. This body of work has contributed much to the former. The latter should heavily employ *in vivo* techniques in future experiments. Thus, the next steps are to investigate the effects of respiration and cardiac pulsations on spinal fluid inflow and outflow in syringomyelia animal models. Such models may include cisterna magna arachnoiditis [174] or spinal epidural constriction [536], post-traumatic [170] or spinal cord tethering [165] (see 5.6).

Drug delivery systems that bypass the BBB can potentially target diseases of the CNS much more effectively than conventional methods [491, 492]. Intrathecally delivered systems may be improved by exploiting the physiological parameters that maximise circulation and penetration of macromolecules from the SAS into the CNS.

Vasospasm after subarachnoid haemorrhage can lead to severe neurological deficits and stroke. Its pathogenesis is unclear, but there is experimental evidence that clot burden in perivascular spaces is implicated [537]. Thus, removal of adherent thrombi on blood vessels could theoretically mitigate vasospasm risk. We have already demonstrated that CSF flow in the spinal SAS is exquisitely sensitive to intrathoracic pressure. Clarifying the physiological effects on cerebral fluid exchange may be the first step in designing therapeutic or preventative measures against vasospasm.

There are no effective medical treatments for the deleterious secondary effects of spinal cord injury. These effects are thought to be mediated by release of excitotoxic factors that further potentiate local damage after primary injury [177]. An efficient system for removal of these metabolites would be advantageous and would be predicated on intimate knowledge of perivascular fluid exchange. Furthermore, some authorities advocate hypertension to prevent hypoperfusion as spinal cord autoregulation may be compromised [177]. We have demonstrated that the effects of hypertension in the spinal cord is still uncertain. This has implications for clinical protocols surrounding augmentation of blood pressure after spinal cord injuries.

4.7   Conclusions

Spinal CSF flow and fluid transport in the spinal cord are sensitive to physiological forces. Intrathoracic pressure changes associated with respiration drive CSF flow in the spinal SAS and inflow into the interstitium. Neither hypertension nor tachycardia alter SAS hydrodynamics substantially. Although there are inconsistent findings on their precise effects, blood pressure and heart rate have smaller impacts than the respiratory cycle on spinal fluid inflow. Tachycardia and hypertension facilitate drainage of ISF and solute from the spinal interstitium, whereas intrathoracic pressure fluxes appear to have little effect. In future laboratory experiments investigating fluid exchange in the CNS,

meticulous attention should be paid to carefully controlling these cardiorespiratory

parameters.

4.8   Acknowledgements

5 General Discussion

The aims of this thesis were borne out of the recognition that much remains unknown about the basic anatomy and physiology that govern fluid and solute transport in the spinal cord. This has hampered attempts to understand the pathophysiology of syringomyelia, a condition arising from a heterogeneous collection of pathologies. There is presumably a common pathway(s) that fundamentally results in an imbalance of fluid inflow and outflow. In order to grasp what abnormal physiology might entail, normal physiology needs to be clarified. Much of the research in this niche field has been performed on the brain, which has spawned a growing body of literature. However, the mechanisms of fluid transport in the spinal cord has remained largely unexplored. Until now, no information has existed on the pathways of normal spinal fluid outflow. After these anatomical pathways were investigated, the physiological forces that promote and inhibit spinal fluid exchange were examined.

5.1 Fluid flow in the subarachnoid space

NIFR imaging of the small ICG fluid tracer in the SAS has confirmed that CSF flow ceases with cardiorespiratory arrest. Elimination of normal inspiratory negative intrathoracic pressure had a greater effect on gross spinal CSF flow (or mixing) than modulation of MAP/pulse pressure or heart rate, within physiological extremes. There is mounting evidence from MRI studies of human subjects that the respiratory cycle is a dominant driver of CSF flow. The apparatus through which forces are transmitted is likely the continuous epidural venous–azygos venous system, and the deformable thecal sac. As spatial and temporal resolutions of specialised MR studies (such as PC-MRI) improve, further insights will be obtained at increasingly microscopic scales.

Many studies have employed intrathecal gadolinium to assess CSF hydrodynamics [331, 538]. The findings from the NIFR experiments investigating flow of CSF *in vivo* need to

be replicated with greater numbers and extended to the thoracolumbar spine. There is also scope for these corroborative studies to employ advanced MRI techniques such as intrathecal gadolinium. MRI can potentially capture the whole neuraxis and provide real-time supplementary data on cardiorespiratory fluxes. PC-MRI techniques enable blood flow, particularly venous, to be simultaneously measured. The non-invasive nature of MRI also eliminates the possibility of surgical dissection of paraspinal muscles (with its attendant haemodynamic changes) disturbing normal physiology.

5.2   Perivascular flow into and out from the spinal cord

The perivascular space is unquestionably a site of paramount importance in mediating spinal fluid exchange. Tracer studies may introduce bias into the relative significance of the multiple pathways of fluid transport (for example transependymal, transpial, etc). It is nevertheless reasonable to conclude that perivascular mechanisms facilitate privileged routes of inflow and outflow. After injection of AFO-647 into the spinal parenchyma, there was selective accumulation of the tracer around radially projecting intramedullary as well as extramedullary blood vessels. There was a contrasting lack of subpial fluorescence, suggesting that solutes could access preferential routes for clearance from the interstitium. With time, it was apparent that tracer drained at least partially into the spinal SAS, redistributing over the pial surface distant to the injection site. Moreover, higher MAP/pulse pressure and heart rates were associated with more endogenous tracer deposition remote from the delivery site, indicating greater clearance locally from the point of injection. Arterial pulsations, therefore, promote spinal outflow. Interestingly, when tracer was injected into the SAS there was predilection for intraparenchymal deposition around penetrating vasculature. There have been consistent findings from multiple imaging modalities of various tracers that elimination of the normal cyclical intrathoracic pressure waveforms leads to dramatic reduction of not only CSF flow, but also inward fluid transport at the microscopic level. There is

mixed evidence to indicate that hypertension and tachycardia result in greater inflow compared with hypotensive and bradycardic controls. These experiments need to be repeated in animals with a wider range of normal and abnormal physiological parameters.

From a microanatomical perspective, AFO-647 tracer accumulated around all vessel types in the same pattern regardless of whether it was delivered into the SAS or into the ECS. There was a predilection for the circumferential compartment between the endothelium and the glia limitans of capillaries, venules and veins. Around muscular arterioles and arteries, tracer was found consistently within and external to the tunica media. The possible post-mortem ultrastructural changes in tracer experiments after cardiorespiratory arrest and fixation with aldehydes deserve further consideration. However, these observations from this body of experimental work raise the possibility of common compartment(s) around arteries and veins and even capillaries where fluids and solutes exchange. In other words, the arena for inflow and outflow is shared and fluid movement is bidirectional. The mechanisms governing this could be characterised by mixing, distinct from diffusion and convection, where solutes move down their concentration gradient [230]. These driving forces are derived from cardiac pulsations and transmitted intrathoracic pressures at both macroscopic (SAS) and microscopic (perivascular) levels. Mathematical modelling will likely be central to furthering understanding of the role of arterial pulsations in perivascular fluid mechanics. To this end, laboratory studies involving live animals and tightly controlled vital parameters are required to generate the necessary substrates for computational experiments. Thus, there is an imperative to investigate spinal intramedullary fluid outflow under *in vivo* conditions. To perform such a study, a novel tracer delivery device would be needed. After delivery of a fluid tracer into the spinal parenchyma in a similar manner described

herein, this device would be severed at the level of the dura. The device is therefore on the one hand, robust enough to withstand durotomy and myelotomy in one pass, but on the other hand delicate enough to be truncated atraumatically. A topical sealant such as cyanoacrylate glue would be applied over the durotomy to prevent fluid leak. Intravital microscopy would then proceed. We have demonstrated in our intravital experiments, z-stacks of more than 1000 μm thickness can be acquired (data not shown). Previous studies have reported laser penetration of only 200–300 μm [327, 461].

5.3 Limitations of studies

One of the fundamental flaws of tracer studies is that injected macromolecules are susceptible to uptake, degradation and metabolism by the interstitium (1.3.7.2). Molecular weight and charge are just two properties that may limit their ability to penetrate barriers (for example, the spinal cord-CSF barrier). These factors may have affected the craniocaudal extent of AFO-647 movement after injection into the spinal cord parenchyma. Compared with a smaller solute such as Evan's blue, dissemination of AFO-647 was likely restricted to some degree by the tortuosity of the ECS (of both grey and white matter). Passage through perivascular spaces, and across the pia, glia limitans and ependyma would have been similarly impeded or facilitated due to its intrinsic properties ("sieving", see 1.3.7.2). The interpretation of these observations would then affect our understanding of physiological fluid outflow.

In many of the *ex vivo* experiments, although CSF leakage was meticulously prevented during and after the delivery of the tracer, removal of the needle was necessary to perfuse and fix the CNS. The innovation of the cisterna magna catheter in the intravital experiments should be implemented in all studies involving intracisternal delivery of tracers in the future. Mestre et al have demonstrated it is possible to perfuse a mouse with PFA *in situ* during multiphoton intravital microscopy [318]. The combination of

these techniques would eliminate CSF leakage and preserve tracer distribution with high fidelity.

In five animals, ICG was delivered in a similar fashion into the spinal grey and white matter in an attempt to study spinal outflow *in vivo*. Fluorescence was detected within one level rostral and caudal to the point of injection (results not shown). No extradural leakage ICG tracer was observed over the course of three hours. Upon perfusion, fixation and subsequent microscopic analysis of axial sections, however, only small amounts of the tracer remained in the tissue. This suggested there may have been poor fixation by PFA, rapid efflux of the ICG upon needle withdrawal, or lack of local tissue binding by tracer. Given that ICG appeared to be readily fixed to the dural and pial surfaces when injected into the cisterna magna, the most likely explanation is either the loss of the small volume of tracer during tissue processing or ICG did not bind to any spinal endogenous structures. Other technical problems were encountered with ICG. Tracer was not able to withstand the rigours of immunohistochemistry processing preventing confirmation of its perivascular deposition. The optimum concentration of ICG for investigating CSF flow has yet to be determined. As quenching of the tracer remains a possibility, future experiments should trial various concentrations of ICG. The possibility of ICG forming precipitates has not been eliminated. Although others have demonstrated that mixing ICG with lipids is not mandatory in its preparation as a fluid tracer, an ICG-human lipoprotein mixture should be considered in the future [528-531].

ICG may have a role in determining whether diffusion prevails as the fluid transport mechanism in the spinal ECS. ICG appeared to diffuse into the spinal parenchyma when infused intracisternally. It has exhibited many similarities to the small antibodies employed by Pizzo and colleagues [331], where the diffusion co-efficient of the brain

was determined based on previous IOI studies. The diffusion co-efficient of the spinal cord can also be determined in a similar manner.

Although *ex vivo* studies enable macroscopic assessment of tracer circulation, or quantification of bulk fluid movements, the effects of death and perfusion with PFA require further investigation. As discussed in 1.3.7.1, if PFA does indeed induce transmural migration of tracer and reduces in the width of the perivascular space, then findings on pathways of fluid flux (particularly in relation to vascular basement membranes) should be interpreted with caution. Attempts should be made by other groups to replicate and histologically confirm the phenomenon of transmural tracer migration as described by Mestre et al [318].

In all experiments investigating effects of physiology on fluid homeostasis, the intention was to precisely match the physiological parameters of control with test cohorts. However, this was not always successfully executed. Respiratory circuit pressures and heart rate were tightly controlled but blood pressure was at times labile and difficult to precisely regulate. This could have been secondary to the use of inhalational, as opposed to intraperitoneal delivered, anaesthetic. Arterial blood gases were also not performed in the intravital experiments due to equipment issues. Phenylephrine was effective at inducing and sustaining hypertension but in smaller animals, moderate tachycardia, unresponsive to hexamethonium, was observed. Therefore, this needs to be considered when interpreting results where the MAP was raised. In future experiments, the heart rate could be controlled with sinoatrial node pacing if this drug were used again. The circuit pressure merely gave an indication of the fluxes in intrathoracic pressure. Body plethysmography is necessary to fully characterise the precise changes in intrathoracic pressures and its transmission to the epidural venous network via the caval and azygos systems. Simultaneous recording of intraabdominal pressure would elucidate the effects

of mechanical ventilation on the epidural venous pressure in the lumbosacral spine. Central venous pressure monitoring may have been useful to ensure all animals were euvolemic. The most useful assessment of venous pressure would be just proximal to the epidural venous network around the thecal sac. This would be a worthy future pursuit, particularly during induced hypertension.

The wide-ranging effects of inhalational anaesthesia on both cardiorespiratory and CNS fluid systems need to be considered. Isoflurane depresses blood pressure, heart rate, respiratory rate and tidal volumes, and such changes are likely mass- and age- dependent. In these experiments, there were minute-to-minute variations in physiological parameters especially in free breathing animals. The results obtained in these cohorts could partially reflect greater cardiorespiratory fluctuations. It would be prudent to repeat these studies using injected anaesthetics, such as ketamine/xylazine, which will likely result in less physiological flux. Anaesthetics may also exert complex effects on cerebral blood flow, choroidal CSF production and CNS fluid exchange. Gakuba and colleagues [483] demonstrated that general anaesthesia (particularly isoflurane) impairs fluid inflow in the mice brain. These findings on the effects of sleep/wake cycle on brain waste clearance directly contradict those from the Nedergaard group. It is not known whether these effects of general anaesthesia increase with time, which would have implications on experimental methodology.

The effects of inotropes on ICP and venous pressure, as well as the impact of mechanical ventilation on thecal sac compliance have not been assessed. Complex relationships exist between ICP, intracranial pulsatility and vascular compliance [288]. Pulsatility refers changes to fluctuations in blood pressure related to the cardiac cycle and is not merely the same as pulsations [288]. Spinal thecal pressure should be measured in the future as

part of a systems analysis that aims to determine how MAP is translated to spinal intrathecal pressure [439].

5.4 Clinical implications

Intrathoracic pressure fluxes from respiration are translated to spinal CSF flow, which affects CSF/ISF exchange at the microscopic level. Obstruction of the SAS, from Chiari malformation, arachnoiditis or spinal deformity, could have downstream effects (literally and figuratively) on fluid homeostasis in the spinal cord. Valsalva manoeuvres are associated with transient, extreme positive pressures. The recoil that is transmitted to the thecal sac may have implications for sudden stasis of fluid exchange, leading to dissection of the syrinx into the parenchyma. If fluid transport is impaired by continuous positive airway pressure, the use of assisted ventilation in sleep apnoea should be reviewed. Ju et al [480] reported reduced Aβ protein levels in the CSF of sleep apnoea patients. It is possible that mechanical ventilation could have reduced solute clearance from the cord as tracer inflow is simultaneously diminished. Patients with upper cervical/brainstem cord syrinxes (or syringobulbia) often have respiratory failure which may necessitate assisted ventilation. Meticulous attention should be paid to the mode of ventilation to strike a balance between appropriate gas exchange and adequate CSF flow and ISF transport.

Syringomyelia may result from spinal dysraphism such as tethered spinal cord, but in these cases subarachnoid obstruction is usually absent. Thus, many hydrodynamic pathophysiology theories do not apply to these syrinxes. Arterial pulsations play a role in mediating fluid ingress and egress from the cord. Tethering of the spinal cord may lead to dysfunction of transmitted arterial impulses, which compromises the efficiency of intraparenchymal fluid transport. Spinal cord injury could result in abnormal

haemodynamic coupling to fluid dynamics via direct insult to the intramedullary vasculature.

Perivascular spaces are sites of great importance in fluid exchange. Regional variations in the density of blood vessels may affect the susceptibility of the spinal parenchyma fluid transport pathologies. The grey matter, for example, likely has more robust fluid drainage pathways and is therefore less likely to be affected by oedema. Blood pressure is likely an important driver of fluid and solute outflow from the parenchyma. Therefore, hypotension in spinal cord injury, either from spinal shock or from haemodynamic shock from other injuries, is particularly deleterious from the perspective of preventing secondary cord injury. An inefficient fluid and solute exchange system may result in accumulation of excitotoxic and oxidative factors and further local tissue damage.

5.5   Unanswered questions

One of the most important unanswered questions has been raised by our findings of tracer within the "vascular basement membrane" of blood vessels, and the fact that arterial pulsations appear to drive ISF/CSF exchange. The synthesis of these observations imply that fluid and solute transport occurs in a fluid filled, compressible perivascular space [431] (1.5.3). However, the precise anatomical configuration of the perivascular space is still a point of intense contention, and its resolution will likely lie in future *in vivo* investigations of the ultrastructure of the perivascular space, ideally free of the biases of tracer injections. No such study currently exists. Furthermore, a consensus should be established on the precise definition and nomenclature surrounding the perivascular space. Whether the perivascular space extends beyond the pia into the SAS, for example, is controversial.

In this thesis, the cervicothoracic spinal cord down to T4 was the focus of the studies. It is conceivable that SAS fluid dynamics are markedly different in the rat thoracolumbar

spine. Modelling studies in human have demonstrated that CSF flow velocities differ greatly between the upper and lower cervical levels (**Fig. *4***). There is also some evidence from MRI studies suggesting SAS flow differences exist between upper thoracic and lower thoracolumbar spine [477]. Thus, future experiments, especially *in silico* ones, need to incorporate a more holistic view of the vertebral column. Outflow has been investigated exclusively near the cervicothoracic junction, but future investigations also need to consider other regions of the spinal cord.

Recently, brain dural lymphatics and their role in fluid outflow have garnered significant attention [260, 320]. There is likely a role for spinal dural lymphatics in CSF/ISF clearance in at least some mammalian species [269]. It is possible that respiration and cardiovascular pulsations have profound effects on lymphatic CNS fluid drainage. Immunofluorescent labelling of lymphatic vessels and *in vivo* characterisation of lymphatic outflow have already been well described in the literature [272, 273]. Future studies could appropriate these techniques to the vertebral column, the superior sagittal sinus and the peripheral circulation. The role of the spinal nerve roots in facilitating fluid outflow has also not been investigated. These structures are richly vascularised and traverse the interface between dura, lymphatic vessels and CSF. They may even provide insight into the connection between extradural lymphatics and ISF (if ones exist).

In adult humans, the central canal is atretic, so its physiological role may be limited. Nevertheless, it may play a role in pathological conditions such as canalicular syringomyelia. With its prodigious depth of penetration, the SP8 DiVE intravital microscope can be employed to capture fluorescence around the central canal. If ependymal cells can be labelled *in vivo*, it might be feasible to characterise the mechanisms that govern solute and fluid exchange across this barrier.

5.6 Animal pathological models

The next step is to repeat many of the experiments detailed in this thesis in animal disease models. SAS block can be achieved either with constriction, whereby a ligature is used to obliterate the SAS circumferentially [536]. NIFR imaging of intracisternally infused ICG tracer can be then performed. The results from this thesis can be used as "normal" controls. Similarly, a multiphoton intravital study of this model would yield detailed *in vivo* data about the effects of altered SAS pressure transmission on fluid exchange at the microscopic level. The Stoodley group has published extensively on syrinx models including excitoxic [174] and spinal cord injury [170] models. These models can also be employed in NIFR and intravital studies. Finally, a tethered cord model was reported by Lee et al recently [165]. Unfortunately, this was more akin to an epidural compression model. Tethering by extradural chronic traction has been demonstrated in cats [539]. A similar set up recreating this in a medium or large animal would enable ultrastructural analysis of blood vessel changes in a tethered spinal cord. Intravital microscopy may give insight into altered intramedullary fluid transport.

The possibility of studying other mammalian species should be explored. A criticism of quadrupedal animal models might be that CSF/ISF dynamics could be subject to different sets of hydrodynamic laws compared with humans. A way to circumvent the need to perform primate experiments could lie in macropodid marsupials. Kangaroos and wallabies exhibit many experimental advantages. They are 1) bipedal 2) large enough to perform invasive pressure monitoring, instrumentation and imaging 3) readily accessible locally 4) born very immature such that developmental studies can be performed easily. Indeed, an Australian group recently published a study on spinal cord regeneration in the tammar wallaby (*Macropus eugenii*) [540].

6 Conclusions

The main conclusions from this thesis are:

1. Spinal cord ISF is transported radially in the grey matter and along parallel axonal fibres in the white matter.

2. The spinal perivascular spaces of both arterial and venous vessels mediate privileged pathways of CSF/ISF exchange. The same anatomical compartments are involved in the influx and efflux of fluid and solutes.

3. Respiration has a more prominent effect on CSF flow in the SAS and fluid inflow than arterial pulsations.

4. Elimination of negative intrathoracic pressure diminishes spinal perivascular and transpial fluid flow but has little effect on fluid and solute clearance from the spinal cord parenchyma.

5. Spinal fluid inflow may be increased in hypertension

6. Tachycardia may have little or no effect on spinal inflow.

7. Spinal fluid outflow into the SAS is increased in hypertension and tachycardia.

7 Appendices

7.1 Adverse events

Perioperative mortality was rare in all experiments. In the fluid outflow experiments (chapter three) there was one intraoperative respiratory arrest, thought to be due to malfunction of wall suction which removed isoflurane from the respiratory circuit. There were another two intraoperative mortalities secondary to similar mechanisms in experiments investigating effect of respiration on fluid inflow and outflow. In the intravital experiments, there were two intraoperative deaths. One was due to suspected endotracheal tube malposition, and another likely related to inadvertent pressure of the microscope objective on the animal's cervical spine. All animal mortalities were reported to the Animal Ethics Committee.

7.2 Results from control studies and other experiments

7.2.1 Practice injections of fluorescent fluid tracers in deceased animals

In all experiments, at least one deceased rat was used for initial practice of surgical techniques and as a negative control. This was repeated for ICG and AFO-647 tracers in inflow studies. In these studies, it was confirmed that no ICG fluorescence propagated down the cervical spinal column over 20 mins. The tracer remained around the injection site in the subarachnoid space, and this was corroborated with macroscopic fluorescence imaging and microscopic analysis of axial sections (employing AFO-647). This confirmed that physiological drivers in the live animals are necessary for CSF flow in the SAS and fluid exchange in the spinal cord.

7.2.2 CSF leaks

CSF leak occurred occasionally in both inflow and outflow experiments. This was evident visually under an operating microscope, in real-time during ICG injections and after macroscopic fluorescence imaging. In ICG inflow experiments, tracer was observed to spill out onto the atlanto-occipital membrane and the surrounding occipitocervical

musculature. Similar results were obtained to those in deceased animal experiments for both ICG and AFO-647. In outflow experiments, little or no appreciable tracer was detected in the parenchyma as most CSF leaks occurred around the time of the tracer infusions. These results support the importance of intact hydrodynamics in the SAS in mediating solute and fluid transport into and out of the spinal cord.

7.3 Supplementary Methods and Results from Chapter 4

7.3.1 Respiration is a major driver of fluid flow in the subarachnoid space

The number of rats analysed for studies where ICG was intracisternally infused was six per cohort. A total of 24 rats were used.

7.3.1.1 *Successful matching of physiological parameters*

The baseline physiological parameters including mass, heart rate, MAP, respiratory rate and pCO2 were well matched between mechanically ventilated controls and free breathing animals. The peak circuit pressures of control rats were significantly higher than that of FB (mean 7.98 vs 1.27mmHg, p< 0.001), while free breathing trough pressures were significantly more negative than that of control (mean –0.55 vs –3.19 mmHg, p <0.001) (**Fig.** *24* b). There was no difference in mass and circuit pressure between hypertensive and control animals, but there were minor significant differences in respiratory rate (mean 50 vs 44.67 breaths/min, p =0.0017) and pCO2 (mean 48 vs 59.67 mmHg, p = 0.0359). In hypertensive rats, the MAP and pulse pressure were successfully maintained at twice that of the control (mean of 139 vs 68.3 mmHg, p < 0.001; 80.05 vs 39.8 mmHg respectively) (**Fig.** *24* j,l). Due to the inotropic α_1 agonist effects of phenylephrine, HR was also slightly elevated in the test arm relative to comparative controls, despite administration of hexamethonium (mean 398.2 vs 34.5 bpm, p = 0.001). In tachycardic rats, the heart rate was successfully increased compared with control (mean 497.7 vs 349.5 bpms, p < 0.0001) without affecting MAP (**Fig.** *24* r, t). There were also no differences in circuit pressure and mass between groups. Again,

there were minor differences in respiratory rate and pCO2 (mean 51.57 vs 44.67 breaths/min, p = 0.0004; mean 39.5 vs 59.67 mmHg, p = 0.0034 respectively).
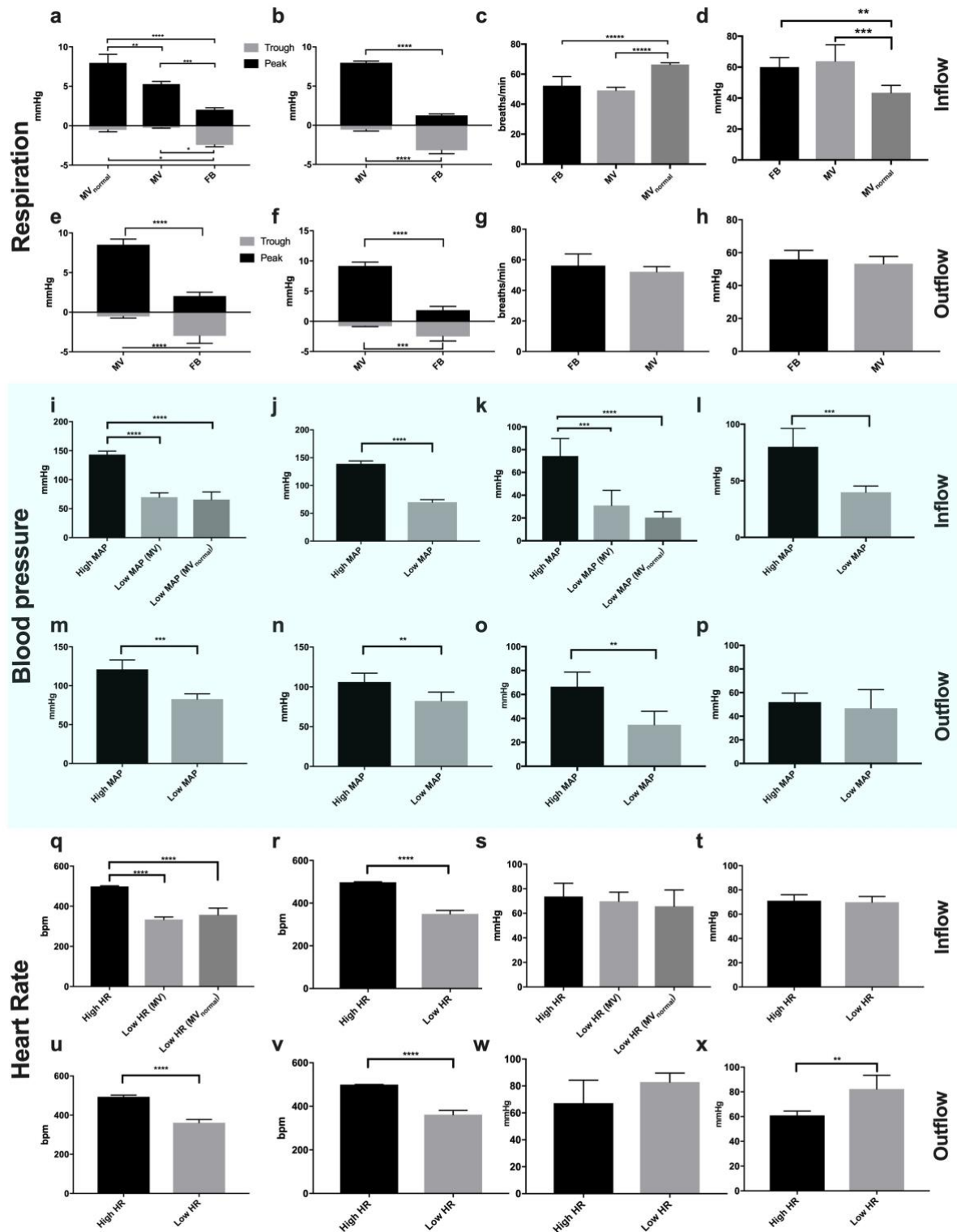
Fig. 24 Comparison of vital parameters between the physiologically modulated and control groups. Rats were allowed to either breathe spontaneously (FB) or were mechanically ventilated to normocarbia (MV$_{normal}$) or to hypercapnia (MV). **a, c, d** AFO-647 inflow studies **b** ICG inflow study. **a, b** In studies of CSF flow in the SAS and inflow into the cord, the peak circuit pressures of MV$_{normal}$ and MV cohorts were significantly higher than that

of FB. Similarly, the trough pressures were more negative in the FB group than either of the mechanically ventilated groups. **c** Free breathing rats had significantly lower respiratory rates (around 50 breaths/ min) than the MV_{normal} animals (set at RR of 66 breaths/ min) but matched that of the MV cohort **d** The lower, physiological $pCO2$ in the MV_{normal} group reflected the circuit pressure and respiratory rate. In outflow studies (**e, g** grey matter injections **f, h** white matter injections), all mechanically ventilated control rats had significantly higher peak respiratory circuit pressures, and more negative trough pressures than the free breathing group, **e, f**. This was due to carefully matched respiratory rate in the MV cohort **g**, resulting in approximately equal $pCO2$, **h**. **i-p** Phenylephrine infusions were administered to induce hypertension. **j, l** In NIFR studies of CSF flow, sustained MAP and pulse pressure of approximately 140 mmHg and 80 mmHg respectively over 20 min were achieved. These values were twice that of controls. **i, k** In the inflow studies employing ovalbumin, similar large MAP and pulse pressure differences between the hypertensive and the two control groups (MV_{normal} and MV) were also attained. **m, o** In outflow studies of injections into the grey matter and white matter (**n, p**), it was more difficult to maintain an elevated MAP and pulse pressure over 180 min to the same degree as 20 min experiments. Nevertheless, significantly higher MAP and pulse pressure values were obtained for grey matter injections. After injection into the white matter, the MAP was significantly higher than controls **o**, but a higher pulse pressure was not achieved **p**. To investigate the effects of tachycardia on CSF flow, **r, t**, inflow into the cord, **q, s**, and fluid outflow from the grey matter **u, w**, and white matter, **v, x**, all cohorts were electrically paced to 500 bpm. **q, r** In the inflow studies, test animals had heart rates approximately 50% higher than the mechanically ventilated controls, without any blood pressure differences, demonstrated in **s, t**. **u** Similarly, after grey matter injections, heart rate was higher in the paced group without any significant changes to MAP, **w**. **x** After white matter injections however, the control group had a significantly higher MAP than the paced group. This could be secondary to the larger, more robust subjects in the control group. There was a significant difference of 45g in mass between the two groups (p = 0.0058). All error bars are expressed as ±SD

7.3.2 Negative intrathoracic pressure promotes fluid flow into the spinal cord

For inflow studies where AFO-647 was used as the tracer, the mean number of rats per

group was seven. A total of 35 rats were used.

For the intravital studies, 12 animals were included for analysis. Four rats were assigned

to the mechanically ventilated control group. There were three rats each in the paced

and free breathing groups. Only two rats were available for analysis in the hypertensive

group. In each animal, data from multiple regions of interest (ROI) were acquired.

Particle tracking was carried out on only one time series video from one animal per

cohort. Further analysis will be carried out in the future.

7.3.2.1 Successful matching of physiological parameters
7.3.2.1.1 Ex vivo studies

The mass, MAP and heart rate were matched successfully between free breathing and

the two mechanically ventilated control groups (MV_{normal} and MV). The peak circuit

pressures of the control cohorts were significantly higher than that of FB (mean 7.97

and 5.29 mmHg vs 2.03 mmHg, p < 0.0001 and 0.0003 respectively), while the trough

pressures were significantly more negative in the free breathing group than the control

groups (mean -2.43 vs -0.53 and -0.26 mmHg, p = 0.0183 and 0.035 respectively) (**Fig. *24*** a, c). The respiratory rate of free breathing rats was significantly lower than the MV$_{normal}$ control group (mean 52.29 vs 66.43 breaths/min, p < 0.0001), but matched that of the MV cohort well (mean 49.17). The pCO2 in the MV$_{normal}$ group was according lower than both the free breathing and MV groups (mean 43.43 vs 60 and 63.83 mmHg, p = 0.0012 and 0.0004, respectively).

Hypertensive rats recorded MAP twice that of ventilated control groups MV and MV$_{normal}$ (mean 143.3 vs 69.78 and 65.74 mmHg, p <0.0001, respectively). A similarly impressive difference was obtained for pulse pressure (mean 74.41 vs 30.96 and 20.34 mmHg, p <0.0001) (**Fig. *24*** i, k). Again, due to limited inotropic selectivity of phenylephrine, minor relative tachycardia was documented in hypertensive group compared with MV$_{normal}$ and MV controls (mean 395.3 vs 357.2 and 333.9 bpm, p = 0.0245 and 0.0006 respectively). The test group respiratory rate was matched to that of MV, which was reflected in the circuit pressure and pCO2. There was an inadvertent difference in mass between test and control groups MV$_{normal}$ and MV (287.1 vs 354.3 and 375.8 g).

Tachycardia without changes in MAP was induced in rats by sinoatrial node pacing. The paced rats therefore had significantly higher heart rate than the controls MV$_{normal}$ and MV (498.6 vs 357.2 and 333.9 bpm, p < 0.0001), but no differences in MAP (**Fig. *24*** q, s). The respiratory rate of paced rats was matched to MV. The mass was inadvertently slightly less in paced rats compared with controls (306.4 vs 354.3 and 375.8 g, p = 0.0468 and 0.0057 respectively).

7.3.2.1.2   In vivo studies

The animals in the intravital studies were larger than those in ex vivo experiments (**Fig. *25*** a). The mean mass of the MV group was 543.5 g and was significantly larger than free breathing (mean 360 g, p = 0.0001) and paced rats (mean 469.3 g, p = 0.031). There was

no difference, however, compared with hypertensive animals. A significantly higher MAP was achieved in hypertensive rats compared with control (mean 133.2 vs 84.6 mmHg, p = 0.0087) (**Fig. *25*** d, e), but the pulse pressures between the two groups were similar (mean 38.4 vs 40.6 mmHg, p = 0.9). All rats were ventilated to 55 breaths/min, with the exception of free breathing animals, which had a significantly lower mean respiratory rate than control (43.1 breaths/min, p = 0.0087) (**Fig. *25*** c). In free breathing rats, the peak and trough circuit pressures demonstrated the same inverse relationship to the mechanically ventilated controls (**Fig. *25*** f) as demonstrated in **Fig. *24***.
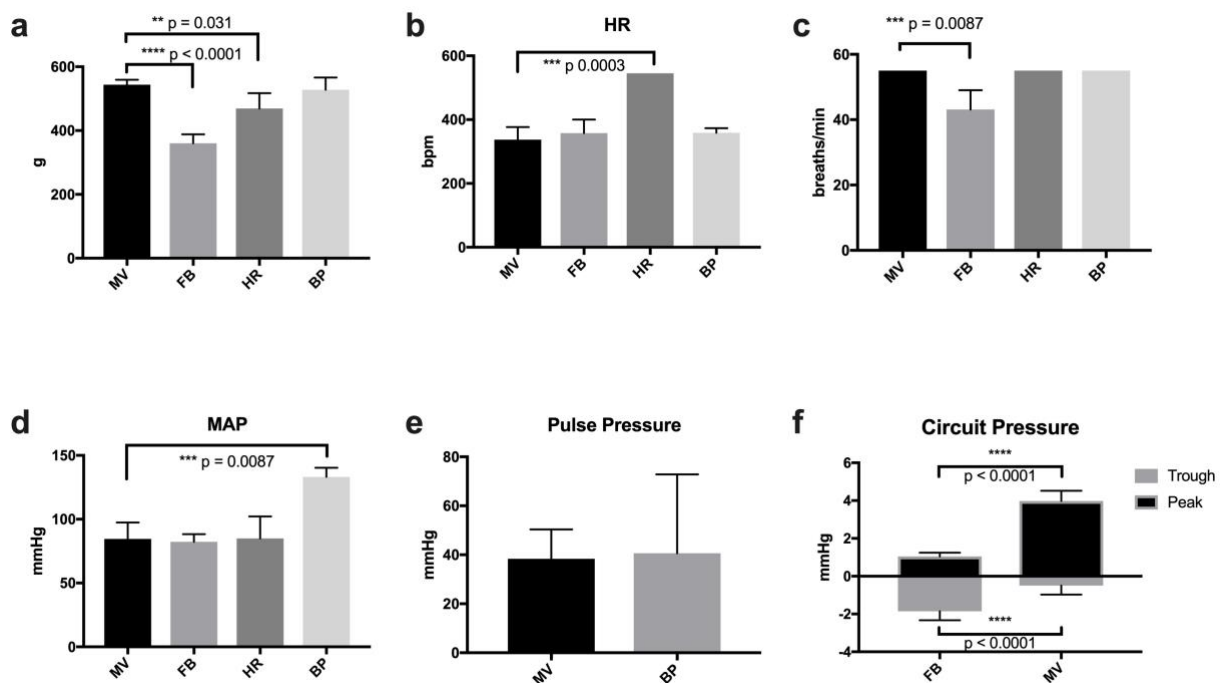
Fig. 25 Comparison of physiological parameters in intravital experiments. **a** The mean mass of the control mechanically ventilated (MV) group was 543.5 g and was significantly larger than free breathing (mean 360 g, p = 0.0001) and tachycardic cohorts (mean 469.3 g, p = 0.031). **b** Tachycardic rats had a significantly higher heart rate than all other groups (which had uniform values). **c** As all animals (other than free breathing group) were mechanically ventilated, a significant difference existed between free breathing and controls (55 vs 43.1 breaths/min, p = 0.0087). **d, e** A significantly higher MAP was achieved in hypertensive rats compared with control (mean 133.2 vs 84.6 mmHg, p = 0.0087), but the pulse pressures between the two groups were similar (mean 38.4 vs 40.6 mmHg, p = 0.9). **f** In free breathing rats, the peak and trough circuit pressures demonstrated an inverse relationship to the mechanically ventilated controls (p < 0.0001 for peak and trough pressures). This was similar to the findings from non-intravital studies (*Fig. 24* a,b)

7.3.3 Tachycardia and hypertension stimulate outflow from the spinal cord

For outflow studies where ovalbumin was used as the tracer, the mean number of rats per group was ten. A total of 40 rats were used.

7.3.3.1 Successful matching of physiological parameters

In studies of AFO-647 tracer outflow from the spinal grey matter (**Fig. *24*** e, g), compared with free breathing animals all mechanically ventilated control rats had significantly higher peak circuit pressures (mean 8.52 vs 2.04 mmHg, p < 0.0001), and less negative trough pressures (mean -0.54 vs -2.99 mmHg, p < 0.0001). This was also observed in rats undergoing white matter injections (**Fig. *24*** f, h). Free breathing animals had lower peak pressures compared with MV controls (mean 1.94 vs 9.18 mmHg, p < 0.0001), but more negative trough pressures (mean -2.51 vs -0.81 mmHg, p = 0006). No significant differences were observed between free breathing and control groups in the other parameters for both grey and white matter injections.

In hypertensive rats, a substantial increase in MAP compared with control was maintained over 180 min after grey matter injections (mean 121.1 vs 82.8 mmHg, p = 0.0002) (**Fig. *24*** m, o). After white matter injections, this difference was smaller but still significant (106.1 vs 82.28 mmHg, p = 0.0094) (**Fig. *24*** n, p). A significant difference in pulse pressure was documented between test and control after grey matter injections (mean 66.56 vs 34.68 mmHg, p = 0.0026), but the significant difference was absent after white matter injections. Small tachycardic increases were observed with phenylephrine infusions after grey matter injections (mean 361.3 vs 418.8 bpm, p = 0.0008) and white matter injections (mean 361.6 vs 440.9 bpm, p = 0.0005). On average the mass of hypertensive rats undergoing white matter injections were somewhat less than their counterpart controls (305 vs 343 g, p = 0.0048). All other parameters between control and test groups in both grey and white matter injections were well matched.

Tachycardic animals had significantly higher heart rate than controls after both grey and white matter injections (mean 493.6 and 499.9 vs 361.1 bpm, both p <0.0001, respectively). There were no significant differences in MAP in the grey matter injection

experiments (**Fig.** *24* u, w). However, after white matter injections the tachycardic rats had relatively lower MAP over three hours compared with controls (mean 60.94 vs 82.28 mmHg, p = 0.0035) (**Fig.** *24* v, x). This was likely secondary to inadvertent difference in size of tachycardic versus control subjects (298 vs 343 g, p = 0.0058). All other parameters were well matched in both white and grey matter injections.

7.4   Supplementary Media
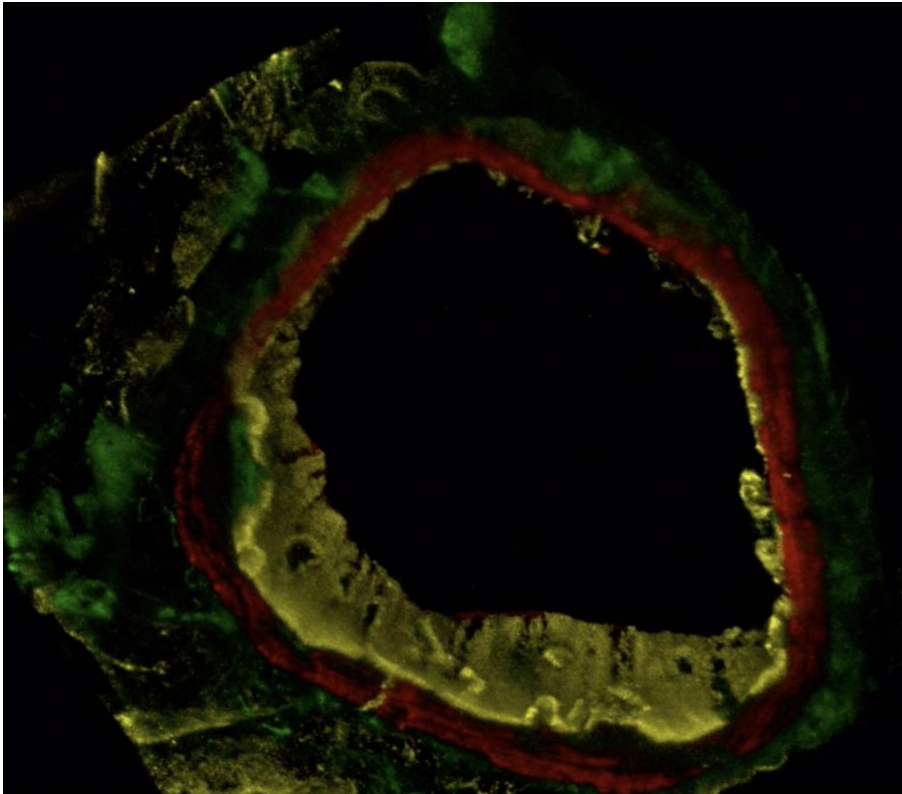
Vid. 7 Inflow and outflow are mediated by the vascular basement membrane. Three-dimensional rendering of a *z*-stack depicting tracer deposition around an anterior spinal artery in a fluid inflow experiment acquired by confocal microscopy (x100 magnification). One of the two-dimensional source images in the z-stack was provided in panel t of **Fig. 20**. Note the discrete layers of green AFO-647 tracer external to and within the red tunica media, labelled red. The endothelium is in yellow. Video access via Supplementary files.

8 References

1. Brodbelt, A.R. and M.A. Stoodley, *Post-traumatic syringomyelia: A review.* Journal of Clinical Neuroscience, 2003. **10**(4): p. 401-408.
2. Hakan, T., *Neurosurgery and a small section from the Greek myth: the God Pan and Syrinx.* Child's Nervous System 2009. **25**(12): p. 1527-9.
3. Pearce, J.M.S., *Syringes and syringomyelia.* European Neurology, 2005. **54**(4): p. 243.
4. Brodbelt AR, S.M., Jones NR, *Syringomyelia*, in *The Cervical Spine*, C. CR, Editor. 2003, Lippincott-Raven: Philadelphia.
5. Sharma, M., Coppa, N. and Sandhu, F.A., *Syringomyelia: A Review.* Seminars in Spine Surgery, 2006. **18**(3): p. 180-184.
6. Klekamp, J., *The pathophysiology of syringomyelia - historical overview and current concept.* Acta Neurochirurgica. 2002. **144**(7): p. 649-64.
7. Bertram, C.D., Brodbelt, A.R. and Stoodley, M.A., *The origins of syringomyelia: Numerical models of fluid/structure interactions in the spinal cord.* Journal of Biomechanical Engineering, 2005. **127**(7): p. 1099-1109.
8. Gardner, W., *Syringomyelia.* Surgical Neurology 1977. **7**: p. 370.
9. Kim, H.G., Oh, H.S., Kim, T.W., Park, K.H., *Clinical Features of Post-Traumatic Syringomyelia.* Korean Journal of Neurotrauma, 2014. **10**(2): p. 66-69.
10. Klekamp, J., *Treatment of posttraumatic syringomyelia.* Journal of Neurosurgery Spine, 2012. **17**(3): p. 199-211.
11. Ballantine, H.T.J., Ojemann, R.G. and Drew, J.H., *Syringohydromyelia, in Progress in Neurological Surgery*, ed. Krayenbuhl, M.P.E. H. and Sweet, W.H. 1971, Basel: Karger.
12. Poser, C.M., *The relationship between syringomyelia and neoplasms*, ed. Thomas, C.C. 1956, Springfield.
13. Madsen P.W., Y.R., and Holets, V.R., *Syringomyelia: clinical observations and experimental studies.* Journal of Neurotrauma, 1994. **11**(3): p. 241-54.
14. Abbe, R.A.C.W., *Syringomyelia. Operation: exploration of cord, withdrawal of fluid, exhibition of patient.* The Journal of Nervous Mental Disease, 1892. **19**: p. 512-520.
15. Schijman, E.a.E.S., *History, anatomic forms, and pathogenesis of Chiari I malformations.* Child's Nervous System, 2004. **20**(5): p. 323-8.
16. Bejjani, G.K., *Definition of the adult Chiari malformation: a brief historical overview.* Neurosurgical Focus, 2001. **11**(1): p. 1-8.
17. Cleland, J., *Contribution to the study of spina bifida, encephalocoele, and anencephalus.* Journal and Anatomy Physiology, 1883. **17**: p. 257-292.
18. Silver, J.R., *History of post-traumatic syringomyelia: post traumatic syringomyelia prior to 1920.* Spinal Cord, 2001. **39**(3): p. 176-83.
19. Milhorat, T.H., *Classification of syringomyelia.* Neurosurgical Focus, 2000. **8**(3): p. 1-6.
20. Koyanagi I, H.K., *Pathogenesis of syringomyelia associated with Chiari type 1 malformation: review of evidences and proposal of a new hypothesis.* Neurosurgical Review, 2010. **33**(3): p. 271-84.
21. Moriwaka, F., Tashiro K., Tachibana, S., Yada, K., *Epidemiology of syringomyelia in Japan--the nationwide survey.* Rinsho Shinkeigaku, 1995. **35** (12): p. 1395-1397.
22. Milhorat, T.H., Capocelli, A.L., Anzil, A.P., Kotzen, R.M., Milhorat, R.H., *Pathological basis of spinal cord cavitation in syringomyelia: analysis of 105 autopsy cases.* Journal of Neurosurgery, 1995. **82**(5): p. 802-812.

23. Ghobrial, G.M., Dalyai RT, Maltenfort MG, Prasad SK, Harrop JS, Sharan AD, *Arachnolysis or cerebrospinal fluid diversion for adult-onset syringomyelia? A Systematic review of the literature.* World Neurosurg, 2015. **83**(5): p. 829-35.

24. Klekamp, J., Batzdorf U, Samii M, Bothe HW., *Treatment of syringomyelia associated with arachnoid scarring caused by arachnoiditis or trauma.* Journal of Neurosurgery, 1997. **86**(2): p. 233-240.

25. Sherman, J.L., A.J. Barkovich, and C.M. Citrin, *The MR appearance of syringomyelia: new observations.* American journal of roentgenology, 1987. **148**(2): p. 381-91.

26. Brodbelt AR, S.M., Jones NR. , *Non-traumatic syringomyelia. In: The cervical Spine Research Society* 4th ed. The cervical spine. 2005.

27. Edgar, R., Quail, P., *Progressive post-traumatic cystic and non-cystic myelopathy.* British journal of neurosurgery, 1994. **8**(1): p. 7-22.

28. Milhorat, T.H., Chou MW, Trinidad EM, Kula RW, Mandell M, Wolpert C, Speer MC, *Chiari I Malformation Redefined: Clinical and Radiographic Findings for 364 Symptomatic Patients.* Neurosurgery, 1999. **44**(5): p. 1005-1017.

29. Heiss JD, P.N., DeVroom HL, Shawker T, Ennis R, Kammerer W, et al, *Elucidating the pathophysiology of syringomyelia.* Journal of Neurosurgery Spine, 1999. **91**: p. 553-562.

30. Di Lorenzo, N.A.F.C., *Adult syringomyelia. Classification, pathogenesis and therapeutic approaches.* Journal of Neurosurgical Sciences, 2005. **49**(3): p. 65-72.

31. Brickell, K.L., Anderson NE, Charleston AJ, Hope JK, Bok AP, Barber PA, *Ethnic differences in syringomyelia in New Zealand.* Journal of Neurology, Neurosurgery, and Psychiatry, 2006. **77**(8): p. 989-991.

32. Bogdanov EI, M.E., *Syrinx size and duration of symptoms predict the pace of progressive myelopathy: retrospective analysis of 103 unoperated cases with craniocervical junction malformations and syringomyelia.* Clinical Neurology and Neurosurgery, 2002. **104**: p. 90-97.

33. Williams, B., *On the pathogenesis of syringomyelia: a review.* Journal of the Royal Society of Medicine, 1980(73): p. 798-806.

34. Abel R, G.H., Smit C, Meiners T, *Residual deformity of the spinal canal in patients with traumatic paraplegia and secondary changes of the spinal cord.* Spinal Cord 1999 **37:** p. 14-19.

35. Backe HA, Betz RR, Mesgarzadeh M, Beck T, Clancy M, *Post-Traumatic spinal cord cysts evaluated by magnetic resonance imaging.* Paraplegia, 1991. **29**: p. 607-612.

36. Perrouin-Verbe B, L.-A.K., Robert R, Auffray-Calvier E, Richard I, Mauduyt de la Greve I, Mathe JF *Post-traumatic syringomyelia and post-traumatic spinal canal stenosis: a direct relationship: review of 75 patients with a spinal cord injury.* Spinal Cord 1998. **36**: p. 137-143.

37. Squier MV, L.R., *Post-traumatic syringomyelia.* Journal of Neurology, Neurosurgery, and Psychiatry, 1994 **57**: p. 1095-1098.

38. Wang D, B.R., Sett P, Gardner B, Frankel H *A clinical magnetic resonance imaging study of the traumatised spinal cord more than 20 years following injury.* Paraplegia 1996 **34**: p. 65-81.

39. Anton HA, S.J., *Posttraumatic syringomyelia: the British Columbia experience.* Spine, 1986. **11**: p. 865-868.

40. Barnett HJ, Botterell EH, Jousse AT, Wynne-Jones M, *Progressive myelopathy as a sequel to traumatic paraplegia.* Brain, 1966. **89**: p. 159-174.

41. el Masry WS, B.A., *Incidence, management, and outcome of post-traumatic syringomyelia. In memory of Mr Bernard Williams.* Journal of Neurology, Neurosurgery, and Psychiatry 1996. **60**: p. 141-146.

42.   Rossier AB, F.D., Shillito J, Dyro FM *Posttraumatic cervical syringomyelia. Incidence, clinical presentation, electrophysiological studies, syrinx protein and results of conservative and operative treatment.* Brain 1985. **108** p. 439-461.

43.   Schurch B, W.W., Rossier AB *Post-traumatic syringomyelia (cystic myelopathy): a prospective study of 449 patients with spinal cord injury.* Journal of Neurology, Neurosurgery, and Psychiatry 1996. **60**: p. 61-67.

44.   Tobimatsu Y, Nihei R, Kimura T, Suyama T, Kimura H, Tobimatsu H, Shirakawa T, *A quantitative analysis of cerebrospinal fluid flow in post-traumatic syringomyelia.* Paraplegia, 1995. **33**: p. 203-207.

45.   Hussey, R., et al., *Prospective study of the occurrence rate of post-traumatic cystic degeneration of the spinal cord utilizing magnetic resonance imaging.* Journal of the American Paraplegia Society 1989. **13**(16).

46.   Oakley, J.C., G.A. Ojemann, and E.C. Alvord, Jr., *Posttraumatic syringomyelia. Case report.* Journal of Neurosurgery, 1981. **55**(2): p. 276-81.

47.   Lee, T.T., et al., *Surgical treatment of post-traumatic myelopathy associated with syringomyelia.* Spine, 2001. **26** (24 Suppl): p. S119-27.

48.   Lee, T.T., et al., *Outcome after surgical treatment of progressive posttraumatic cystic myelopathy.* Journal of Neurosurgery, 2000. **92**(2 Suppl): p. 149-54.

49.   Birbamer, G., et al., *Spontaneous collapse of posttraumatic syringomyelia: serial magnetic resonance imaging.* European Neurology, 1993. . **33**(5): p. 378-81.

50.   Biyani, A. and el Masry, W.S., *Post-traumatic syringomyelia: a review of the literature.* Paraplegia, 1994. **32**(11): p. 723-31.

51.   Schlesinger, E.B., et al., *Hydromyelia: clinical presentation and comparison of modalities of treatment.* Neurosurgery, 1981. **9**(4): p. 356-65.

52.   Mariani, C., et al., *The natural history and results of surgery in 50 cases of syringomyelia.* Journal of Neurology, 1991. **238**(8): p. 433-8.

53.   Ducreux D, A.N., Parker F, Bouhassira D *Mechanisms of central neuropathic pain: a combined psychophysical and fMRI study in syringomyelia.* Brain 2006. **129**: p. 963-976.

54.   Honan, W.P. and Williams, B., *Sensory loss in syringomyelia: not necessarily dissociated.* Journal of the Royal Society of Medicine, 1993. **86**(9): p. 519-20.

55.   Nakamura, M., et al., *Clinical significance and prognosis of idiopathic syringomyelia.* Journal of Spinal Disorders & Techniques, 2009. **22**(5): p. 372-5.

56.   Todor DR, M.H., and Milhorat T.H., *Pain and syringomyelia: a review.* Neurosurgical Focus, 2000. **8**(3): p. E11.

57.   Nogues, M.A., *Syringomyelia and syringobulbia.* Handbook of Clinical Neurology, 1987. **6**(50): p. 443 - 464.

58.   Berry, R.G., R.A. Chambers, and F.D. Lublin, *Syringoencephalomyelia (Syringocephalus).* Journal of Neuropathology & Experimental Neurology, 1981. **40**(6): p. 633-644.

59.   Levy WJ, M.L., Hahn JF *Chiari malformation presenting in adults: a surgical experience in 127 cases.* Neurosurgery 1983. **12**: p. 377-390.

60.   Fukushima T, M.T., Tsuchimochi H, Yamamoto M, Tsugu H, Tomonaga M, Mitsudome A, Utsunomiya H, Asakawa K *Symptomatic Chiari malformation and associated pathophysiology in pediatric and adult patients without myelodysplasia.* Neurol Med Chir (Tokyo) 1994. **34**: p. 738-743.

61.   Bindal AK, D.S., Tew JM, Jr., *Chiari I malformation: classification and management.* Neurosurgery 1995. **37**: p. 1069-1074.

62.   Milhorat TH, K.R., Mu HT, Capocelli AL, Jr., Milhorat RH *Dysesthetic pain in patients with syringomyelia.* Neurosurgery 1996. **38**: p. 940-946.

63. Steinbok, P., *Clinical features of Chiari I malformations.* Childs Nerv Syst 2004. **20**: p. 329-331.

64. Aghakhani N, P.F., David P, Morar S, Lacroix C, Benoudiba F, Tadie M, *Long-term follow-up of Chiari-related syringomyelia in adults: analysis of 157 surgically treated cases.* Neurosurgery 2009 **64**: p. 308-315.

65. Hida, K., et al., *Pediatric syringomyelia with chiari malformation: its clinical characteristics and surgical outcomes.* Surgical Neurology, 1999. **51**(4): p. 383-90.

66. Isu, T., et al., *Scoliosis associated with syringomyelia presenting in children.* Child's nervous system. 1992. **8**(2): p. 97-100.

67. Mehalic, T.F., R.T. Pezzuti, and B.I. Applebaum, *Magnetic Resonance Imaging and Cervical Spondylotic Myelopathy.* Neurosurgery, 1990. **26**(2): p. 217-227.

68. Gottschalk, A., et al. *Dynamic visualization of arachnoid adhesions in a patient with idiopathic syringomyelia using high-resolution cine magnetic resonance imaging at 3T.* Journal of magnetic resonance imaging, 2010. **32**(1): p. 218-22.

69. Akiyama, Y., et al., *Interstitial spinal-cord oedema in syringomyelia associated with Chiari type 1 malformations.* Journal of Neurology, Neurosurgery, and Psychiatry, 2008. **79**(10): p. 1153-8.

70. Fischbein, N.J., et al., *The "presyrinx" state: a reversible myelopathic condition that may precede syringomyelia.* American Journal of Neuroradiology, 1999. **20**(1): p. 7-20.

71. Donauer, E., and Rascher, K., *Syringomyelia: a brief review of ontogenetic, experimental and clinical aspects.* Neurosurgical review, 1993. **16**(1): p. 7-13.

72. Panigrahi, M., et al., *CSF flow study in Chiari I malformation.* Child's nervous system 2004. **20**(5): p. 336-40.

73. Lichtor, T., P. Egofske, and N. Alperin, *Noncommunicating cysts and cerebrospinal fluid flow dynamics in a patient with a Chiari I malformation and syringomyelia-- part II.* Spine, 2005. **30**(12): p. 1466-72.

74. Klekamp, J., Samii, M., *Syringomyelia: Diagnosis and Management.* 2002, Berlin: Springer.

75. Singounas EG, K.P., *Terminal ventriculostomy in syringomyelia.* Acta Neurochir (Wien) 1979. **46**: p. 293-295.

76. Profeta G, M.G., *Terminal ventriculostomy for syringomyelia.* J Neurosurg Sci 1980. **24**(161-168.)

77. Hashiguchi K, M.T., Samura K, Yoshida F, Miyagi Y, Nagata S, Kokubo T, Yoshiura T, Sasaki T *Holocord hydrosyringomyelia with terminal myelocystocele revealed by constructive interference in steady-state MR imaging.* Pediatr Neurosurg 2008. **44**: p. 509-512.

78. Wetjen, N.M., J.D. Heiss, and E.H. Oldfield, *Time course of syringomyelia resolution following decompression of Chiari malformation Type I.* J Neurosurg Pediatr, 2008. **1**(2): p. 118-23.

79. Attenello, F.J., et al., *Suboccipital decompression for Chiari I malformation: outcome comparison of duraplasty with expanded polytetrafluoroethylene dural substitute versus pericranial autograft.* Childs Nervous System, 2009. **25**(2): p. 183-90.

80. Logue V, E.M., *Syringomyelia and its surgical treatment--an analysis of 75 patients.* Journal of Neurology, Neurosurgery, and Psychiatry 1981. **44**: p. 273-284.

81. Iwasaki Y, H.K., Koyanagi I, Abe H *Reevaluation of syringosubarachnoid shunt for syringomyelia with Chiari malformation.* Neurosurgery, 2000. **46**: p. 407-412

82. Hida K, I.Y., Imamura H, Abe H., *Posttraumatic syringomyelia: its characteristic magnetic resonance imaging findings and surgical management.* Neurosurgery, 1994. **35**: p. 886-891.

83.	Ergun R, A.G., Gezici AR, Tezel K, Beskonakli E, Ergungor F, Taskin Y *Surgical management of syringomyelia-Chiari complex. .* Eurpean Spine Journal 2000. **9**: p. 553-557.

84.	Heiss, J.D., et al., *Pathophysiology of persistent syringomyelia after decompressive craniocervical surgery. Clinical article.* Journal of Neurosurgery Spine, 2010. **13**(6): p. 729-42.

85.	Munshi I, F.D., Stine-Reyes R, Weir BK, Hekmatpanah J, Brown F *Effects of posterior fossa decompression with and without duraplasty on Chiari malformation-associated hydromyelia.* Neurosurgery 2000. **46**: p. 1384-1389.

86.	Genitori L, P.P., Nurisso C, Macinante L, Mussa F *Chiari type I anomalies in children and adolescents: minimally invasive management in a series of 53 cases.* Child's Nervous System 2000. **16**: p. 707-718.

87.	Reis, A.J., *New surgical approach for late complications from spinal cord injury.* BMC Surgery, 2006. **6**: p. 12.

88.	Lam S, B.U., Bergsneider M *Thecal shunt placement for treatment of obstructive primary syringomyelia.* Journal of Neurosurgery Spine 2008. **9**: p. 581-588.

89.	Batzdorf, U., J. Klekamp, and J.P. Johnson, *A critical appraisal of syrinx cavity shunting procedures.* Journal of Neurosurgery, 1998. **89**(3): p. 382-8.

90.	Sgouros, S. and Williams, B., *A critical appraisal of drainage in syringomyelia.* Journal of Neurosurgery, 1995. **82**(1): p. 1-10.

91.	Shannon, N., et al., *Clinical features, investigation and treatment of post-traumatic syringomyelia.* Journal of Neurology, Neurosurgery, and Psychiatry, 1981. **44**(1): p. 35-42.

92.	Parker, F., N. Aghakhani, and M. Tadie, *Non-traumatic arachnoiditis and syringomyelia. A series of 32 cases.* Neuro-Chirurgie, 1999. **45** p. 67-83.

93.	Tator, C.H.a.C.B., *Treatment of syringomyelia with a syringosubarachnoid shunt. .* The Canadian Journal of Neurological Sciences 1988. **15**(1): p. 48-57.

94.	Gezen, F., et al., *Application of syringosubarachnoid shunt through key-hole laminectomy. Technical note.* Neurosurgical Focus 2000. **8**(3): p. E10.

95.	McIlroy WJ, R.J., *Syringomyelia: a clinical review of 75 cases.* Canadian Medical Association Journal 1965. **93**: p. 731-734.

96.	Falci S, H.A., Akesson E, Azizi M, Ertzgaard P, Hultling C, Kjaeldgaard A, Levi R, Ringden O, Westgren M, Lammertse D, Seiger A *Obliteration of a posttraumatic spinal cord cyst with solid human embryonic spinal cord grafts: first clinical attempt. .* Journal of Neurotrauma 1997. **14**: p. 875-884.

97.	Thompson FJ, R.P., Uthman B, Mott S, Fessler RG, Behrman A, Trimble M, Anderson DK, Wirth ED, *Neurophysiological assessment of the feasibility and safety of neural tissue transplantation in patients with syringomyelia.* Journal of Neurotrauma 2001. **18**: p. 931-945.

98.	Wirth ED, Reier PJ, Fessler RG, Thompson FJ, Uthman B, Behrman A, Beard J, Vierck CJ, Anderson DK *Feasibility and safety of neural tissue transplantation in patients with syringomyelia.* Journal of Neurotrauma 2001. **18**: p. 911-929.

99.	Alzate JC, K.K., Jallo GI, Epstein FJ, *Treatment of Chiari I malformation in patients with and without syringomyelia: a consecutive series of 66 cases.* Neurosurg Focus 2001. **11**: p. E3.

100.	Wiedemayer, H., et al., *Operative treatment and prognosis of syringomyelia.* Neurosurgical review, 1994. **17**(1): p. 37-41.

101.	Ronen J, C.A., Spasser R, Gepstein R, *The treatment dilemma in post-traumatic syringomyelia.* Disability and Rehabilitation 1999. **21**: p. 455-457.

102.	Vernon, J.D., J.R. Silver, and L. Symon, *Post-traumatic syringomyelia: the results of surgery.* Paraplegia, 1983. **21**(1): p. 37-46.

103. Bonfield, C.M., et al., *Surgical management of post-traumatic syringomyelia.* Spine, 2010. **35**(21 Supp): p. S245-58.

104. Levine, D.N., *The pathogenesis of syringomyelia associated with lesions at the foramen magnum: a critical review of existing theories and proposal of a new hypothesis.* Journal of the Neurological Sciences, 2004. **220**(1-2): p. 3-21.

105. Newton, E.J., *Syringomyelia as a manifestation of defective fourth ventricular drainage.* Annals of the Royal College of Surgeons of England, 1969. **44**(4): p. 194-213.

106. Mavinkurve, G.G., et al., *Familial Chiari type I malformation with syringomyelia in two siblings: case report and review of the literature.* Child's Nervous System, 2005. **21**(11): p. 955-9.

107. Zakeri, A., F.E. Glasauer, and J.G. Egnatchik, *Familial syringomyelia: case report and review of the literature.* Surgical Neurology 1995. **44**(1): p. 48-53.

108. Bentley, S.J., M.J. Campbell, and P. Kaufmann, *Familial syringomyelia.* Journal of Neurology, Neurosurgery, and Psychiatry, 1975. **38**(4): p. 346-9.

109. Speer, M.C., et al., *A genetic hypothesis for Chiari I malformation with or without syringomyelia.* Neurosurgical Focus, 2000. **8**(3): p. E12.

110. Hida, K., et al., *Birth injury as a causative factor of syringomyelia with Chiari type I deformity.* Journal of Neurology, Neurosurgery, and Psychiatry, 1994. **57** (3): p. 373-4.

111. Newman, P.K., T.R. Terenty, and J.B. Foster, *Some observations on the pathogenesis of syringomyelia.* Journal of Neurology, Neurosurgery & Psychiatry, 1981. **44**(11): p. 964-969.

112. Tabor, E.N. and Batzdorf U., *Thoracic spinal Pantopaque cyst and associated syrinx resulting in progressive spastic paraparesis: case report.* Neurosurgery, 1996. **39**(5): p. 1040-2.

113. Appleby, A., et al. *Syringomyelia due to chronic arachnoiditis at the foramen magnum.* Journal of the Neurological Sciences 1969. **8**(3): p. 451-64.

114. Milhorat, T.H., R.M. Kotzen, and A.P. Anzil, *Stenosis of central canal of spinal cord in man: incidence and pathological findings in 232 autopsy cases.* Journal of Neurosurgery, 1994. **80**(4): p. 716-22.

115. Blagodatsky, M.D., et al., *Surgical treatment of "hindbrain related" syringomyelia: new data for pathogenesis.* Acta Neurochirurgica, 1993. **124**(2-4): p. 82-5.

116. Blaylock, R.L., *Hydrosyringomyelia of the conus medullaris associated with a thoracic meningioma: case report.* Journal of Neurosurgery, 1981. **54**(6): p. 833-5.

117. Durward, Q.J., et al., *Selective spinal cordectomy: clinicopathological correlation. .* Journal of Neurosurgery, 1982. **56**(3): p. 359-67.

118. Davis, C.H.a.L.S., *Mechanisms and treatment in post-traumatic syringomyelia. .* British Journal of Neurosurgery, 1989. **3**(6): p. 669-74.

119. Ellertsson A.B., and Greitz T., *The distending force in the production of communicating syringomyelia.* Lancet, 1970. **1**(7658): p. 1234.

120. Stoodley, M.A., et al., *The Filling Mechanism, in Syringomyelia: A Disorder of CSF Circulation*, ed. Flint, G. and Rusbridge. 2011, Heidelberg: Springer.

121. Koyanagi, I. and K. Houkin, *Pathogenesis of syringomyelia associated with Chiari type 1 malformation: review of evidences and proposal of a new hypothesis.* Neurosurgical Review, 2010. **33**(3): p. 271-84; discussion 284-5.

122. Chang HS, N.H., *Theoretical analysis of the pathophysiology of syringomyelia associated with adhesive arachnoiditis.* Journal of Neurology, Neurosurgery and Psychiatry 2004. **75**: p. 754-757.

123. Greitz, D., *Unraveling the riddle of syringomyelia.* Neurosurg Rev, 2006. **29**: p. 251–264.

124. Rusbridge, C., Greitz, D., and Iskandar, B.J., *Syringomyelia: current concepts in pathogenesis, diagnosis, and treatment.* Journal of veterinary internal medicine/ American College of Veterinary Internal Medicine, 2006. **20**(3): p. 469-79.

125. Ravaglia, S., et al., *Pathogenetic role of myelitis for syringomyelia.* Clinical Neurology and Neurosurgery, 2007. **109**(6): p. 541-6.

126. Hemley, S.J., J. Tu, and M.A. Stoodley, *Role of the blood-spinal cord barrier in posttraumatic syringomyelia: Laboratory investigation.* Journal of Neurosurgery: Spine, 2009. **11**(6): p. 696-704.

127. Barnett, H.J., *Syringomyelia and tumours of the nervous system, in Syringomyelia*, ed. J.B.F. Barnett, H.J., and Hudgson, P., 1973, London: Saunders.

128. Lohle, P.N., et al., *The pathogenesis of syringomyelia in spinal cord ependymoma.* Clinical Neurology and Neurosurgery, 1994. **96**(4): p. 323-6.

129. Lonser, R.R., Butman, J.A., and Oldfield, E.H., *Pathogenesis of tumor-associated syringomyelia demonstrated by peritumoral contrast material leakage. Case illustration.* Journal of neurosurgery. Spine, 2006. **4**(5): p. 426.

130. Lonser, R.R., et al., *Edema is a precursor to central nervous system peritumoral cyst formation.* Annals of Neurology, 2005. **58**(3): p. 392-9.

131. Fried, L.C. and Aparicio O., *Experimental ischemia of the spinal cord. Histologic studies after anterior spinal artery occlusion.* Neurology, 1973. **23**(3): p. 289-293.

132. Tauber, E.S. and Langworthy, .O.R., *A Study of syringomyelia and the formation of cavities in the spinal cord* The Journal of Nervous and Mental Disease, 1935. **81**(3): p. 245-264.

133. Fried, L.C., et al., *The animal experimental model ischemic injuries.* Procedure Veterans Administration Spinal Cord Injection Conference, 1973. **19**(106).

134. Feigin I, O.J., Budzilovich G, *Syringomyelia: The role of edema in its pathogenesis.* Journal of Neuropathology & Experimental Neurology, 1971. **30**(2): p. 216-232.

135. Bertram, C.D., *Evaluation by fluid/structure-interaction spinal-cord simulation of the effects of subarachnoid-space stenosis on an adjacent syrinx.* J Biomech Eng, 2010. **132**(6): p. 061009.

136. Bertram, C.D., L.E. Bilston, and M.A. Stoodley, *Tensile radial stress in the spinal cord related to arachnoiditis or tethering: A numerical model.* Medical and Biological Engineering and Computing, 2008. **46**(7): p. 701-707.

137. Klekamp J, V.K., Bartels CJ, Samii M, *Disturbances of cerebrospinal fluid flow attributable to arachnoid scarring cause interstitial edema of the cat spinal cord.* Neurosurgery 2001. **48**: p. 174-185.

138. Yang, L., Jones NR, Stoodley MA, Blumbergs PC, Brown CJ., *Excitotoxic model of post-traumatic syringomyelia in the rat.* Spine, 2001. **26**(17): p. 1842-1849.

139. Cho KH, I.Y., Imamura H, Hida K, Abe H *Experimental model of posttraumatic syringomyelia: the role of adhesive arachnoiditis in syrinx formation.* Journal of Neurosurgery 1994. **80**: p. 133-139.

140. Gardner, W.J. and J. Angel, *The mechanism of syringomyelia and its surgical correction.* Clinical Neurosurgery, 1958. **6**: p. 131-40.

141. Gardner, W.J. and J. Angel, *The cause of syringomyelia and its surgical treatment.* Cleveland Clinic Quarterly 1958. **25**(1): p. 4-8.

142. Williams, B. and Bentley, J., *Experimental communicating syringomyelia in dogs after cisternal kaolin injection. Part 1. Morphology.* Journal of the Neurological Sciences, 1980. **48**(1): p. 93-107.

143. Ball MJ, D.A., *Pathogenesis of syringomyelia.* Lancet, 1972. **2**: p. 799-801.

144. Aboulker, J., *Syringomyelia and intra-rachidian fluids. X. Rachidian fluid stasis.* Neuro-Chirurgie, 1979. **25**(Suppl 1): p. 98-107.

145. Oldfield E.H, Muraszko, K., Shawker T.H, Patronas N.J, *Pathophysiology of syringomyelia associated with Chiari I malformation of the cerebellar tonsils. Implications for diagnosis and treatment.* Journal of Neurosurg Spine, 1994. **80**: p. 3-15.

146. Stoodley, M.A., Brown SA, Brown CJ, Jones NR., *Arterial pulsation-dependent perivascular cerebrospinal fluid flow into the central canal in the sheep spinal cord.* Journal of Neurosurgery, 1997. **86**(4): p. 686-693.

147. Stoodley, M.A., Gutschmidt, B. and Jones, N.R., *Cerebrospinal fluid flow in an animal model of noncommunicating syringomyelia.* Neurosurgery, 1999. **44**(5): p. 1065-1076.

148. Stoodley, M.A., Jones, N.R. and Brown, C.J., *Evidence for rapid fluid flow from the subarachnoid space into the spinal cord central canal in the rat.* Brain Research, 1996. **707**(2): p. 155-164.

149. Stoodley, M.A., et al., *Mechanisms underlying the formation and enlargement of noncommunicating syringomyelia: experimental studies.* Neurosurgical focus [electronic resource]. 2000. **8**(3).

150. Bilston, L.E., Fletcher DF, Brodbelt AR, Stoodley MA., *Arterial pulsation-driven cerebrospinal fluid flow in the perivascular space: A computational model.* Computer Methods in Biomechanics and Biomedical Engineering, 2003. **6**(4): p. 235-241.

151. Bilston, L.E., Stoodley, M.A., and Fletcher, D.F., *The influence of the relative timing of arterial and subarachnoid space pulse waves on spinal perivascular cerebrospinal fluid flow as a possible factor in syrinx development.* Journal of Neurosurgery, 2010. **112**(4): p. 808-813.

152. Clarke, E.C., Fletcher DF, Stoodley MA, Bilston LE., *Computational fluid dynamics modelling of cerebrospinal fluid pressure in Chiari malformation and syringomyelia.* Journal of Biomechanics, 2013. **46**(11): p. 1801-1809.

153. Brodbelt, A.R., Stoodley MA, Watling AM, Tu J, Jones NR., *Fluid flow in an animal model of post-traumatic syringomyelia.* European Spine Journal, 2003. **12**(3): p. 300-306.

154. Elliott, N.S., Lockerby, D.A. and Brodbelt, A.R., *A lumped-parameter model of the cerebrospinal system for investigating arterial-driven flow in posttraumatic syringomyelia.* Medical Engineering and Physics, 2011. **33**(7): p. 874-82.

155. Carpenter, P.W., Berkouk, K. and Lucey, A.D., *Pressure wave propagation in fluid-filled co-axial elastic tubes. Part 2: Mechanisms for the pathogenesis of syringomyelia.* Journal of Biomechanical Engineering, 2003. **125** (6): p. 857-63.

156. McLaurin, R., Bailey, O.T, Schurr, P.H, Ingraham, F.D., *Myelomalacia and multiple cavitations of spinal cord secondary to adhesive arachnoiditis; an experimental study.* A.M.A. Archives of Pathology, 1954. **57**(2): p. 138-46.

157. Nakamura, S., Camins, M.B. and Hochwald, G.M. *Pressure-absorption responses to the infusion of fluid into the spinal cord central canal of kaolin-hydrocephalic cats.* Journal of Neurosurgery, 1983. **58**(2): p. 198-203.

158. Hall, P.V., Muller, J. and Campbell, R.L., *Experimental hydrosyringomyelia, ischemic myelopathy, and syringomyelia.* Journal of Neurosurgery, 1975. **43**(4): p. 464-70.

159. Becker, D.P., Wilson, J.A. and Watson, G.W., *The spinal cord central canal: response to experimental hydrocephalus and canal occlusion.* Journal of Neurosurgery, 1972. **36**(4): p. 416-24.

160. Yamazaki, Y., Tachibana S, Ohta N, Yada K, Ohama E., *Experimental model of chronic tonsillar herniation associated with early stage syringomyelia.* Acta Neuropathologica, 1995. **90**(5): p. 425-31.

161. Yamazaki, Y., Tachibana, S. and Fujii, K., *Role of active cerebrospinal fluid transport in syrinx formation: An experimental study on a model of chronic tonsillar herniation in rats, in Syringomyelia: Current concepts in pathogenesis and management,* ed. U.B. N. Tamaki, and T. Nagashima. 2001, Tokyo: Springer-Verlag.

162. Williams, B. and Weller, R.O., *Syringomyelia produced by intramedullary fluid injection in dogs.* Journal of Neurology, Neurosurgery, and Psychiatry, 1973. **36**(3): p. 467-77.

163. Chakrabortty, S., Tamaki N, Ehara K, Takahashi A, Ide C., *Experimental syringomyelia: late ultrastructural changes of spinal cord tissue and magnetic resonance imaging evaluation.* Surgical Neurology, 1997. **48**(3): p. 246-54.

164. Milhorat, T.H., Adler DE, Heger IM, Miller JI, Hollenberg-Sher JR, *Histopathology of experimental hematomyelia.* Journal of Neurosurgery, 1991. **75**(6): p. 911-5.

165. Lee JY, Kim SW, Kim SP, Kim H, Cheon JE, Kim SK, Paek SH, Pang D, Wang KC, *A rat model of chronic syringomyelia induced by epidural compression of the lumbar spinal cord.* Journal of Neurosurgery Spine, 2017. **27**(4): p. 458-467.

166. Allen, A.R., *Surgery of experimental lesion of spinal cord equivalent to crush injury of fracture dislocation of spinal column. A preliminary report.* JAMA : the Journal of the American Medical Association, 1911. **57**: p. 878 - 880.

167. Allen, A.R., *Remarks of the histological changes in the spinal cord due to impact. An experimental study.* Journal of Nervous and Mental disease, 1914: p. 141 - 147.

168. Noble, L.J. and Wrathall JR., *An inexpensive apparatus for producing graded spinal cord contusive injury in the rat.* Experimental Neurology, 1987. **95**(2): p. 530-533.

169. Radojicic, M., G. Nistor, and H.S. Keirstead, *Ascending central canal dilation and progressive ependymal disruption in a contusion model of rodent chronic spinal cord injury.* BMC Neurology, 2007. **7**(1): p. 30.

170. Wong, J., Hemley S, Jones N, Cheng S, Bilston L, Stoodley M., *Fluid outflow in a large-animal model of posttraumatic syringomyelia.* Neurosurgery, 2012. **71**(2): p. 474-480.

171. Mizuno, J., et al., *Histological evaluation for the mechanism of syrinx formation in the rat experimental model with injury and secondary adhesive arachnoiditis, in Syringomyelia: current concept in pathogenesis and management.*, ed. Batzdorf, U.B., Tamaki, N., and Nagashima, T., 2001, Tokyo: Springer-Verlag. 49 - 55.

172. Seki, T. and Fehlings, M.G., *Mechanistic insights into posttraumatic syringomyelia based on a novel in vivo animal model. Laboratory investigation.* Journal of Neurosurgery Spine, 2008. **8**(4): p. 365-75.

173. Josephson, A., Greitz D, Klason T, Olson L, Spenger C., *A spinal thecal sac constriction model supports the theory that induced pressure gradients in the cord cause edema and cyst formation.* Neurosurgery, 2001. **48**(3): p. 636-45.

174. Brodbelt, A.R., Stoodley MA, Watling A, Rogan C, Tu J, Brown CJ, Burke S, Jones NR., *The role of excitotoxic injury in post-traumatic syringomyelia.* Journal of Neurotrauma, 2003. **20**(9): p. 883-893.

175. Seki, T. and Fehlings, M.G., *Mechanistic insights into posttraumatic syringomyelia based on a novel in vivo animal model. Laboratory investigation.* Journal of Neurosurgert Spine, 2008. **8**(4): p. 365-75.

176. Longatti, P., et al., *Expanding cerebral cysts (lacunae): a treatable cause of progressive midbrain syndrome. .* Journal of Neurology, Neurosurgery, and Psychiatry, 2003. **74**(3): p. 393-394.

177. Yezierski, R.P., Liu S, Ruenes GL, Kajander KJ, Brewer KL., *Excitotoxic spinal cord injury: behavioral and morphological characteristics of a central pain model.* Pain, 1998. **75**(1): p. 141-155.

178. Marsala, M., Sorkin, L.S., and Yaksh, T.L., *Transient spinal ischemia in rat: characterization of spinal cord blood flow, extracellular amino acid release, and concurrent histopathological damage.* Journal of Cerebral Blood Flow and Metabolism, 1994. **14**(4): p. 604-614.

179. Liu, D., Thangnipon, W. and McAdoo, D.J., *Excitatory amino acids rise to toxic levels upon impact injury to the rat spinal cord.* Brain Research, 1991. **547**(2): p. 344-348.

180. Young, B., *Central nervous system, in Wheater's Functional Histology: a text and colour atlas.* 2000, London: Churchill Livingstone.

181. McMinn, R.M.H., *Spinal cord, in Last's Anatomy: regional and applied*, ed. R.M.H. McMinn. 1998, London: Churchill Livingstone.

182. Young, B., *Wheater's Functional Histology: a text and colour atlas.* 2000, London: Churchill Livingstone.

183. Koshinaga, M. and Whittemore, S.R., *The temporal and spatial activation of microglia in fiber tracts undergoing anterograde and retrograde degeneration following spinal cord lesion.* Journal of Neurotrauma, 1995. **12**(2): p. 209-222.

184. Watanabe, T., Yamamoto T, Abe Y, Saito N, Kumagai T, Kayama H., *Differential activation of microglia after experimental spinal cord injury.* Journal of Neurotrauma, 1999 **16**(3): p. 255-65.

185. Milhorat, T.H., Nobandegani F, Miller JI, Rao C., *Noncommunicating syringomyelia following occlusion of central canal in rats. Experimental model and histological findings.* Journal of Neurosurgery, 1993. **78**(2): p. 274-9.

186. Rexed, B., *The cytoarchitectonic organization of the spinal cord in the cat.* The Journal of Comparative Neurology, 1952. **96**(3): p. 414-95.

187. Kiernan, J.A., *Spinal Cord, in Barr's The Human Nervous System: An anatomical viewpoint*, ed. J.A. Kiernan. 2005, Philadelphia: Lippincott Williams & Wilkins: .

188. Netsky, M.G., *Syringomyelia; a clinicopathologic study.* A.M.A. Archives of Neurology and Psychiatry, 1953. **70**(6): p. 741-77.

189. Bruni J.E., and Reddy, K., *Ependyma of the central canal of the rat spinal cord: a light and transmission electron microscopic study.* Journal of Anatomy, 1987. **152**: p. 55-70.

190. Del Bigio, M.R., *The ependyma: a protective barrier between brain and cerebrospinal fluid.* Glia, 1995. **14**(1): p. 1-13.

191. Brightman MW, R.T., *Junctions between intimately apposed cell membranes in the vertebrate brain.* Journal of Cell Biology, 1969. **40**(3): p. 648-77.

192. Honda T, Y.S., Gang, F.G, Takahashi, M., Sugiura, Y., *Evidence for the c-ret protooncogene product (c-Ret) expression in the spinal tanycytes of adult rat.* Journal of Chemical Neuroanatomy, 1999. **17**(3): p. 163-8.

193. Leonhardt, H. and Desaga, U., *Recent observations on ependyma and subependymal basement membranes.* Acta Neurochir (Wien). 1975. **31**(3-4): p. 153-9.

194. Cifuentes, M., Fernández-LLebrez, P., Pérez, J., Manuel Pérez-Fígares, J., Rodríguez, E.M., *Distribution of intraventricularly injected horseradish peroxidase in cerebrospinal fluid compartments of the rat spinal cord.* Cell and Tissue Research, 1992. **270**: p. 485-494.

195. Cifuentes M, Rodríguez, S., Pérez J, Grondona JM, Rodríguez EM, Fernández-Llebrez P., *Decreased cerebrospinal fluid flow through the central canal of the spinal cord of rats immunologically deprived of Reissner's fibre.* Experimental Brain Research, 1994. **98**(3): p. 431-40.

196. Davson, H. and Segal, M., *Physiology of the CSF and Blood Brain Barriers*. 1996, Boca Raton: CRC Press.

197. Shah, L.M., Eisenmenger, L.B. and Hutchins, T.A., *Altered CSF Flow Due to Spinal Arachnoid Membrane Pathology.* Neurographics 2017. **7**(4): p. 291–304.

198. Sakka L, C.G., Chazal J. *Anatomy and physiology of cerebrospinal fluid.* European Annals of Otorhinolaryngological and Head and Neck Disorders, 2011;. **128**: p. 309–16.

199. Nicholas, D.S. and Weller, R., *The fine anatomy of the human spinal meninges. A light and scanning electron microscopy study.* Journal of Neurosurgery, 1988. **69**: p. 276–82.

200. Sakka L, G.J., Coll G., *Anatomy of the spinal meninges.* Operative Neurosurgery 2016. **12**(168 – 88).

201. Naidiach TP, Castillo, M., Cha, S., Raybaud, C., Smirniotopoulos, J., and Kollias, S. *Imaging of the Spine.* 2011, Philadelphia: Saunders Elsevier.

202. Reina MA, De Leon Casasola, O, López, A, De Andrés, JA, Mora, M, and Fernández A., *The origin of the spinal subdural space: ultrastructure findings.* Anesthesia and Analgesia 2002. **94**: p. 991–95.

203. Tubbs RS, Salter G, Grabb PA, Oakes WJ., *The denticulate ligament: anatomy and functional significance.* Journal of Neurosurgery, 2001. **94**: p. 271–75.

204. Vandenabeele F, Creemers J, Lambrichts I., *Ultrastructure of the human spinal arachnoid mater and dura mater.* Journal of Anatomy, 1996. **189**: p. 417–30.

205. Kido DK, Gomez DG, Pavese AM, Potts DG., *Human spinal arachnoid villi and granulations.* Neuroradiology, 1976. **11**: p. 221–28.

206. Elman, R., *Spinal arachnoid granulations with special reference to the cerebrospinal fluid.* Johns Hopkins Hospital Bulletin, 1923. **34**: p. 99–104.

207. Luedemann W, K.D., Kondziella D, Tienken K, Klinge P, Brinker T, Berens von Rautenfeld D., *Spinal cerebrospinal fluid pathways and their significance for the compensation of kaolin-hydrocephalus.* Acta Neurochir Supplement, 2002. **81**: p. 271–73.

208. Pollay, M., *The function and structure of the cerebrospinal fluid outflow system.* Cerebrospinal Fluid Research, 2010. **7**: p. 9.

209. Marmarou, A., Shulman, K., LaMorgese J. *Compartmental analysis of compliance and outflow resistance of the cerebrospinal fluid system.* Journal of Neurosurg 1975. **43**: p. 523–34

210. Kahn, V., *The pia mater at the site of the entry of blood vessels into the central nervous system.* Anatomy and Embryology (Berlin), 1982. **164**: p. 257–63.

211. Martin, B.A., Reymond, P., Novy, J., Balédent, O., and Stergiopulos, N., *A coupled hydrodynamic model of the cardiovascular and cerebrospinal fluid system.* American Journal of Physiology. Heart and Circulation Physiology, 2012. **302**(7): p. H1492-509.

212. J., C., *Spinal cord.* Anaesthesia and Intensive Care 2004. 32(5): p. 144–146.

213. Brockstein B, J.L., Gewertz BL. *Blood supply to the spinal cord: anatomic and physiologic correlations.* Annals of Vascular Surgery. 1994. **8**: p. 394–399.

214. Thron, A.K., *Vascular anatomy of the spinal cord : neuroradiological investigations and clinical syndromes* 1988, New York: Springer-Verlag.

215. Bosmia, A.N., Hogan, E.A., Loukas, M., Tubbs, R.S., & Cohen-Gadol, A.A. *Blood Supply to the Human Spinal Cord. I. Anatomy and Hemodynamics.* Clinical Anatomy, 2015. **28**(1): p. 52-64.

216. Koyanagi T, K.N., Kurimoto Y, Ito T, Baba T, Nakamura M, Watanebe A, Higami T. , *Examination of intercostal arteries with transthoracic Doppler sonography.* Echocardiography 2010. **27**: p. 17–20.

217. Lazorthes G, G.A., Zadeh JO, Jacques Santini J, Lazorthes Y, Burdin P., *Arterial vascularization of the spinal cord.* Journal of Neurosurgery 1971. **35**: p. 253–262.

218. Uotani K, Y.N., Kono AK, Taniguchi T, Sugimoto K, Fujii M, Kitagawa A, Okita Y, Naito H, Sugimura K., *Preoperative visualization of the artery of Adamkiewicz by intra-arterial CT angiography.* American Journal of Neuroradiology 2008. **29**: p. 314–318.

219. Nomura H., O.A., Tashiro A, Morimoto T, Hu JW, Iwata K., *Induction of Fos protein-like immunoreactivity in the trigeminal spinal nucleus caudalis and upper cervical cord following noxious and non-noxious mechanical stimulation of the whisker pad of the rat with an inferior alveolar nerve transection.* Pain 2002 **95**: p. 225-238.

220. Santillan, A., Nacarino V, Greenberg E, Riina HA, Gobin YP, Patsalides A., *Vascular anatomy of the spinal cord.* Journal of NeuroInterventional Surgery, 2012. **4**(1): p. 67-74.

221. Koyanagi I, T.C., Lea PJ, *Three-Dimensional Analysis of the Vascular System in the Rat Spinal Cord with Scanning Electron Microscopy of Vascular Corrosion Casts. Part 1: Normal spinal cord.* Neurosurgery, 1993. **33**(2): p. 277–284.

222. Nystrom B, S.J., Smedegard G., *Regional spinal cord blood flow in the rabbit, cat and monkey.* Acta Neurology Scandanavia 1984. **70**: p. 307–313.

223. Duggal N, and Lach, .B., *Selective vulnerability of the lumbosacral spinal cord after cardiac arrest and hypotension.* Stroke 2002. **33**: p. 116–121.

224. Scremin, OU, *Cerebral vascular system in The rat nervous system*, ed. P. G. 1995, San Diego: Academic Press.

225. Tveten L., *Spinal cord vascularity. III. The spinal cord arteries in man.* Acta Radiological: Diagnosis (Stockholm), 1976. **17**: p. 257-273.

226. Matsumae, M., Sato O, Hirayama A, Hayashi N, Takizawa K, Atsumi H, Sorimachi T., *Research into the Physiology of Cerebrospinal Fluid Reaches a New Horizon: Intimate Exchange between Cerebrospinal Fluid and Interstitial Fluid May Contribute to Maintenance of Homeostasis in the Central Nervous System.* Neurologia Medico Chirurgica (Tokyo), 2016. **56**(7): p. 416-41.

227. Magendie, F. *Recherches physiologiques et cliniques sur le liquide céphalo-rachidien ou cérébro-spinal.* 1842, Paris: Méquignon-Marvis fils.

228. Brodbelt, A. and Stoodley, M.A., *CSF pathways: A review.* British Journal of Neurosurgery, 2007. **21**(5): p. 510-520.

229. Spector, R., S. Snodgrass, R. and Johanson, C.E. *A balanced view of the cerebrospinal fluid composition and functions: Focus on adult humans.* Experimental Neurology, 2015. **273**: p. 57-68.

230. Hladky, S.B. and Barrand, M.A. *Mechanisms of fluid movement into, through and out of the brain: evaluation of the evidence.* Fluids Barriers CNS, 2014. **11**(1): p. 26.

231. Kimelberg, H., *Water homeostasis in the brain: basic concepts.* Neuroscience, 2004. **129**(4): p. 851-860.

232. Ganong, W.F., *Review of Medical Physiology.* 21st edition ed. 2003 New York: McGraw-Hill.

233. Brown, P.D., Davies SL, Speake T, Millar ID., *Molecular Mechanisms of Cerebrospinal Fluid Production.* Neuroscience, 2004. **129**(4): p. 957-970.

234. Lehtinen, M.K., Bjornsson CS, Dymecki SM, Gilbertson RJ, Holtzman DM, Monuki ES., *The Choroid Plexus and Cerebrospinal Fluid: Emerging Roles in Development, Disease, and Therapy.* The Journal of Neuroscience, 2013. **33**(45): p. 17553-17559.

235. Yamada, S. and Kelly, E. *Cerebrospinal Fluid Dynamics and the Pathophysiology of Hydrocephalus: New Concepts.* Seminars in Ultrasound CT MR, 2016. **37**(2): p. 84-91.

236. Johanson, C.E., Duncan JA, Klinge PM, Brinker T, Stopa EG, Silverberg GD., *Multiplicity of cerebrospinal fluid functions: New challenges in health and disease.* Cerebrospinal Fluid Res, 2008. **5**: p. 10.

237. Spector, R., *Nutrient transport systems in brain: 40 years of progress.* Journal of Neurochemistry, 2009. **111**: p. 315–320.

238. Davson, H., Welch, K., Segal, M.B., *The Physiology and Pathophysiology of the Cerebrospinal Fluid.* 1987, New York, NY.: Churchill Livingstone.

239. Watanabe S, K.T., Suenaga K, Wada S, Tsuda K, Kasama S, Takaoka T, Kajiyama K, Takeda M, Yoshikawa H., *Decreased chloride levels of cerebrospinal fluid in patients with amyotrophic lateral sclerosis.* Journal of Neurological Sciences, 2009. **285**(1-2): p. 146-8.

240. Milhorat TH, D.D., Hammock MK., *Experimental intracerebral movement of electron microscopic tracers of various molecular sizes.* Journal of Neurosurgery, 1975. **42**(3): p. 315-29.

241. Davson, H. *Physiology of the CSF and blood brain barriers.* 1996, Boca Raton: CRC Press.

242. Bartanusz V, J.D., Alajajian B, Digicaylioglu M., *The blood-spinal cord barrier: morphology and clinical implications.* Annals of Neurology, 2011. **70**(2): p. 194-206.

243. Nabeshima S, R.T., Landis DM, Brightman MW., *Junctions in the meninges and marginal glia.* Journal of Comparative Neurology, 1975. **164**(2): p. 127-69.

244. Whish, S., Dziegielewska, K.M., Møllgård, K., Noor, N.M., Liddelow, S.A., Habgood, M.D., and S.J. Richardson, Saunders, N.R., *The inner CSF–brain barrier: developmentally controlled access to the brain via intercellular junctions.* Frontiers of Neuroscience, 2015. **9**

245. Mullier A, B.S., Prevot V, and Dehouck B., *Differential distribution of tight junction proteins suggests a role for tanycytes in blood hypothalamus barrier regulation in the adult mouse brain.* Journal of Comparative Neurology, 2010. **518**(7): p. 943-62.

246. Milhorat T.H. and Clark, RG., *Some observations on the circulation of phenosulfonpthalein in cerebrospinal fluid: normal flow and the flow in hydrocephalus.* Journal of Neurosurgery, 1970. **32**(5): p. 522-8.

247. Fishman, R.A., *Cerebrospinal Fluid in Diseases of the Central Nervous System*. 1992, Philadelphia: W.B. Saunders.

248. Redzic, Z.B. and Segal, M.B., *The structure of the choroid plexus and the physiology of the choroid plexus epithelium.* Advanced Drug Delivery Reviews, 2004. **56**(12): p. 1695-1716.

249. Brinker, T., Stopa E, Morrison J, Klinge P, *A new look at cerebrospinal fluid circulation.* Fluids Barriers CNS, 2014. **11**: p. 10.

250. Welch, K., *Secretion of cerebrospinal fluid by choroid plexus of the rabbit.* American Journal of Physiology, 1963. **205**: p. 617-24.

251. Kao L, K.L., Shao X, Papadopoulos MC, Liu L, Bok D, Nusinowitz S, Chen B, Stella SL, Andre M, Weinreb J, Luong SS, Piri N, Kwong JM, Newman D, Kurtz I., *Severe neurologic impairment in mice with targeted disruption of the electrogenic sodium bicarbonate cotransporter NBCe2 (Slc4a5 gene).* Journal of Biological Chemistry, 2011. **286**(37): p. 32563-74.

252. Milhorat TH, H.M., Fenstermacher JD, Levin VA., *Cerebrospinal fluid production by the choroid plexus and brain.* Science, 1971 **173**(3994): p. 330-2.

253. Milhorat, T.H. *Choroid plexus and cerebrospinal fluid production.* Science, 1969. **166**(3912): p. 1514-6.

254. Hammock MK and Milhorat TH, *Recent Studies on the Formation of Cerebrospinal Fluid.* Developmental Medicine and Child Neurology, 1973. **15**(29).

255. Tamburrini G, C.M., Di Rocco F, Massimi L, D'Angelo L, Fasano T, Di Rocco C., *The role of endoscopic choroid plexus coagulation in the surgical management of bilateral choroid plexuses hyperplasia.* Childs Nervous System, 2006. **22**(6): p. 605-8.

256. Warf, BC., *The impact of combined endoscopic third ventriculostomy and choroid plexus cauterization on the management of pediatric hydrocephalus in developing countries.* World Neurosurg., 2013. **79**(2 Suppl): p. S23.e13-5.

257. Pollay, M., and Curl, F., *Secretion of cerebrospinal fluid by the ventricular ependyma of the rabbit.* American Journal of Physiology, 1967 **213**(4): p. 1031-8.

258. Sonnenberg H, S.S., Frazier DT., *Sodium and chloride movement into the central canal of cat spinal cord.* The Society for Experimental Biology and Medicine, 1967. **124**(4): p. 1316-20.

259. Sato O, A.T., Amano Y, Hara M, Tsugane R, Yagi M., *Extraventricular origin of the cerebrospinal fluid: formation rate quantitatively measured in the spinal subarachnoid space of dogs.* Journal of Neurosurgery, 1972 **36**(3): p. 276-82.

260. Orešković D, R.M., Klarica M, *Role of choroid plexus in cerebrospinal fluid hydrodynamics.* Neuroscience, 2017 **354**: p. 69-87.

261. Bering, EA., *Cerebrospinal fluid production and its relationship to cerebral metabolism and cerebral blood flow.* American Journal of Physiolopgy, 1959. **197**: p. 825-8.

262. Weed, L.H., *Studies on Cerebro-Spinal Fluid. No. III : The pathways of escape from the Subarachnoid Spaces with particular reference to the Arachnoid Villi.* Journal of Medical Research, 1914. **31**(1): p. 51-91.

263. Kida S, Y.T., Kubota T, Ito H, Yamamoto S., *A light and electron microscopic and immunohistochemical study of human arachnoid villi.* Journal of Neurosurgery, 1988. **69**(3): p. 429-35.

264. Murtha, L.A., Yang Q., Parsons, M.W., Levi, C.R., Beard, D.J., Spratt, N.J., McLeod, DD, *Cerebrospinal fluid is drained primarily via the spinal canal and olfactory route in young and aged spontaneously hypertensive rats.* Fluids Barriers CNS, 2014. **11**: p. 12.

265. Pollay, M., *The function and structure of the cerebrospinal fluid outflow system.* Cerebrospinal Fluid Research, 2010. **7**(9).

266. Tubbs RS, H.A., Stetler, W., Kelly, D,R,, Blevins, D., Humphrey, R., Chua, G.D., Shoja, M.M., Loukas, M., Oakes, W.J. *Human spinal arachnoid villi revisited: immunohistological study and review of the literature.* Journal of Neurosurgery Spine 2007. **7**: p. 328–331.

267. Kido DK, G.D., Pavese AM Jr, Potts DG, *Human spinal arachnoid villi and granulations.* Neuroradiology, 1976. **11**(5): p. 221-8.

268. Luedemann, W., Kondziella D, Tienken K, Klinge P, Brinker T, Berens von Rautenfeld D, *Spinal cerebrospinal fluid pathways and their significance for the compensation of kaolin-hydrocephalus.* Acta Neurochirurgica Supplement, 2002. **81**: p. 271-3.

269. Voelz, K., et al., *A ferritin tracer study of compensatory spinal CSF outflow pathways in kaolin-induced hydrocephalus.* Acta Neuropathologica, 2007. **113**(5): p. 569-75.

270. Boulton, M., Young A, Hay J, Armstrong D, Flessner M, Schwartz M, Johnston M., *Drainage of CSF through lymphatic pathways and arachnoid villi in sheep: measurement of 125I-albumin clearance.* Neuropathology and Applied Neurobiology, 1996. **22**(4): p. 325-33.

271. Johnston M, Z.A., Papaiconomou C, Salmasi G and Armstrong D, *Evidence of connections between cerebrospinal fluid and nasal lymphatic vessels in humans, non-human primates and other mammalian species.* Cerebrospinal Fluid Research, 2004. **1**(2).

272. Louveau, A., Smirnov, I., Keyes, T.J., Eccles, J.D., Rouhani, S.J., Peske, J.D., Derecki, N.C., Castle, D., Mandell, J.W., Lee, K.S., Harris, T.H., Kipnis, J., *Structural and functional features of central nervous system lymphatic vessels.* Nature, 2015. **523**(7560): p. 337-341.

273. Aspelund A, A.S., Proulx ST, Karlsen TV, Karaman S, Detmar M, Wiig H, Alitalo K., *A dural lymphatic vascular system that drains brain interstitial fluid and macromolecules.* Journal of Experimental Medicine. 2015. **212**(7): p. 991-9.

274. Dolman, C.L., *Lymph node metastasis as first manifestation of glioblastoma. Case report.* Journal of Neurosurgery, 1974. **41**(5): p. 607-9.

275. Koh L, Z.A., Nagra G, Armstrong D, Friendship R, Johnston M., *Development of cerebrospinal fluid absorption sites in the pig and rat: connections between the subarachnoid space and lymphatic vessels in the olfactory turbinates.* Anatomy and Embryology (Berlin) 2006. **211**: p. 335–344.

276. Mollanji R, P.C., Boulton M, Midha R, Johnston M, *Comparison of cerebrospinal fluid transport in fetal and adult sheep.* American Journal of Physiology Regulatory Integrative and Comparative Physiology 2001. **281**: p. R1215–1223.

277. Nagra G, Johnston, M.G., *Impact of ageing on lymphatic cerebrospinal fluid absorption in the rat.* Neuropathology and Applied Neurobiology, 2007. **33**: p. 684–691.

278. Bradbury MW, Cole, D., *The role of the lymphatic system in drainage of cerebrospinal fluid and aqueous humour.* Journal of Physiology, 1980. **299**: p. 353–365.

279. Boulton M, F.M., Armstrong D,Mohamed R, Hay J, Johnston M, *Contribution of extracranial lymphatics and arachnoid villi to the clearance of a CSF tracer in the rat.* American Journal of Physiology 1999. **276**(R818–823).

280. Boulton M, F.M., Armstrong D, Hay J, Johnston M *Determination of volumetric cerebrospinal fluid absorption into extracranial lymphatics in sheep.* American Journal of Physiology, 1998. **274**: p. R88–96.

281. Boulton M, A.D., Flessner M, Hay J, Szalai JP, Johnston M, *Raised intracranial pressure increases CSF drainage through arachnoid villi and extracranial lymphatics.* American Journal of Physiology, 1998. **275**: p. R889–896.

282. Edsbagge, M., Tisell M, Jacobsson L, Wikkelso C., *Spinal CSF absorption in healthy individuals.* American Journal of Physiology Regulatory Integrative and Comparative Physiology, 2004. **287**(6): p. R1450-5.

283. Hladky, S.B., Barrand, M., *Fluid and ion transfer across the blood-brain and blood-cerebrospinal fluid barriers; a comparative account of mechanisms and roles.* Fluids Barriers CNS, 2016. **13**(1): p. 19.

284. Dreha-Kulaczewski S, J.A., Merboldt K-D, Ludwig H-C, Gartner J, Frahm J, *Inspiration Is the Major Regulator of Human CSF Flow.* The Journal of Neuroscience 2015. **35**: p. 2485–2491.

285. Bateman GA, Brown, K.M., *The measurement of CSF flow through the aqueduct in normal and hydrocephalic children: from where does it come, to where does it go?* Child's Nervous System , 2012. **28**(1): p. 55-63.

286. Nilsson, C., Stahlberg, F., Thomsen, C., Henriksen, O., Herning, M., Owman, C., *Circadian variation in human cerebrospinal fluid production measured by magnetic resonance imaging.* American Journal of Physiology, 1992. **262**: p. R20–R24.

287. Enzmann DR, Pelc, N.J., *Cerebrospinal fluid flow measured by phase-contrast cine MR.* AJNR American Journal of Neuroradiology, 1993. **14**(6): p. 1301-7.

288. Wagshul ME, E.P., Madsen JR., *The pulsating brain: A review of experimental and clinical studies of intracranial pulsatility.* Fluids Barriers CNS., 2011. **8**(1).

289. Linninger AA, T.K., Hsu CY, Frim D, *Cerebrospinal Fluid Mechanics and Its Coupling to Cerebrovascular Dynamics.* Annual Review of Fluid Mechanics, 2016. **48**(1): p. 219-257.

290. Bunck, A.C., et al., *Magnetic resonance 4D flow analysis of cerebrospinal fluid dynamics in Chiari I malformation with and without syringomyelia.* European Radiology, 2012. **22**(9): p. 1860-70.

291. Enzmann, D.R. and N.J. Pelc, *Brain motion: measurement with phase-contrast MR imaging.* Radiology, 1992. **185**(3): p. 653-60.

292. Martins, A.N., Wiley, J.K. and Myers, P.W. *Dynamics of the cerebrospinal fluid and the spinal dura mater.* Journal of Neurology Neurosurgery and Psychiatry, 1972. **35**(4): p. 468-73.

293. Haughton, V. and Mardal, K.A. *Spinal fluid biomechanics and imaging: an update for neuroradiologists.* AJNR American Journal of Neuroradiology, 2014. **35**(10): p. 1864-9.

294. Tangen KM, H.Y., Zhu DC, Linninger AA, *CNS wide simulation of flow resistance and drug transport due to spinal microanatomy.* Journal of Biomechanics, 2015. **48**(10): p. 2144-54.

295. Shah S, H.V., del Río AM., *CSF flow through the upper cervical spinal canal in Chiari I malformation. .* AJNR American Journal of Neuroradiology, 2011. **32**: p. 1149–53.

296. Haughton V, Mardal, K.A., *Spinal fluid biomechanics and imaging: an update for neuroradiologists.* AJNR American Journal of Neuroradiology., 2014. **35**(10): p. 1864-9.

297. Støverud KH, L.H., Haughton V, et al. , *CSF pressure and velocity in obstructions of the subarachnoid spaces.* The Neuroradiology Journal, 2013. **26**: p. 218–26.

298. Heidari Pahlavian, S., et al., *The impact of spinal cord nerve roots and denticulate ligaments on cerebrospinal fluid dynamics in the cervical spine.* PLoS One, 2014. **9**(4): p. e91888.

299. Hettiarachchi HD, H.Y., Harris TJ Jr, Penn R, Linninger AA., *The effect of pulsatile flow on intrathecal drug delivery in the spinal canal.* Annals of Biomedical Engineering, 2011. **39**(10): p. 2592-602.

300. Stockman, H.W., *Effect of anatomical fine structure on the flow of cerebrospinal fluid in the spinal subarachnoid space.* Journal of Biomechanical Engineering, 2006. **128**: p. 106–114

301. Bunck AC, K.J., Juettner A, et al. , *Magnetic resonance 4D flow analysis of cerebrospinal fluid dynamics in Chiari I malformation with and without syringomyelia.* European Radiology 2012. **22**: p. 1860–70.

302. Drøsdal, I.N., Mardal KA, Støverud K, Haughton V, *Effect of the Central Canal in the Spinal Cord on Fluid Movement within the Cord.* The neuroradiology journal, 2013. **26**(5): p. 585-590.

303. Kim, K., et al., *Cerebrospinal fluid dynamics at the lumbosacral level in patients with spinal stenosis.* Fluids and Barriers of the CNS, 2015. **12**(Suppl 1): p. P24-P24.

304. Di Rocco C, M.D., Shimoji T, Raimondi AJ, *Continuous intraventricular cerebrospinal fluid pressure recording in hydrocephalic children during wakefulness and sleep.* Journal of Neurosurgery, 1975. **42**: p. 683–689.

305. Cifuentes M, F.L.L., Perez J, Perez Figares J.M., Rodriguez E.M., *Distribution of intraventricularly injected horseradish peroxidase in cerebrospinal fluid compartments of the rat spinal cord.* Cell and Tissue Research, 1992. **270**: p. 485-494.

306. Cifuentes, M., et al., *Decreased cerebrospinal fluid flow through the central canal of the spinal cord of rats immunologically deprived of Reissner's fibre.* Experimental Brain Research, 1994. **98**(3): p. 431-40.

307. Milhorat THNS, H.I., Nobandegani F, Murray S. *Ultrastructural evidence of sink function of central canal of spinal cord as demonstrated by clearance of horseradish peroxidase.* Proceedings of the Electron Microscopy Society of America, 1992. **50**: p. 700–701.

308. Brodbelt, A.R., Stoodley MA, Watling AM, Tu J, Burke S, Jones NR., *Altered subarachnoid space compliance and fluid flow in an animal model of posttraumatic syringomyelia.* Spine, 2003. **28**(20): p. E413-419.

309. Wei, F., et al., *The pathway of subarachnoid CSF moving into the spinal parenchyma and the role of astrocytic aquaporin-4 in this process.* Life Science, 2017. **182**: p. 29-40.

310. Milhorat, T.H., Kotzen, R.M. and Anzil, A.P., *Stenosis of central canal of spinal cord in man: incidence and pathological findings in 232 autopsy cases.* Journal of Neurosurgery, 1994. **80**(4): p. 716-22.

311. Yasui K, H.Y., Yoshida M, Kameyama T, Sobue G., *Age-related morphologic changes of the central canal of the human spinal cord.* Acta Neuropathologica, 1999. **97**(3): p. 253-9.

312. Muthukumar, N., *Syringomyelia as a presenting feature of shunt dysfunction: Implications for the pathogenesis of syringomyelia.* Journal of Craniovertebral Junction and Spine, 2012. **3**(1): p. 26-31.

313. Snodgrass, S.R, and Lorenzo, A., *Temperature and cerebrospinal fluid production rate.* American Journal of Physiology, 1972. **222**(6): p. 1524-1527.

314. Ghazi SR, Gholami S., *Allometric growth of the spinal cord in relation to the vertebral column during prenatal and postnatal life in the sheep.* Journal of Anatomy 1994. **185**: p. 427–431.

315. Réthelyi M, L.E., Boros C., *The caudal end of the rat spinal cord: transformation to and ultrastructure of the filum terminale.* Brain Research, 2004. **1028**(2): p. 133-9.

316. Galarza, M., *Evidence of the subcommissural organ in humans and its association with hydrocephalus.* Neurosurgical Review, 2002. **25**: p. 205–215.

317. Xu, Q., et al., *Head movement, an important contributor to human cerebrospinal fluid circulation.* Scientific Reports, 2016. **6**: p. 31787.

318. Mestre H, T.J., Du T, Song W, Peng W, Sweeney AM, Olveda G, Thomas JH, Nedergaard M, Kelley DH, *Flow of cerebrospinal fluid is driven by arterial pulsations and is reduced in hypertension.* Nature Communications, 2018. **9**(1): p. 4878.

319. Albargothy NJ, J.D., MacGregor-Sharp M, Weller RO, Verma A, Hawkes CA, Carare RO., *Convective influx/glymphatic system: tracers injected into the CSF enter and leave the brain along separate periarterial basement membrane pathways.* Acta Neuropathologica, 2018. **136**(1): p. 139–152.

320. Ma Q, R.M., Decker Y, Müller A, Riner C, Bücker A, Fassbender K, Detmar M, Proulx ST., *Rapid lymphatic efflux limits cerebrospinal fluid flow to the brain.* Acta Neuropathologica, 2018. **[Epub ahead of print]**.

321. Di Chiro, G., *Movement of the Cerebrospinal Fluid in Human Beings.* Nature, 1964. **204**: p. 290–291.

322. Di Chiro, G., *Observations on the circulation of the cerebrospinal fluid.* Acta Radiologica: Diagnosis (Stockholm). 1966. **5**: p. 988-1002.

323. Howarth, F., and Cooper, E., *The fate of certain foreign colloids and crystalloids after subarachnoid injection.* Cells Tissues Organs, 1955. **25**(2-4): p. 112-140.

324. Milhorat, T.H., *The third circulation revisited.* Journal of Neurosurgery, 1975. **42**(6): p. 628-645.

325. Wei F, Z.C., Xue R, Shan L, Gong S, Wang G, Tao J, Xu G, Zhang G, Wang L *The pathway of subarachnoid CSF moving into the spinal parenchyma and the role of astrocytic aquaporin-4 in this process.* Life Sciences, 2017. **182**: p. 29-40.

326. Greitz, D., *Cerebrospinal fluid circulation and associated intracranial dynamics. A radiologic investigation using MR imaging and radionuclide cisternography.* Acta Radiologica Supplement, 1993. **386**: p. 1-23.

327. Iliff, J.J., et al., *A Paravascular Pathway Facilitates CSF Flow Through the Brain Parenchyma and the Clearance of Interstitial Solutes, Including Amyloid β.* Science Translational Medicine, 2012. **4**(147): p. 147ra111-147ra111.

328. Hladky, S.B., and Barrand, .M., *Elimination of substances from the brain parenchyma: efflux via perivascular pathways and via the blood-brain barrier.* Fluids Barriers CNS, 2018. **15**(1): p. 30.

329. Bedussi, B., A.M., de Vos, J., VanBavel, E., Bakker, E.N., *Paravascular spaces at the brain surface: Low resistance pathways for cerebrospinal fluid flow.* Journal of Cerebral Blood Flow and Metabolism, 2018. **38**(4): p. 719-726.

330. Korogod N, P.C., Knott GW *Ultrastructural analysis of adult mouse neocortex comparing aldehyde perfusion with cryo fixation.* Elife, 2015. **4**: p. 1–17.

331. Pizzo ME, W.D., Kumar NN, Brunette E, Brunnquell CL, Hannocks MJ, Abbott NJ, Meyerand ME, Sorokin L, Stanimirovic DB, Thorne RG, *Intrathecal antibody distribution in the rat brain: surface diffusion, perivascular transport and osmotic enhancement of delivery.* Journal of Physiology, 2018. **1**(596): p. 445-475.

332. Yamada, S., et al., *Influence of respiration on cerebrospinal fluid movement using magnetic resonance spin labeling.* Fluids and Barriers of the CNS, 2013. **10**(1): p. 36.

333. Yildiz, S., et al., *Quantifying the influence of respiration and cardiac pulsations on cerebrospinal fluid dynamics using real-time phase-contrast MRI.* Journal of Magnetic Resonance Imaging, 2017. **46**(2): p. 431-439

334. Bhadelia, R.A., Madan N, Zhao Y, Wagshul ME, Heilman C, Butler JP, Patz S., *Physiology-based MR imaging assessment of CSF flow at the foramen magnum with a valsalva maneuver.* AJNR American Journal of Neuroradiology, 2013. **34**(9): p. 1857-62.

335. Sarntinoranont M, C.X., Zhao J, Mareci TH, *Computational model of interstitial transport in the spinal cord using diffusion tensor imaging.* Annals of Biomedical Engineering, 2006. **34**: p. 1304–1321.

336. Loth F, Y.M., Alperin N., *Hydrodynamic modeling of cerebrospinal fluid motion within the spinal cavity.* Journal of Biomechanical Engineering, 2001. **123**(1): p. 71-9.

337. Cheng, S., Stoodley MA, Wong J, Hemley S, Fletcher DF, Bilston LE, *The presence of arachnoiditis affects the characteristics of CSF flow in the spinal subarachnoid space: A modelling study.* Journal of Biomechanics, 2012. **45**(7): p. 1186-1191.

338. Haller, FR, and Low, FN, *The fine structure of the peripheral nerve root sheath in the subarachnoid space in the rat and other laboratory animals.* Developmental Dynamics, 1971. **131**(1): p. 1-19.

339. Stockman, HW, *Effect of anatomical fine structure on the dispersion of solutes in the spinal subarachnoid space.* Journal of Biomechanical Engineering, 2007. **129**(5): p. 666-75.

340. Gupta S, S.M., Grzybowski DM, Boesiger P, Biddiscombe J, Poulikakos D, Kurtcuoglu V., *Cerebrospinal fluid dynamics in the human cranial subarachnoid space: an overlooked mediator of cerebral disease. I. Computational model.* Journal of Royal Society, Interface, 2010. **7** (40): p. 1195-204.

341. Sweetman, B. and A.A. Linninger, *Cerebrospinal fluid flow dynamics in the central nervous system.* Annals of Biomedical Engineering, 2011. **39**(1): p. 484-96.

342. Linninger AA, X.M., Sweetman B, Ponkshe S, Guo X, Penn R, *A mathematical model of blood, cerebrospinal fluid and brain dynamics.* Journal of Mathematical Biology, 2009. **59**(6): p. 729-59.

343. Penn RD, B.S., Sweetman B, Guo X, Linninger A, *Ventricle wall movements and cerebrospinal fluid flow in hydrocephalus.* Journal of Neurosurgery, 2011. **115**(1): p. 159-64.

344. Sweetman B, X.M., Zitella L, Linninger AA., *Three-dimensional computational prediction of cerebrospinal fluid flow in the human brain.* Computers in Biology and Medicine, 2011. **41**(2): p. 67-75.

345. Linge SO, H.V., Løvgren AE, et al., *Effect of tonsillar herniation on cyclic CSF flow studied with computational flow analysis.* AJNR American Journal of Neuroradiology 2011. **32**: p. 1474–81.

346. Hrabeˇtova S, and Nicholson, C., *Contribution of dead-space microdomains to tortuosity of brain extracellular space.* Neurochemistry International, 2004. **45**(4): p. 467–477.

347. Morris AW, C.R., Schreiber S, Hawkes CA, *The cerebrovascular basement membrane: role in the clearance of b-amyloid and cerebral amyloid angiopathy.* Frontiers in Aging Neuroscience, 2014. **6**(19): 251

348. Bakker EN, B.B., Arbel-Ornath M, Aldea R, Bedussi B, Morris AW, Weller RO, Carare RO., *Lymphatic Clearance of the Brain: Perivascular, Paravascular and Significance for Neurodegenerative Diseases.* Celleular and Molecular Neurobiology, 2016. **36**(2): p. 181-94.

349. Abbott, N.J., *Evidence for bulk flow of brain interstitial fluid: significance for physiology and pathology.* Neurochemistry International, 2004. **45**(4): p. 545-52.

350. Hladky, S.B. and M.A. Barrand, *Fluid and ion transfer across the blood–brain and blood–cerebrospinal fluid barriers; a comparative account of mechanisms and roles.* Fluids and Barriers of the CNS, 2016. **13**(1): p. 19.

351. Spector, R., Keep RF, Robert Snodgrass S, Smith QR, Johanson CE, *A balanced view of choroid plexus structure and function: Focus on adult humans.* Experimental Neurology, 2015. **267**: p. 78-86.

352. Mokgokong, R., Wang S, Taylor CJ, Barrand MA, Hladky SB., *Ion transporters in brain endothelial cells that contribute to formation of brain interstitial fluid.* Pflugers Archives: European Journal of Physiology, 2014. **466**(5): p. 887-901.

353. Abbott NJ, P.M., Preston JE, Janigro D, Thorne RG, *The role of brain barriers in fluid movement in the CNS: is there a 'glymphatic' system?* Acta Neuropathologica, 2018. **135**(3): p. 387-407.

354. Abbott, NJ, *Blood–brain barrier structure and function and the challenges for CNS drug delivery.* Journal of Inherited Metabolic Disorders, 2013 **36**(3): p. 437–449.

355. Abbott, N.J., *Evidence for bulk flow of brain interstitial fluid: significance for physiology and pathology.* Neurochemistry International, 2004. **45**: p. 545–552.

356. Abbott, NJ, *Evidence for bulk flow of brain interstitial fluid: significance for physiology and pathology.* Neurochemistry International, 2004. **45**(4): p. 545–552.

357. Schielke GP, B.A., *Physiology and pharmacology of the blood–brain*, ed. Bradbury, MWB. 1992, Berlin: Springer.

358. Cushing, H., *Studies on the cerebro-spinal fluid: I. Introduction.* Journal of Medical Research, 1914. **31**: p. 1–19.

359. Cserr HF, D.M., Patlak CS, Pullen RG, *Convection of cerebral interstitial fluid and its role in brain volume regulation.* Annals of New York Academy of Sciences 1986. **481**: p. 123–134.

360. Cserr HF, Ostrach LH., *Bulk flow of interstitial fluid after intracranial injection of blue dextran 2000.* Experimental Neurololgy, 1974 **45**: p. 50–60.

361. Cserr HF, C.D., Milhorat TH *Flow of cerebral interstitial fluid as indicated by the removal of extracellular markers from rat caudate nucleus.* Experimental Eye Research, 1977. **25(Suppl)**: p. 461–473.

362. Rennels, M.L., Gregory TF, Blaumanis OR, Fujimoto K, Grady PA., *Evidence for a 'paravascular' fluid circulation in the mammalian central nervous system, provided by the rapid distribution of tracer protein throughout the brain from the subarachnoid space.* Brain Research, 1985. **326**(1): p. 47-63.

363. Weller RO, K.S., Zhang ET, *Pathways of fluid drainage from the brain– morphological aspects and immunological significance in rat and man.* Brain Pathology 1992. **2**(277–284).

364. Ohata K, M.A., *Clearance of brain edema and macromolecules through the cortical extracellular space.* Journal of Neurosurgery, 1992. **77**: p. 387–396.

365. Syková E, N.C., *Diffusion in brain extracellular space.* Physiological Review , 2008. **88**(4): p. 1277-340.

366. Levin VA, F.J., Patlak CS *Sucrose and inulin space measurements of cerebral cortex in four mammalian species.* American Journal of Physiology 1970. **219**: p. 1528–1533.

367. Rall DP, O.W., Patlak CS *Extracellular space of brain as determined by diffusion of inulin from the ventricular system.* Life Sciences, 1962. **1**: p. 43–48.

368. Patlak CS, F.J., *Measurements of dog blood–brain transfer constants by ventriculocisternal perfusion.* American Journal of Physiology, 1975. **229**: p. 877–884.

369. Nicholson C, P.J., *Ion diffusion modified by tortuosity and volume fraction in the extracellular microenvironment of the rat cerebellum.* Journal of Physiology, 1981. **321**: p. 225–257.

370. Brightman MW, and Reese, T., *Junctions between intimately apposed cell membranes in the vertebrate brain.* Journal of Cell Biology, 1969. **40**: p. 648–677.

371. A, V.H., *The structure and function of nervous tissue* ed. Bourne, G. Vol. 4. 1972, New York: Academic Press,.

372. Peters A, P.S., Webster HD, *The fine structure of the nervous system: neurons and their supporting cells.* 3rd ed. 1991, New York: Oxford University Press.

373. Thorne RG, and Nicholson, C., *In vivo diffusion analysis with quantum dots and dextrans predicts the width of brain extracellular space.* Proceedings of the National Academy of Sciences USA 2006. **103**: p. 5567–5572.

374. Thorne RG, H.S., Nicholson C *Diffusion of epidermal growth factor in rat brain extracellular space measured by integrative optical imaging.* Journal of Neurophysiology, 2004. **92**: p. 3471–3481.

375. Holter KE, K.B., Devor A, Sejnowski TJ, Dale AM, Omholt SW, Ottersen OP, Nagelhus EA, Mardal KA, Pettersen KH, *Interstitial solute transport in 3D*

reconstructed neuropil occurs by diffusion rather than bulk flow. Proceedings of the National Academy of Sciences USA, 2017. **114**(37): p. 9894-9899.

376. Jin, B.J., A.J. Smith, and A.S. Verkman, *Spatial model of convective solute transport in brain extracellular space does not support a "glymphatic" mechanism.* Journal of General Physiology, 2016. **148**(6): p. 489-501.

377. Wolak DJ, and Thorne, R., *Diffusion of macromolecules in the brain: implications for drug delivery.* Molecular Pharmaceutics, 2013. **10**: p. 1492–1504.

378. Fenstermacher JD, P.C., *Dynamics of brain edema.* ed. Feindel, W. and Pappius HM. 1976, Berlin: Springer.

379. Rosenberg GA, K.W., Estrada E, *Bulk flow of brain interstitial fluid under normal and hyperosmolar conditions.* American Journal of Physiologyu 1980. **238**: p. F42–F49.

380. Endo, T., Fujii Y, Sugiyama SI, Zhang R, Ogita S, Funamoto K, Saito R, Tominaga T, *Properties of convective delivery in spinal cord gray matter: laboratory investigation and computational simulations.* Journal of Neurosurgery Spine, 2015: p. 1-8.

381. Sykova, E. and C. Nicholson, *Diffusion in brain extracellular space.* Physiological Review, 2008. **88**(4): p. 1277-340.

382. Prokopova, S., L. Vargova, and E. Sykova, *Heterogeneous and anisotropic diffusion in the developing rat spinal cord.* Neuroreport, 1997. **8**(16): p. 3527-32.

383. Simonova, Z., Svoboda J, Orkand P, Bernard CC, Lassmann H, Syková E., *Changes of extracellular space volume and tortuosity in the spinal cord of Lewis rats with experimental autoimmune encephalomyelitis.* Physiological Research, 1996. **45**(1): p. 11-22.

384. Svoboda, J. and E. Sykova, *Extracellular space volume changes in the rat spinal cord produced by nerve stimulation and peripheral injury.* Brain Researcj, 1991. **560**(1-2): p. 216-24.

385. Sykova, E., Vargová L, Prokopová S, Simonová Z., *Glial swelling and astrogliosis produce diffusion barriers in the rat spinal cord.* Glia, 1999. **25**(1): p. 56-70.

386. Lonser, R.R., Lonser RR, Gogate N, Morrison PF, Oldfield EH, *Direct convective delivery of macromolecules to the spinal cord.* Journal of Neurosurgery, 1998. **89**(4): p. 616-22.

387. Wood, J.D., Lonser RR, Gogate N, Morrison PF, Oldfield EH., *Convective delivery of macromolecules into the naive and traumatized spinal cords of rats.* Journal of Neurosurgery, 1999. **90**(1 Suppl): p. 115-20.

388. Bedussi B, v.L.M., Bartstra JW, de Vos J, Siebes M, VanBavel E, Bakker EN., *Clearance from the mouse brain by convection of interstitial fluid towards the ventricular system.* Fluids Barriers CNS 2015. **5**(12): p. 23.

389. Nualart F. et al, *Vitamin C transporters, recycling and the bystander effect in the nervous system: SVCT2 versus gluts.* Journal of Stem Cell Research and Therapy, 2014. **4**(209).

390. Spector, V., *Vitamin transport diseases of brain: focus on folates, thiamine and riboflavin.* Brain Disorders and Therapy, 2014. **3**(120).

391. Borlongan CV, S.S., Geaney M, Vasconcellos AV, Elliott RB, Emerich DF, *Intracerebral transplantation of porcine choroid plexus provides structural and functional neuroprotection in a rodent model of stroke.* Stroke 2004. **35**: p. 2206–2210.

392. Penn RD, L.M., Linninger AA, Miesel K, Lu SN, Stylos L. *Pressure gradients in the brain in an experimental model of hydrocephalus.* Collections 2009. **116**: p. 1069–75.

393. Penn RD, B.S., Sweetman B, Guo X, Linninger AA., *Ventricle wall movements and cerebrospinal fluid flow in hydrocephalus.* Journal of Neurosurgery, 2011. **115**: p. 159–64.

394. Hammarstrom, L., *Autoradiographic studies on the distribution of C14-labelled ascorbic acid and dehydroascorbic acid.* Acta Physiologica Scandinavica , 1966 **289**: p. 1–75.

395. Spector, R., *Penetration of ascorbic acid from cerebrospinal fluid into brain.* Experimental Neurology, 1981. **72**(645–653).

396. Spector, R., Johanson, C.E., *Sustained choroid plexus function in human elderly and Alzheimer's disease patients.* Fluids and Barriers of the CNS, 2013. **10**(28).

397. Spector, R., Spector, A.Z., Snodgrass, R.R., *Model for transport in the central nervous system.* American Journal of Physiology, 1977. **232**: p. R73–R79.

398. Spector, R., Johanson, C.E, *Micronutrient and urate transport in choroid plexus and kidney: implications for drug therapy.* Pharmaceutical Research, 2006. **23**: p. 2515–2524.

399. Proescholdt, M.G., Hutto, B., Brady, L.S., Herkenham, M., *Studies of cerebrospinal fluid flow and penetration into brain following lateral ventricle and cisterna magna injections of tracer [14C]inulin in rat.* Neuroscience, 2000. **95**: p. 577–592.

400. Smith, O.R., Rapoport, S.I., *Cerebrovascular permeability coefficients to sodium, potassium and chloride.* Journal of Neurochemistry, 1986. **46**(1732–1742).

401. Spector, R., *Nature and consequences of mammalian brain and CSF efflux transporters: four decades of progress.* Journal of Neurochemistry, 2010 **112**: p. 13–23.

402. Lam MA, H.S., Najafi E, Vella NGF, Bilston LE, Stoodley MA., *The ultrastructure of spinal cord perivascular spaces: Implications for the circulation of cerebrospinal fluid.* Scientific Report, 2017. **7**(1): p. 12924.

403. Morris, A.W., Sharp MM, Albargothy NJ, Fernandes R, Hawkes CA, Verma A, Weller RO, Carare RO, *Vascular basement membranes as pathways for the passage of fluid into and out of the brain.* Acta Neuropathologica, 2016. **131**(5): p. 725-36.

404. Frederickson RG, and Low, FN., *Blood vessels and tissue space associated with the brain of the rat.* American Journal of Anatomy, 1969. **125**: p. 123–145.

405. Zhang ET, I.C., Weller RO *Interrelationships of the pia mater and the perivascular (Virchow–Robin) spaces in the human cerebrum.* Journal of Anatomy, 1990. **170**: p. 111–123.

406. Wu C, I.F., Anderson P, Hallmann R, Vestweber D, Nilsson P, Robenek H, Tryggvason K, Song J, Korpos E, Loser K, Beissert S, Georges-Labouesse E, Sorokin LM *Endothelial basement membrane laminin alpha5 selectively inhibits T lymphocyte extravasation into the brain.* Nature Medicine, 2009. **15**: p. 519–527.

407. Sixt M, E.B., Pausch F, Hallmann R, Wendler O, Sorokin LM *Endothelial cell laminin isoforms, laminins 8 and 10, play decisive roles in T cell recruitment across the blood–brain barrier in experimental autoimmune encephalomyelitis.* Journal of Cell Biology, 2001. **153**: p. 933–945.

408. Weller, RO, *Microscopic morphology and histology of the human meninges.* Morphologie 2005. **89**(284): p. 22–34.

409. Hannocks MJ, P.M., Huppert J, Deshpande T, Abbott NJ, Thorne RG, Sorokin L., *Molecular characterization of perivascular drainage pathways in the murine brain.* Journal of Cerebral Blood Flow and Metabolism, 2018. **38**(4): p. 669-686.

410. Coles, J.A., Myburgh E, Brewer JM, McMenamin PG, *Where are we? The anatomy of the murine cortical meninges revisited for intravital imaging, immunology, and clearance of waste from the brain.* Progress in Neurobiology, 2017. **156**: p. 107-148.

411. Bakker, E.N., Bacskai BJ, Arbel-Ornath M, Aldea R, Bedussi B, Morris AW, Weller RO, Carare RO, *Lymphatic Clearance of the Brain: Perivascular, Paravascular and Significance for Neurodegenerative Diseases.* Cellular and Molecular Neurobiology, 2016. **36**(2): p. 181-94.

412. Gutiérrez AM, G.E., Echevarría M, Hernández CS, Whittembury G *The proximal straight tubule (PST) basolateral cell membrane water channel: selectivity characteristics.* The Journal of Membrane Biology, 1995(143): p. 189–197.

413. Jung JS, B.R., Preston GM, Guggino WB, Baraban JM, Agre Pahlavian, Soroush Heidari, *Molecular characterization of an aquaporin cDNA from brain: candidate osmoreceptor and regulator of water balance.* Proceedings of the National Academy of Sciences USA, 1994. **91**: p. 13052–13056.

414. Nielsen S, N.E., Amiry-Moghaddam M, Bourque C, Agre P, Ottersen OP *Specialized membrane domains for water transport in glial cells: high-resolution immunogold cytochemistry of aquaporin-4 in rat brain.* Journal of Neuroscience, 1997. **17**: p. 171–180.

415. Badaut J, L.F., Magistretti PJ, Regli L, *Aquaporins in brain: distribution, physiology, and pathophysiology.* Journal of Cerebral Blood Flow and Metabolism, 2002. **22**: p. 367–378.

416. Li X, K.H., Wu W, Xiao M, Sun X, Hu G *Aquaporin-4 maintains ependymal integrity in adult mice.* Neuroscience, 2009. **162**(1): p. 67–77.

417. Nagelhus, E.A., and Ottersen, O., *Physiological roles of aquaporin-4 in brain.* Physiological Reviews, 2013. **93**(4): p. 1543–1562.

418. Haj-Yasein NN, V.G., Eilert-Olsen M, Gundersen GA, Skare Ø, Laake P, Klungland A, Thorén AE, Burkhardt JM, Ottersen OP, Nagelhus EA *Glial-conditional deletion of aquaporin-4 (Aqp4) reduces blood–brain water uptake and confers barrier function on perivascular astrocyte endfeet. .* Proceedings of the National Academy of Sciences USA, 2011. **108**: p. 17815–17820.

419. Papadopoulos MC, M.G., Krishna S, Verkman AS *Aquaporin-4 facilitates reabsorption of excess fluid in vasogenic brain edema.* The FASEB Journal, 2004. **18**: p. 1291–1293.

420. Yao X, H.S., Nicholson C, Manley GT *Aquaporin-4-deficient mice have increased extracellular space without tortuosity change.* Journal of Neuroscience, 2008. **28**: p. 5460–5464.

421. Kress BT, I.J., Xia M, Wang M, Wei HS, Zeppenfeld D, Xie L, Kang H, Xu Q, Liew JA *Impairment of paravascular clearance pathways in the aging brain.* Annals of Neurol, 2014. **76**(6): p. 845–861.

422. Ichimura, T., P.A. Fraser, and H.F. Cserr, *Distribution of extracellular tracers in perivascular spaces of the rat brain.* Brain Research, 1991. **545**(1-2): p. 103-13.

423. Asgari, M., D. de Zélicourt, and V. Kurtcuoglu, *Glymphatic solute transport does not require bulk flow.* Scientific Reports, 2016. **6**: p. 38635.

424. Smith AJ, J.B., Verkman AS, *Muddying the water in brain edema?* Trends in Neuroscience, 2015. **38**(6): p. 331-2.

425. Pizzo, W.D., Thorne RG, *Diffusion of macromolecules in the brain: implications for drug delivery.* Molecular Pharmaceutics, 2013. **10**: p. 1492–1504.

426. Smith AJ, Y.X., Dix JA, Jin BJ, Verkman AS, *Test of the 'glymphatic' hypothesis demonstrates diffusive and aquaporin-4-independent solute transport in rodent brain parenchyma.* eLife, 2017. **6**: p. e27679.

427. Carare, R.O., Bernardes-Silva M, Newman TA, Page AM, Nicoll JA, Perry VH, Weller RO., *Solutes, but not cells, drain from the brain parenchyma along basement membranes of capillaries and arteries: significance for cerebral amyloid*

angiopathy and neuroimmunology. Neuropathology and Applied Neurobiol, 2008. **34**(2): p. 131-44.

428. Weller, R.O., Djuanda E, Yow HY, Carare RO., *Lymphatic drainage of the brain and the pathophysiology of neurological disease.* Acta Neuropathologica, 2009. **117**(1): p. 1-14.

429. Hawkes, C.A., Jayakody N, Johnston DA, Bechmann I, Carare RO., *Failure of perivascular drainage of beta-amyloid in cerebral amyloid angiopathy.* Brain Pathology, 2014. **24**(4): p. 396-403.

430. Arbel-Ornath, M., et al., *Interstitial fluid drainage is impaired in ischemic stroke and Alzheimer's disease mouse models.* Acta Neuropathologica, 2013. **126**(3): p. 353-64.

431. Faghih MM, and Sharp MK, *Is bulk flow plausible in perivascular, paravascular and paravenous channels?* Fluids and Barriers of the CNS, 2018. **15**(17).

432. Rey J, and Sarntinoranont M, *Pulsatile flow drivers in brain parenchyma and perivascular spaces: a resistance network model study.* Fluids and Barriers of the CNS, 2018. **15**(20).

433. Asgari M, de Zelicourt, D., Kurtcuoglu V, *Barrier dysfunction or drainage reduction: differentiating causes of CSF protein increase.* Fluids and Barriers CNS, 2017. **14**(14).

434. Ball KK, C.N., Mrak RE, Dienel GA., *Trafficking of glucose, lactate, and amyloid-beta from the inferior colliculus through perivascular routes.* Journal of Cerebral Blood Flow and Metabolism, 2010. **30**(1): p. 162-76.

435. Szentistvanyi I, P.C., Ellis RA, Cserr HF., *Drainage of interstitial fluid from different regions of rat brain. .* American Journal of Physiology, 1984. **246**: p. F835–44.

436. Weller RO, D.E., Yow HY, Carare RO *Lymphatic drainage of the brain and the pathophysiology of neurological disease.* Acta Neuropathologica, 2009. **117**: p. 1–14.

437. Pappolla M, S.K., Vidal R, Pacheco-Quinto J, Poeggeler B, Matsubara E, *Evidence for lymphatic Aβ clearance in Alzheimer's transgenic mice.* Neurobiology of Disease, 2014 **71**: p. 215-9.

438. Bhadelia, R.A., Bogdan AR, Kaplan RF, Wolpert SM., *Cerebrospinal fluid pulsation amplitude and its quantitative relationship to cerebral blood flow pulsations: a phase-contrast MR flow imaging study.* Neuroradiology, 1997. **39**(4): p. 258-64.

439. Zou R, P.E., Kelly EM, Egnor M, Wagshul ME, Madsen JR., *Intracranial pressure waves: characterization of a pulsation absorber with notch filter properties using systems analysis: laboratory investigation.* Journal of Neurosurgery Pediatrics, 2008. **2**: p. 83–94.

440. Czosnyka M, Pickard, J., *Monitoring and interpretation of intracranial pressure.* Journal of Neurology, Neurosurgery and Psychiatry 2004. **75**: p. 813–821.

441. Baledent O, H.-F.M., Idy-Peretti I., *Cerebrospinal fluid dynamics and relation with blood flow: a magnetic resonance study with semiautomated cerebrospinal fluid segmentation.* Investigative Radiology, 2001. **36** p. 368–377.

442. Baledent O, G.-J.C., Meyer ME, De Marco G, Le Gars D, Henry-Feugeas MC, Idy-Peretti I., *Relationship between cerebrospinal fluid and blood dynamics in healthy volunteers and patients with communicating hydrocephalus.* Investigative Radiology, 2004. **39**: p. 45–55.

443. Alperin N, S.A., Lichtor T., *Magnetic resonance imaging-based measurements of cerebrospinal fluid and blood flow as indicators of intracranial compliance in patients with Chiari malformation.* Journal of Neurosurgery, 2005. **103**: p. 46–52.

444. Du Boulay, G.H., *Pulsatile Movements in the CSF Pathways.* The British Journal of Radiology, 1966. **39**(460): p. 255-262.

445. Freund M, A.M., Kooijman H, Heiland S,Thomsen M, et al., *Measurement ofCSF flow in the spinal canal using MRI with an optimized MRI protocol: experimental and clinical studies.* Rofo, 2001. **173**: p. 306–14.

446. Greitz D, W.R., Franck A, Nordell B, Thomsen C, Ståhlberg F., *Pulsatile brain movement and associated hydrodynamics studied by magnetic resonance phase imaging. The Monro-Kellie doctrine revisited.* Neuroradiology, 1992. **34**(5): p. 370-80.

447. Zhu DC, X.M., Linninger AA, Penn RD., *Dynamics of lateral ventricle and cerebrospinal fluid in normal and hydrocephalic brains.* Journal of Magnetic Resonance Imaging, 2006. **24**(4): p. 756-70.

448. Linninger AA, T.C., ZhuDC, Xenos M, Roycewicz P, et al., *Pulsatile cerebrospinal fluid dynamics in the human brain.* IEEE Transactions on Biomedical Engineering, 2005. **52**: p. 557–65.

449. Du Boulay G, O.C.J., Currie J, Bostick T, Verity P., *Further investigations on pulsatile movements in the cerebrospinal fluid pathways.* Acta Radiologica: Diagnosis (Stockholm), 1972. **13**(0): p. 496-523.

450. du Boulay G, S.S., Currie JC, Logue V., *The mechanism of hydromyelia in Chiari type 1 malformations.* British Journal of Radiology, 1974. **47**(561): p. 579-87.

451. Bering, E.A., *Circulation of the cerebrospinal fluid. Demonstration of the choroid plexuses as the generator of the force for flow of fluid and ventricular enlargement.* Journal of Neurosurgery, 1962. **19**: p. 405-13.

452. Buishas J, Gould IG, Linninger AA, *A computational model of cerebrospinal fluid production and reabsorption driven by Starling forces.* Croatian Medical Journal, 2014. **55**: p. 481–97.

453. Adolph, R.J., H. Fukusumi, and N.O. Fowler, *Origin of cerebrospinal fluid pulsations.* American Journal of Physiology, 1967. **212**(4): p. 840-6.

454. Greitz D, Hannerz J, Rähn T, Bolander H, Ericsson A., *MR imaging of cerebrospinal fluid dynamics in health and disease on the vascular pathogenesis of communicating hydrocephalus and benign intracranial hypertension.* Acta Radiologica, 1994. **35**: p. 204–11.

455. Hamer J, A.E., Hoyer S, Wiedemann K., *Influence of systemic and cerebral vascular factors on the cerebrospinal fluid pulse waves.* Journal of Neurosurgery, 1977. **46**(1): p. 36-45.

456. Dunbar, H.S., T.C. Guthrie, and B. Karpell, *A study of the cerebrospinal fluid pulse wave.* Archives of Neurology, 1966. **14**(6): p. 624-630.

457. Takizawa, H., T. Gabra-Sanders, and J.D. Miller, *Variations in pressure-volume index and CSF outflow resistance at different locations in the feline craniospinal axis.* Journal of Neurosurgery, 1986. **64**(2): p. 298-303.

458. Urayama, K, *Origin of lumbar cerebrospinal fluid pulse wave.* Spine (Philadelphia 1976), 1994. **19**(4): p. 441-5.

459. Iliff, J.J., Wang M, Zeppenfeld DM, Venkataraman A, Plog BA, Liao Y, Deane R, Nedergaard M., *Cerebral arterial pulsation drives paravascular CSF-interstitial fluid exchange in the murine brain.* Journal of Neuroscience, 2013. **33**(46): p. 18190-9.

460. Hadaczek P, Y.Y., Mirek H, Tamas L, Bohn MC, Noble C, Park JW, Bankiewicz K., *The "perivascular pump" driven by arterial pulsation is a powerful mechanism for the distribution of therapeutic molecules within the brain.* Molecular Therapy, 2006. **14**(1): p. 69-78.

461. Iliff JJ, W.M., Zeppenfeld DM, Venkataraman A, Plog BA, Liao Y, Deane R, Nedergaard M, *Cerebral arterial pulsation drives paravascular CSF-interstitial fluid*

exchange in the murine brain. Journal of Neuroscience, 2013. **33**(46): p. 18190–18199.

462. Okamoto Y, Y.T., Kalaria RN, Senzaki H, Maki T, Hase Y, Kitamura A, Washida K, Yamada M, Ito H, Tomimoto H, Takahashi R, Ihara M *Cerebral hypoperfusion accelerates cerebral amyloid angiopathy and promotes cortical microinfarcts. .* Acta Neuropathologica, 2012. **123**(3): p. 381–394.

463. Schley, D., Carare-Nnadi, R, Please, CP, Perry, VH, Weller, RO., *Mechanisms to explain the reverse perivascular transport of solutes out of the brain.* Journal of Theoretical Biology, 2006. **238**(4): p. 962-74.

464. Weller RO, B.D., Nicoll JA *Microvasculature changes and cerebral amyloid angiopathy in Alzheimer's disease and their potential impact on therapy.* Acta Neuropathologica, 2009. **118**(1): p. 87–102.

465. Diem AK, M.S.M., Gatherer M, Bressloff NW, Carare RO, Richardson G, *Arterial Pulsations cannot Drive Intramural Periarterial Drainage: Significance for Aβ Drainage.* Frontiers in Neuroscience, 2017. **11**(475).

466. Bilston, L.E., D.F. Fletcher, and M.A. Stoodley, *Focal spinal arachnoiditis increases subarachnoid space pressure: A computational study.* Clinical Biomechanics, 2006. **21**(6): p. 579-584.

467. Wang P, Olbricht WL., *Fluid mechanics in the perivascular space.* Journal of Theoretical Biology, 2011. **274**(1): p. 52-7.

468. Williams, B., *Cerebrospinal fluid pressure changes in response to coughing.* Brain, 1976. **99**(2): p. 331-46.

469. Williams, B., *Simultaneous cerebral and spinal fluid pressure recordings. 2. Cerebrospinal dissociation with lesions at the foramen magnum.* Acta Neurochirurgica (Wien), 1981. **59**(1-2): p. 123-42.

470. Feldman Z, R.C., Contant CF, Gopinath SP, Grossman RG., *Positive end expiratory pressure reduces intracranial compliance in the rabbit.* Journal of Neurosurgical Anesthesiology, 1997. **9**: p. 175–179.

471. Schley D, C.-N.R., Please CP, Perry VH, Weller RO., *Mechanisms to explain the reverse perivascular transport of solutes out of the brain.* Journal of Theoretical Biology, 2006. **238**: p. 962–974.

472. Dreha-Kulaczewski, S., Joseph AA, Merboldt KD, Ludwig HC, Gärtner J, Frahm J., *Identification of the Upward Movement of Human CSF In Vivo and its Relation to the Brain Venous System.* The Journal of Neuroscience, 2017. **37**(9): p. 2395-2402.

473. Kao, Y.H., Guo WY, Liou AJ, Hsiao YH, Chou CC., *The respiratory modulation of intracranial cerebrospinal fluid pulsation observed on dynamic echo planar images.* Magnetic Resonance Imaging, 2008. **26**(2): p. 198-205.

474. Schroth, G. and U. Klose, *Cerebrospinal fluid flow. II. Physiology of respiration-related pulsations.* Neuroradiology, 1992. **35**(1): p. 10-5.

475. Chen, L., Beckett A, Verma A, Feinberg DA, *Dynamics of respiratory and cardiac CSF motion revealed with real-time simultaneous multi-slice EPI velocity phase contrast imaging.* Neuroimage, 2015. **122**: p. 281-7.

476. Chen L, B.A., Verma A, Feinberg D, *Dynamics of respiratory and cardiac CSF motion revealed with real-time simultaneous multi-slice EPI velocity phase contrast imaging. .* NeuroImage 2015. **122**(281–287).

477. Dreha-Kulaczewski S, K.M., Joseph AA, Kollmeier J, Merboldt KD, Ludwig HC, Gärtner J and Frahm J *Respiration and the watershed of spinal CSF flow in humans.* Scientific Reports, 2018. **8**(5594).

478. Takizawa K, M.M., Sunohara S, Yatsushiro S, Kuroda K, *Characterization of cardiac- and respiratory-driven cerebrospinal fluid motion based on asynchronous*

phase-contrast magnetic resonance imaging in volunteers. Fluids and Barriers of the CNS, 2017. **14** (25).

479. Yiallourou, T.I., et al., *Continuous positive airway pressure alters cranial blood flow and cerebrospinal fluid dynamics at the craniovertebral junction.* Interdisciplinary Neurosurgery, 2015. **2**(3): p. 152-159.

480. Ju YE, F.M., Sutphen CL, Herries EM, Jerome GM, Ladenson JH, Crimmins DL, Fagan AM, Holtzman DM, *Obstructive sleep apnea decreases central nervous system-derived proteins in the cerebrospinal fluid.* Annals of Neurology, 2016. **80**(1): p. 154-9.

481. Kiviniemi V, W.X., Korhonen V, Keinänen T, Tuovinen T, Autio J, LeVan P, Keilholz S, Zang YF, Hennig J, Nedergaard M., *Ultra-fast magnetic resonance encephalography of physiological brain activity - Glymphatic pulsation mechanisms?* Journal of Cerebral Blood Flow and Metabolism, 2016. **36**(6): p. 1033-45.

482. Xie L, K.H., Xu Q, Chen MJ, Liao Y, Thiyagarajan M, O'Donnell J, Christensen DJ, Nicholson C, Iliff JJ, Takano T, Deane R, Nedergaard M., *Sleep drives metabolite clearance from the adult brain.* Science, 2013. **342**(6156): p. 373-7.

483. Gakuba C, G.T., Goursaud S, Bourges J, Di Palma C, Quenault A, Martinez de Lizarrondo S, Vivien D, Gauberti M, *General Anesthesia Inhibits the Activity of the "Glymphatic System".* Theranostics, 2018. **8**(3): p. 710-722.

484. Schain AJ, M.-C.A., Strassman AM, Burstein R, *Cortical Spreading Depression Closes Paravascular Space and Impairs Glymphatic Flow: Implications for Migraine Headache.* J Neurosci. , 2017. **37**(11): p. 2904-2915.

485. Siyahhan B, K.V., de Zélicourt D, Asgari M, Schmid Daners M, Poulikakos D, Kurtcuoglu V., *Flow induced by ependymal cilia dominates near-wall cerebrospinal fluid dynamics in the lateral ventricles.* J R Soc Interface. , 2014. **11**(94): p. 20131189.

486. Stokum JA, G.V., Simard JM, *Molecular pathophysiology of cerebral edema.* J Cereb Blood Flow Metab. , 2016. **36**(3): p. 513-38. .

487. Geer, C.P. and S.A. Grossman, *Interstitial fluid flow along white matter tracts: a potentially important mechanism for the dissemination of primary brain tumors.* Journal of Neurooncology, 1997. **32**(3): p. 193-201.

488. Rasmussen MK, M.H., Nedergaard M, *The glymphatic pathway in neurological disorders.* Lancet Neurology, 2018. **17**: p. 1016–24.

489. Hawkes CA, H.W., Kacza J, Schliebs R, Weller RO, Nicoll JA, et al, *Perivascular drainage of solutes is impaired in the ageing mouse brain and in the presence of cerebral amyloid angiopathy.* Acta Neuropathologica, 2011. **121**(431-443).

490. Tachikawa M, T.K., Yokoyama R, Higuchi T, Ozeki G, Yashiki A, et al, *A clearance system for prostaglandin D2, a sleep-promoting factor, in cerebrospinal fluid: role of the blood-cerebrospinal barrier transporters.* Journal of Pharmacology and Experimental Therapeutics, 2012. **343**: p. 608-616.

491. Wong HL, W.X., Bendayan R, *Nanotechnological advances for the delivery of CNS therapeutics.* Advanced Drug Delivery Reviews, 2012. **64**: p. 686-700.

492. Bevan AK, D.S., Foust KD, Morales PR, Braun L, Schmelzer L, et al, *Systemic gene delivery in large species for targeting spinal cord, brain, and peripheral tissues for pediatric disorders.* Molecular Therapy: the Journal of the American Society of Gene Therapy, 2011. **19**: p. 1971-1980.

493. Rekate, HL., *The definition and classification of hydrocephalus: a personal recommendation to stimulate debate.* Cerebrospinal Fluid Research, 2008. **5**(2).

494. Hodel J, B.P., Rahmouni A, Petit E, Lebret A, et al., *3D mapping of cerebrospinal fluid local volume changes in patients with hydrocephalus treated by surgery: preliminary study.* . Eur. Radiol. , 2013. **24**(24:1): p. 136–42.

495. Lebret A, H.J., Rahmouni A, Decq P, Petit E, *Cerebrospinal fluid volume analysis for hydrocephalus diagnosis and clinical research.* Computerized Medical Imaging and Graphics, 2013. **37**: p. 224–33.

496. Sæhle T, Eide, PK, *Association between ventricular volume measures and pulsatile and static intracranial pressure scores in non-communicating hydrocephalus.* Journal of Neurological Sciences, 2015. **350** p. 33–39.

497. Weller, RO., *Pathology of cerebrospinal fluid and interstitial fluid of the CNS: significance for Alzheimer disease, prion disorders and multiple sclerosis.* Journal of Neuropathology and Experimental Neurology, 1998. **57**(10): p. 885–894.

498. Alperin N, O.C., Bagci AM, Lee SH, Kovanlikaya I, Adams D, Katzen H, Ivkovic M, Heier L, Relkin N, *Low-dose acetazolamide reverses periventricular white matter hyperintensities in iNPH.* Neurology, 2014. **82**(15): p. 1347–1351.

499. Hopkins LN, B.L., Kinkel WR, Grand W., *Demonstration of transventricular CSF absorption by computerized tomography.* Acta Neurochirurgica, 1977. **39**: p. 151–57.

500. Tomycz LD, H.A., George TM., *Emerging Insights and New Perspectives on the Nature of Hydrocephalus.* Pediatric Neurosurgery, 2017. **52**(6): p. 361-368.

501. Verkman AS, T.L., Smith AJ, Yao X, *Aquaporin Water Channels and Hydrocephalus.* Pediatric Neurosurgery, 2017. **52**(6): p. 409–416.

502. Orešković D, R.M., Klarica M., *New Concepts of Cerebrospinal Fluid Physiology and Development of Hydrocephalus.* Pediatric Neurosurgery, 2017. **52**(6): p. 417-425.

503. Limbrick DD Jr, C.-R.L., Han RH, Berger D, McAllister JP, Morales DM., *Cerebrospinal Fluid Biomarkers of Pediatric Hydrocephalus.* Pediatric Neurosurgery, 2017. **52**(6): p. 426-435.

504. Rodríguez EM1, Guerra, .M., *Neural Stem Cells and Fetal-Onset Hydrocephalus.* Pediatric Neurosurgery, 2017. **52**(6): p. 446-461.

505. Wang J, G.B., Masters CL, Wang YJ. , *A systemic view of Alzheimer disease—insights from amyloid-β metabolism beyond the brain.* Nature Reviews Neurology, 2017. **13**: p. 612–23.

506. Xu Z, Xiao N, Chen Y, Huang H, Marshall C, Gao J, Cai Z, Wu T, Hu G, Xiao M, *Deletion of aquaporin-4 in APP/PS1 mice exacerbates brain Aβ accumulation and memory deficits.* Molecular Neurodegeneration, 2015. **10** (58).

507. Ma Q, I.B., Detmar M, Proulx ST *Outflow of cerebrospinal fluid is predominantly through lymphatic vessels and is reduced in aged mice.* Nature Communications, 2017. **8**(1434).

508. Zeppenfeld DM, Simon M, Haswell JD, D'Abreo D, Murchison C, Quinn JF, Grafe MR, Woltjer RL, Kaye J, Iliff JJ., *Association of perivascular localization of aquaporin-4 with cognition and Alzheimer disease in aging brains.* JAMA Neurology, 2017. **74**: p. 91–99.

509. Peng W, A.T., Li B, et al. , *Suppression of glymphatic fluid transport in a mouse model of Alzheimer's disease.* Neurobiology of Disease, 2016. **93**: p. 215–25.

510. Iliff JJ, C.M., Plog BA, Zeppenfeld DM, Soltero M, Yang L, Singh I, Deane R, Nedergaard M., *Impairment of glymphatic pathway function promotes tau pathology after traumatic brain injury.* Journal of Neuroscience, 2014. **34**(49): p. 16180-93.

511. Plog BA, Dashnaw ML, Hitomi E, Peng W, Liao Y, Lou N, Deane R, Nedergaard M, *Biomarkers of traumatic injury are transported from brain to blood via the glymphatic system.* Journal of Neuroscience, 2015. **35** (518–26.).

512. Sakka L, G.J., Coll G, *Anatomy of the Spinal Meninges.* Operative Neurosurgery, 2016. **12**: p. 168–188.

513. Cserr, H.F., Cooper, D.N. and Milhorat, T.H., *Flow of cerebral interstitial fluid as indicated by the removal of extracellular markers from rat caudate nucleus.* Experimental Eye Research, 1977. **25 Suppl**: p. 461-73.

514. Bedussi, van Lier MG, Bartstra JW, de Vos J, Siebes M, Van Bavel E, Bakker EN., *Clearance from the mouse brain by convection of interstitial fluid towards the ventricular system.* Fluids Barriers CNS, 2015. **12**: p. 23.

515. Jessen, N.A., Munk AS, Lundgaard I, Nedergaard M, *The Glymphatic System: A Beginner's Guide.* Neurochemical Research, 2015. **40**(12): p. 2583-99.

516. Milhorat TH, N.S., Heger I, Nobandegani F, Murray S. *Ultrastructural evidence of sink function of central canal of spinal cord as demonstrated by clearance of horseradish peroxidase.* Proceedings of the Electron Microscopy Society of America, 1992. **50**: p. 700–701.

517. Rossi, C., Boss A, Steidle G, Martirosian P, Klose U, Capuani S, Maraviglia B, Claussen CD, Schick F, *Water diffusion anisotropy in white and gray matter of the human spinal cord.* Journal of Magnetic Resonance Imaging, 2008. **27**(3): p. 476-482.

518. Schneider, C.A., W.S. Rasband, and K.W. Eliceiri, *NIH Image to ImageJ: 25 years of image analysis.* Nature Methods, 2012. **9**(7): p. 671-5.

519. Ellingson, B.M., Ulmer JL, Kurpad SN, Schmit BD., *Diffusion tensor MR imaging in chronic spinal cord injury.* AJNR American Journal of Neuroradiology, 2008. **29**(10): p. 1976-82.

520. Sarntinoranont, M., Chen X, Zhao J, Mareci TH, *Computational model of interstitial transport in the spinal cord using diffusion tensor imaging.* Annals of Biomedical Engineering, 2006. **34**(8): p. 1304-21.

521. Nicholson, C., Chen KC, Hrabětová S, Tao L, *Diffusion of molecules in brain extracellular space: theory and experiment.* Progress in Brain Research, 2000. **125**: p. 129-54.

522. Woollam, D.H. and J.W. Millen, *The perivascular spaces of the mammalian central nervous system and their relation to the perineuronal and subarachnoid spaces.* Journal of Anatomy, 1955. **89**(2): p. 193-200.

523. Lam, M.A., Hemley SJ, Najafi E, Vella NGF, Bilston LE, Stoodley MA, *The ultrastructure of spinal cord perivascular spaces: Implications for the circulation of cerebrospinal fluid.* Scientific Report, 2017. **7**(1): p. 12924.

524. Morrison, P.F., Laske DW, Bobo H, Oldfield EH, Dedrick RL., *High-flow microinfusion: tissue penetration and pharmacodynamics.* American Journal of Physiolology, 1994. **266**(1 Pt 2): p. R292-305.

525. Stoodley, M.A., Jones NR, Yang L, Brown CJ, *Mechanisms underlying the formation and enlargement of noncommunicating syringomyelia: experimental studies.* Neurosurgical focus, 2000. **8**(3).

526. Tan I, B.M., Liu YY, Ng K, Avolio AP, *Heart rate dependence of aortic pulse wave velocity at different arterial pressures in rats.* Hypertension, 2012. **60**(2): p. 528-33.

527. Liu, S., Lam MA, Sial A, Hemley SJ, Bilston LE, Stoodley MA., *Fluid outflow in the rat spinal cord: the role of perivascular and paravascular pathways.* Fluids and Barriers of the CNS, 2018. **15**(13).

528. Kwon S, Janssen CF, Velasquez FC, Sevick-Muraca EM., *Fluorescence imaging of lymphatic outflow of cerebrospinal fluid in mice.* Journal of Immunological Methods, 2017. **449**: p. 37-43.

529. Sakatani K, Kashiwasake-Jibu M, Taka Y, Wang S, Zuo H, Yamamoto K, Shimizu K., *Noninvasive optical imaging of the subarachnoid space and cerebrospinal fluid pathways based on near-infrared fluorescence.* Journal of Neurosurgery, 1997. **87**(5): p. 738-45.

530. Shibata Y, Kruskal JB, and P. MR, *Imaging of cerebrospinal fluid space and movement of hydrocephalus mice using near infrared fluorescence.* Neurological Sciences, 2007. **28**(2): p. 87-92.

531. Shibata Y, Kruskal JB, and P. MR, *Imaging of cerebrospinal fluid space and movement in mice using near infrared fluorescence.* Journal of Neuroscience Methods, 2005. **147**(2): p. 82-7.

532. Alander JT, Kaartinen I, Laakso A, Pätilä T, Spillmann T, Tuchin VV, Venermo M, Välisuo P., *A Review of Indocyanine Green Fluorescent Imaging in Surgery.* International Journal of Biomedical Imaging, 2012. **2012**(940585).

533. Hutteman M, M.J., van der Vorst JR, Liefers GJ, Putter H, Löwik CW, Frangioni JV, van de Velde CJ, Vahrmeijer AL., *Randomized, double-blind comparison of indocyanine green with or without albumin premixing for near-infrared fluorescence imaging of sentinel lymph nodes in breast cancer patients.* Breast Cancer Research and Treatment, 2011. **127**(1): p. 163-70.

534. Arbel-Ornath M, Hudry E, Eikermann-Haerter K, Hou S, Gregory JL, Zhao L, Betensky RA, Frosch MP, Greenberg SM, Bacskai BJ, *Interstitial fluid drainage is impaired in ischemic stroke and Alzheimer's disease mouse models.* Acta Neuropathologica, 2013. **126**(3): p. 353-64.

535. Li YC, B.W., Sakai K, Hashikawa T., *Fluorescence and electron microscopic localization of F-actin in the ependymocytes.* Journal of Histochemistry and Cytochemistry, 2009. **57**(8): p. 741-51.

536. Berliner JA, W.T., Najafi E, Hemley SJ, Lam M, Cheng S, Bilston LE, Stoodley MA, *Effect of extradural constriction on CSF flow in rat spinal cord.* Fluids and Barriers of the CNS., 2019. **26**(16(1)): p. 7.

537. Luo C, Y.X., Li J, He B, Liu Q, Ren H, Liang F, Li M, Lin H, Peng J, Yuan TF, Pei Z and Su H, *Paravascular pathways contribute to vasculitis and neuroinflammation after subarachnoid hemorrhage independently of glymphatic control.* Cell Death and Disease, 2016 **7**(3): p. e2160.

538. Iliff JJ, L.H., Yu M, Feng T, Logan J, Nedergaard M, Benveniste H., *Brain-wide pathway for waste clearance captured by contrast-enhanced MRI.* Journal of Clinical Investigation, 2013. **123**(3): p. 1299-309.

539. Huang SL, P.J., Yuan GL, Ding XY, He XJ, Lana BS, *A new model of tethered cord syndrome produced by slow traction.* Scientific Report, 2015. **5**: p. 9116.

540. Saunders NR, D.K., Whish SC, Hinds LA, Wheaton BJ, Huang Y, Henry S, Habgood MD, *A bipedal mammalian model for spinal cord injury research: The tammar wallaby.* F1000Research, 2017. **6**(921).

9 Animal Ethics

MACQUARIE University
ANIMAL RESEARCH AUTHORITY (ARA)

AEC Reference No.: 2016/032-15   <u>Date of Expiry:</u> 21 December 2019

Full Approval Duration: 21 December 2016 to 19 February 2020

This ARA remains in force until the Date of Expiry (unless suspended, cancelled or surrendered) and will only be renewed upon receipt of a satisfactory Progress Report before expiry (see Approval email for submission details).

Principal Investigator:
Dr Magdalena Lam
Faculty of Medicine and Health Sciences
Macquarie University, NSW 2109
0434 712 030
magdalena.lam@mq.edu.au

Associate Investigators:	
Simon McMullan	0402 073 146
Marcus Stoodley	0407 896 492
Sarah Hemley	0403 513 899
Others Participating:	
Shinuo Liu	0424 065 968
Atieh Najafi	0435 148 822
Joel Berliner	0406 019 753

> **In case of emergency, please contact:**
> *the Principal Investigator / Associate Investigator named above*
> or Manager, CAF: 9850 7780 / 0428 861 163 and Animal Welfare Officer: 9850 7758 / 0439 497 383

The above-named are authorised by MACQUARIE UNIVERSITY ANIMAL ETHICS COMMITTEE to conduct the following research:

Title of the project: Cerebrospinal fluid (CSF) flow in the spinal cord and subarachnoid space with relevance to syringomyelia pathogenesis.

Purpose: 4 - Research: Human or Animal Biology

Aims: To Determine: 1. How fluid flows out of the spinal cord under normal conditions. 2.The effects of a) heart rate, b) blood pressure and c) respiration, on CSF flow in and around the spinal cord. 3.The effect of spinal cord cysts on the spinal cord ultrastructure using 2 models of syringomyelia

Surgical Procedures category: 5 - Major Surgery with Recovery

All procedures must be performed as per the AEC-approved protocol, unless stated otherwise by the AEC and/or AWO.

Maximum numbers approved (for the Full Approval Duration):

Species	Strain	Sex/Weight/Age	Total	Supplier/Source
02 - Rat	Sprague-Dawley	Male/Any/Any	337	ARC Perth
		TOTAL	337	

Location of research:

Location	Full street address
Central Animal Facility	Building F9A, Research Park Drive, Macquarie University, NSW 2109
FMHS Laboratory	Level 1, F10A, 2 Technology Place, Macquarie University, NSW 2109

Amendments approved by the AEC since initial approval:

1. Amendment 1 - Amend starting date of ARA from 02/02/2017 to 21/12/2016 (Approved by the Animal Welfare Officer. Ratified by AEC 16 February 2017).
2. Amendment 2 - Add a variation to existing procedure/ administration of substances (add injection of 4 x 0.5uL of quisqualic acid 24mg/mL into the dorsal spinal cord) (Executive approved. Ratified by AEC 16 February 2017).
3. Amendment #3 – Additional 10 animals (Executive approved. Ratified by AEC 16 March 2017).
4. Amendment #4(a) - Amend age and weight of animals from Age: 6 weeks and Weight 200-300g to Age: Any and Weight: Any (Approved by AEC 19 May 2017).
5. Amendment #4(b) - Amend number of animals to be housed at any one time from 20 to 35 (Approved by AEC 19 May 2017).
6. Amendment #4(c) - Amend maximum time an individual animal is held from 14 to 20 weeks (Approved by AEC 19 May 2017).
7. Amendment #5 – Additional 10 animals (5 per time line). (Executive Approved. Ratified by AEC 20 July 2017).
8. Amendment #6(a) - Add a surgical procedure (Executive Approved. Ratified by AEC 14 December 2017).
9. Amendment #6(b) - Add 40 animals (from 297 to 337)(Executive Approved. Ratified by AEC 14 December 2017).
10. Amendment #7 - Modify technique to include the use of a different dye and invivo imaging after a minor surgical procedure (Executive approved. Ratified by ARA 22 March 2018).
11. Amendment – 06/06/2018 – Additional procedure to include an invivo imaging study at a different location (Executive approved. Ratified by AEC 19 July 2018).
12. Amendment – 14/06/2018 – Additional procedure to include atrial pacing during experiments on cardiac function under anaesthesia (Executive approved. Ratified by AEC 20 September 2018).

Conditions of Approval: N/A

Being animal research carried out in accordance with the Code of Practice for a recognised research purpose and in connection with animals (other than exempt animals) that have been obtained from the holder of an animal suppliers' licence.

A/Prof. Nathan Hart (Chair, Animal Ethics Committee)   **Approval Date:** 13 December 2018

Adapted from Form C (issued under part IV of the Animal Research Act, 1985)

THE UNIVERSITY OF SYDNEY

A copy of this approval letter must be kept in the facility where your animals are housed.

Friday, 12 October 2018

Dr Jeffrey Rogers
Behavioural and Social Sciences in Health; Faculty of Health Sciences
The University of Sydney

Email: jeffrey.rogers@sydney.edu.au

Dear Dr Rogers

I am pleased to inform you that the University of Sydney Animal Ethics Committee (AEC) has approved your project entitled **"CSF flow in the spinal cord and subarachnoid space with relevance to syringomyelia pathogenesis"**.

Details of the approval are as follows:

Project Number:	2018/1402
Project Type:	Experimental (non-wildlife)
Project Duration:	12 October 2018 – 12 October 2021
Approval Period:	**12 October 2018 – 12 October 2019**
Annual Report Due:	12 October 2019

In compliance with Section 27 of the NSW *Animal Research Act 1985*, this Animal Research Authority (ARA) remains in force for a period of 12 months from the date of issue, unless cancelled sooner.

Renewal of the ARA is conditional upon submission of a satisfactory annual report to the AEC in accordance with the *Australian code for the care and use of animals for scientific purposes 8th Edition 2013*.

Authorised Personnel:　　Rogers Jeffrey (CI); Hemley Sarah; Liu Shinuo

Project Description:
Fluid homeostasis in the central nervous system (CNS) is essential for normal neurological function. Abnormalities in cerebrospinal fluid (CSF) homeostasis can lead to serious neurological disorders, including syringomyelia, a disorder characterised by the formation of a fluid-filled cavity within the spinal cord. Clinical outcomes are poor and the mechanisms involved in syringomyelia formation are not well understood. This is largely due to a general lack of understanding of the normal CSF circulation. Many fundamental aspects such as the effect of respiration and cardiac parameters on CSF flow are unknown. This project will investigate these questions using intravital multiphoton microscopic analysis in Sprague-Dawley rats.
Specific aims of the project are to:
1. Determine the effects of a) heart rate, b) blood pressure and, c) respiration on CSF flow in and around the spinal cord.

Documents Approved:

Date	Type	Document
05/10/2018	Standard Operating Procedure	SOP Phrenic Nerve Transection

05/10/2018	Standard Operating Procedure	SOP Anaesthetic Protocol
05/10/2018	Monitoring Sheet	Monitoring sheet - isoflurane
27/08/2018	Other	AEC-SOP-Intubation of rodents
27/08/2018	Other	AEC-SOP-Femoral artery and vein cannulation of rodents
27/08/2018	Other	AEC-SOP-insertion of atrial pacing wire
27/08/2018	Other	AEC-SOP-Intravital microscopy
27/08/2018	Other	AEC-SOP-Laminectomy
27/08/2018	Other	AEC-SOP-Cisterna Magna cannulation of rodents

Animals Approved:
Please refer to the document at the end of this letter, which details your approved animal usage and location(s).

Approved protocol
The Committee has approved the following changes to the original protocol:
1. Replacement of urethane with isoflurane.
2. Inclusion of premedication with buprenorphine and midazolam.
3. Animals who are not receiving the neuromuscular blockade are to be done first to establish an estimated imaging timeframe.
4. Addition of phrenic nerve transection to the surgical protocol as an alternative to neuromuscular blockade. This will be performed if the microscopy is found to exceed 1 hr and following discussion with the Animal Welfare Veterinarian team.

Special Condition/s of Approval

You may commence the project without any further review by the AEC, provided the following conditions have been met:

1. Given the complexity of the anaesthetic protocol in this project and to ensure competency, we require for all investigators involved to be assessed and deemed competent by Dr Shaun Miller or Dr Danny Lee (Animal Welfare Veterinarian team) before each investigator is permitted to proceed. Please ensure you contact Dr Miller or Dr Lee (resint.veterinarian@sydney.edu.au) to discuss the assessment arrangements.

Conditions of Approval

1. This project must be conducted according to the approved project including continuing compliance with the conditions outlined in this ARA and with the *Animal Research Act 1985*, *Animal Research Regulation 2010*, the *Australian code for the care and use of animals for scientific purposes 8th edition 2013* (the Code) and all other relevant legislation.

2. Any changes to the project must be approved by the AEC prior to their implementation.
   This includes notifying the AEC of any changes to named personnel, source of animals, animal numbers, location of animals and experimental procedures.

3. An annual progress report or completion report must be submitted on or before the anniversary of approval of the project.

4. All unexpected adverse events that may impact on the wellbeing of an animal must be reported to the AEC within 48 hours, as per Clause 2.1.5 [v] [d] and 2.4.34 [ii] in the Code. Please refer to the Animal Ethics website and log into IRMA to complete an Adverse Event form.

5. The AEC must be notified if rodents are required to be singly housed.

6.   All animal enclosures (e.g. pens, cages and containers) must be clearly identified with chief investigator name, number of animals, DOB if provided and date of arrival, sex and strain.

7.   The following documentation must be kept in the facility where your animals are housed or with you when undertaking fieldwork:
   - A copy of this ARA
   - Emergency contact details in case of an animal emergency
   - Approved monitoring records

8.   Personnel working on this project must be sufficiently qualified by education, training and experience for their role, or adequately supervised.
   All new investigators must successfully complete the Introduction to Animal Research (ITAR) course.

9.   Data must be retained and stored in accordance with the relevant legislation and University guidelines.

10. The AEC will make regular announced inspections of all animal facilities and/or specific research projects. The Animal Welfare Veterinarian will be conducting unannounced inspections of all animal facilities and/or specific research projects.

11. Any drugs to be used for procedures involving animals must within date (not expired) and stored appropriately as per the manufacturer's recommendations. It is the responsibility of the Chief Investigator to ensure that all relevant and current authority for the use of restricted drugs is obtained.

Please do not hesitate to contact the Ethics Office at animal.ethics@sydney.edu.au should you require further information or clarification.

Yours sincerely

Dr Lois Cavanagh
Chair
Animal Ethics Committee
On behalf of the University of Sydney

The AEC is constituted and operates in accordance with the NSW Animal Research Act 1985 and its associated Regulations, the Australian code for the care and use of animals for scientific purposes 8th Edition 2013 and the Australian Code for the Responsible Conduct of Research 2007. All personnel named on the project should be conversant with these documents.

THE UNIVERSITY OF SYDNEY

A copy of this approval letter must be kept in the facility where your animals are housed.

Animals Approved:

Country	State	Invasiveness	Location	Classification one	Classification two	Common/strain name	Approved	Total used to date
Australia	NSW	2. Animal unconscious without recovery	Brain and Mind Research Institute (M02G), Camperdown	Laboratory mammals	Rats	Sprague-Dawley	30	0